A Detailed Performance Examination of Electrical Machines of High Power And Speed

Master's

In

Electrical Engineering

Aditya Desiraju

Abstract

High Speed High Power (HSHP) electrical machines push the limits of electromagnetics, material capabilities and construction techniques. In doing so they are able to match the power performance of high speed turbomachinery such as gas turbines, compressors and expanders. This makes them attractive options for direct coupling to such machinery as either a power source or as a generator; eliminating the need for gearboxes and achieving a smaller system size and greater reliability.

The design of HSHP machines is a challenging, iterative process. Mechanical, electromagnetic and thermal constraints are all placed on the machine shape, topology, operating point and materials. The designer must balance all of these constraints to find a workable solution that is mechanically stable, can work within the available electrical supply and will not overheat.

This thesis researches the fundamental origins and interaction of the mechanical, electromagnetic and thermal constraints on electrical machines. Particular attention was paid to improving the accuracy of traditional mechanical rotor design processes, and improving loss estimation in inverter fed machines. The issues of selecting an appropriate electric loading for low voltage machines and choosing effective, economic cooling strategies were explored in detail.

An analytical iterative design process that combines mechanical, electromagnetic and thermal design is proposed; this process balances the need for speed versus accuracy for the initial design of a machine, with Finite Element Analysis used only for final validation of performance and losses.

The design process was tested on the design and manufacture of a 1.1MW 30,000rpm PM dynamometer used in an industrial test stand. The machine operating point was chosen to meet a gap in the industrial machines market and exceed the capabilities of other commercially available machines of the same speed. The resulting machine was successfully tested and comfortably meets the performance criteria used in the design process.

Contents

List of Figures

List of Tables

List of Symbols

The following is a list of the symbols used in this thesis, subscripts are added in the text to denote specific meaning to some symbols and are defined in the main body of the text where used.

A	Vector Potential
α	Coefficient of Linear Thermal Expansion
B	Flux Density
c_p	Specific Heat Capacity
C_d	Drag Coefficient
d_c	Wire Diameter
□	Small Time Increment
$□_{interference}$	Interference Fit
$□_T$	Thermally Induced Interference
□T	Change in Temperature
E	Young's Modulus
ε	Strain
f	Frequency
g	Magnetic Pole Pitch
F	Force
h_c	Convection Coefficient
H	Magnetic Field Strength
I	Second Moment of Area
J	Current Density
k	Coefficient of Thermal Conduction
K_{AC}	DC to AC Loss Multiplier
K_z	Magnetic Field Strength of Current Sheet
K_a	Anomalous Loss Coefficient
K_e	Eddy Current Loss Coefficient
K_h	Hysteresis Loss Coefficient
	Axial length
L	Inductance
□	Slot Pitch
m	Mass
μ	Permeability
n	Rotational speed in rpm
N	Number of Turns / Number of Conductors
ν	Poissons Ratio
ω	Rotational velocity ($rads^{-1}$)
ω_c	Critical Speed
ω_d	Design Speed
ω_o	Operating Speed
p	Pole Pair Number
P	Power
$P_{Anomalous}$	Anomalous Power Loss
P_{AC}	AC Power Loss
$P_{Average}$	Average Pressure
P_{Drag}	Drag Power Loss
$P_{Eddy\ Current}$	Eddy Current Power Loss
$P_{Hysteresis}$	Hysteresis Power Loss

	Load Angle
q	Internal Pressure
Q	Heat Transfer Rate
Q_{gen}	Internal Heat Generation per Unit Volume
r	Radius
R_{AC}	Equivalent AC Resistance
R_s	Surface Resistance
Re	Reynolds Number
R_{Cond}	Conduction Thermal Resistance
R_{Convec}	Convection Thermal Resistance
ρ	Mass Density
ρ_c	Conductor Resistivity
σ	Stress
σ_h	Hoop Stress
σ_r	Radial Stress
T	Torque
τ	Shear Stress
□	Angle
vf	Volume Fraction
v_{tip}	Tip Speed

Chapter 1. Introduction

The design of a High Speed, High Power (HSHP) machine is a complex problem requiring a multidisciplinary approach; the high demands on the machine require careful mechanical and thermal as well as electromagnetic design. Significant challenges are experienced in all three design domains, which are closely coupled, where material and system capabilities are pushed to their limits when trying to achieve the most power and torque dense solution. The desire to achieve high torque density through a high electrical loading pushes the machine to its thermal limits, while the desire for a high power density solution through very high speeds pushes the design close to its mechanical limits. The combination or high speeds and loadings cause significant electromagnetic challenges, both in achieving a sound electrical design, and in minimising the losses in the machine.

The thermal limits present themselves in the peak operating temperatures allowed by the machine materials and insulation system, and are controlled via the capability of the cooling system and the intensity of the losses produced by the electromagnetic design. The mechanical limits are caused by stressing induced by the high speed centrifugal forces on the rotor components and the natural vibration frequency of the shaft, which can be close to the operating speed. These factors are affected by material choice and the size and shape of the rotor, which in turn has effects on the thermal and electromagnetic design. The electromagnetic design is limited by the capability and voltage of the drive electronics and the losses caused in the machine, which in turn directly affect the thermal and mechanical design via heating and constraints on the machine geometry. The close coupling of all three design domains requires an iterative design approach; the effects of a change in one domain must be fully characterised in the others, which can lead to a lengthy design phase. This thesis will define a rapid, analytical based design routine to speed up this design process..

High Speed, High Power machines are generally a bespoke design for a specific application, and the requirements and available technologies of the application heavily influence the design of the machine. The particular applications where HSHP are an attractive choice include those where the mass and volume are critical, such as offshore oil and gas pumping. In addition the large speed and power ranges achievable in a single unit allow direct coupling with gas turbines to provide efficient and reliable distributed and CHP (Combined Heat and Power) generation without the need for a gearbox. Other niche applications for HSHP machines are as direct drive dynamometers, for the testing of high performance combustion and gas turbine machinery and drive trains, where the use for a gearbox is precluded for reasons of space, cost, reliability or

measurement accuracy. Some general duty HSHP machines exist in the marketplace, with a broad range of speed and power capabilities, and are marketed as general purpose prime movers or generators for various industrial applications, however an HSHP machine is generally designed to match the performance of the prime mover or load in its target application.

There are two main topologies used for HSHP machines: Permanent Magnet (PM) synchronous machines or Asynchronous machines, both driven from Variable Frequency Drives (VFD) that allow the generation of frequencies higher than the grid frequency. Asynchronous HSHP machines are favoured in large industrial settings where space is not constrained, whereas PM solutions are favoured when system size and weight constraints are critical.

1.1 Motivation

The chief motivation for this work was to research, design and manufacture a high performance Dynamometer for an aerospace test stand. The sponsoring partner, Torquemeters Ltd., received a commercial order for a high performance direct drive test stand for the testing of aerospace components with a specification that could not be matched by any market ready machines. The use of gearboxes and pulleys was precluded in the required system at the customer's request, due to their effects on measurement accuracy, thus the dynamometer must be directly coupled to the article under test and be able to match its speed and torque range. In order to meet these requirements a bespoke high performance machine had to be researched and prototyped, as no current machine of required performance was available commercially. This research and development work forms the bulk of this thesis. The requirements of the dynamometer were 30,000rpm maximum speed and a full torque capability across the speed range of 350Nm, delivering 1.1MW at full speed, while the whole system must be fed from a standard independently sourced Voltage Source Inverter (VSI) connected to an industrial three phase power supply at distribution level voltages (<1kV). This performance specification and the constraints on the power supply presented a challenging combination that had not been fully explored in the existing literature. The speed and torque requirements will be shown to be at the limit of what is technically possible with current materials and manufacturing processes, and indeed beyond what has been commercially achieved before. The limitation on power supply voltage levels will be shown to place specific constraints on the machine design at high powers; constraints that are not present in other commercial designs where higher supply voltage levels are available.

The research into the dynamometer design explored the capabilities of the available materials and technologies used in the construction of electrical machines and allowed the development of a standardised design process for use on future product enquiries. The design process was used to push the capabilities of these materials and processes to achieve a higher torque and power capability than other market ready machine designs. The design process must be capable of allowing rapid iteration between the three design domains, using analytical methods, to enable the machine to be sized quickly and to complete the majority of the design details before the need to use any computationally costly and lengthy Finite Element Analysis (FEA) analysis for validation.

1.2 Prior work

Existing research and development into HSHP machines can be split into industrial work and academic research. In both cases the design of the machines is highly influenced by the final application, which often imposes strict environmental or materials limitations on the design, leaving a bespoke solution unique to that application. Industrial solutions offer a tried and tested machine that should have an inherent level of reliability greater than that of academic demonstrators, which are often focused more to proof of concept for a particular design or technology; as such industrial motors may appear to have more limited capabilities than some academic designs, however they can be expected to have an improved service life. The following section will summarise HSHP machines currently commercially available, either as single units or as part of an industrial solution; this will be followed by a summary of academic research into high speed machines, HSHP machines and the technologies linked to their application.

1.2.1 A method for comparing HSHP designs

Given the wide range of potential applications, industrial HSHP machines span a broad range of performances, where the term ‘high speed’ is relative given the power output of the machine. What would appear to be low speed very high power output machines can be compared with higher speed, lower power machines as both push the mechanical, thermal and electromagnetic capabilities of the available technologies and materials used in their construction. High speeds cannot be defined as an absolute value but instead must be defined as those which push the stress limits of the rotor components. High power designs can be considered as those that maximise the rotor volume achievable from the rotor topology and materials, by pushing both the stress limits

and rotor resonance limits [1]. By considering this, a low speed very high torque rotor with a large volume can be just as mechanically challenging to construct as a much smaller higher speed rotor operating at a lower torque. As will be discussed in more detail in Chapter 2, the mechanical limits on the rotor dimensions caused by stress and resonance (critical speeds) are shown in Figure 1-1. The stresses caused by rotating body forces on the rotor components place a maximum radius limit on the rotor, given material limits, whereas the resonance limits for the machine place a maximum length limit on the rotor, for a given radius; within these boundaries a mechanically sound rotor can be constructed.

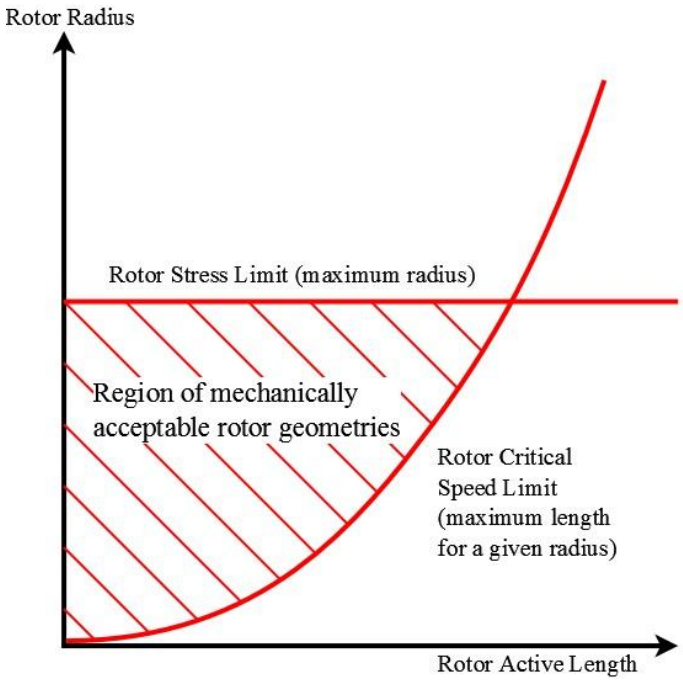

Figure 1-1: Mechanical Limits on rotor Dimensions for a Fixed Maximum Speed

Any rotor shape that approaches one of these limits of either stress or resonance, can be considered high speed, for that reason; however if it approaches both limits simultaneously is can be considered a HSHP rotor as the volume is maximised for a given magnetic and electrical loading. This method of defining what is classed as HSHP, based on the mechanical limits of the rotor; allows comparison across a wide range of speeds and powers, it is further consistent with the method of quantifying rotating machinery by its $n\sqrt{P}$ value [2] as used internally by the project sponsors, Torquemeters. The $n\sqrt{P}$ figure of merit is found by multiplying the machinery's speed, n, in rpm, by the square root of the power P, in kW; the number obtained allows a quick comparison of the mechanical engineering difficulty of various types of rotating machinery, including pumps, fans, turbines, gearboxes and couplings. A piece of machinery with an $n\sqrt{P}$ value of 1,000,000 is considered very difficult to engineer from a mechanical standpoint, whereas lower values of 500,000-800,000 are considered to be readily achievable, with only moderate mechanical engineering difficulty. It should be noted that the $n\sqrt{P}$ class leading figure

of merit of 1,000,000 applies to subcritical machines (i.e. below their first bending mode) with an expected variable operating speed. Machines performing in excess of 1,000,000 $n\sqrt{P}$ are discussed at the end of section 1.2.3.

The origin of $n\sqrt{P}$ as a mechanical based figure of merit can be traced back to mechanical stress limits on rotating machines, both from rotating body forces and torque transmission via the radius of the machine. The stresses caused in rotating components of various geometries are described in [3] and the relationship between radius, r, speed, ω, and stress, σ, can be simplified in (1.1) . This relationship can be shown to hold true assuming all component dimensions within the machine scale linearly with the radius of the machine.

$$\sigma \propto r^2\omega^2 \qquad (1.1)$$

For a constant stress level in the machine, (1.1) can be re-arranged to give (1.2), relating the radius of the machine directly to the inverse of the operating speed. This additionally gives a constraint of constant tip speed v_{tip} in the machine, as defined by (1.3).

$$\omega \propto \frac{1}{r} \quad (1.2)$$

$$v_{tip} = r\omega \qquad (1.3)$$

Comparing the power or torque ratings of various electrical machines is not a valid basis for comparison due the varying methods of generation, operating temperatures and bearing arrangements. Increasing power generation from a package can always be achieved by increasing the working length of the machine, or electric loading around the rotor (delivering a higher operating temperature for the same cooling level). What can be compared however, are the torque transmission capabilities of the machines, which is related to the power capability of the machine by the speed, via the shaft dimensions. From [3] again, the maximum torsion or torque carrying capability of a solid circular shaft is described by (1.4), where T is the torque, I the second moment of area of the shaft, r_{outer}, the shaft outer radius and τ_{max} the peak shear stress, found at the shaft outer surface.

$$T = \frac{I}{r_{outer}}\tau_{max} \qquad (1.4)$$

The second moment of area for a circular shaft is given in (1.5) and can be combined with (1.4) to give (1.6), showing a strong relationship between shaft radius and torque carrying capability. For the machines being considered, this relationship can be simplified to the expression in (1.7) assuming the shaft radius scales as with the other machine components. Multiplying both sides of the expression by the shaft speed ω, gives (1.8), relating the power delivered by the machine (and shaft) to the operating speed and shaft radius via the shaft shear stress limit.

$$I = \frac{\pi r^4}{4} \quad (1.5)$$

$$T = \frac{\pi r_{outer}^3}{4} \tau_{max} \quad (1.6)$$

$$\tau_{max} \propto \frac{T}{r^3} \quad (1.7)$$

$$\tau_{max} \propto \frac{P}{\omega r^3} \quad (1.8)$$

For a constant shear stress state in the shaft and noting that it was previously found that the tip speed of the machine must be kept constant for a constant rotational stress state, (1.8) can be simplified to (1.9) using (1.3).

$$P \propto r^2 \quad (1.9)$$

The two expressions, (1.2) and (1.9), can thus be combined in the $n\sqrt{P}$ expression to deliver a figure of merit for the machine that is independent of machine radius but describes a constant stress state both due to the rotating stresses and the torsional stresses. To maintain constant rotational stresses in the rotor, the rotor radius is limited to be inversely proportional to the speed; but conversely the power transmission capability of the machine is directly proportional to the square of the shaft radius. An assumption is made that the relationship between shaft and maximum rotor radius is arbitrarily fixed at some ratio; a fair assumption for machines such as turbines and gearboxes where blade root stress and gear tooth shear are linked to the radius of the rotor. Deviation from this ratio allows some variation in the range of $n\sqrt{P}$ figures for various machines, as does the design operating stress, material selection and operating temperature.

Thus, machines of widely differing powers or speeds can be compared by their $n\sqrt{P}$ figure, which implies that they are operating at broadly the same level of mechanical stressing. Material capabilities, operating temperatures and geometry differences will all affect the maximum $n\sqrt{P}$ that could be achieved by a machine via the associated constants implied in the proportional relationships described in (1.2) and (1.9). Machine types can be broadly grouped on the spectrum

of speed and power, as done by [2], due to their similar geometries, materials and operation principles, which will give a broadly similar $n\sqrt{P}$ for the constant stress state. Any machine that does not have an $n\sqrt{P}$ as large as others in its group can be considered to be less stressed and more straightforward to engineer, whereas those with the largest $n\sqrt{P}$ can be considered class leaders in terms of capability.

The $n\sqrt{P}$ figure of merit can be similarly applied to electrical machines, providing a mechanical figure of merit for the machine. For a given electrical loading the relationship between torque and rotor volume for an electrical machine is well defined and the rotor volume achievable at a given operating speed is defined by the relationships that describe the $n\sqrt{P}$ figure of merit. Thus the power capability of an electrical machine at a given speed is linked back to it's mechanical $n\sqrt{P}$ value for a given electrical loading and cooling capacity. The work of other authors to derive an electromagnetic figure of merit for high speed machines will be examined in the following sections.

1.2.2 Industrial Solutions

A comprehensive survey of existing high performance electrical machines was undertaken to gauge the state of the art in commercially available technology; this survey covered machines across a wide speed range, predominantly 10,000 to 100,000 rpm and power range from fractions of kW to multi-Megawatt machines; including PM, induction and synchronous wound field machines. The commercially produced machines are listed in Table 1-1 and Table 1-2 along with their manufacturers and target applications and their relative performances are compared in Figure 1-2, where the curves of constant $n\sqrt{P}$ equal to 500,000 and 1,000,000 are plotted as a guide. It was clear from the survey that most HSHP machines are developed for a specific function, ranging from motors for pumps compressors and spindles to generators for turbines and expanders. By far most common function for HSHP machines, and the main driver for research into increasing performance, is as the prime mover for compressor/expander systems in the oil and gas industry. Here the aim is to replicate or replace gas turbines as the prime mover in the system for reasons of cost and efficiency, reliability and fault tolerance, emissions and safety [4]; this proves a significant engineering challenge for the electrical machines. Where space is not a concern, such as in land based installations, induction motors and synchronous machines operating at high voltages and high powers are favoured, and deliver $n\sqrt{P}$ values in excess of 1,000,000; examples of these machine types are listed in Table 1-2.

Where machine size and weight is an issue, for example in offshore, urban or factory applications, PM machines are favoured due to their increased power density, although it can be seen that they generally do not reach the same high $n\sqrt{P}$ values that the nonspace constrained machines do, as shown in Figure 1-2. This shortfall is seen as a major commercial avenue for development.

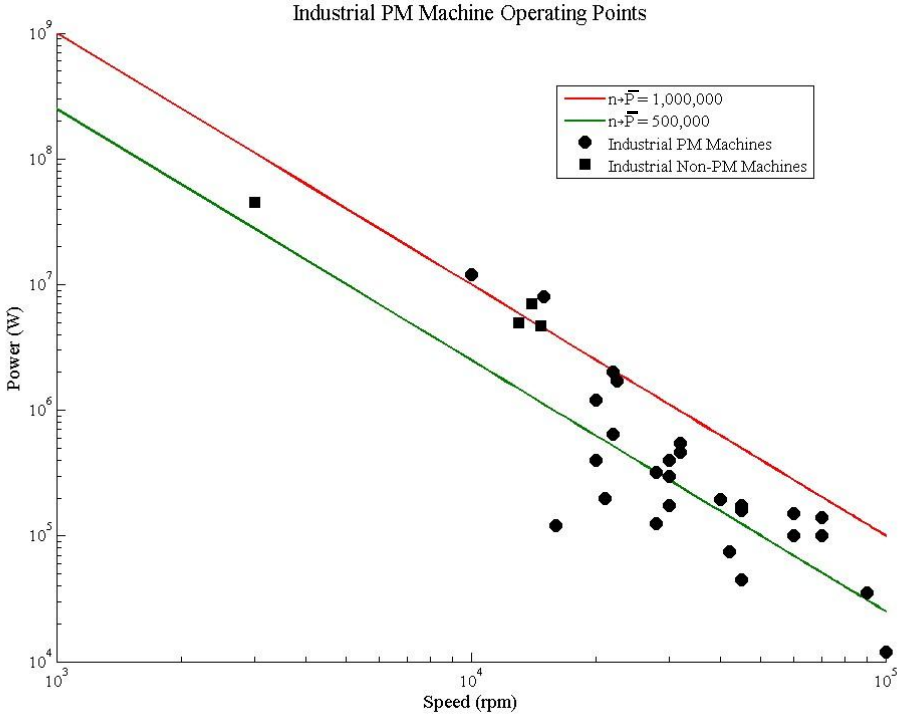

Figure 1-2: Industrial PM Machine Operating points

Of the PM machines shown in Figure 1-2 and Table 1-1, those that approach or exceed the $n\sqrt{P}$ value of 1,000,000 can be considered either to still be experimental, or not fully four quadrant in design. The two HSHP machines produced by Direct Drive Systems (DDS) with $n\sqrt{P}$ values over 1,000,000 have been announced but are not commercially available yet [5], while the high performance Ansaldo machine operates as a rectified generator only, avoiding some of the significant engineering challenges associated with achieving motoring operation from a Variable Speed Drive (VSD). Ignoring these machines, only one surveyed machine comes close to meeting the 1,000,000$n\sqrt{P}$ mark, also made by DDS. This shortfall in capability was a major factor in selection of the performance of the demonstrator machine to be developed as part of this thesis.

Speed (rpm)	Power (kW)	n√P (x 10 ^{6})	Manufacturer/Application
70000	140	0.828	S2M/SKF Pressure Let Down Expanders
60000	150	0.735	
45000	175	0.595	
30000	300	0.520	
120000	7	0.317	
70000	100	0.700	ABB/Turbec CHP Turbine
500000	0.5	0.354	E&A Spindle Motors
100000	12	0.346	
90000	35	0.532	
45000	45	0.302	
42000	75	0.364	
60000	100	0.600	
16000	120	0.175	
28000	125	0.313	
21000	200	0.297	
28000	320	0.501	
22000	2000	0.934	DDS Oil/Gas Pump motor
15000	8000	1.342	DDS Announced motors
10000	12000	1.095	
60000	100	0.600	Calnetix General purpose motors
30000	175	0.397	
20000	1200	0.693	TPS Turbine motor/generator
30000	400	0.600	
40000	195	0.559	
60000	100	0.600	Synchrony General Purpose Motor
20000	400	0.400	
22000	640	0.557	AVL Formula 1 Engine Simulator
22500	1700	0.928	Ansaldo Rectified Generator
32000	460	0.686	RMG Expansion Turbines

32000	550	0.750	
45000	160	0.569	

Table 1-1 List of Industrial PM HSHP Machines

Speed (rpm)	**Power (kW)**	**n√P (x10⁶)**	**Manufacturer / Application**
14700	4700	1.008	MAN Induction Compressor Motors
14000	7000	1.171	
3000	45000	0.636	Ansaldo Synchronous Generator
13000	5000	0.919	Ansaldo Induction Motor

Table 1-2 List of Non-PM HSHP Machines

Where it could be determined, the topology of the rotor choice of material for retaining the magnets was noted; the most common topology was a surface or buried magnet assembly with a composite retaining sleeve. Motors by E&A, Ansaldo, RMG and Calnetix were all noted to use this technology combination and as such it is considered the state of the art for commercial HSHP Machines. The rated voltages, phase configuration and accompanying drive information for the surveyed machines was not always readily available, which hindered comparison on electrical grounds. The predominant cooling methods for the machines listed were a combination of water cooling of the stator and forced air cooling of the rotor and end windings; the exception being the spindle motors produced by E&A which were water cooled at the stator outer surface only. This limitation of cooling on the E&A motors – coupled with the sacrifice of torque performance in order to produce a very low torque ripple as required by spindle applications – can be postulated as a reason for their lower $n\sqrt{P}$ values than other machines in the list.

1.2.3 Academic Research

Academic research into HSHP PM Machines is driven by application specific problems which present particular machine specifications that require a bespoke design; the specifications can

range from simply the power and speed set points of the application to geometry, material, environmental and electrical supply constraints. The research into HSHP machines can be split into four broad categories: high absolute speed research, turbomachinery matching, predicting and reducing losses and 'multiphysics' design of machines. The focus of this review is on the particular aspects of permanent magnet machine design contained with these research areas, rather than the particulars of system design and integration with the application. Beyond the four broad areas, the variation in rotor design and materials across the range of HSHP machines will be investigated in detail; this is of particular interest to HSHP design as the mechanical limitations of the rotor design are often the most severe constraints on machine performance. The sintered nature of PM materials causes them to be weak in tension and much rotor design effort is placed into ensuring the mechanical integrity of the magnets; the generally accepted method is to hold them in compression throughout their design speed range, through the use of a tensioned sleeve placed over the magnets that delivers a large compressive force.

The range of machines presented in literature can be divided into distinct groups based on their application and speed range, these groups are shown in Figure 1-3.

The ultra-high speed range, from 100,000 to 1,000,000 rpm coincides with the high absolute speed research grouping, whereas the microturbine and turbomachinery matching groups sit within the turbomachinery matching research group and consists of both PM and IM machines, particularly in the turbo machinery matching grouping. The very high power machines group is limited to very large footprint synchronous machines used to power compressors in LNG refrigeration and gas pumping.

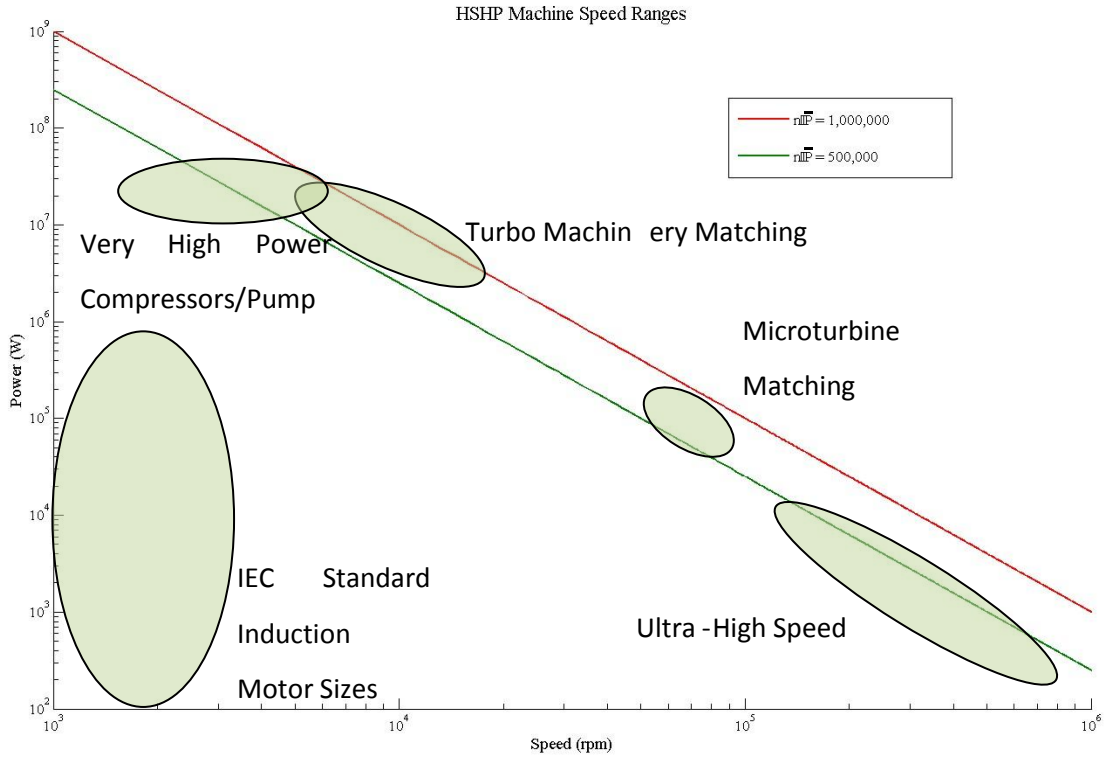

Figure 1-3: HSHP Machine speed ranges

Absolute High Speed Research

There is an academic niche focussed on the production of the highest possible absolute speeds in electrical machines, with applications ranging from motors for machine tool spindles and compressors to generators coupled to microturbines. Research into achieving the highest possible absolute speeds with PM machines is led by academics at ETH University in Zurich, with several 500,000 rpm machines having been developed [6, 7] and a spin out company offering speeds up to 1million rpm [8, 9]. These machines represent the benchmark for the highest speed PM machines built, often referred to as 'ultra-high speed machines', although a high speed SR Machine has also been developed [10] offering 750,000rpm performance. Other researchers have developed PM machines in the ranges of 120,000-150,000rpm, [11-13] for machine tool and compressor/blower applications. All these machines have an $n\sqrt{P}$ value in the range of 300,000-500,000, which indicates they are not pushing the limits of HSHP performance, however other specific aspects may be limiting the extension of their performance, namely application requirements, rotor geometry and power electronic capability. The rotor design of the highest speed machines consists of a solid PM cylinder encased in a sleeve which also acts to connect the magnet to the shaft ends as shown in Figure 1-4. To allow magnetisation of the solid magnet piece and to minimise electrical frequency, the machine is necessarily a two pole design.

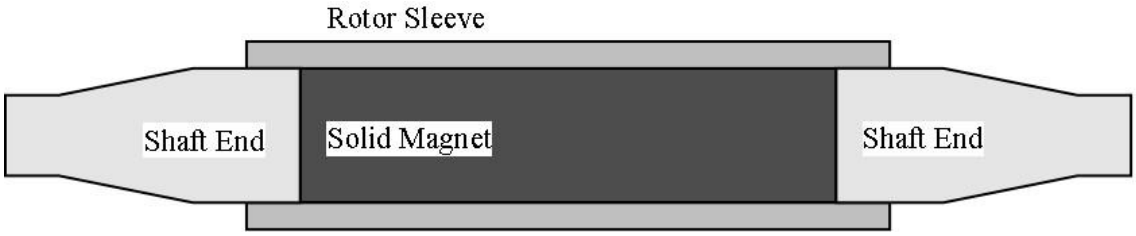

Figure 1-4: Ultra high Speed Rotor Geometry

The torque capability of this design is limited by the sleeve as it must transfer torque from the magnets to the shaft, necessitating a large thickness, however for the magnetic design it must be as thin as possible, limiting the torque transmission possible. This geometry was observed in [6, 7, 11, 14] with metallic sleeves being used, either titanium or Inconel; giving an additional rotor eddy current loss damping effect. The machines in [12, 13] consist of a more conventional surface mounted magnet design seen in lower speed machines, with a sleeve of either glass fibre or stainless steel being used for containment. The solid PM design shown in Figure 1-4 is limited in application to this ultra-high speed niche due in part to the limitation in torque transmission capability but also by pure economics. As described in (1.2), the radius of HSHP machines is inversely proportional to operating speed for constant $n\sqrt{P}$, implying that lower speed machines will need a much larger volume of magnet material to maintain this criterion, while the saturation of electrical steels would limit any benefit in terms of magnetic loading of the machine gained from all the additional magnet material. For this reason this rotor geometry is limited to the ultra-high speed niche and will not be considered further.

Beyond the high speed niche, which defines the upper limit of speed performance, the trend for matching turbomachinery performance, specifically microturbines, continues at speeds less than 100,000rpm, and defines the application and development of machines in that speed range.

Turbomachinery matching

At speeds below the ultra-high speed range, generally below 100,000rpm the trend for matching turbo machinery performance continues. The main application for HSHP machines in this region is the generator in a Combined Heat and Power (CHP) unit, connected to the output of a small gas turbine. Examples of these machines can be seen in [15-18] with speed ranges of 61,000-70,000 rpm, power outputs of 60-120kW and $n\sqrt{P}$ values of 460,000-760,000 indicating an improved performance over the ultra high speed machines. The design of these machines is characterised by surface mounted magnet rotors underneath a composite retaining sleeve, the

exception being [17] which uses a solid two pole PM encased in an 'alloy' sleeve, in a similar topology to the ultrahigh speed machines in the previous section. This inferior design for the speed range leads to the $n\sqrt{P}$ to be 460,000, the low value in the range for this type of machine, the other three examples all being much closer to 700,000 $n\sqrt{P}$.

An interesting additional design in this speed range is presented in [19], which uses a different rotor topology and delivers and $n\sqrt{P}$ of 990,000, close to the state of the art 1,000,000 value. The rotor topology, a composite of a sleeved and a carrier design is shown in Figure 1-5, where the magnets are held in titanium carriers attached to a hollow titanium shaft and over wrapped by an un-tensioned composite sleeve.

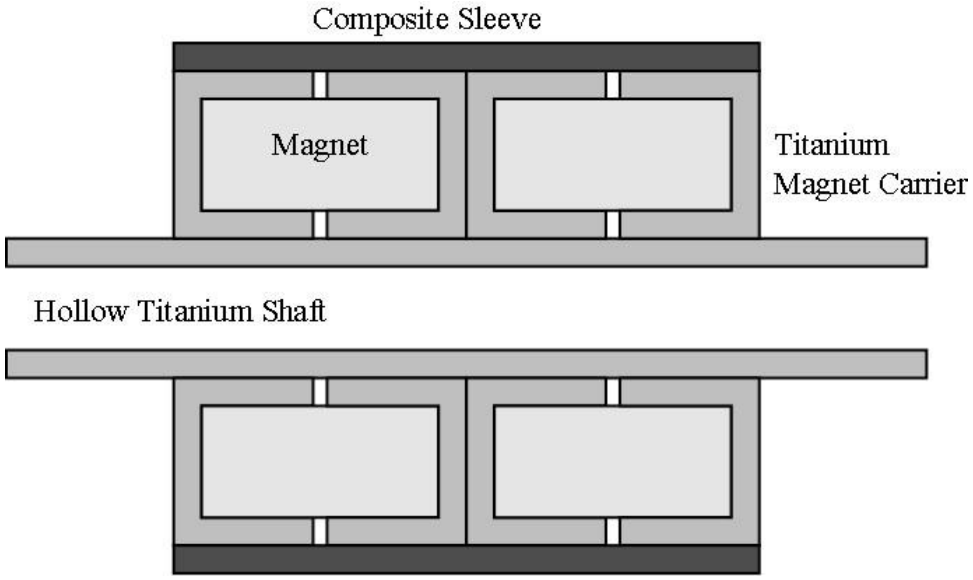

Figure 1-5: Castagnini et al. Hybrid Rotor Design [19]

This design is of particular academic interest as it reverses the convention of using a pre-tensioned sleeve over the magnets to resist their centrifugal body forces during operation, but instead uses those body forces to apply the compression onto the composite sleeve during rotation. The implication being that they are not bonded to the shaft but rest freely inside the carriers, which are used to hold the magnets in a stable position and transmit the torque to the shaft. This is a rather elegant way to remove the need for pre-stressing the retaining sleeve, which, as discussed in later chapters, can present a significant limitation to the mechanical performance of HSHP rotors. The drawback to this design is that the titanium and sleeve components force a large effective air gap upon the design, limiting its magnetic loading; however the machine in which it was used was a slotless design, ensuring that the additional titanium thickness below the sleeve was of little consequence. Unfortunately little information is provided by the authors about the performance of the design, only that it reached speeds of

67,000 rpm [20] under no load conditions and, given that there is no evidence of operation at full power, the $n\sqrt{P}$ of 990,000 cannot be confirmed. The unique design however remains a valid addition to the literature.

The research of machines in this speed and power range begins to highlight some of the major design issues faced by HSHP machine designers. Close attention is paid by all authors to the prediction of all losses and in particular the minimisation of rotor losses, to prevent overheating of the rotors and damage to the magnets or retaining sleeve; a common design method employed is the use of an eddy current shield [15-17]. Thermal design methods are also introduced, using both FEA and lumped parameter models as the impact of the machine losses on steady state temperature is recognised as a factor in limiting the performance and lifetime of the machine, additionally, litz wire is introduced [16] as a method for minimising the AC loss effects in the armature windings of the machine.

A theoretical design study of the peak performances of machines in this range has been undertaken by [21]; using a constant machine topology and investigating the peak power performance of machines in the speed range 20,000-100,000rpm. A specific attempt was made to capture the interaction of mechanical, thermal and electromagnetic design effects using analytical design equations to perform a multi physics design. The results of the design study are given in Table 1-3 and show a consistent $n\sqrt{P}$ range of 740,000-820,000, indicating that the machine performance levels are similarly consistent across the speed range.

The analysis presented by [21] is limited by the consideration of the electrical design, where operation is as a generator only, so the full electromagnetic constraints and loss mechanisms are not fully explored. The proposed limitations in peak powers for a given speed also appear to be rather limited, given that proven designs approaching an $n\sqrt{P}$ of 1,000,000 are available on the market.

Speed (rpm)	**Power (kW)**	**n√P (x10^6)**
20,000	1,500	774597
40,000	425	824621
60,000	181	807217
80,000	93	771492

100,000	55	741620

Table 1-3 Theoretical peak performances, Kolodzovski et al. [21]

As lower machine speeds are considered, below 30,000rpm, the power levels rise significantly, in line with the relationship defined by $n\sqrt{P}$. There is a dearth of literature available about machines at these power levels, possibly because of the commercial interests involved. The size and complexity of HSHP PM machines in this speed range leads to them being expensive to develop and build, both in terms of man-hours and material and processing costs. As such little academic work is funded in this range due to the high costs, and the details of any industrial designs that are successful are closely guarded to maintain a commercial advantage. Three papers exist that reveal some of the established design process for machines in this range.

The first paper, by Bailey et al. [22] is from DDS and details the design of an 8MW, 15,000rpm PM machine of conventional surface mount design. The work by Bailey et al. provides an insight into the industrial design process for a HSHP machine, where the focus is shown to be on rotordynamic and thermal design, using FEA tools for stress, loss and temperature prediction, rather than analytical methods; there is a lack of electrical design consideration presented in the paper, possibly due to the design being medium voltage (6.6kV). Performance up to 3MW load was reported in [23] and if

8MW is reached, at an $n\sqrt{P}$ 1,300,000 this design would be distinguished as the highest performing PM machine surveyed, despite conventional cooling using a water jacket and forced air being used. The implication of [23] was that the measured losses exceeded those predicted during the design stage, so it is not certain that the full performance and hence $n\sqrt{P}$ value was achieved for this machine.

The second paper describes the initial design study of shipboard HSHP generator of rating 2MW at 22,500rpm, ($n\sqrt{P}$ 1,010,000) by Calnetix [24]. Though no information is provided on the actual build and test of a prototype, the authors discuss several relevant issues with regards to HSHP machine design. In particular they highlight the overlapping and interactive nature of the three design domains; additional observations cover the choice of sleeve material, noting that carbon fibre reinforced sleeves offer significant structural advantages and that FEA methods are required for accurate validation of machine parameters. The design presented in this paper is notable for the use of ‘breadloaf’ shaped permanent magnets, rather than the more common surface mounted arc shape used in HSHP machines in this speed range; the merits of this shape will be discussed in more detail in chapter 2.

The third paper, produced by Smith and Watson [25], is unique in terms of topology, using a carrier system for the rotor magnets similar to that in [26]; the rotor was made of axial segments that can be stacked to alter the machine performance across a broad range. One of the axial segments is shown in exploded view in Figure 1-6; note the design is 8-pole given the relatively low rotor speed. The design was successfully tested to 11.1MW output, however even this output only delivers an $n\sqrt{P}$ of 650,000 implying a relatively poor performance relative to the machine designed by Bailey et al.

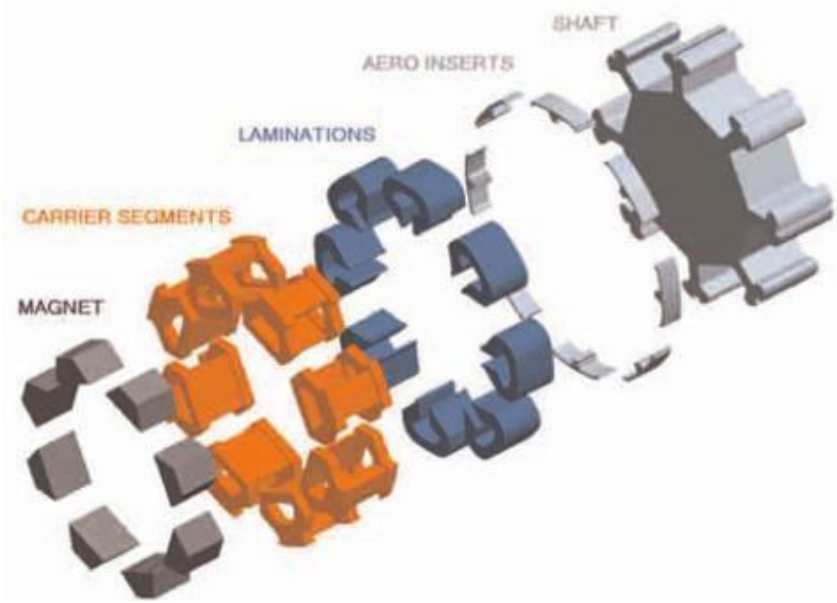

Figure 1-6: Smith and Watson Carrier design, taken from [25]

The focus of the design work presented in [25] was on the mechanical integrity and rotor dynamic performance of the unique design, with little information presented on the electrical or thermal design, making it difficult to just the efficacy of this topology. It can be assumed however that the rotor design is severely limiting in terms of performance compared to a conventional PM machine; the PM area at the periphery is limited by the carrier segments and non-magnetic shaft protrusions, implying a low magnetic loading. The full centrifugal load of the magnets, laminations and carriers must be taken on the shaft protrusions, which will have a lower tensile stress performance than the best composite sleeve materials, implying a more stringent stress limit and hence speed limit, on the rotor for the same magnet volume. One advantage of the design is that it allows a small air gap as no sleeve is required over the rotor surface, and will go some way to improving the magnetic loading achievable. Due to the low $n\sqrt{P}$ value of this design it exists purely for academic interest and will not be considered further.

Beyond the two designs for lower speed range HSHP machines that are presented above, further information about HSHP machines in this range can be gleaned from various survey papers that collate the performance points of multiple machines mentioned in literature but not explored in detail. These surveys are presented in [21, 27-31] and cover both induction and PM machines in the speed range 0-300,000rpm. The surveyed PM machine operating points are collated in Figure 1-7; overlaid on this chart are the $n\sqrt{P}$ boundaries for 500,000 and 1,000,000 as well as the power law trend for the full spectrum of machines.

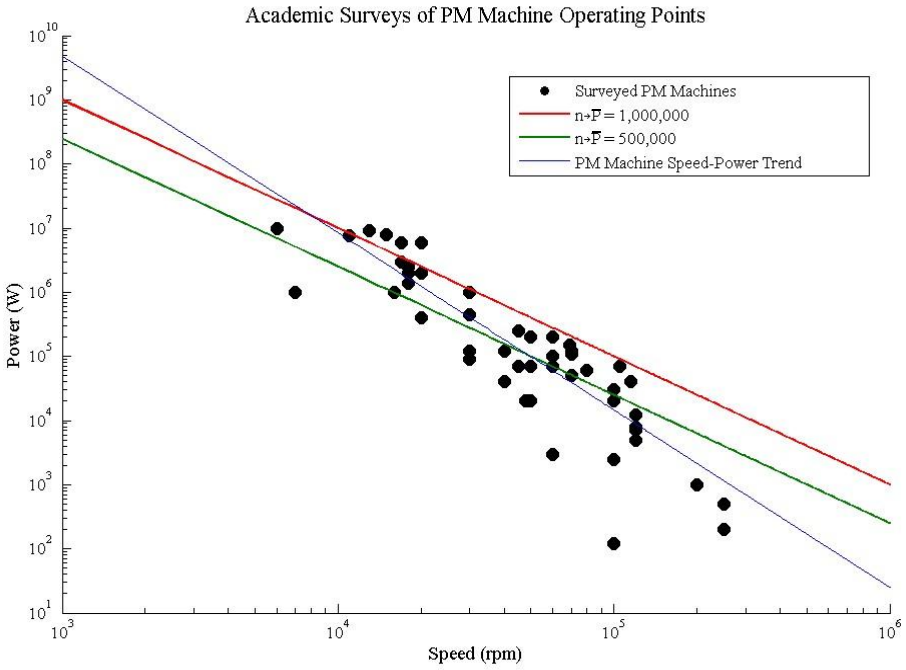

Figure 1-7: Collated PM Machine Operating Points

The trend for the surveyed machines appears to follow the relationship given in (1.10) taken from a log fit curve of the operating points. This gives a steeper curve than that for $n\sqrt{P}$, implying that machines at the higher end of speed range struggle to reach the same level of performance as those at lower speeds.

$$P \propto {}^{1}/_{\omega^{2.76}} \quad (1.10)$$

The authors of [30] have attempted to explore the reason for this trend and have come to two main conclusions; firstly that as ultra-high speeds are approached, the iron losses and AC copper losses in the machine start to dominate, requiring a reduction in the electric and magnetic loading

to compensate; thus leading to a less power dense machine. Their second conclusion is a corollary to the first; due to the low electric loading, the machine p.u. inductance is also low, leading to large current ripples from the supply inverter, which increases machine loss. The effects of the first conclusion are noted in [29] where the surveyed machines in the ultra-high speed range are dominated by air gap winding designs, which have an associated lower loading.

Two additional effects that can be postulated for the perceived lower performance of ultra-high speed machines are the effects of increased inductance and the small feature sizes of these machines. The proportion of leakage inductance in a machine can be expected to increase as speed increases for the same electric loading and current density; as the radius of the rotor is inversely proportional to speed, the slot depth as a proportion of machine diameter increases as the rotor radius reduces, leading to a high proportion of leakage inductance and end winding inductance from the larger end winding bundles. This effect is compounded by the need to reduce the pole number in ultra-high speed machines to 2, leading to a proportionately larger end winding bundle size than in lower speed, higher power machines. In addition to the increase in leakage inductance, the requirement to reduce the pole numbers further increases the p.u. inductance of the machine as the flux per pole increases. The main effect of this proportional increase in inductances is to worsen the power factor of the system, which will lead to a reduction in performance if it is already at the limits of its capability. The second, feature size, limitation arises from the tolerances and capabilities of the manufacturing technologies used to manufacture HSHP machines. As the radii of ultrahigh speed machines reduces, the required component sizes and feature widths (tooth width for example) reduce below what is manufacturable with current technologies, leading to impossible designs. The effect of both increasing inductance and diminishing feature sizes can be evidenced by the shift towards air gap winding designs at ultra-high speeds, due to their lower p.u. armature reaction and simplified stator structure, which is easier to manufacture.

Loss Estimation

Beyond research into pushing the performance capabilities of HSHP machines, much effort is devoted by authors to improving the loss estimation methods for PM machines, particularly using analytical methods. In the era of high performance computing, CAD and FEA these methods remain valid due to their relative speed of computation and ability to allow rapid iteration and comparison between multiples designs.

Of particular relevance to HSHP PM machines is research into predicting rotor losses caused by armature MMF harmonics and into methods for their minimisation. Much of this analytical research centres on the solution of the fundamental equations of the magnetic field in the air gap of the machine as defined by Stoll [32, 33]. The original analysis used a simplified air gap model 'unwrapped' onto a Cartesian plane, however further refinements have used polar co-ordinates and more complete air gap geometry models to refine the predictions [34, 35]. Further research into methods of reducing rotor loss has been carried out, with the most widely accepted methods being the use of eddy current shields [36] and the segmentation of the rotor magnets [37, 38]; the analysis of the effects of these methods is performed using the same tools as outlined by Stoll. Of particular relevance to HSHP machines is the effect of magnet segmentation and it's interaction with time harmonic MMF's; the interaction is described and analysed in [39] and will be discussed in greater detail in chapter 3.

In addition to improving the analytical prediction of electromagnetic rotor losses, the prediction of rotor windage losses in the air gap of the machine are widely accepted to be important, given the high surface speeds encountered in HSHP machines. The commonly accepted method [18, 40] is derived from work by [41] performed at NASA in the 1960's and is an empirically proven method of predicting drag losses across the rotor active length. The rotor active length losses tend to dominate the drag loss due to the lower radii and larger effective air gap encountered in other sections of the rotor. Analysis in [42] has shown that the end region losses constitute only a small percentage of the drag losses of the machine, given the different Reynolds numbers found in the two regions. With the improvement in computer performance seen in the last decade, CFD analysis is now seen as a valid method for evaluation rotor drag losses [22, 23] and is used in conjunction with analytical predictions to improve confidence in the predictions.

Multiphysics design

The fact that the design of HSHP machines is constrained by mechanical, thermal and electromagnetic effects requires designers to consider the interaction between these design domains and the need to balance the effects of each domain on the performance of the machine. This is often performed in a piecemeal way, during the process of solving a specific design problem or meeting a particular application specification. Authors tend to consider each design domain independently and react iteratively to constraints or limitations discovered in one domain, by altering the properties in the other [14, 19, 22, 24, 43].

A few authors have attempted to combine analytical design expressions for the mechanical, electromagnetic and thermal design domains, either partially (e.g. electrical-thermal domains only) or fully [44, 45] in order to allow an optimisation algorithm to be run. This design process has been shown to be successful for the specific applications it was designed for, however the lack of current literature relating to HSHP machines implies multiphysics analysis is difficult to implement. A compelling reason for this lack of application is the wide range of application specific limitations placed on such machines, from environmental effects, to the available drive electronics and material availability. Each application specific design of an HSHP machine requires its own set of design equations, limiting the ability to apply one process across the whole surveyed speed range.

Additional Observations

The largest single $n\sqrt{P}$ value observed for an electrical machine was 2,900,000; for wound field turbogenerators used in power stations [46]. The particular advantages for these generators that allow such an extreme performance rating include pressurised hydrogen cooling, direct water cooling of the stator conductors, allowing an incredibly high electric loading, and the ability for the rotor to run super critical due to the fixed operating speed, removing the critical speed constraint on rotor length, as well as the low current ripple associated with direct grid connection without a drive or rectifier. As such they cannot be classified in the same league as conventional PM HSHP machines, but do provide an interesting performance benchmark for the ultimate performance possible with the best cooling and reduced mechanical constraints. Similar extreme mechanical performances are noted with static gas turbines used for power generation, which achieve $n\sqrt{P}$ values in the 1,000,000 to 2,000,000 range These machines also benefit from the ability to run super critically at a fixed speed, thus removing length constraints from their ability to generate power

The materials used for rotor sleeving or magnet retention have undergone a design evolution over the past three decades [1], from stainless steels [13, 47], to titanium [6, 9, 19], to Inconel [14, 42] and most recently to Carbon Fibre based composites [15, 16, 18, 22]. Each evolution in sleeve materials can be characterised by an improvement in either ultimate tensile strength or in strength-to weight performance of the materials. It can be further seen that initial interior permanent magnet (IPM) rotor designs for sleeved machines [47] have been abandoned in favour of surface mounted magnet designs for HSHP or solid magnet rotor for ultra high speeds, both of which maximise the strength of the sleeving material. The abandonment of IPM designs for

HSHP machines has been explained by [48], where additional torque density can be achieved via the reluctance torque of IPM rotor designs: power density is reduced due to the mechanical weakness of the rotor core, limiting rotor speed and size when compared to a sleeved surface mounted design.

1.3 Objectives

In collaboration with the industrial sponsors of this thesis, the objectives of the research were defined as fourfold:

- Research and define a design process that could be used for the development of HSHP motors across a broad range of speed and power ratings, for use in low voltage (<1kV) industrial applications.
- Research improvements in and optimise the mechanical design of high speed PM rotors.
- Research the improvements in the accuracy and speed of analytical loss estimation in HSHP machines, due to the iterative nature of the design process and critical need to accurately assess losses and heating in such machines.
- Test the design process via the design, manufacture and test of a HSHP demonstrator machine of $n\sqrt{P}$ 1,000,000, the rating of which to be selected based on an observed gap in the existing machine market.

In consultation with customers and via an assessment of the market shown in Figure 1-2, a constant output rating of 1.1MW at 30,000rpm was chosen for the demonstrator machine, giving an $n\sqrt{P}$ of 995,000 which was deemed acceptably close to 1,000,000. The chosen rating is shown relative to industrial and academic surveys in Figure 1-8 and Figure 1-9; highlighting the uniqueness of its location compared to both available industrial machines and prior research in academia. An existing design or design study for a machine of 1MW at 30,000rpm suggested in [28] has not been validated via publication or press despite extensive searching in academic journals and on the internet; as such it is not considered a realistic competitor to the demonstrator.

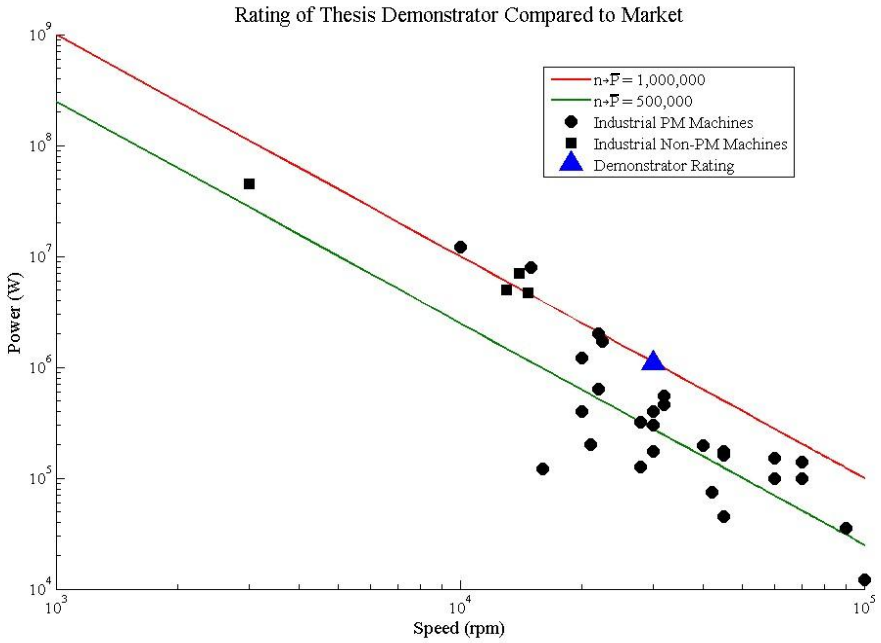

Figure 1-8: Rating of Thesis Demonstrator Compared to Market

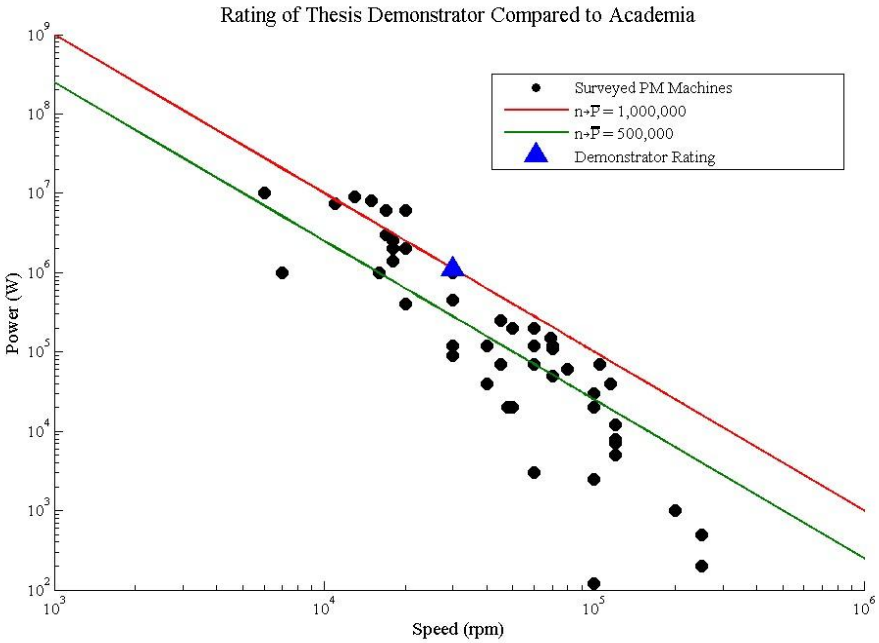

Figure 1-9: Rating of Thesis Demonstrator Compared to Academia

1.4 Contribution to Knowledge

This thesis is designed to contribute to the knowledge base regarding the design of

HSHP machines. Specific improvements in machine loss prediction and mechanical design are delivered, with two publications linked to these issues [1, 39]. Additional contributions are made through the surveying and summarising of the state of the art, and merits of available materials and technologies. Of particular use is the definition of a fast, analytical iterative design process for HSHP machines that allows consideration of the Mechanical, Electrical and Thermal design constraints encountered in machines of this nature. Finally, the thesis will detail the design, manufacture and testing of a uniquely capably machine with a rating deliberately chosen to separate it from existing designs and capabilities.

1.5 Structure of Thesis

The thesis is structured into two sections. The first section, comprising chapters 2, 3 and 4, contains a discussion of the constraints encountered in HSHP machine design. Each chapter covers a particular design domain; it will define the constraints on HSHP machine design found in that domain and then provide tools to analyse them and quantify their effects. The best practice existing techniques will be used and modified to make them relevant to HSHP design.

Chapter 2 focuses on the mechanical design constraints caused by operating at high speeds, namely stress effects and shaft resonances. Improved analytical tools will be presented for evaluating these mechanical constraints and the effects of material, construction and topology choices are explained.

Chapter 3 deals with the electromagnetic constraints cuased largely by high power densities. The effects of low operating voltages on machine design are explored and improved analytical and computationally efficient methods for predicting losses are presented.

Chapter 4 describes the main methods of cooling HSHP machines and explores the implications cooling technology and machine topology on the machine design process. Best practice in thermal design using 3rd party software is described.

The second section comprises a further three chapters covering the design, manufacture and testing of the 1.1MW, 30,0000rpm demonstrator machine, using the tools described in the first section. In these chapters the iterative design tool is developed and then used, the challenge of manufacturing a machine of this rating is explained and finally the successful testing of the demonstrator is detailed, as a validation of the design tool and the processes used.

Chapter 2. Mechanical constraints

The challenges of High Speed, High Power machine design are primarily mechanical, and in particular dominated by the need for a stable, mechanically robust rotor. The combination of high speeds and large rotors lead to significant stresses being developed in rotor components and can cause the natural mechanical resonances (Critical Speeds) of the rotor assembly to be close to the operating speeds. Thus two significant limits are placed on the rotor, a stress limit and a critical speed limit, both of which will be discussed in this chapter. The stress limit for the rotor is driven primarily by material properties; permanent magnet materials, being very weak in tension, need to be held in compression at all operating speeds to ensure their mechanical stability. The critical speed limit is driven by the ratio of the rotor radius to rotor length and the choice of bearing type and spacing which fundamentally define the stiffness of the system; in attempting to maximise the possible torque out of the rotor for a given speed, this ratio is often pushed very close to the limits of what is mechanically stable.

Satisfying the limits posed by these stresses and vibration modes is commonly the first and dominating factor in determining the initial machine topology and size, with electromagnetic and thermal constraints being of secondary concern. Therefore it is vitally important to accurately predict the mechanical behaviour of the rotor in order to deliver a design that utilises the capabilities of the available materials to their maximum.

The issues surrounding mechanical design of high speed rotors have been widely covered in literature, with each author following their own preferred methods. For calculating the expected stresses most authors use simplified analytical calculations for predicting operating stresses in the rotor and then use mechanical FEA methods to validate the predictions for the chosen rotor topology. For calculating the critical speed of the rotor, FEA is the preferred method, though various analytical options also exist. This chapter will explore the origins of these limits as they apply to PM machines and define methods for predicting and hence designing to meet them, additionally the effects of material choices and construction methods and changes in geometry will be quantified. While the stress and critical speed limits apply to all electrical machines, the analysis is limited to the target application PM type electrical machine.

2.1 Stresses

As noted in the review of prior work, Interior permanent magnet motors compare poorly in terms of speed performance to a sleeved, surface mounted motor and will not be analysed further, in particular they cannot deliver the high power densities that a sleeved rotor can.

The generation of stress in the rotor is dominated by the action of body forces acting on the rotor components, caused by their rotation and commonly referred to as centrifugal forces. These forces are generated radially, and can be calculated as the reaction to the centripetal force required to keep the bodies on a circumferential trajectory. The magnitude of this force for a point mass, m, at a given radius, r, at rotational speed, ω, is given in equation (2.1).

$$F = m\omega^2 r \qquad (2.1)$$

For simple unconstrained components, this net force can be approximated as acting radially through the centre of mass of the component. When the components are constrained in an assembly, the forces must be integrated across the cross section of the component. For a magnet attached to a shaft, the integral of the centrifugal force shows there must be a tensile force (the centripetal force) acting toward the rotor axis; increasing from zero at the magnet outer surface to a maximum at the magnet shaft interface; otherwise the magnet would separate from the rotor. The tensile strength of both magnets and glues is relatively low compared to other engineering materials [49, 50] and acts to seriously limit the speed and size of a surface mounted rotor, as the forces and hence stresses induced are proportional to both rotor radius and speed squared for a fixed size piece of magnet. As discussed in Chapter 1, it is now standard practice in high speed and power machine construction to encase the magnet assembly with a pre-stressed sleeve that applies a compressive force to the assembly throughout its operating range. It can be seen from [49, 50] that the compressive strength of magnet materials and glues is much higher than their tensile strength, which allows a significant increase in stress state if they are held in compression. In order to keep the sleeve thin, and hence minimise its effect on the electromagnetic performance of the machine, the stresses in the sleeve must be an order of magnitude greater than those in the magnets. The choice of a suitable engineering material for the sleeve is thus critical to the rotor design, as is a method of accurately predicting the stresses in the constructed rotor and then during operation. In order to analyse the stresses, a model rotor topology and set of axes must be defined as the basis for the analysis, this model is shown in Figure 2-1.

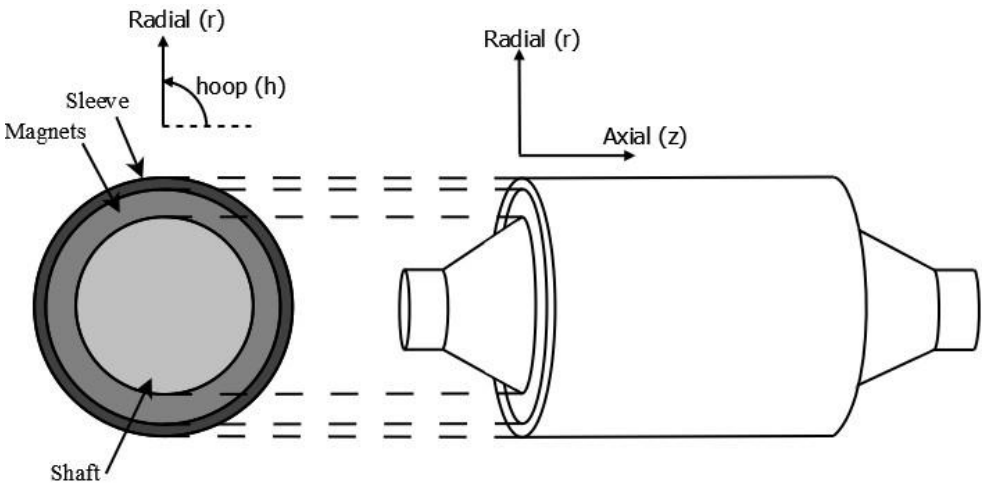

Figure 2-1: Analytical Rotor Model for Mechanical Analysis

As can be seen from Figure 2-1, the rotor components form a series of concentric rings upon the shaft and so lend themselves to be analysed analytically using Lame's equations for rotating disks and the equations for thick walled pressure vessels [3]. Before the analysis can be performed it is important to define the design criteria which must be satisfied by the analysis, there are three which must be met:

1. The magnet material must be held in compression throughout the operating speed range, and that compression must not exceed the magnet material limits.
2. The analysis must predict how much pre-stress is required in the sleeve to hold the magnets in compression at the design speed and predicted operating temperature.
3. The analysis must predict the stress level in the sleeve at the design speed, ω_d, and predicted operating temperature rise, ΔT; which must be less than the material failure stress.

A particular differentiation between the design speed, ω_d, and the operating speed, ω_o, must be made; the mechanical design of the motor must ensure that overspeed conditions can safely be met to avoid mechanical damage to the rotor. Therefore the design speed for stress prediction must be higher than the operating speed by a certain factor, typically 1.2x, as for example in the IEC traction motor standards, [51].

Therefore the mechanical design of the rotor must be performed usingω_d, while ω_o is reserved for predicting the stress variation due to operation.

To meet the three criteria the designer must first calculate the pre-stress required to contain the rotor assembly at the design speed and temperature, and then predict the stresses on the assembly during operation, which will be shown to change due to the effects of the rotating body forces.

All the analysis can be performed by considering the stress state in the sleeve alone, which can be calculated as the superposition of the stress in a rotating disc – due to the rotating body forces induced in the sleeve – and the stresses in a pressurised cylinder – due to the pressure of the magnet body forces acting radially outward – and finally the thermal stresses caused by an increased operating temperature above ambient. Each source of stress will be analysed independently and combined at the end of this section. To simplify the analysis, some assumptions can be made about the rotor sleeve. Noting that the sleeve is generally much longer than it is thick, a state of 2D plane strain can be assumed and so the axial stress is independent of stresses and strains in the hoop and radial directions. When developing the model it is helpful to assume that there is no friction present between the magnets and sleeve, thus shear stresses between the components can be ignored. The lack of friction initially allows the axial stresses to be treated as zero by recognising that the magnets and sleeve are unbounded axially and so cannot support any stress in that direction.

2.1.1 Required sleeve pre-stress

The first step in the analysis is to predict the stress induced in the sleeve due to its own rotation,

The radial and hoop stresses at a given radius, r, in the sleeve caused by rotation are given in equations (2.2) and (2.3), as adapted from [3],

$$\sigma_r(r) = \frac{3+\nu}{8}\rho_{m(sleeve)}\omega_d^2\left(r_o^2 + r_i^2 - \frac{r_o^2 r_i^2}{r^2} - r^2\right) \quad (2.2)$$

$$\sigma_h(r) = \frac{3+\nu}{8}\rho_{m(sleeve)}\omega_d^2\left(r_o^2 + r_i^2 + \frac{r_o^2 r_i^2}{r^2} - \frac{1+3\nu}{3+\nu}r^2\right) \quad (2.3)$$

Where ν is the poissons ratio of the material and ρ_m is the material mass density. The values of r_m, r_i and r_o are defined in Figure 2-2.

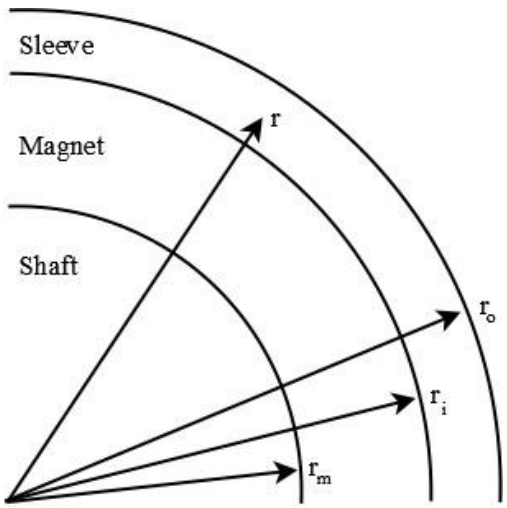

Figure 2-2: Analytical Rotor Model Variables

This stress state can then be superimposed onto the stress state caused by the equivalent pressure of the magnet body forces acting radially outward on the inner surface of the sleeve. The stress state in the sleeve can be predicted using the equivalent equations for a pressurised cylinder, and is given in (2.4) and (2.5) for an internal pressure of q MPa above the external pressure, as adapted from [3].

$$\sigma_r(r) = \frac{-qr_i^2(r_o^2 - r^2)}{r^2(r_o^2 - r_i^2)} \qquad (2.4)$$

$$\sigma_h(r) = \frac{qr_i^2(r_o^2 + r^2)}{r^2(r_o^2 - r_i^2)} \qquad (2.5)$$

The magnet pressure itself can be calculated by integrating the body forces for an incremental magnet area and then dividing those forces by the circumference of the sleeve that they are acting on. The integral is defined in (2.6) and the bounds for a surface mounted arc magnet are described in Figure 2-3; the resultant average pressure across the arc sleeve circumference encompassing the magnet is given in (2.7). The integral can be used to calculate the total radial force for any magnet shape, given the appropriate bounds.

$$F_{Total} = \iint_{Magnet\ Area} \left(\rho_{m(magnets)}\omega_d^2 r\right) r dr d\theta \qquad (2.6)$$

$$P_{Average} = {F_{total}}\Big/{\int_{Arc} r_i d\theta} \qquad (2.7)$$

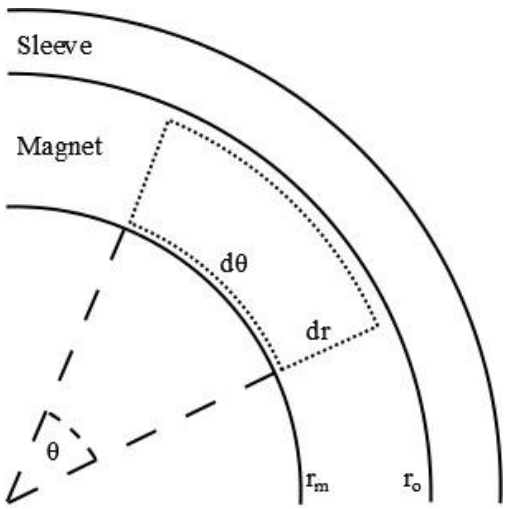

Figure 2-3: Magnet force and pressure integral bounds for surface mount arc magnets

For the generalised rotor design and bounds shown in Figure 2-3 equations (2.6) and (2.7) can be solved to give the result in (2.8), for the average pressure exerted by the magnet material at the design speed.

$$P_{Average} = \frac{\rho_{m(magnets)}\omega_d^2}{3r_i}(r_i^3 - r_m^3) = q \quad (2.8)$$

In the case analysed here the stress distribution is uniform around the circumference of the rotor and equal to $P_{Average}$. When designing rotors for other magnet shapes using $P_{Average}$ is sufficient to ensure contact does remain between the shaft and magnets.

However portions of the magnet bottom surface may lift off from the shaft as the pressure exerted at the top edge radially above this point is greater than $P_{Average}$. This situation is undesirable, as torque transmission between the shaft and magnets will occur between a smaller area, creating stress concentrations; additionally, bending stresses will be developed in the magnet material and sleeve. It is more prudent to use P_{Max} to ensure that no part of the magnet lifts off from the shaft, which can be found by evaluating (2.6) and (2.7) across an infinitesimal arc at the thickest point of the magnet circumferential profile.

The final component of stress to be designed for, thermal, is relatively simple to calculate, by considering the strain caused in the sleeve due to the relative thermal expansions of the magnets and shaft compared to the sleeve material. The equation for predicting the hoop stress at the

inner surface of the sleeve caused in the sleeve by the relative thermal expansions is given in (2.9) [3].

$$\sigma_{h(pre-stress)}(r) = \frac{E_{sleeve}\delta_T r_i(r_o^2 + r^2)}{r\left(r_o^2 + r_i^2 + \upsilon(r_o^2 - r_i^2)\right)} \qquad (2.9)$$

Where E_{sleeve} is the Young's modulus of the sleeve and δ_T is the interference between sleeve and magnets created by the thermal expansion of the rotor assembly calculated in (2.10). The change in temperature between ambient and the design temperature is given by ΔT and α_l is the linear coefficient of thermal expansion of the corresponding material.

$$\delta_T = \left(\alpha_{l(shaft)} r_m + \alpha_{l(magnets)}(r_i - r_m) - \alpha_{l(sleeve)} r_i\right)\Delta T \qquad (2.10)$$

The corresponding radial stress variation, σ_r, in the sleeve can be back calculated from using (2.5) to calculate the pressure generated by the thermal strain with r_i as the radius, then using the resulting pressure in (2.4).

From (2.9) it can be seen that if the thermal expansion of the shaft assembly is greater than that of the sleeve, a negative stress is developed (in terms of required pre-stress), so that at the operating temperature this expansion would act to reduce the required prestress. If this is the case then the thermal expansion stress prediction can be ignored when predicting the required pre-stress, and its effects need only be considered when predicting the operating condition stresses. (The designer cannot utilise the effect to reduce the desired pre-stress, as the machine cannot be guaranteed to be at the operating temperature at all times, for example during cold starts).

Thus equations (2.3), (2.5), (2.8) and (2.9) can be combined to give a prediction of the hoop-pre-stress required in the sleeve of the rotor assembly described in Figure 2-1.
Equation (2.11) describes the case when δ_T is positive and (2.12) describes the prestress when δ_T is negative.

$$\sigma_{h(pre-stress)}(r) = \frac{3+\nu}{8}\rho_{m(sleeve)}\omega_d^2\left(r_o^2 + r_i^2 + \frac{r_o^2 r_i^2}{r^2} - \frac{1+3\nu}{3+\nu}r^2\right) + \frac{\rho_{m(magnets)}\omega_d^2}{3r_i}(r_i^3 - r_m^3)\frac{r_i^2(r_o^2 + r^2)}{r^2(r_o^2 - r_i^2)} \qquad (2.11)$$

$$\sigma_{h(pre-stress)}(r) = \frac{3+\nu}{8}\rho_{m(sleeve)}\omega_d^2\left(r_o^2 + r_i^2 + \frac{r_o^2 r_i^2}{r^2} - \frac{1+3\nu}{3+\nu}r^2\right) + \frac{\rho_{m(magnets)}\omega_d^2}{3r_i}(r_i^3 - r_m^3)\frac{r_i^2(r_o^2+r^2)}{r^2(r_o^2-r_i^2)} + \frac{E_{sleeve}\delta_T r_i(r_o^2+r^2)}{r\left(r_o^2 + r_i^2 + \upsilon(r_o^2 - r_i^2)\right)} \quad (2.12)$$

The radial pre-stress cannot be predicted in the same manner as the hoop pre-stress, as the method of creating the pre-stress produces a different stress state in the sleeve than that created by the combination of magnet pressure, thermal expansion and sleeve self stress under rotation.

The hoop pre-stress of the retaining sleeve is achieved by introducing an interference fit between the sleeve and the underlying rotor structure, which creates a radial stress state, governed by the pressurised cylinder equations (2.4) and (2.5); this will be different to the stress predicted by the combination of equations (2.2), (2.4) (2.8) , and (2.9), due in particular to the stress state caused by rotation of the sleeve not being equivalent to the stress state created by the pressurised cylinder equations.

Therefore the designer must design the sleeve hoop pre-stress to meet the predicted hoop stress levels at the design speed, the radial pre-stress at the sleeve magnet interface $\sigma_{r(pre-stress)}$ can then be calculated using (2.5) with $\sigma_h(r)$ equal $\sigma_{h(pre-stress)}(r)$ and

r equal to r_0. The amount of interference fit required can be calculated simply using (2.13) which is adapted from [3].

$$\delta_{Interference} = \frac{\sigma_{r(pre-stress)} r_i}{E_{sleeve}}\left(\frac{(r_o^2 + r_i^2)}{(r_o^2 - r_i^2)} + \nu\right) \quad (2.13)$$

The implications of material choice, manufacturing methods and stress levels will be discussed in section 2.4. Once the pre-stress requirements and interference fits are predicted, it is then possible to analyse how the stresses change during operation.

2.1.2 Operating stress levels

With the pre-stress levels now fixed by the interference fit the analysis must now consider the effects of rotation and elevated temperature on the stress state, to ensure that at no point of operation the three design rules are broken. Focussing on the effects of rotation to begin with, it can be seen to have a particularly interesting effect; relieving and then replacing the interference stresses in the sleeve while altering the level of compression in the magnets. The effect is best broken down to consider the components of stress caused by the sleeve self stressing and the magnet pressure separately.

For the hoop stresses in the sleeve, as ω increases, a self hoop stress is induced in the sleeve as per (2.3) (with$\omega_d = \omega$). This causes the sleeve to expand radially, relieving the proportion of the interference fit that corresponded to the sleeve self stress calculated using (2.13). The relief of this portion of interference fit causes a reduction in the interference hoop stress as ω increases, at the same rate that the hoop stress due to rotation rises, causing zero net change in the hoop stress though the operating speed range.

The same effect occurs in relation to the magnet pressure which increases and causes the sleeve to want to expand, as per (2.13). This in turn relieves the equivalent proportion of interference fit associated with the magnet pressure and replaces it with actual magnet centrifugal pressure, so that the net amount of hoop stress does not change. It is important to note that although the stress level has not changed with the increase in speed, the cause of the stresses has changed from being the interference fit to being expansion due to the magnet pressure and sleeve self stress.

The radial stresses behave differently as ω increases. In the case of the magnet pressure increasing with ω, the same mechanism occurs: the magnet radial pressure relieves the interference fit radial stress and replaces it with a reaction stress of equal magnitude. However, the radial stresses linked to the sleeve self stress under rotation do not behave as the other stresses do; (2.2) can be solved to show that the radial self stresses caused by sleeve rotation are so small in comparison to the hoop stresses as to be negligible, which conflicts with the fact that the interference generated pre-stress created in the sleeve to counteract the effects of rotation does create a significant radial stress. Thus as ω increases and the sleeve tends to expand under the effects of rotation and magnet pressure, the net radial pressure drops from $\sigma_{r(pre-stress)}$ to be just equal to the magnet pressure at ω_d.

Both the above observations on sleeve stresses run contrary to theories about the sleeve stress state proposed in [48] which assume that the radial pre-stress is a constant during operation, and not relieved by the expansion of the sleeve under stress. The above analysis provides a more

accurate analytical prediction of stress during operation, by avoiding the simplification made by previous authors.

The effects of elevated operating temperatures can be treated more simply by superposition of the stresses caused. If δ_T is positive then the thermal stresses will add to the sleeve stress and hoop stresses as the magnets and shaft expand against the sleeve. If instead, δ_T is negative, the stresses at the operating temperature reduce the sleeve pre-stress and hence the total stress as the sleeve expands away from the magnet surface, relieving some of the pre-stress interference fit.

The effects of rotation and elevated temperature can then be added to the pre-stresses to give (2.14) and (2.15).

$$\sigma_{r(operating\ stress)}(r, \omega_o, \delta_T) = \sigma_{r(pre-stress)}(r) - \left[\frac{3+\nu}{8}\rho_{m(sleeve)}\omega_o^2\left(r_o^2 + r_i^2 + \frac{r_o^2 r_i^2}{r^2} - \frac{1+3\nu}{3+\nu}r^2\right)\right]\frac{r^2(r_o^2 - r_i^2)}{r_i^2(r_o^2 + r^2)} + \frac{\delta_T E_{sleeve}}{r_i\left(\frac{(r_o^2 + r_i^2)}{(r_o^2 - r_i^2)} + \nu\right)} \quad (2.14)$$

$$\sigma_{h(operating\ stress)}(r, \omega_o, \delta_T) = \sigma_{h(pre-stress)}(r) + \frac{E_{sleeve}\delta_T r_i(r_o^2 + r^2)}{r\left(r_o^2 + r_i^2 + \upsilon(r_o^2 - r_i^2)\right)} \quad (2.15)$$

2.2 Resonances

All rotating systems experience vibrating forces during operation, stemming from the fact that the centre of mass of the system does not lie on the axis of rotation, i.e. it is not perfectly balanced. As the system rotates the centripetal forces acting on the unbalanced mass create an oscillating transverse load and vibration on the system, known as whirling. As the rotation speed approaches a resonant frequency of the system it can cause catastrophic levels of deflection that

are likely to destroy or damage the rotor and stator, if sustained for a long period of time. In the case of a rotating shaft mounted on bearings there are several resonant modes to consider: firstly the bearings act as springs and the rotor assembly either bounces, parallel to its axis of rotation, or rocks alternately upon them. Secondly there is a resonance associated with deformation of the rotor assembly, which bends under transverse loads. The deflection increases dramatically when the oscillation of the transverse loading approaches a certain frequency inherent to the shaft shape and stiffness, known as its bending mode. The frequency of the first bending mode of a rotating system, where deformation in a simple linear beam takes the shape of a half sine wave, is often called the critical speed for this reason. The bounce, rock, first and second modes of a simple shaft on bearings is shown in Figure 2-4. The rotors of high performance machines are no exception to this and thus the designer must ensure that any unbalance is minimised and that the resonant frequency of the rotor system is far from any of the expected operating speeds. For most electrical machines the critical speed is chosen to be in excess of the maximum operating frequency and the rotor is said to be operated sub critically. It is possible to run super critically, if the time spent at resonant speeds is minimised to prevent the associated shaft deflection from building up to damaging levels. This can be taken advantage of in continuous duty systems with a fixed operating speed. The effects of the bounce and rock modes can be minimised by reducing the effective bearing stiffness so that they occur at very low frequencies and provide a minimum operating speed for the machine. There are multiple analytical, numerical and Finite Element methods for predicting the various critical speeds of a shaft and bearing system. Analytical solutions can give a reasonable first approximation for a simplified model of the system, but numerical and, in particular, Finite Element solutions give much more accurate results for complex shaft assemblies.

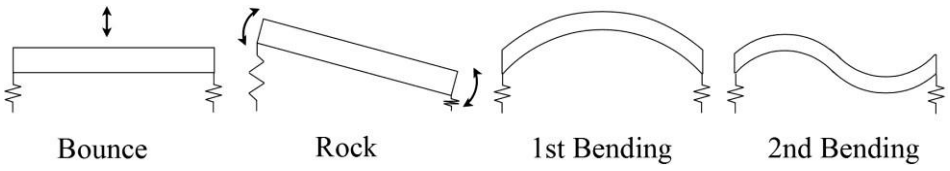

Figure 2-4: Bounce, Rock and Bending modes of shaft on bearings

While the analytical methods are less accurate they allow a rapid, low computational cost, first look at the expected resonances of a shaft assembly which is useful for placing a limit on the initial sizing of the rotor and allowing rapid iteration between the mechanical and the electrical or thermal aspects of design. Therefore they are still of importance to the machine designer, with Finite Element Analysis being kept for later stage prediction of the critical speeds, once the

initial machine size and profile have been chosen. The rotor assembly of a High Speed High Power machine often includes variations in both the shaft mass and stiffness along its length, which lends itself best to analysis using Rayleigh's method. Variation in shaft diameter along the rotor length will cause variation in stiffness and mass while the magnetic components and retaining sleeve add additional mass along the active length.

2.2.1: Rayleigh's Method for Critical Speeds

Rayleigh's method determines the critical speed of the rotating assembly by comparing the potential (strain) energy when it is deformed to the kinetic energy gained by that deformation from the axis of rotation. When the two are equal a resonance occurs and the corresponding frequency can be determined by equating the two. The energies are found by integration along the shaft length using the variation in shaft deflection from the shaft axis based upon the mode shape of interest, usually the first. The degree of accuracy in the shape function that describes the deflection, y, of the shaft at an axial distance z, has a direct effect on the accuracy of the analysis method; inaccuracies will cause an over prediction of the critical speed. The equation for the prediction of critical speed, ω_c, for a shaft of length L is given in (2.16), adapted from [52].

$$\omega_c^2 = \frac{\int_0^L E(z)I(z)\left(\frac{d^2y(z)}{dz^2}\right)^2 dz}{\int_0^L y^2(z)m(z)dz} \qquad (2.16)$$

Where E is the Young's Modulus, I the second moment of area, y the deflection, m the mass per length and z the axial distance along the rotor. All the functions can be easily described along the length of the rotor assembly, based on material properties and dimensions; it is often helpful to break the integrals at discontinuities in the shaft section, allowing each function of z to be described in simple terms.

In order to provide a worst case estimate for the critical speed it is most useful to consider the rotor and sleeve assembly as a parasitic mass that adds nothing to the rotor stiffness, but increases the motor mass per length along the active area, as noted in [53]. In keeping with the analysis of the stresses the shaft is considered to be made from a single piece of material upon which the magnets and sleeve sit.

A typical shape function, for the nth mode of a uniform beam with pinned ends [52], is given in (2.17), where y_o is the maximum deflection.

$$y(z) = y_o sin\left(\frac{n\pi z}{L}\right) \quad (2.17)$$

In the shaft of a HSHP machine, this mode shape can be expected to be modified due to variations in the second moment of area along the shaft length, with the large radius area under the magnetic assembly being much stiffer than the ends that taper to the bearing mounts, causing a flattening of the shape function along the active region of the shaft.

One significant feature of Rayleigh's method enables its use for fast, first pass, estimation of critical speed across a wide range of rotor sizes. By considering the form of the shape function one can see that the magnitude of the deflection is irrelevant when computed, and that only the shape information contained in the function is relevant to the analysis. This feature allows rapid comparison between a wide range of rotor active geometries, requiring only that the shape of the rotor deformation is similar, without any a priori estimation of the magnitude of the rotor deformation. To enable this estimation the ratios of the rotor geometry must be kept the same, with the length of the shaft transition from active region to the bearing mounts being held as a fixed ratio of the active length of the rotor, as shown in Figure 2-5.

A typical shaft geometry is shown in Figure 2-5, with example ratios between shaft lengths shown, the variations in the second moment of area, I, and mass, m, with length are shown, with the added effect of parasitic mass shown. The shaft thickness tapers from a maximum under the magnetic assembly to a minimum where it meets the bearings; this general shape is driven by the inner diameters for high speed bearings being much thinner than the diameter achievable at the magnetic assembly. The axial distance along which the shaft taper occurs is driven by the bearing spacing, which in turn is defined by the size of the end winding overhang on the stator. At the initial stages of the design it is best to assume worst case distance, which can be refined at a later stage.

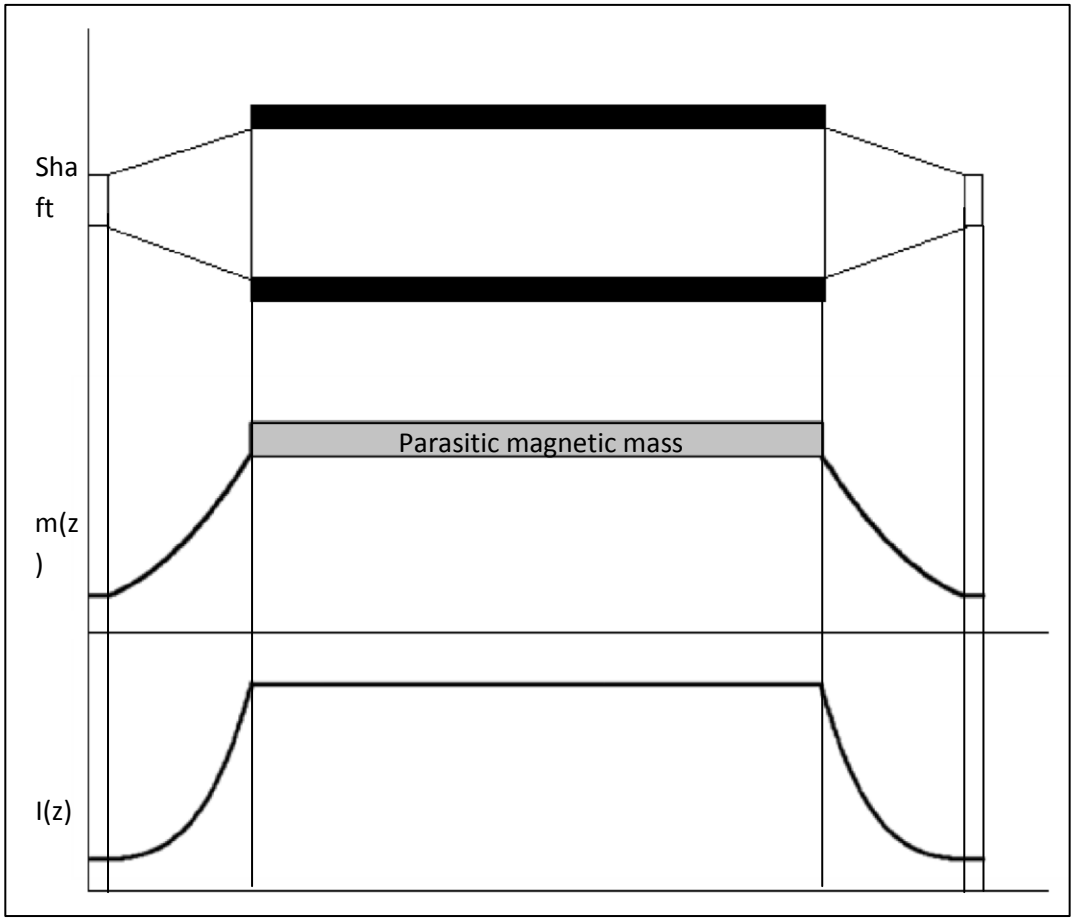

Figure 2-5: Typical Shaft Geometry and property variation

In Figure 2-6 the shape functions for various shaft geometries are shown, it can be seen that there is little variation in the shape function over a reasonable range of different shaft geometries, only when the shaft aspect ratio tends to extremes does the shape function vary greatly, moving to the limits shown.

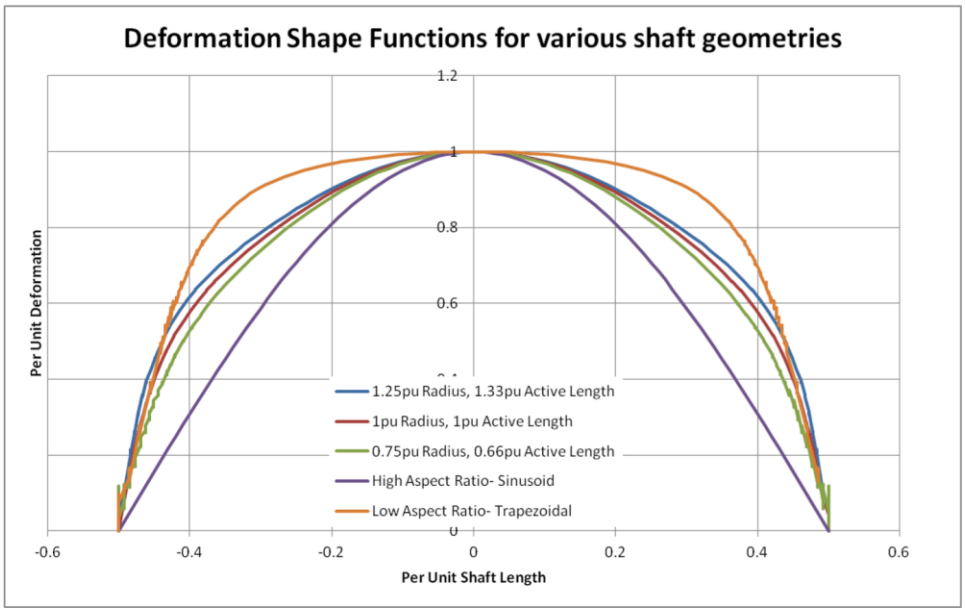

Figure 2-6: Deformation Shape Functions for Various Shaft Geometries

The Aspect Ratio of a shaft can be defined as the ratio of the active length over the radius of the active part of the shaft, thus a high aspect ratio shaft resembles a simple beam of uniform radius, with the aforementioned sine wave shape function, while a low aspect ratio shaft resembles a disc, with a trapezoidal shape function.

Using these properties of the shape function, the designer can quickly compare many shafts of similar aspect ratio using only one shape function, all that is required is that the function is scaled to the length of each shaft when the computation is undertaken. As noted in [52], even approximate shape functions can still give a good estimate of the critical speed, allowing the designer to quickly iterate through many shaft geometries when performing the initial mechanical sizing of the rotor. What is left to the designer is to define an appropriate shape function, which can be extracted from an FEA analysis of a representative shaft, for example.

2.2.2: FEA method for Critical Speeds

FEA analysis offers the most accurate predictions of critical speeds, particularly of shafts with complex shapes and additional features, but at an increased computational cost that can slow down the initial mechanical sizing process. For this reason it is most useful for the designer to avoid using this method until a final shaft geometry is chosen, after electromagnetic and thermal sizing, to act as a final check that the shaft will meet the requirements. It is at this stage that other factors such as the bearings' stiffness and the weight of couplings on the shaft ends can be

included to get the most accurate estimate of the system modes and critical speeds. The stiffness of the magnetic assembly can also be included, although it is useful to include an analysis where the stiffness is discounted as a worst case estimate.

2.3 Bearings

There are many bearing types and configurations for rotating machinery; however the operating demands of high speed machines quickly act to limit the selection. The most common type of bearings are rolling element bearings, relying on balls or cylinders moving in a lubricated raceway to allow low friction rotation of the shaft, while supporting and normal loads to the shaft axis. As the operating speed of these bearings increases the diameter decreases; this is due predominantly due to frictional heat generation and wear which are linked to the tip speed of the rolling elements in the raceway. As a result, the appropriate bearings for a high speed machine can have a much smaller diameter than the active magnetic portion of the shaft, leading to the geometries seen in the previous section. This can adversely affect the shaft stiffness, as it constrains the shaft to be very narrow at certain sections, thus any improvement in bearing diameter would make the shaft stiffer, enable a longer spacing between the bearings and allow more active magnetic length in the machine. The easiest way to improve the service speed and life of rolling element bearings is to apply a continuous lubrication stream that acts as a heat exchanger for the bearing losses and ensures that wear is limited by minimising contact between bearings and raceways.

An alternative method is to use active magnetic bearings, which can allow much larger shaft diameters at the same speeds as rolling element bearings as they have no contact surfaces, leading to little wear and heating, and have the added advantage of being able to operate in a vacuum as no lubrication is needed. Magnetic bearings are an attractive choice for High Speed High Power machines and can enable large shaft lengths (due to the larger possible shaft radii) and hence output torques; however they come with a significant engineering cost to design that can limit their application to machines with a large production volume, or where cost is not a constraint.

In general, mechanical bearings remain the most common choice for High Speed High

Power machines due to their lower costs and engineering complexity. The designer must assess the available bearing types against lifetimes and lubrication methods for the chosen design speed, from which a choice of bearing diameter can be made, which will define the minimum shaft thickness.

2.4 Materials

2.4.1 Magnet materials

The choice between magnet materials for High Speed High Power machines focuses on the desire to maximise the magnetic loading of the machine; given the highly stressed nature of the machine this can be evaluated by considering the residual flux density per unit mass of the magnet material. As discussed in Section 2.1, the stressing of the sleeve is directly related to the magnet density, thus for a given stress limit in a sleeve it is possible to have a larger volume of a lower density magnet. The residual flux density in the magnet material will determine the magnetic loading of the machine, along with the depth of magnet material that can be achieved, so it is of little use if the lower density magnet has a corresponding lower residual flux density. Therefore the designer should choose the material with the maximum residual flux density per unit mass to maximise the potential magnetic loading of the machine; this parameter is summarised in Table 24 for the four most common commercially available magnet types.

	NdFeB	SmCo	Alnico	Ferrite
Residual Flux Density, Br (T)	1.35	1.12	1.08	0.385
Density (kg/m^3)	7500	8300	7000	4900
Residual Flux Density per unit Mass (mTm^3/kg)	0.18	0.13	0.15	0.08

Table 2-4: Magnet Residual Flux Density per unit mass

From this table it can be seen that Neodymium Iron Boron, NdFeB, is clearly the most flux dense, both in absolute terms and per unit mass and thus can deliver the highest possible magnetic loading for a given stress limit. It can be seen that Alnico is the second best performing material, however given its low coercivity it is not likely to perform well in a High Speed High Power machine. It cannot sustain large armature fields without the risk of demagnetising, which would limit the potential electric loading, and it should therefore be discounted from use. Ferrite performs poorly both in terms of flux density and in flux density per unit mass, thus it is not a realistic choice for High Speed High Power design.

The designer is then faced with a choice between NdFeB and SmCo, and while NdFeB can clearly allow a higher performance machine, the choice can still be affected by secondary factors of cost and temperature performance. The mechanical performance of both sintered magnets is

broadly similar; each material has a similar Flexural Strength [49, 50], which in general is higher than the tensile strength of the material. Given the design criteria of keeping the magnets in compression throughout all operating conditions, the difference in mechanical performance of each is irrelevant for comparison, as both have high compressive strengths of approximately 1GPa, [49, 50, 54] which are far in excess of the compressive stresses that will be required in any design.

Due to the scarcity of rare earth materials and the cost of their extraction, the prices of both magnets have varied dramatically in the early 2010's [55] and while historically NdFeB has been cheaper than SmCo, this has not been the case in recent years. Material cost can often be a compelling factor in magnet choice for High Speed High Power machines due to the large amounts of magnet material required.

The temperature performance of the magnetic materials is also a significant factor in their selection; the rotors of HSHP machines often operate at high temperatures, well over 100^{o}C, where the high temperature stability of SmCo can make it a more attractive choice. The selection choice is often interlinked with the choice of sleeve materials, composite sleeves have a reduced operating temperature due to the glass temperature of the resin used which can limit shaft operating temperatures to 150^{o}C or below, where NdFeB is clearly the best material. However, metallic sleeves and some exotic (and expensive) resins can allow operating temperatures in the 150-200^{o}C range, where SmCo is a better performing material.

2.4.2 Sleeve materials

As described in the review of prior work, the material selection for the rotor sleeves has evolved in search of ever higher operating stresses. Stainless steel and Inconel have been used in the past as they are simple to machine and assemble onto the rotor, however they are limited in both stress limits and self stressing when compared to modern composite materials that are both lighter and stronger. Modern HSHP rotors are commonly encased in Carbon Fibre Reinforced Polymer (CFRP) composites as they offer better strength to weight ratios, better electromagnetic performance and, as noted in [1], offers improved resistance to stress concentrations caused by axial stress effects. The choice of sleeve materials has significant secondary effects upon the thermal and electromagnetic design of the machine, beyond simply the mechanical. In particular, the material electric and thermal conductivities affect the machine equivalent circuit, the amount of rotor losses expected and the ability to remove those losses from the rotor. The metallic sleeve materials generally have a high electrical conductivity and can expect to have significant eddy

currents generated in them, which have significant effects on the electrical and thermal design of the machine, as discussed in the later chapters. The metallic materials also have good thermal conductivities, which aid in the thermal design, aiding heat extraction from the rotor via the air gap of the machine. In contrast, though CFRP has the best strength and weight performance, its low bulk conductivity and thermal conductivities add challenges to the designer by potentially increasing eddy current losses in the magnets, thus shifting them deeper into the rotor structure which reduces the ability to extract the heat loss from the rotor.

Table 2-5 summarises the most pertinent material properties of several common rotor sleeve materials.

	Stainless Steel (304)	Inconel (718)	Titanium (6AL-4V)	CFRP (typical 0.6 vf)
Ultimate Tensile Strength (MPa)	505	1375	895	3000
Density (kg/m^3)	8000	8190	4430	1200
Strength to weight ratio (kNm/kg)	63	168	202	2500
Electrical Conductivity (S/m)	1.38E6	0.800E6	0.562E6	0.05E6 (parallel) 1E3 (perpendicular)
Thermal Conductivity (W/mK)	16.2	11.4	6.7	0.5-1 (perpendicular)

Table 2-5: Properties of common sleeve materials

From this table it can be seen that CFRP offers the best strength and self-stressing performance, allowing larger rotor volumes to be attained compared to using metallic sleeves, however the designer must balance this gain against its poor thermal conductivity and operating temperature and the effect of its low electrical conductivity on the electromagnetic design of the machine.

2.4.3 Shaft and Coreback materials

The general choice for high speed machines is for the shaft to provide the rotor coreback by being made of high strength magnetic steel. This option provides the stiffest, strongest rotor combination that allows for a longer bearing spacing and active length compared to the use of laminations for the coreback which add mass, rather than stiffness.

2.5 Construction Techniques

2.5.1 Magnetic Assembly

The assembly of large magnet pieces is a delicate process, as strong attractive and repulsive forces exist between the magnets in the assembly and there is a significant attractive force between all magnets and the rotor coreback. As a result, care is required to move the magnets in a controlled manner to their final position on the rotor and secure them there. The strength of the forces involved often limits the size of single magnet piece that can safely be handled, for both operator safety and potential for material damage. There also exists a minimum size of magnet piece that can be accurately and reliably machined, due to the brittle nature of the material. These limits on the maximum size of magnet piece can have significant effects on the electromagnetic design and will be described in Chapter 3. The manufacturing partners for this project requested a size limit of 2-50mm on any dimension for safety and handling reasons.

It is common to use a loctite™ glue to hold the magnets during the assembly process, however it confers negligible strength during operation, due to their low tensile capabilities and temperature performance and can be ignored in the mechanical design. Jigs are often also required to guide the magnets into position and hold them while the loctite™ sets. Figure 2-7 illustrates the assembly of a magnet piece onto a shaft using rudimentary jigs to aid in alignment; each magnetic pole is made of three magnet pieces due to the maximum size limits placed on magnet pieces.

Figure 2-7: Assembly of rotor magnets using a Jig

After assembly, the outer surface of the magnets is commonly ground, to ensure concentricity with the shaft and provide a smooth defined tolerance surface for placing the sleeve.

2.5.2 Sleeve Pre-stressing

Several methods exist for the pre-stressing of rotor sleeves; the choice is driven largely by the material chosen for the sleeve. The choices are as follows:

- Thermal Shrink Fit
- Axial Pressing
- Tension Winding

The most common choice for metallic sleeves is thermal shrink fitting, while for composite sleeves all three options are commonly used, each with its advantages and disadvantages.

Thermal Shrink Fit

This process takes advantage of the thermal expansion coefficients of the sleeve materials to generate an interference fit between them. Both components are machined so that a defined overlap exists between the inner radius of the sleeve and outer radius of the magnets, so that when assembled the sleeve is forced outward to a larger radius and the required hoop pre-tension

is generated. Assembly is achieved by heating the sleeve so that it expands and cooling the magnet assembly so that it contracts, such that the overlap in dimensions is negated and the sleeve can be easily slid along the magnet assembly into place; as the temperatures of the components normalise, the interference fit is re-imposed. The degree of pre-stress that can be developed by this method is limited by the thermal expansion coefficients of the materials and their safe heating temperatures. From (2.10) it is possible to define (2.18) which shows that the strain and hence pre-stress that can be developed is directly related to the change in temperature and coefficient of thermal expansion of a material and hence the maximum interference stress that can be attained is defined by this and the material Young's Modulus.

$$\epsilon = \alpha_l \Delta T \qquad (2.18)$$

Carbon Fibre Composites have very low coefficients of thermal expansion, approximately zero and even negative, and so the stress that can be developed via this method is dictated by the ability to cool and shrink the magnetic assembly. Metallic sleeves are better suited to thermal shrink fits but the safe heating temperatures of around 400°C for materials used limit the possible pre-stress to approximately 1GPa.

Axial Press Fit

The principle of generating the stress via an interference fit is the same as for a thermal shrink fit, but assembly is achieved by axially pressing the sleeve over the rotor using a high force. There is theoretically no upper limit to the interference stresses that could be generated by this method; however in practice damage to the sleeve, and magnetic assembly caused by the high shear between the two during pressing limits the maximum interference that can be generated. CFRP is particularly prone to damage, specifically to the fibres in the inner surface of the sleeve, which effectively increase the sleeve inner diameter and reduce the interference fit generated. Specially designed tooling and splitting the sleeve axially into rings can alleviate some of the damage caused by pressing, and anecdotally, the author has been told of pre-stress levels of 1.5GPa being achieved.

Tension winding

This process is adapted for a standard filament winding process for composites (such as for constructing pipes and shafts with specific winding patterns) and adds tension to the fibre tow as it is wound directly onto the magnet sub assembly. It is clearly only possible for use with composite sleeves. Two types of fibre tow can be used, preimpregnated and raw; a pre-impregnated tow is pre-coated with the reinforcing matrix of the composite, which is a thermoplastic that is then heated immediately before contact with the rotor, the raw fibre tow has a thermosetting matrix added as a liquid immediately before contact with the rotor. Raw fibre tows are prone to damage (fraying) during winding; the degree of fraying is linked to the tension applied, placing an effective limit of 500MPa on the pre-stress that can be generated. 'Pre-pregged' tows protect against the fraying, allowing tensions of up to 1GPa to be developed, however the thermoplastic matrix used has significant temperature limitations compared to the thermosetting plastics that are used with the raw fibre tows.

2.6 Moving away from the simplified stress model

By relaxing some of the assumptions made in the simplified model, it can be seen that small changes in topology or material properties can significantly affect the rotor stress state and reduce the potential size and magnetic loading.

2.6.1 Alternative Magnet Shapes

The idealised magnet shapes presented in Figure 2-1 are not always the most practical for construction. As mentioned in 2.5.1, there exist maximum dimensions for magnet pieces, thus any pole face is usually made of multiple pieces. There is significant engineering cost associated in ensuring the concentricity of curved faces for the inner surface of the magnets, thus it is considerably easier and cheaper to design the magnet pieces with a flat inner surface that is mated to a flat surface on the rotor coreback. With a high number of magnet pieces, the polygonal inner surface approximates a curve but as the number of pieces decreases the geometry differs significantly, leading to the need to use the formulation for P_{Max}rather than $P_{Average}$ as noted in 2.1.1. It can be shown that the performance of the rotor, in terms of magnetic loading for a given stress limit, reduces as the magnet piece count reduces. Introducing

a flat across a larger arc of magnet adds material that gives an improvement in the magnetic loading, but delivers a larger increase in the operating stress. Therefore it is in the designers interest to balance having a large number of magnet pieces against their effect on the electromagnetic performance and the costs of construction.

2.6.2 Stress Concentrations

Changes in material properties and component profiles around the circumference of the rotor can lead to significant stress concentration, above that which the basic model would predict. This can be shown by considering two cases. Firstly, in some rotor designs it is common to remove some magnet material and replace it with filler, as shown in rotor A in Figure 2-8.

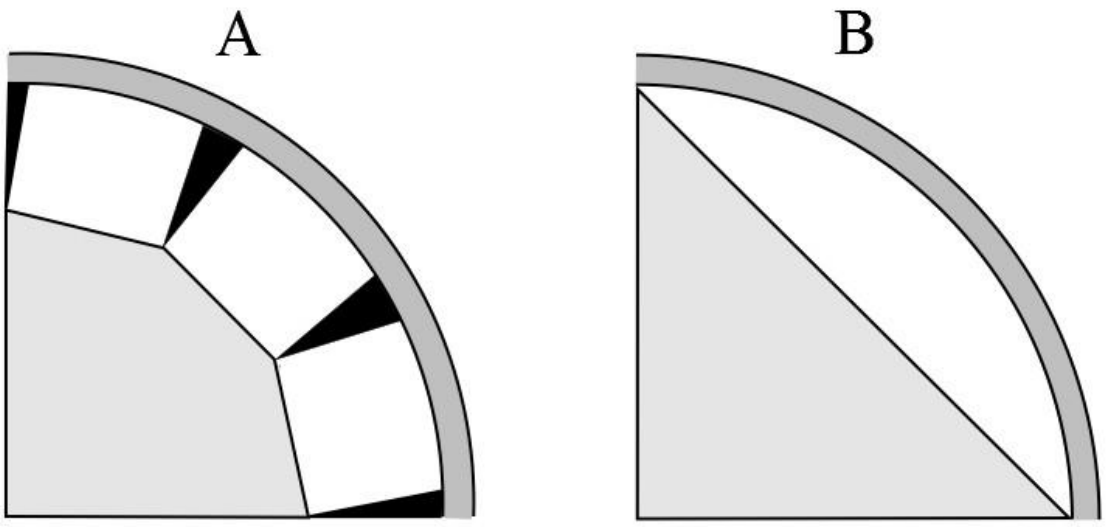

Figure 2-8: Rotor geometries with stress concentrations

The changes in compressibility between the magnets, in white, and the filler, black, in rotor A can lead to a bending stress and concentration near the outer corner of the magnet as the filler will compress more when the pre-stress is applied. In rotor B, the arc shaped magnet also induces a bending stress due to the higher centrifugal forces generated at the thickest point of the magnet, compared to those generated at the magnet corners. The variation in radial force with circumference in this case causes a bending moment along the sleeve circumference and a concentration in the sleeve at the join between two magnets.

The designer must recognise the possibility of stress concentrations in a given rotor design during the initial sizing and apply an appropriate safety factor during the iterative sizing process.

The stresses associated with these concentrations are best computed using FEA once the initial rotor sizing is completed.

2.6.3 Shear Stresses

The assumption that there is no friction between rotor components is one of the factors that allows a 2D stress model. If this is relaxed, significant axial stresses can be seen to develop, as detailed in [1], caused by the effects of poissons ratio. Poisson's ratio defines the strain in a specific axis of a material caused by stresses acting in the orthogonal axes to that strain. In the simplified 2D rotor model this effect has been accounted for in the derivation of the stresses in the hoop and radial directions, but it's effect on the axial strains has been ignored. The high hoop stress levels inherent in HSHP motors mean that the strains developed in the axial direction can be significant, if friction is ignored then the rotor components are assumed to be unconstrained in the axial direction and no-axial stress can be sustained. However if friction between rotor components is considered, the strains in different materials with different poissons ratios and which are under different stresses can lead to the generation of significant tensile shear stresses between the material surfaces. These shears can be large enough to break the magnets, due to their brittle nature; an example of shear cracking in rotor magnets held by a metal sleeve is shown in Figure 2-9.

For example, as in [1], if the rotor sleeve is under a high tensile hoop stress it will experience a negative axial strain causing it to contract axially, the magnets beneath the sleeve are in compression, which causes an axial growth and positive strain to be developed. The difference in strains is converted to a shear stress at the material interfaces, the magnitude of which is proportional to the strain, the friction between the sleeve and the magnets and the compressive stress exerted on the magnets. The effect can easily be shown using an FEA model of the magnet assembly, such as that shown in Figure 2-10.

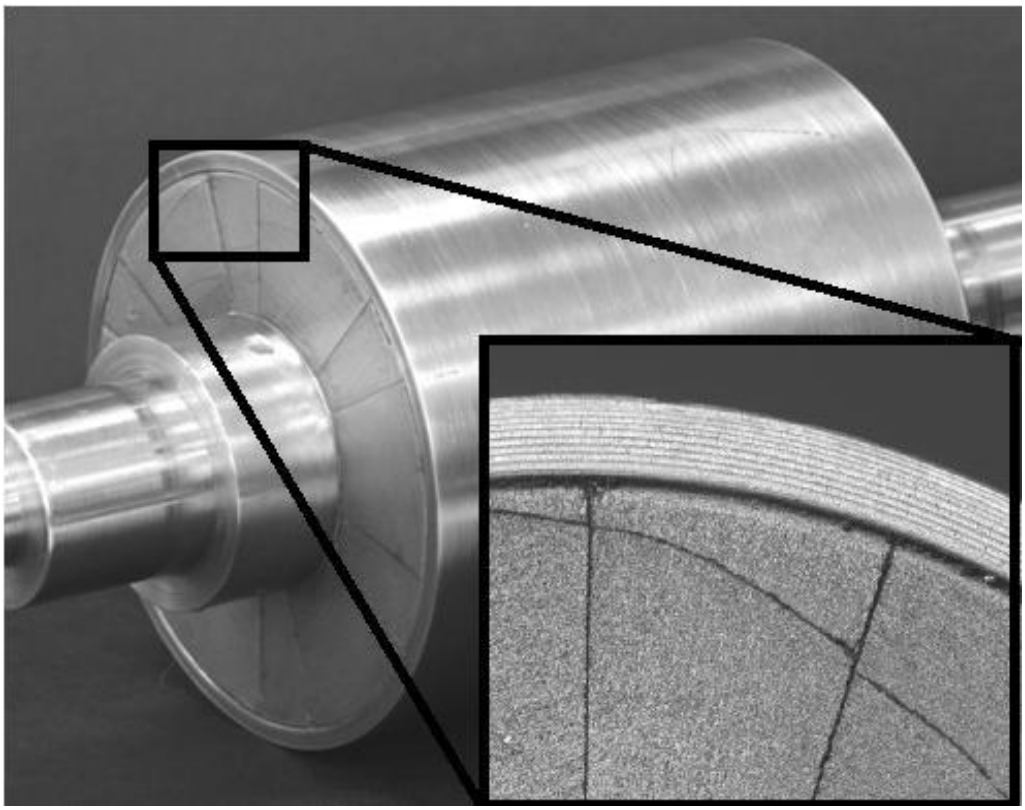

Figure 2-9: Shear Cracking of Magnets From use of a Metallic Sleeve [1]

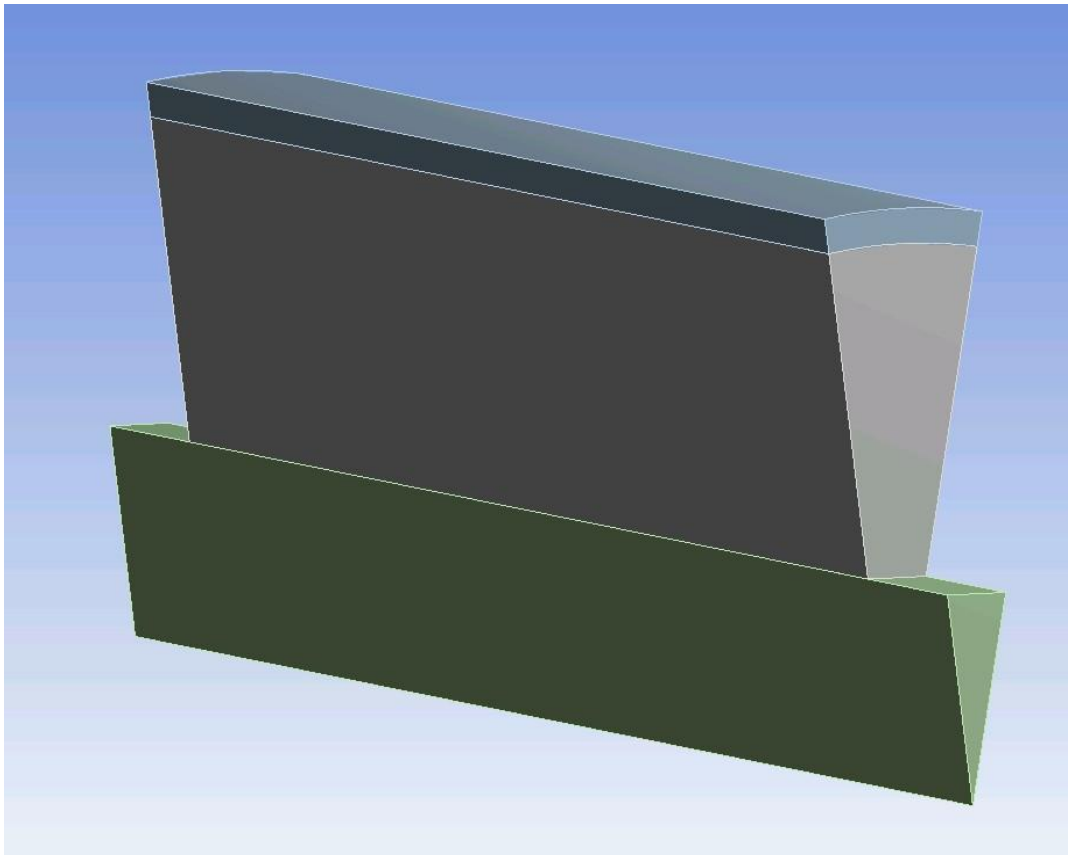

Figure 2-10: Simplified Rotor Structure for Analysing Shear Stress [1]

In the examined rotor the radial compressive stress on the magnets was 35.5MPa, while the maximum peak shear stress was calculated to be 53MPa, high enough to damage the magnets.

The effects of different coefficients of friction are shown in Figure 2-11, taken from [1], which clearly shows that the coefficient of friction limits the level of shear stress to be a proportion of the compressive stress.

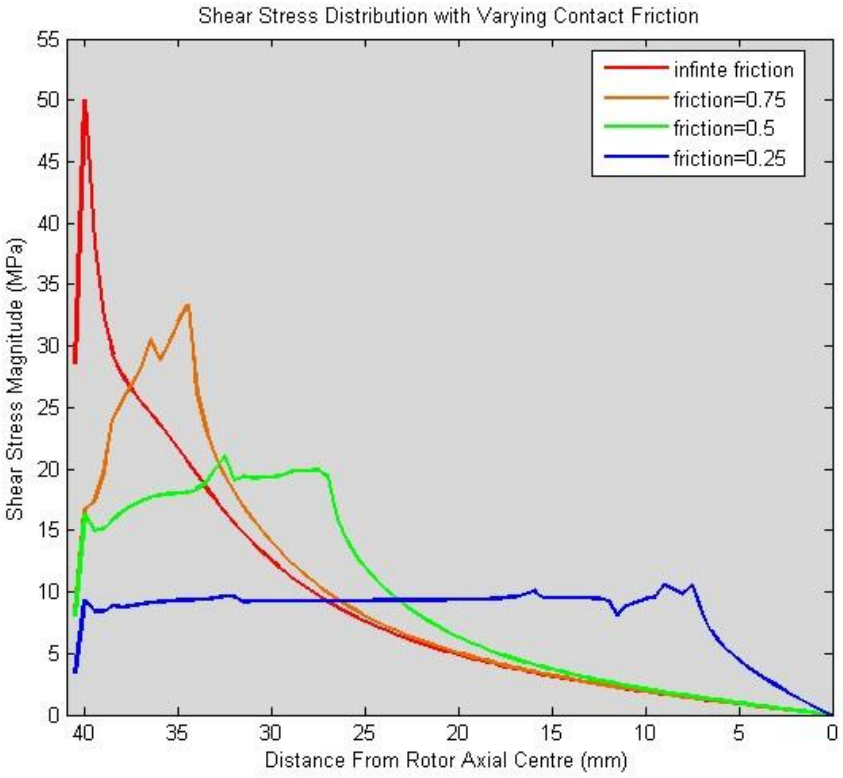

Figure 2-11: Effect of friction on shear stresses [1]

Even with a low coefficient of friction, the high levels of stress in High Speed High Power rotors can still cause significant amounts of shear stress, thus the designer must consider other methods for mitigating the effects of this stress. There are two practical methods for reducing shear stresses on the magnet surfaces; the first involves the use of a layer of ductile material, such as aluminium, between the sleeve and magnets, which deforms under the shear and absorbs the majority of it, before it can be passed to the magnets. This method is complementary to the use of an eddy current shield, which is used to improve the electromagnetic losses in the rotor, and also requires a thin layer of conducting material between the magnets and the sleeve [56].

The second method is to use orthotropic composites for the sleeve, thus limiting the material choice to that of CFRP. The sleeve is made orthotropic by aligning the fibres primarily in the hoop direction, which gives strong hoop tensile properties, but radial and axial properties that are much closer to the resin matrix, which is much more ductile and gives a very low Poisson's ratio between the hoop and axial directions. As a result, the sleeve tends to extend axially with the magnets, independent of its hoop state, leading to zero shear between the surfaces.

The designer must then consider the shear state in the rotor being designed. If a CFRP sleeve is being used, the shear can be ignored and the 2D stress model proposed above is sufficient. However if a metallic sleeve is being used, the expected axial-radial shear should be calculated using [1] to gauge whether it poses a risk to the magnets. If the shear stress level is sufficient to pose a mechanical risk to the magnets an appropriate alteration to the design must be made; either to replace the metallic sleeve with composite, include a ductile material layer or reduce the friction between the magnets and sleeve during assembly.

2.7 Rotor sizing based on mechanical constraints

The constraints highlighted in this chapter, namely rotor stress issues and rotor critical speeds, define a region of acceptable rotor dimensions for any HSHP machine. By considering the pre-stress and operating stress equations, it can be seen that for a given speed, material choice and magnet thickness there exists a fixed maximum radius that satisfies the design criteria. Similarly, by considering (2.16) it can be seen that for a given rotor radius, topology and material choice, a maximum length exists in order for the rotor to remain sub-critical. These limits can be plotted, as in Figure 1-1 to define a region of acceptable rotor dimensions for the machine being designed. Given the design and operating speeds and an initial choice of rotor materials and topology the designer can quickly asses the size of rotor achievable. The span and shape of this space can then be manipulated by altering the materials and the thicknesses of the rotor components, Table 2-6 summarises the effects of these changes on the bounds of the mechanical design space.

The design space of mechanically possible rotor dimensions defined in this chapter can be combined with an electromagnetic loading estimate for the machine, which will be detailed in the next chapter. The electromagnetic loading estimate will describe the required rotor active volume to deliver the machine design torque, given the electrical design of the stator; and the designer can quickly see if the required rotor volume can be achieved in the mechanical design space. Both the mechanical and electromagnetic design equations are analytic in nature, which allows very rapid iteration between mechanical and electromagnetic rotor sizing to ensure a High Speed High Power design that maximises torque output from a mechanically sound rotor.

Design Variable		**Stress Limit** (maximum radius**)**	**Resonant** length given **Speed Limit** for (maximum radius)
Sleeve Design Stress Increase		Increases	No Change
Material Choices	stronger	Increases	No change
	lighter	Increases	Increases
	stiffer	No Change	Increases
Bearing Diameter Increase		No change	Increases
Magnet Thickness Increase		Reduces	Reduces
Sleeve Thickness Increase		Increases	Reduces
Bearing spacing increase		No effect	Reduces

Table 2-6: Effect of design choices on rotor mechanical limits

2.8 Conclusions

This chapter has explored the main mechanical constraints that affect high speed rotor design; these constraints are exclusive to the rotor and stem from the high relative operating speeds of this type of machine. The rotor radius is limited by the build up of stress in the rotor components, which is caused by the need to keep the magnets in compression at all times. The length of the rotor is limited by mechanical resonance in the system, most High Speed High Power rotors are designed to operate below their first bending mode frequency, which places a limit on the bearing spacing of the rotor, between which the active portion of the machine and the end windings must accommodated. The biggest effect the designer can have on the rotor sizing is through altering the ratio of the magnet thickness to the sleeve thickness; adding more magnet material under the sleeve will increase its stress levels, and conversely having a thicker sleeve will reduce the stress it carries. Additionally, altering the mass of the magnetic assembly will shift the resonant speed of the rotor. Both these design choices have significant effects on the electromagnetic performance of the machine, which will be discussed in the next chapter, and form the basis of the variations in design when iterating between electromagnetic and mechanical designs to find a suitable machine geometry.

Changing materials in the machine can have a dramatic effect on the mechanical design space, for example moving from an Inconel sleeve to a CFRP one can give a step change in achievable rotor size, due to its high stress limits and lower weight. The construction method chosen for the rotor can also significantly alter the available design space due to the stress limits that can be reached with each method. Both materials and construction methods can be affected by the expected operating environment and temperatures, which can prelude the use of certain materials, such as CFRP in high temperature environments. A simple estimate of the thermal operating point of the machine is required to enable the designer to eliminate certain materials, and will be presented in chapter Chapter 4.

Chapter 3. Electromagnetic constraints

After the initial mechanical sizing is complete an electromagnetic design can be undertaken. The estimation of the required rotor volume from the chosen magnetic and electrical loadings is trivial, using standard machine design equations, however there are numerous factors that affect the loadings, which the designer must consider carefully. The most significant factor affecting the electrical loading of the machine is the choice of drive technology available; depending on the speed and power requirements of the machine the available drive can put severe limitations on the machine size, turn number and frequency. The universal choice for High Speed High Power machines is a Voltage Source Inverter (VSI), providing a PWM (Pulse Width Modulated) voltage signal to the machine terminals and using position, speed and current feedback for control. Given the choice of available drive the designer can perform an initial rotor sizing in both electromagnetic and mechanical design spaces, before progressing to estimate the loss and performance of the design which can require alterations to both the mechanical and electromagnetic designs.

Secondary to the size constraints of the machine imposed by the available drive are the losses caused for the design, these pose significant issues with respect to cooling and must be estimated accurately. Accurate loss estimation requires feedback from the drive design, as time harmonics in the supplied current waveform can create significant amount of loss throughout the machine. Close collaboration is required with the drive design as the choice of machine components and topology can affect the equivalent circuit seen by the drive and hence affect the Total Harmonic Distortion (THD) of the drive supplied signals. Analysis without considering the THD of the drive currents, i.e. only using sinusoidal current inputs, is insufficient to provide accurate loss estimation. Once machine losses are estimated, a thermal design is required to assess their impact and whether there is a need for an electromagnetic redesign. The majority of losses can be estimated analytically to allow a quick iterative thermal-electromagnetic, design which can then be fed into the mechanical-electromagnetic design loop.

This chapter will describe the effects of the choice of drive on the design of the machine and provide analytical methods for estimating the most important losses in the machine. Using the observations on drive choice and estimations of losses in the machine, the designer can perform rapid estimations of the machine electromagnetic performance, and couple this with the rapid mechanical design tools presented in the previous chapter, to quickly produce a base design that meets both the electromagnetic and mechanical constraints.

3.1 VSI constraints

As noted in the introduction, when designing a High Speed High Power machine, the first consideration should be what electronics are available to power and control it. The availability, cost and performance of high power level inverters can place severe limitations on the machine design. There are multiple VSI topologies available for the design of PM machines, as summarised in the introduction, however the following work will focus only on the design of machines connected to a single VSI operating at low voltages. Solutions involving medium voltage inverters and multi-phase systems with parallel inverters will not be considered in detail.

3.1.2 VSI Voltage levels

Commercially available medium voltage inverters exist for use in industry; however they are not well suited to operation with a High Speed High Power machine that requires a highly dynamic performance and connection to factory level power supply. As noted in [57], medium voltage converters with device voltages in the range 2-8kV and multiple MVA ratings are readily available, but their switching frequencies are limited, thus limiting the highest motor frequency they could supply. Furthermore, in high speed machines the dV/dt associated with rapid switching of a multiple kV signal would lead to significant voltage stress on the motor insulation – adding mass and cost to the machine design – and can be expected to create a large harmonic content in the waveform, increasing the losses significantly or requiring costly and lossy filters to be placed between the drive and machine. Finally, in order to achieve a medium voltage from a factory level power supply, a large isolation transformer with a step up is required, which adds significant space, cost and losses to the motor-drive system.

For these reasons the only appropriate VSI's available operate at low voltages, i.e. a DC link voltage of less than 1kV. At this level of operation, several commercially available VSI's exist, with power capabilities in the MVA range and the ability to supply large motor fundamental frequencies of 500Hz-1kHz, notably in the UK from suppliers such as Control Techniques and Unico.

The use of low voltage level VSI's has multiple implications on the design of a HSHP machine, both physically and through the choice of winding design. First, by considering the power requirements of a machine and the basic power equation for a three phase machine, as in (3.1) for

a DC link voltage less than 1kV, the RMS phase voltage will be significantly lower, and hence the phase currents for a high power machine will be very large, typically over 1000A RMS.

$$P = 3V_{phase(RMS)}I_{phase(RMS)}\cos(\emptyset) \quad (3.1)$$

For Example, a 1MW capable machine running off a 1kV DC link (408V RMS per phase) and a power factor of 0.707 ($\emptyset = 45^o$, 1pu armature reactance) will require a phase current of 1154A RMS. The large operating currents pose significant challenges when designing the cables. With water jacket cooling limiting conductor current densities to 10-15A/mm^2 [40] the required cross sectional area for a turn is approximately 76-115mm^2, which is a wire diameter of 10-12mm. There are three implications of this conductor sizing; firstly it is likely to require the conductors to be multi-stranded, as even at 500Hz, the electrical frequency of a 2 pole 30,000rpm machine, the skin depth of a copper conductor is 3mm. Secondly, the large space required per turn will significantly affect the winding design and turn numbers; low turn numbers will be required in order to limit slot areas and prevent long, deep slots that are mechanically weak and create large amounts of leakage inductance. Finally, the required thickness of a single stand conductor would render it very stiff and difficult to wind by hand; requiring significant investment in mechanical forming equipment for the windings similar to that used for forming generator bars.

The second effect of using low voltage level VSI's is to limit the machine Back EMF. It is desirable to maximise the magnetic loading of the rotor, to deliver the most torque per unit volume and this, coupled with the high operation speeds in general leads to a low turn number being required to limit the maximum EMF to be lower than the VSI voltage [58]. The specifics of a particular machine design may cause variations in the severity of this constraint; however HSHP designs are commonly limited to very low numbers of turns per phase.

There are advantages to a low voltage design, the most significant being the low level of voltage stress on the insulation of the machine. As per [59] a limit of 1kV on the DC link limits the voltage stresses in the machine windings to 2kV, which can be protected using conventional wire enamels and slot liners, thus limiting the amount of dielectric insulation required in the slots, improving slot fill and hence machine thermal performance.

3.1.2 Switching frequency

Though of better performance than medium voltage VSI's, the switching frequencies of low voltage VSI's still pose a significant limit on the design of the machine. The best performing 'off the shelf' inverters are limited to motor fundamental frequencies of 500Hz [60] and 1000Hz [61]. This in turn limits the pole number choice, as summarised in Table 1-1, speeds above 30,000rpm are only possible with a 1000Hz capable inverter, while the other maximum operating speeds leave little choice over pole number, thus affecting rotor and stator core back depths and frequency dependent losses and demagnetisation.

Maximum operating speed:	**500Hz VSI**	**1000Hz VSI**
15,000rpm	4pole	8pole
30,000rpm	2pole	4pole
60,000rpm	Not Possible	2pole

Table 3-1 Highest pole number choice for common HSHP machine speeds

In general, opting for the lowest possible pole number will give the lowest loss design due to the limitation of operating frequencies; however there is still a benefit to aiming for more than a two pole design. Moving from two to four poles halves the coreback depth and enables new rotor topologies by halving the minimum magnet depths (to resist demagnetisation of the portion of the magnets that lie in the q axis); both of which can have significant economic effects on the machine by dramatically reducing the amount of expensive magnet and lamination materials required. A notable disadvantage of maximising the pole number is that it can affect the harmonic content of the current waveform, going from two to four poles halves the number of switching cycles per fundamental current period, leading to a higher level of voltage harmonics being present, which can lead to increased current harmonics and hence losses.

3.2 Inductance Limited Design

3.2.1 Impact of low VSI voltages

As noted in section 3.1, the impact of using low voltage level VSI's on the design of HSHP machines is to severely limit the machine turn number through a combination of requiring a low back EMF and through phase currents requiring a large copper area per turn. As a result the electrical loading around the periphery of the machine is low and the machine has a low inductance.

The requirement for low inductance can also be approached from an alternative definition, by considering the phasor diagram of the machine and the armature reaction. The phasor diagram for a non-salient HSHP machine is shown in Figure 3-1, the current I is typically placed in phase with the back EMF, E, to ensure peak torque per amp operation, the resistance drop in the machine can be considered negligible. The inductance of the system (machine, cables and filters) is defined as L and the V as the VSI supply voltage;.

.

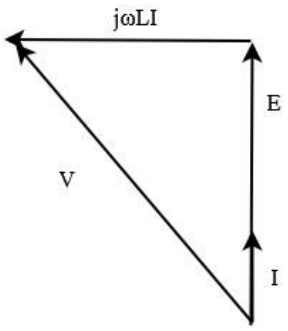

Figure 3-1: Phasor Diagram for Non Salient HSHP Machine

Given the previously noted high phase currents and the high speed operating range, the machine inductance must be kept low, in order to ensure that the armature reaction and back EMF remain low enough to be controlled by the available drive voltage at the maximum speed and torque operating points. Typically the inductance values required for a HSHP machine are in the μH range, which can be a significant challenge to achieve, given the limitations on rotor size and the leakage inductances present. The designer should therefore consider choosing an initial full speed operating point phasor diagram that allows the maximum inductance headroom, to ensure

that that the armature reaction does not become too large and limit the ability to achieve rated torque at full speed. The operating point that allows the largest amount of inductance in the machine can be found by considering the machine phasor diagram, power requirements and the fixed nature of the available drive voltage. The machine corner point represents the maximum speed and power that must be achieved, the power, P, delivered at that operating point can be described by (3.2), using the line to line EMF, E, and phase current I.

$$P = \sqrt{3} E_{Line(RMS)} I_{Phase(RMS)} \quad (3.2)$$

Now, considering the phasor diagram for the machine in Figure 3-1 the magnitude of the line to line voltage V, can be defined from (3.3).

$$V_{Line(RMS)} = \sqrt{\left(\left(E_{Line(RMS)}\right)^2 + \left(j\omega L I_{Phase(RMS)}\right)^2\right)} \quad (3.3)$$

We can now equate (3.2) and (3.3) to form (3.4)

$$V_{Line(RMS)}^2 = E_{Line(RMS)}^2 + \left(j\omega L \frac{P}{\sqrt{3} E_{Line(RMS)}}\right)^2 \quad (3.4)$$

This can then be arranged in terms of the machine inductance to give (3.5)

$$L^2 = \frac{V_{Line(RMS)}^2 - E_{Line(RMS)}^2}{\left(\omega \frac{P}{\sqrt{3} E_{Line(RMS)}}\right)^2} \quad (3.5)$$

Which can be simplified to (3.6).:

$$L^2 = \frac{3V_{Line(RMS)}^2 E_{Line(RMS)}^2 - 3E_{Line(RMS)}^4}{(\omega P)^2} \quad (3.6)$$

We can find the maxima of this expression by equating the implicit differentiation $\partial L / \partial E_{Line(RMS)} = 0$, giving (3.7).

$$3V_{Line(RMS)}^2 - 6E_{Line(RMS)}^2 = 0 \qquad (3.7)$$

The solution to this lies at $E_{Line(RMS)} = \frac{1}{\sqrt{2}} V_{Line(RMS)}$. From this the maximum allowable inductance of the machine can be calculated from the known power, speed and drive requirements.

It should be noted that the initial choice of operating point of placing current in phase with EMF is arbitrary, however the resultant power factor of 0.7 provides a balance between field and armature flux in the machine which in turn represents a balance between the mechanical constraints (stress) which limit the field flux generation capability and the thermal/electromagnetic constraints which limit the armature flux generation capability.

Thus the designer should aim for this back EMF value as the initial operating point of the machine, given the line voltage constraint applied by the drive. To choose a higher EMF value would require a lower phase current to achieve the rated power but would also constrict the available volts for overcoming the armature reaction at a greater rate, and the drive would not be able to supply the new rated phase current. Conversely, reducing EMF from this point would require a higher phase current but would not free up enough volts to allow that current to flow.

Clearly, if achieving the required field or armature fluxes prove not to be as difficult as expected the power factor and machine operating point can be altered to provide greater flexibility in the design process. However, this operating point for maximum allowable inductance provides a useful starting point for designing the machine when this is not known beforehand.

3.2.2 Requirements for Low Electric Loading

As noted in the previous section, the use of low voltage level VSI's places a limit on the maximum inductance of the system, this can often be so low that it poses a significant constraint on the machine design. The most direct way to alter the machine inductance is via the electric loading of the periphery, by reducing the electric loading, via reducing the number of turns, the inductance is reduced and a larger rotor is required to deliver the rated torque. This is in direct conflict to the mechanical constraints limiting the size of the rotor and can present one of the most significant hurdles in delivering a mechanically and electromagnetically sound design. Due to the low turn numbers, altering the number of turns in a High Speed High Power machine to alter the electric loading, can cause large alterations in the required rotor size, as a single turn can

represent a large portion of the MMF around the periphery. In the most extreme case, moving from two turns to one turn would halve the machine inductance but double the length of rotor required, assuming the radius is fixed by the speed-stress constraints on he rotor. Thus it can be seen that careful iteration between the mechanical and electromagnetic constrains is required at the outset of the design, in order to find a rotor size and topology that gives satisfactory performance in both domains.

3.2.3 Parallel Windings

The requirement for low turn numbers can have a significant effect on the winding design of the machine, limiting the ability to use distributed windings to minimise rotor loss. To overcome this limitation and return flexibility to the winding design, parallel windings are commonly used. Each phase can be split into parallel paths that can be treated as fractions of a turn and distributed as required. This method can prove highly effective at allowing a more distributed winding for a low turn number machine, which not only improves the loss reduction options by increasing the effective number of turns but can also help provide better thermal design by allowing a better distribution of copper to slot around the periphery. The conductors for a parallel path need not all be in the same slot, which allows individual slot areas to be smaller, resulting in a lower temperature rise across the windings, for the same current density, when conducting the ohmic winding losses out to the machine coreback.

As noted in [62] the most essential design consideration when choosing a parallel winding path design is to ensure that the impedance of each path and the induced EMFs are equal and in phase, in order to minimise circulating currents between the paths. To do this, each path must occupy the same number of slots and share the same slot potentials as the other paths. These requirements place limitations on the degree of parallelism that is achievable with different rotor pole numbers; for a given pole number the number of parallel paths allowable to give a balanced phase winding must be an integer sub-multiple of the pole number.

Whilst the use of parallel paths can aid in better winding design, their use poses the same constraints on rotor sizing as low turn numbers due to the large changes in the electrical loading of the machine caused by splitting the current per turn.

3.2.4 Geometry effects on machine inductance

There are several additional methods for affecting the machine inductance, which are achieved by alterations to the geometry. These options can be summarised as, altering the slot profile to affect leakage, altering the end winding lengths and altering the effective armature air gap.

Altering the slot profile

It is well known that adjusting the shape of an electrical machines slots can affect the leakage inductance component of the machine inductance [63]. In High Speed High Power machines, the leakage inductance caused by slot closures can be altered as a method of altering the machine inductance to meet the constraints detailed in 3.2.1. It is often useful to widen slot openings to reduce the leakage inductance, but this comes at the cost of reducing the torque density via altering the effective air gap length of the machine (via the carter coefficient, [63, 64]) and altering the losses in the rotor via the slotting effect.

Altering the end winding lengths

The amount of machine inductance can be altered by adjusting the length of the end winding paths and hence the volume they enclose, with extra length paths adding extra inductance to the machine. In general with HSHP machine design, the mechanical constraints on rotor length and the need to minimise machine inductance favour the shortest possible end winding lengths, subject to the constraints of minimising losses. As will be seen in section 3.4, the need to minimise losses favours the use of distributed windings, giving relatively large end winding bundle sizes and inductances compared to a single tooth winding, thus other methods must be considered to minimise the inductance and bundle size. Such options include the choice of lap or wave windings, and compressing of the end winding bundles against the stator axial ends.

Altering the Effective Armature Air Gap

As noted in [65] the effective air gap of a PM machine is different when considered from the armature or from the field. The low recoil permeability of the rotor magnet material means that the reluctance seen by the armature windings is significantly larger than that caused by the air

gap and sleeve alone. This reluctance has a direct effect on the machine magnetising inductance. The difference between the effective armature air gap and the effective field air gap is shown in Figure 3-2. The nature of this air gap allows the designer to alter the machine inductance significantly, without altering the magnetic loading; this is achieved by altering magnet and sleeve depths in conjunction, to maintain the fixed mechanical stress requirement and the same air gap flux density but with a different overall distance between stator and rotor coreback. For example, increasing the sleeve thickness will increase both effective air gaps while reducing the stress state in the sleeve; the magnet thickness can then be increased to compensate for the drop in the effective field air gap by increasing the magnetisation strength across it, without increasing the stress state of the rotor beyond its original level. Careful iteration between the mechanical constraints and the inductance constraint is required in this procedure as both the stress state and natural frequencies (via the parasitic mass of the rotor active materials) of the rotor are being altered, and it can form the bulk of the initial sizing with regards to the inductance constraints. The biggest drawback to this method is that it can lead to large volumes of magnet material being required, which can add significant cost to the rotor.

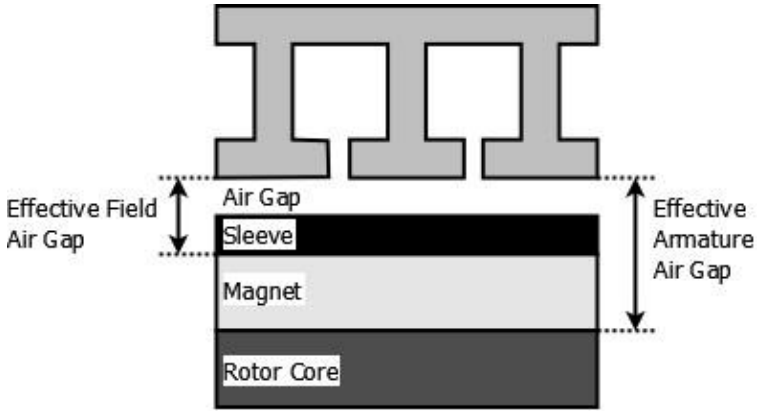

Figure 3-2: Effective Field and Armature Air Gaps

3.3 Loss Estimation

The high speed and high power nature of the machines being considered lead to there being several significant sources of loss. The large powers encountered in High Speed High Power machines result in even the most efficient machine dissipating large amounts of loss in the form of heat, the concentrations of which and locations within the machine require large amounts forced cooling to maintain safe operating temperatures. High electrical frequencies cause significant iron losses and AC loss effects in the armature conductors, while striving to achieve

the highest possible electrical loadings leads to the high current densities in the armature and rotor losses being the most critical design issues. The low inductance nature of the machine, coupled with a low ratio of switching to fundamental frequencies of the associated drives, can lead to significant time harmonics being present in the current waveforms of the machine, which cause associated armature and rotor losses. Finally, the high speed leads to significant friction losses in the bearings and windage losses on the rotor surface.

The machine designer must be able to predict the expected losses to a high degree of accuracy, in order to allow accurate thermal modelling and hence adequate design of the cooling systems for the machine. Rapid analytical based techniques allow the designer to quickly predict the expected losses of a design early in its development and make suitable alterations and rapid iterations to minimise or adequately extract the losses.

This section will summarise the main causes of the losses in HSHP machines and present analytical methods for quickly estimating their magnitude in the initial iterative design stages. Specific methods for their reduction and mitigation in HSHP machines will also be presented.

3.4 Rotor Losses

This section is concerned specifically with losses created by the magnetic fields within the High Speed High Power machine. Other, mechanically based, rotor losses are described in section 3.6.

The time varying nature of the magnetic fields that interact with the rotor of an electrical machine create potentials within any conducting components which drive currents to flow that actively oppose the fields and try to cancel them out. The potentials are induced by fields that rotate asynchronously with the rotor in the air gap of the machine; the asynchronous fields consist of harmonics of the fundamental armature MMF, generated by the spacing of the stator windings and time harmonics in the phase currents. The fundamental torque producing MMF in the windings does not generate rotor losses as it rotates synchronously with the rotor and so appears stationary to the rotor components, and thus induces no voltage.

The problem can be analysed by considering the armature MMFs as a current sheet travelling tangentially at the stator inner surface (bore) that is rich in harmonics due to the effect of the stator slots and the winding arrangement. This method of analysis has led to many proposed models in the literature for estimating the magnitude of the losses caused, [33, 34, 66, 67]; the following sections will present a simplified method for analysing such losses, tailored for rapid

estimation of the losses in High Speed High Power machines when different geometries and winding designs are considered.

In PM machines there can exist an additional 'slotting loss' caused by variations in the stator permeance which cause the flux density in the magnets to vary depending on whether they are sitting underneath a tooth tip or a slot opening [68]. This effect can generally be minimised in HSHP machines by the large effective air gap and the use of high slot numbers, which minimise the variation in stator permeance seen by the rotor [69, 70], minimising the ripple in flux density of the magnets which causes the no load loss [67, 68, 71]. As such the no load losses can be ignored for speed and convenience during the initial sizing of a High Speed High Power machine. The following section will focus on accurate, rapid analytical methods for the prediction of the harmonics present in air gap of the machine due the armature MMFs and the estimation of the losses they cause.

3.4.1 MMF Harmonics in the Air gap

A machine designer needs a tool that can rapidly assess the harmonic content of different winding designs and slot shapes and quickly provide an estimate of the rotor losses they might cause. A simple computational method has been developed that can quickly and simply be implemented in a computer program, it relies on an iterative summation of the harmonics of each individual slot in the air gap of the machine, followed by an analytical based estimate of the losses these harmonics cause. The advantage of this method is that it can deal with variations in slot numbers and geometry and in winding turn numbers, phase numbers and the distribution and pitching of the windings; the only required inputs are the machine geometry and a vector of the slot MMF's at a given point in time.

The analysis is performed by considering the harmonic spectrum of the tangential air gap magnetising field strength, H, created by the slot MMF drop across the slot openings. The total rotor losses caused can be computed by superposition of the losses caused by each harmonic, each of which can be treated as a current sheet moving parallel to the rotor surface, which has a classic solution, as presented in [32]. The harmonics in the air gap of the machine can be separated into space harmonics – caused by the distribution of the armature windings – and time harmonics – caused by harmonics present in the phase current waveform. The space harmonic distribution can be evaluated using the above mentioned method of calculating the MMF across the slot openings, while the air gap distribution of the time harmonics can be estimated by applying each time harmonic waveform to the space harmonic distribution.

3.4.2 MMF Space Harmonics in the Air gap

At any given point in time, the tangential magnetic field, $H_t(t)$, crossing the opening of a slot can be related to the MMF in that slot, $MMF_{Slot}(t)$, using Amperes Circuital Law, as defined in (3.8), where C is a loop around the slot periphery, encompassing the slot opening and S is the surface it encloses – as shown in Figure 3-3. The net MMF in the slot at any point in time is defined by the winding arrangement and may contain additional turns from multiple phases if the winding is an overlapping kind.

$$\oint_C H_t(t)dl = \iint_S JdS = MMF_{Slot}(t) \qquad (3.8)$$

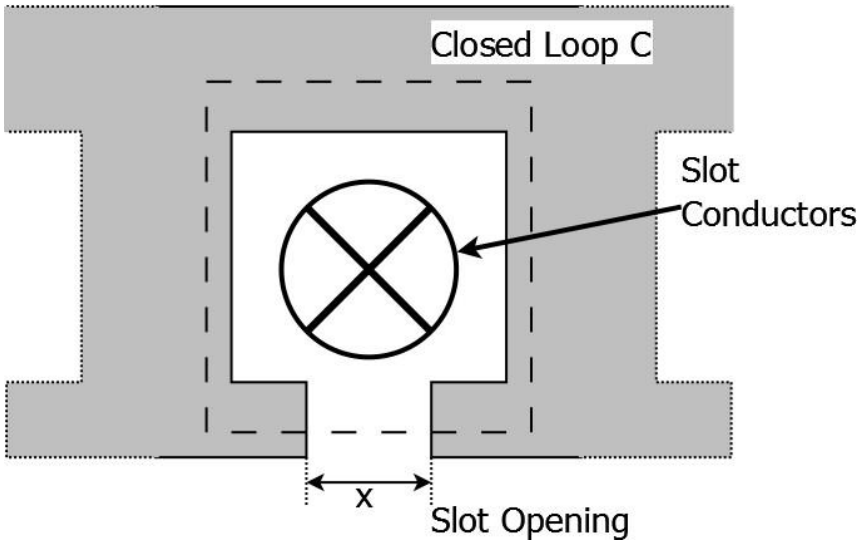

Figure 3-3: Magnetic field across slot opening

Noting that the permeability of the lamination material is many orders of magnitude higher than that of free space, it can be assumed that the H field in the portion of the loop that lies inside the laminations is negligible. Given the slot geometry shown in Figure 3-3 this allows $H_{T,slot}(t)$ to be defined as in (3.9), where x is the distance across the slot opening.

$$H_{T,slot}(t) = \frac{MMF_{Slot}(t)}{x} \qquad (3.9)$$

The value of $MMF_{Slot}(t)$ is dependent on the winding arrangement and the phase currents at any particular time, t. The value obtained for $H_{T,slot}(t)$ can be considered as constant and uniform

across the slot opening, which is an idealisation of the real case, but a very close approximation. Thus the tangential field around the bore of a stator, caused by a single energised slot is shown in Figure 3-4, the angles of the slot opening edges are defined as θ_a and θ_b respectively.

From Figure 3-4 it can be seen that the waveform of $H_{T,slot}(t)$ is periodic in 2π, and can thus be analysed as a Fourier series to decompose it into its harmonic components. $H_{T,slot}(t)$ for a single slot can then be described tangentially around the stator bore giving $H_{T,slot}(t,\theta)$ using (3.10), the Fourier series expansion for $H_{T,slot}(t)$ evaluated between θ_a and θ_b, where n is the harmonic order.

$$H_{T,slot}(t,\theta) = \frac{H_{T,slot}(t)(\theta_b - \theta_a)}{2\pi} + \sum_{n=1}^{\infty} \frac{H_{T,slot}(t)}{n\pi} \{(\sin(n\theta_b) - \sin(n\theta_a))\cos(n\theta) + (\cos(n\theta_a) - \cos(n\theta_b))\sin(n\theta)\} \quad (3.10)$$

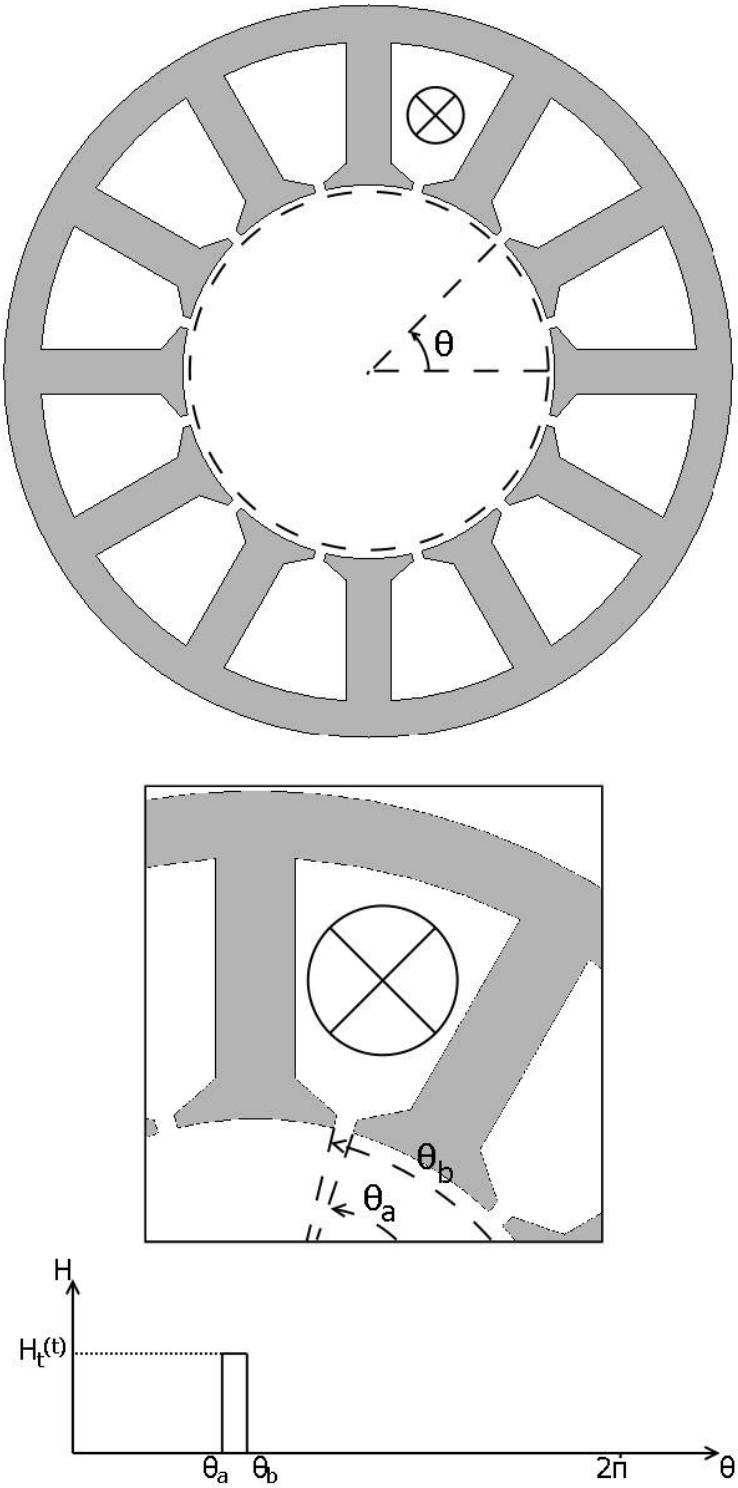

Figure 3-4: Tangential H field in air gap of one energised slot

Each subsequent slot around the stator bore can be analysed in a similar manner, with its corresponding $H_{T,slot}(t)$ depending on the winding arrangement and the values of θ_a and θ_b modified by the slot pitch as defined in (3.11) for a regularly spaced set of stator slots, where m is the slot number and λ_{slot} is the pitch between stator slots.

$$\theta_a(m)=\theta_a + (m-1)\lambda_{slot}$$

$$\theta_b(m)=\theta_b + (m-1)\lambda_{slot} \tag{3.11}$$

Using this method, the harmonic spectrum of the tangential H field in the air gap can be built up using space addition of each harmonic around the circumference of the stator bore. For each harmonic, the contribution from each slot can be summated around the air gap of the machine using (3.12), where slot no. is the total number of slots in the machine. $H_{T,slot}(t,m)$ must be described by the designer as an array containing the values of $H_{T,slot}(t)$ for each slot in the machine, based on the of turn numbers and phases contained in each slot. The magnitude of the resulting waveform can then be used for estimating the losses caused by that harmonic, once the direction of rotation has been ascertained.

$$H_{T,n}(t,\theta) = \sum_{m=1}^{slot\ no.} \frac{H_{T,slot}(t,m)}{n\pi}\{(\sin(n\theta_b(m)) - \sin(n\theta_a(m)))\cos(n\theta) + (\cos(n\theta_a(m)) - \cos(n\theta_b(m)))\sin(n\theta)\} \tag{3.12}$$

The designer can now look at the time variation of each harmonic to ascertain which direction it rotates in the air gap of the machine. The solution to $H_{T,n}(t,\theta)$ for $\theta = 0 \rightarrow 2\pi$ describes the waveform of the harmonic around the air gap of the machine, analysing this at consecutive points in time will illustrate which direction the harmonic rotates.

The described numerical based method for analysing the harmonic content of the tangential air gap H field has advantages compared to purely analytical methods as it allows for rapid comparisons between different slot, phase, turn, pole and winding combinations without requiring a large amount of effort by the designer to calculate of redefine the equations. All that is required is to define the slot $H_{T,slot}(t,m)$ vector, based on the desired slot and turn numbers and the winding arrangement. An example of the required vector is given in (3.13) for a four pole, 12 slot, single layer winding with 10 turns per slot and 50A peak phase current, the stator bore radius is 100mm and slot opening of 5 degrees, giving a slot opening, x, of 8.73mm as defined by Figure 3-3.

$$I_A(t) = 50\sin(\omega t)$$

$$I_B(t) = 50\sin(\omega t - \frac{2\pi}{3})$$

$$I_C(t) = 50\sin(\omega t - \frac{4\pi}{3})$$

$$H_{T,slot}(t,m) = \frac{MMF_{Slot}(t)}{x} = \frac{NI_{phase}(t)}{x}$$

So:

$$\begin{aligned}
H_{T,slot}(t,1) &= \hat{H}\sin(\omega t) \\
H_{T,slot}(t,2) &= -\hat{H}\sin(\omega t - \frac{4\pi}{3}) \\
H_{T,slot}(t,3) &= \hat{H}\sin(\omega t - \frac{2\pi}{3}) \\
H_{T,slot}(t,4) &= -\hat{H}\sin(\omega t) \\
H_{T,slot}(t,5) &= \hat{H}\sin(\omega t - \frac{4\pi}{3}) \\
H_{T,slot}(t,6) &= -\hat{H}\sin(\omega t - \frac{2\pi}{3}) \\
H_{T,slot}(t,7) &= \hat{H}\sin(\omega t) \\
H_{T,slot}(t,8) &= -\hat{H}\sin(\omega t - \frac{4\pi}{3}) \\
H_{T,slot}(t,9) &= \hat{H}\sin(\omega t - \frac{2\pi}{3}) \\
H_{T,slot}(t,10) &= -\hat{H}\sin(\omega t) \\
H_{T,slot}(t,11) &= \hat{H}\sin(\omega t - \frac{4\pi}{3}) \\
H_{T,slot}(t,12) &= -\hat{H}\sin(\omega t - \frac{2\pi}{3})
\end{aligned} \qquad (3.13)$$

Where:

$$\hat{H} = \frac{N\hat{I}}{x} = 57.3kA/m$$

In the example in (3.13), λ_{slot} is 30 degrees and the resultant tangential air gap field at the stator bore at time $t = \frac{\pi}{2\omega} + \delta$ is shown in Figure 3-5, superimposed on the graph are the waveforms of the fundamental torque producing harmonic (4 pole, red) and the first major harmonics above that, the 5th (green) and 7th (blue) order harmonics (which ate 10 and 14 pole fields respectively due to the fundamental field being 4 pole)

The full harmonic spectrum for this result is shown in Figure 3-6; the magnitude of the harmonics can be seen to roll off and create side bands, at the higher orders. The rate of this roll-off is governed by the width of the slot opening, with a wider slot causing a faster rate of roll off. The results for this example can be seen to match the classical results expected for a three phase winding, with even and triplen harmonics being zero and the remaining harmonics being of equal

magnitude to the fundamental, i.e. with $k_p$and k_w being equal to 1 [63, 72, 73], but with the additional effect of the roll off due

to the slot opening being included for greater accuracy.

Further analysis of the harmonic spectrum at consecutive time points allows identification of the direction of rotation of each harmonic. In the case above showing the 5th rotating in the opposite direction to the fundamental and 7th harmonics, as shown in Figure 3-7, this result again matches with the classical analysis that states the$(3n-1)^{th}$ harmonic rotates backward, or against the direction of the fundamental, while the $(3n+1)^{th}$ harmonic rotates forward, with the direction of the fundamental.

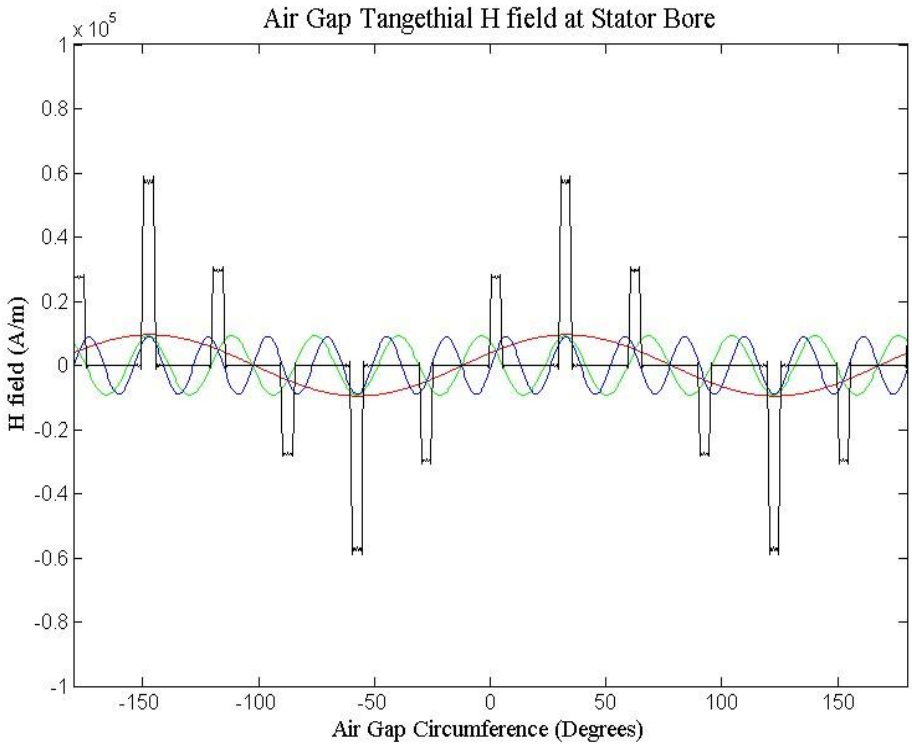

Figure 3-5: Air Gap Tangential H field at Stator Bore

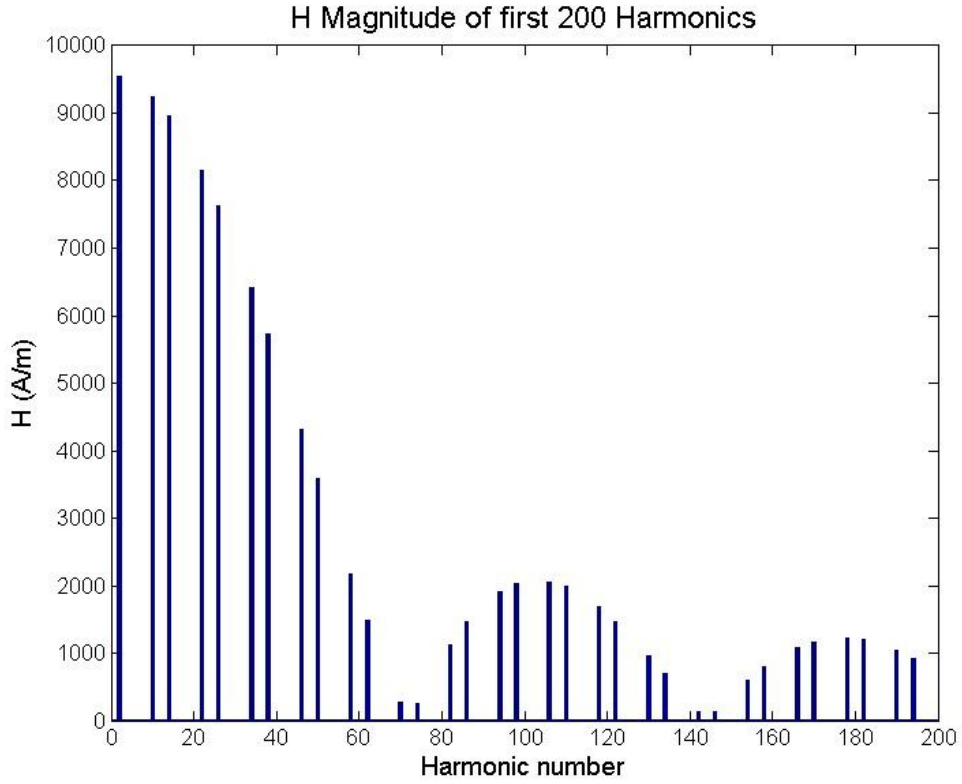

Figure 3-6: Harmonic Content of Air Gap Tangential H field

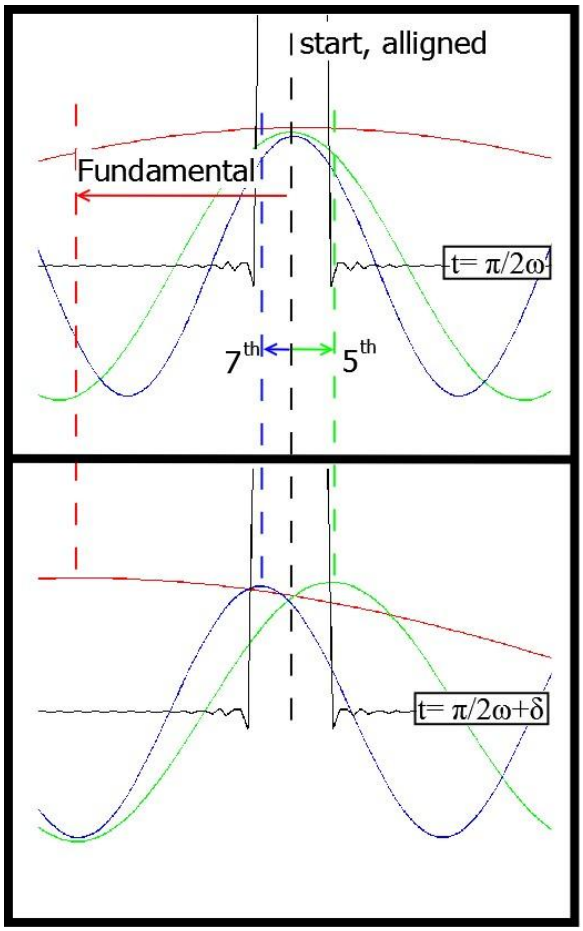

Figure 3-7: Rotational Direction of Harmonics

The magnetic fields created by the first two harmonics, 5 and 7, for the example rotor are displayed in Figure 3-8, which highlights an important feature of the space harmonics, as the harmonic order and hence number of poles in the field increases, the depth of penetration of the field into the rotor diminishes. This is helpful to the designer as only the lower order harmonics penetrate the rotor and create eddy currents; the higher order harmonics, though potentially large in magnitude do not interact or create losses.

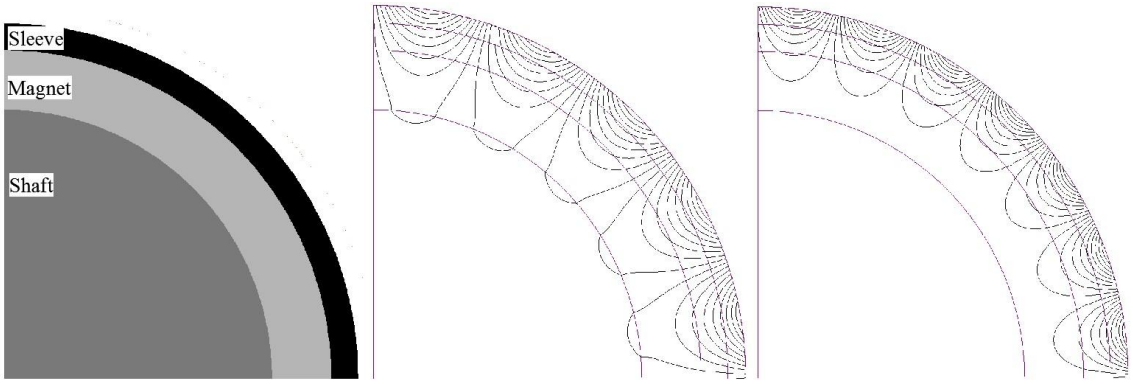

Figure 3-8: Magnetic Fields Associated with Harmonics

The frequency, f_n, of each harmonic is given by (3.14), which shows that each harmonic rotates at a rate slower than the fundamental field.

$$f_n = \frac{f_{mechanical}}{n} \qquad (3.14)$$

3.4.3 MMF Time Harmonics in the Air gap

The above analysis can also be performed with higher order current time harmonics, to define the magnitude and direction of their harmonic components. Noting that a 5th time harmonic will rotate relative to the rotor in the air gap of the machine at the same speed at the 5th space harmonic but with a pole pitch equal to the fundamental pole number. Furthermore, each time harmonic will also generate its own, even higher order space harmonics via the mechanism described in the previous section.

With the magnitude and rotational directions of the air gap harmonics defined, it is possible to analyse the losses caused by each and hence build up an estimate of the rotor loss of a specific design.

3.4.4 Eddy Current Loss Prediction

The information determined about the MMF harmonics in the previous section can be used to estimate the losses in the rotor caused by each harmonic. The losses are caused by eddy currents flowing in conductive components in the rotor due to the harmonics rotating asynchronously with the rotor. The magnitude of the losses can be estimated using a classical solution for the eddy currents induced in a plate by a current sheet presented by Stoll [33]; although certain assumptions are required and the prediction must be altered depending on the geometry of the rotor and its material properties. To simplify the analysis, it must be assumed that the rotor radius is sufficiently large compared to the magnet thickness, the air gap and the wavelength of the harmonics to allow the problem to be analysed in Cartesian coordinates rather than in polar coordinates; and that the machine is suitably long that the end effects can be ignored and a 2D analysis performed. The analysis requires the solution of simultaneous PDE's which is both more complex and lengthy in polar coordinates. The use of a Cartesian frame is a fair assumption as long as the ratio of the air gap length to rotor radius is sufficiently small that the curvature can be ignored, this generally holds true for High Speed High Power machines as the designer aims to maximise rotor volume using a large radius [33].

In [32] Stoll presents an analytical solution to the currents induced in a plate by a current sheet travelling parallel to the sheet and a defined distance from it; this is directly analogous to an H field travelling at the stator bore, above a set of magnets or other conductive components located on the rotor. As stated the rotor radius must be sufficiently large to assume it can be "unfurled" to sit on a Cartesian reference frame. Figure 3-9 illustrates Stoll's model and the equivalent rotor model used for the analysis. In this model a simple, although common, topology is chosen, which consists of full span surface mounted magnets mounted on a magnetically conductive shaft, the sleeve material is assumed to have zero conductivity in this case (i.e. a basic model of a composite) and can be treated as air, so is ignored in this model. The current sheet is represented by K_z travelling parallel to, and a distance b from, a plate of thickness d, the form of K_z is given in (3.15) taken directly from [32], where g is the pole pitch of the current and ω its speed relative to the plate.

$$K_z = \widehat{K}_z \cos(\omega t - \pi x/g) \qquad (3.15)$$

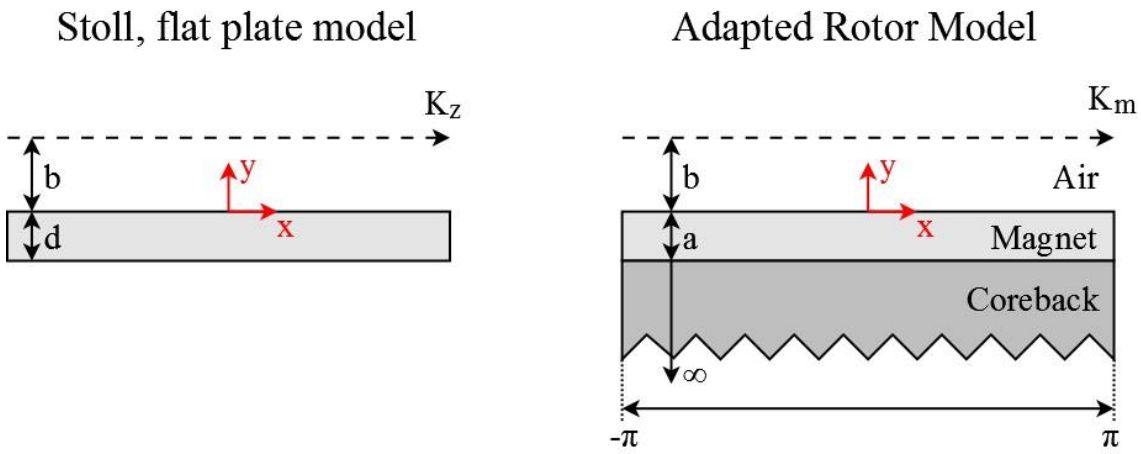

Figure 3-9: Equivalent Rotor for Current Sheet Model

The solution to the problem relies on solving the differential equation that defines the vector potential in a component, subject to the boundary conditions posed by the model and the assumptions made. From the vector potential, the current distribution J in any conducting components can be defined, which can then be integrated across the component cross section to give the loss density. The vector potential, A, in air is defined by Laplace's equation, (3.16), and by (3.17) in any conductive material, .

$$\frac{\partial^2 A}{\partial x^2} + \frac{\partial^2 A}{\partial y^2} = 0 \qquad (3.16)$$

$$\frac{\partial^2 A}{\partial x^2} + \frac{\partial^2 A}{\partial y^2} = \alpha^2 A \qquad (3.17)$$

Where:

$$\alpha = {}^{(1+j)}/_{\delta} \quad (3.18)$$

And:

$$\delta = \sqrt{({}^{2}/_{\omega\sigma\mu})} \text{(Skin Depth)} \quad (3.19)$$

The material conductivity is σ and the material permeability is μ, following the common definitions of these values.

The most significant assumption that must be made is that the stator material is considered to be infinitely permeable, which enables the field generated by the current sheet to pass perpendicularly through the sheet and hence provide a defined boundary condition at the stator bore. This assumption allows the stator geometry and material properties to be excluded from the

analysis and is a fair assumption given the large disparity in permeability between laminations and air.

The general solutions to (3.16) and (3.17) for the vector potentials A_i, in each material, i, for the model presented in Figure 3-9 are given below, the subscript A refers to the air gap, M to the magnets and C to the coreback.

For the air gap:

$$A_A = (C_A e^{qy} + D_A e^{-qy}) e^{-jqx} \qquad (3.20)$$

For the magnets:

$$A_M = (C_M e^{\gamma_m y} + D_M e^{-\gamma_m y}) e^{-jqx} \qquad (3.21)$$

And for the coreback:

$$A_C = C_C e^{\gamma_c y} e^{-jqx} \qquad (3.22)$$

Where:

$$q = \pi / g \qquad (3.23)$$

$$\gamma_i = \sqrt{\left(q^2 + {}^{j2}\!/_{\delta_i^2} \right)} \qquad (3.24)$$

The five constants C_A, D_A, C_M, D_M and C_C, are all to be found, based on the boundary conditions. (NB: the expected constant D_C in (3.22), based on the similar forms of (3.20) and (3.21), is forced to be zero by the condition that the coreback extends to $-\infty$ in the y axis, and so must prevent A_C from trending to ∞ also).

There exist several interface boundary conditions based on the continuity of flux density and felid strength at material boundaries, as defined in (3.25) and (3.26) taken from [32]. Where B_n is the flux denity normal to the material boundary, H_t is the H field tangential to the boundary and K is the surface current on that boundary. The subscript numerals define the values for materials 1 and 2 respectively.

$$B_{n1} = B_{n2} \qquad (3.25)$$

$$H_{t2} - H_{t1} = K \qquad (3.26)$$

Equations (3.25) and (3.26) can be combined with (3.17) and (3.27) to give (3.28) and (3.29),

$$curlA = B$$
$$divA = 0 \quad (3.27)$$

$$H_x = \frac{1}{\mu}\frac{\partial A}{\partial y} \quad (3.28)$$

$$H_y = -\frac{1}{\mu}\frac{\partial A}{\partial x} \quad (3.29)$$

By applying (3.28) and (3.29) to (3.20), (3.21) and (3.22) at the material boundaries, five simultaneous equations can be derived to define the five unknowns:

At the stator bore, using (3.30) at $y = b$:

$$\frac{q}{\mu_0}(C_A e^{qb} - D_A e^{-qb}) = \widehat{K}_z e^{j\omega t} \quad (3.30)$$

At the magnet surface, using (3.31) at $y = 0$:

$$C_A + D_A = C_M + D_M \quad (3.31)$$

At the magnet surface, using (3.32) at $y = 0$:

$$\frac{q}{\mu_0}(C_A - D_A) = \frac{q}{\mu_M}(C_M - D_M) \quad (3.32)$$

At the magnet-coreback boundary, using (3.33) at $y = -a$:

$$C_M e^{-\gamma_m a} + D_M e^{\gamma_m a} = C_C e^{-\gamma_c a} \quad (3.33)$$

And finally, at the magnet-coreback boundary, using (3.34) at $y = -a$

$$\frac{\gamma_m}{\mu_M}(C_M e^{-\gamma_m a} - D_M e^{\gamma_m a}) = \frac{\gamma_c}{\mu_C} C_C e^{-\gamma_c a} \quad (3.34)$$

The five equations, (3.30) to (3.34) can then be solved to find expressions for each of the five constants that are a function of the material properties, rotor geometry and the pole pitch and speed of the harmonic H field applied. With the vector potential defined fully throughout the model, the losses can be calculated using (3.35)-(3.37), were σ_i is the conductivity of the material, i, over which the integral is performed and V the volume of the material.

$$E = -\frac{\partial A}{\partial t} \tag{3.35}$$

$$J = \sigma_i E \tag{3.36}$$

$$P_{loss} = \int_V \frac{1}{2\sigma_i} |J|^2 dV \tag{3.37}$$

This analysis can be shown to have very close correlation with FEA predictions of the same effect. Figure 3-10 shows a comparison between FEA (using Infolytica Magnet) and analytical predictions for various harmonics, and also between Polar, and Cartesian FEA models and the Analytical model for varying geometries. It can be seen that the Analytical prediction provides a close approximation to FEA results, despite varying geometries, harmonic orders and field intensities.

The method presented for estimating the eddy current loss in magnets of a rotor can be expanded and modified for different geometries by placing additional material layers into the model shown in Figure 3-9. The number of unknown coefficients will increase, but the same method of comparing the fields at material interfaces can be used to generate sufficient simultaneous equations to define them. This would be required if a conductive sleeve or eddy current shield were to be included in the rotor. A reduction in magnet span can be accounted for by reducing the volume integral appropriately. The limitation of this analysis becomes apparent when the magnet shape is changed, only surface mounted arc shaped magnets with good electrical contact between pole piece and segments conform to the simplified geometry in Cartesian co-ordinates, other shapes would present too complex a geometry for simple analytical prediction, and would lend themselves to direct FEA analysis for the losses. However most HSHP motors use surface mounted magnets in some form, and indeed other geometries are less attractive from a stress-to-

magnetic loading point of view, as discussed in Chapter 2, which allows this method and model to remain relevant and useful for the rapid analytical prediction of losses during the initial sizing iterations of the design.

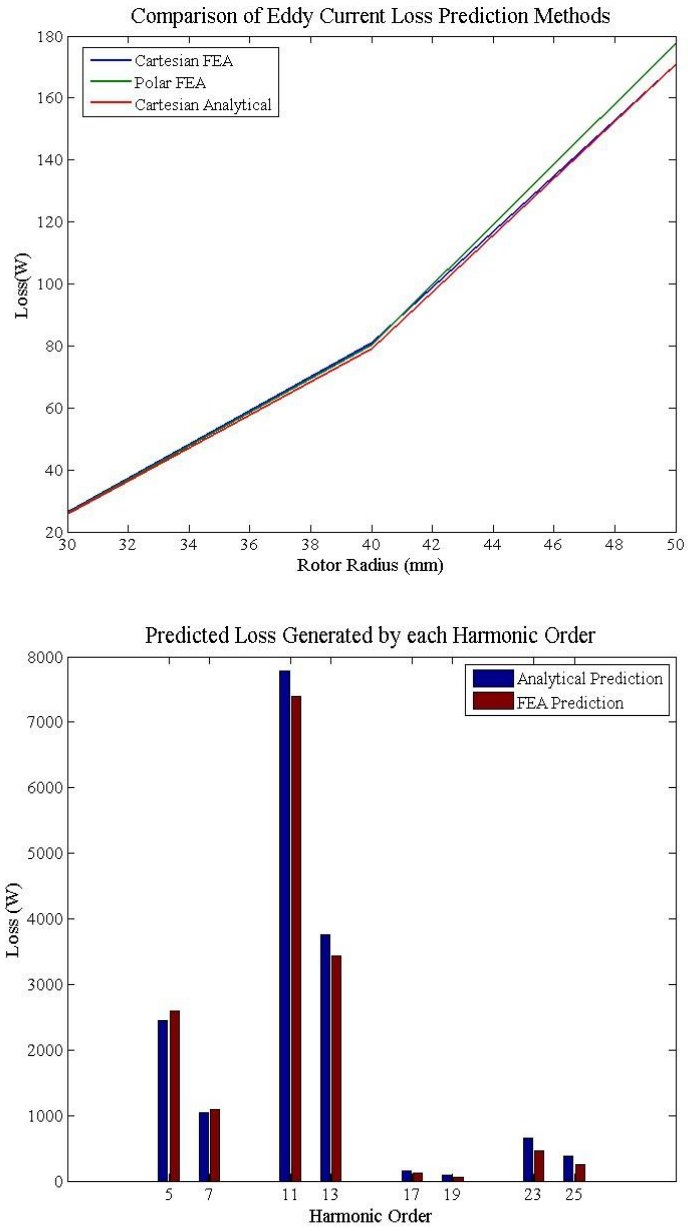

Figure 3-10: Comparison of FEA and Analytical Predictions for Eddy Current Loss

3.4.5 Rotor Loss Mitigation

As rotor losses are a major problem for PM machines working at high loadings and high speeds, techniques that can reduce the loss or distribute it are of particular interest to the High Speed

High Power machine designer. The techniques can be split into two strands, stator based methods and rotor based methods. Stator based methods are primarily focussed on reducing the harmonics present in the MMF waveform, via changing the winding design of the machine and altering the slot dimensions. Rotor side methods for reducing losses focus on reducing the effects of the harmonics by altering the conductivity of rotor components; these methods include magnet segmentation [37, 38], the use of eddy current shields [36, 56] and the use of bonded magnets which have very low conductivities [74].

The winding design of motors is a classical problem that has been tackled for various reasons throughout the history of motor design; either to reduce torque ripple, rotor loss or end winding sizes. There are many classic texts on winding factors however the design process is well summarised in [63]. For High Speed High Power motors a double layer distributed winding is preferable to create an MMF waveform in the air gap most like a sinusoid, in order to minimise the rotor losses. Distribution factors and pitch factors can both be used to damp the harmonics in the air gap. As noted in the previous analysis, altering the slot widths can give an additional benefit in reducing higher order harmonics, though this must be balanced against creating a significant ripple in the stator permeance that can lead to significant no load losses.

The rotor side techniques for minimising rotor loss are particularly useful to the machine designer; however their full effects are expensive to model during the initial sizing of the machine. It is of more use to investigate their effects of specific methods individually once the initial sizing is complete, if they are required.

Magnet Segmentation

As noted in [37, 38] segmentation of the rotor magnets can significantly reduce the rotor eddy current losses, by increasing the distance of the eddy current paths. The effect is maximised using axial segmentation which can dramatically increase the eddy current paths by adding additional circumferential return paths at each segment axial edge.

However, as noted in [38] there is an “anomaly of segmentation” whereby segmentation increases the amount of rotor loss caused by time harmonics. This anomaly is due to the large pole pitch of these harmonics (the same as the winding fundamental pitch) causing them to have a high depth of penetration into the rotor. The high frequency causes the eddy currents to flow in a skin at the magnet edges rather than on the magnet outer radial surface as happens with space harmonics. The skin effect limitation on eddy current flow produces a fixed eddy current MMF

per pole pitch; segmenting the magnets increases the path resistance for the eddy currents which, due to the fixed MMF of the total eddy current flow per pole, increases loss via the I^2R effect. This contrasts with the segmentation effect on space harmonics losses; the high pole numbers of space harmonic fields lead to a low depth of penetration in the rotor and low relative frequency so the skin effect does not occur. The eddy currents are thus unrestricted and flux driven rather than MMF driven, so increasing the path resistance via segmentation reduces their loss via the V^2/R effect. The effects of segmentation on time harmonic eddy currents are shown in Figure 3-11, it can be seen that segmentation constrains the time harmonic induced eddy currents to flow around the periphery of the segment in high concentrations while the space harmonic induced eddy currents are affected only by an increased return path distance at each axial segment end.

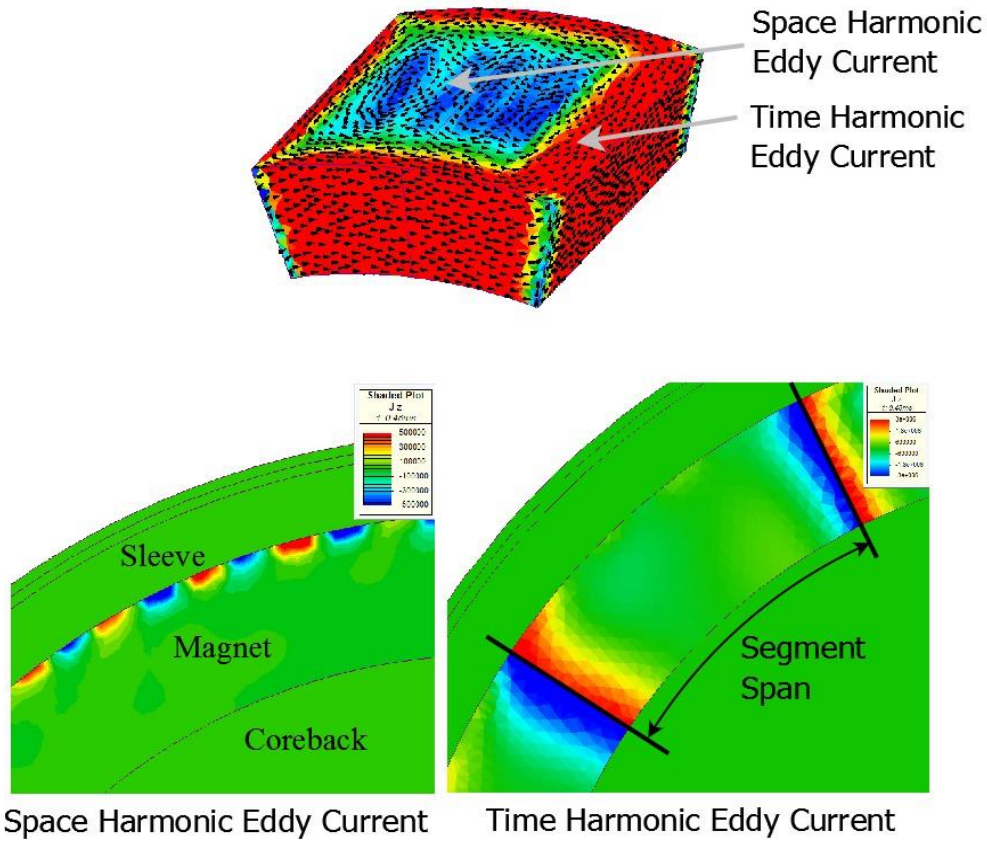

Figure 3-11: Effect of Segmentation on Eddy current paths

As the time harmonic eddy currents are skin limited by the high frequency, the additional surface area for their flow presented by magnet segmentation allows an increased loss overall, The governing equation (3.38) is presented in [38, 49] which dictates the power loss per component surface, which is independent of the component dimensions, where H_{tan} is the H field tangential to the surface and R_s is the surface resistance given by $1/\delta\mu$.

$$P_{surface\ area} = \frac{1}{2}|H_{tan}|^2 R_s \quad (3.38)$$

Segmentation of magnets therefore only acts to reduce the losses caused by time harmonics when the segment dimensions are smaller than the skin depth of the eddy currents; this can often be impractical for High Speed High Power machines, requiring segments dimensions that push the limits of manufacturing technology and safe handling, in addition to requiring many thousands of segments per rotor to be manually assembled, adding significant cost and time to the machine construction.

Thus for a High Speed High Power machine where significant time harmonics are expected in the phase currents, it is often counter intuitive to standard practice and design for the largest magnet segments possible, subject to the constraints of pole numbers and safe handling during assembly. It is common then, to require further design methods to reduce the losses in High Speed High Power machines, in particular the use of eddy current shields.

Eddy Current Shields

Because time harmonic induced losses increase with practical levels of segmentation, there is a strong case for preventing the interaction of the time harmonic fields with the magnets in the first place. One method for achieving this is via the use of an eddy current shield; this common rotor component has been well studied [36, 56] and is a proven method of preventing magnetic fields from entering the bulk of the rotor. It generally consists of a continuous cylinder of highly conductive material, such as copper or aluminium, placed close to the surface of the rotor, (generally between the retaining sleeve and the magnets). The shield operates by freely allowing eddy currents to flow, which in turn act to oppose the harmonic fluxes and prevent their penetration further into the rotor, where they would cause excessive loss in the magnets.

Losses are generated in the shield, where the high conductivity acts to reduce their impact, and can be significant though the reduction in magnet loss that can be achieved leads to a lower net rotor loss. The sizing of the shield is particularly important as noted in [32]. The thickness of a conducting plate relative to the skin depth affects the loss density; where thickness is less than the skin depth of the eddy current, the loss is resistance limited and rises with the cube of thickness, however when the plate thickness is much larger than the skin depth, the eddy current is skin limited and becomes constant, related to the skin depth, as described in (3.38). Thus for very thin eddy current shields, the opposing currents do not fully form due to the high resistance

and so allow some harmonic field to pass and penetrate the rotor causing loss. Too thick a shield would impinge on the air gap length and rotor stressing, affecting both torque density and mechanical strength. A complicated optimisation is required to find the optimum sleeve thickness that minimises net rotor loss without impinging on the mechanical or torque performance of the machine. For the initial machine sizing operations, the eddy current shield can be included by altering the model in Figure 3-9, to include a conductive sheet above the magnet. Finding the optimum shield thickness to balance rotor loss and magnetic performance requires FEA design iterations to assess the magnet losses and is best left until after the sizing; thus the designer should choose an initial shield thickness that is larger than the skin depth of the first time harmonic eddy current that will be induced in it (the 5^{th} in a balanced 3 phase system), ensuring that the opposing eddy currents are fully developed and the magnet time harmonic losses minimised.

The inclusion of an eddy current shield has an important effect on the machine equivalent circuit. The action of the eddy currents changes the magnetic circuit for the time harmonic fields, effectively acting like a damper winding and reducing their inductances to just the leakage inductance of the machine as described in [39]. This has serious implications for the performance of the drive electronics, the lower inductances seen by the harmonics makes them harder to control and it is common to see an increase in their magnitudes.

The effect of the shield on the harmonic fields is shown in Figure 3-12, on the left, the fundamental field rotates synchronously with the rotor and penetrates fully, whereas the screening effect of the shield prevents the 5^{th} harmonic from penetrating into the rotor and constrains it to a shorter magnetic circuit.

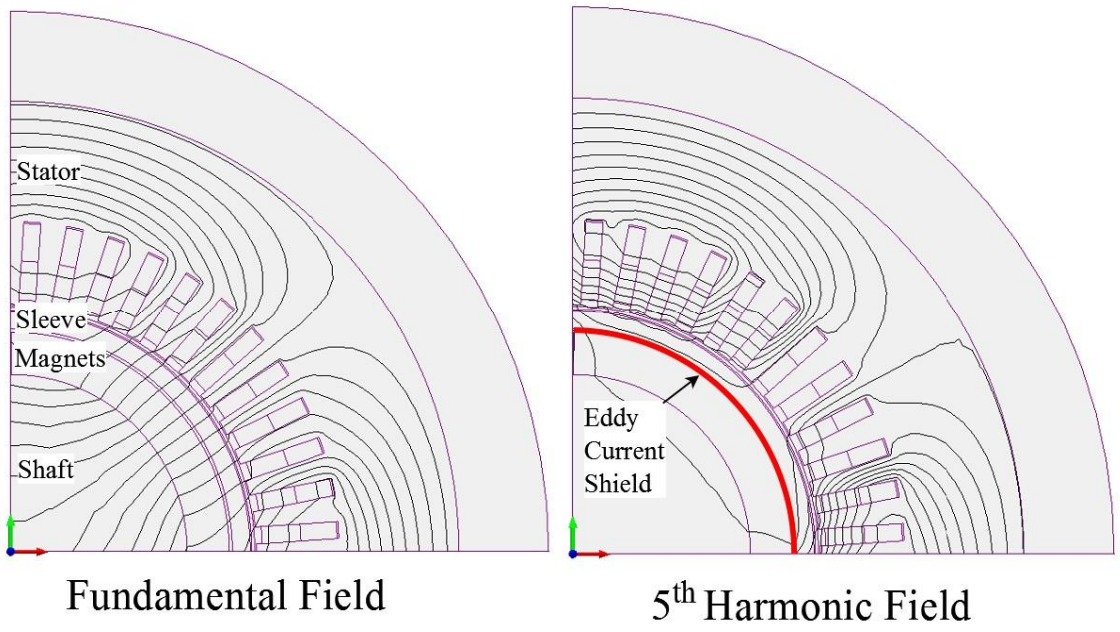

Figure 3-12: Effect of eddy current shield on harmonic fields

The effects of the shield can be measured by plotting the inductance vs frequency for the machine, deriving a plot similar to that shown in Figure 3-13. Frequency is shown relative to the rotor speed, i.e. 0Hz is synchronous with the rotor. There is a clear transition between low and high frequency inductances, associated with the transition from resistance to skin limited eddy currents in the shield.

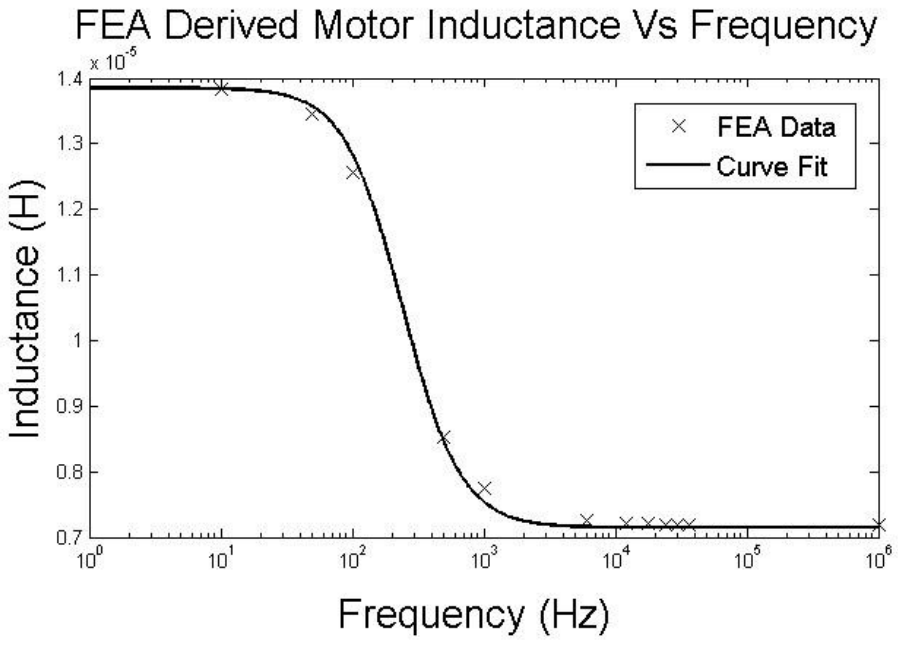

Figure 3-13: Machine Inductance Variation with Frequency due to Eddy Current Shield

The curve is similar to those seen in large wound field generators with damper windings, and can be modelled by including transient reactance terms in the motor equivalent circuit, [75, 76]. The value of the transient reactance can be determined from the inductance curve using standard techniques for Stand Still Frequency Response (SSFR) recommended by the IEEE [77]. The transient reactances can then be included in the motor model as shown in Figure 3-14, where R_s is the stator resistance L_l the leakage inductance L_a the magnetising inductance and R_k and L_k the transient resistance and inductance respectively. For the case of the eddy current shield, the transient inductance is very small and the transition to low inductance at high frequencies is dominated by the transient resistance; thus it can be seen that high frequency current harmonics completely bypass the magnetising inductance of the motor and only see the leakage inductance, which can be considerably lower than the combination of leakage and magnetising inductance seen by the fundamental current. Further terms could be included in the model to relate the effect of eddy current fields generated in the magnets altering the magnetic circuit for the harmonics; this would be analogous to the sub-transient response of large generators. However the dominating effect of the eddy current shield in screening the rotor from harmonic fields means that one, transient, term is sufficient to model the behaviour to a high degree of accuracy.

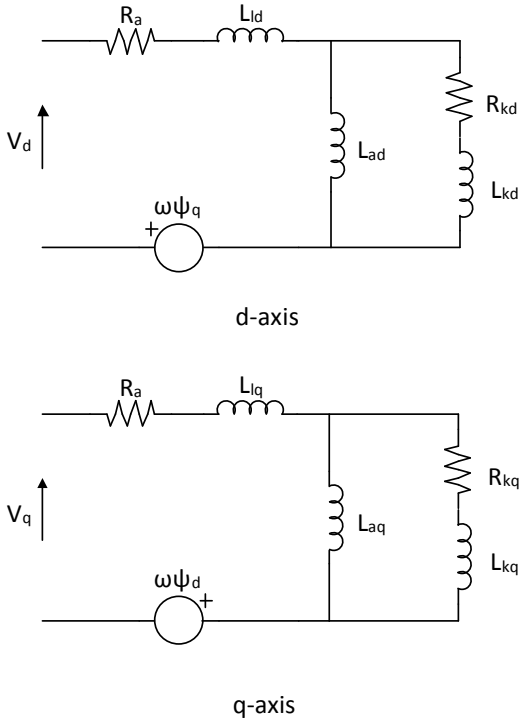

Figure 3-14: Equivalent d-q circuit with transient reactance

This interaction between motor and drive is a critical consideration when using an eddy current shield, as eddy currents in the magnets can similarly alter the inductance seen by various harmonic frequencies. The designer must consider this interaction when predicting rotor losses as it can lead to a significant error in the rotor loss if the drive model used to predict current harmonics does not include the transient reactance terms in the equivalent machine model. If the rotor loss is not adequately predicted an adequate cooling capability may not be designed into the system [39].

Bonded Magnets

A final solution to reduce magnet loss is to reduce the magnet conductivity by using bonded materials. Bonded magnets consist of powdered rare earth magnetic materials held in a polymer or epoxy matrix that effectively reduces the bulk conductivity of the magnet to zero; this is at the cost of the magnet strength, where the remnant flux density is typically 0.5-0.7T [78], and service temperature which is limited by the matrix material properties. The low strength generally renders these magnets unsuitable for High Speed High Power machines as it will significantly limit the torque density that can be achieved in the rotor, while the low operating temperature places additional strains on the cooling system design to ensure safe operating conditions.

There is an additional effect to be considered when eliminating eddy currents completely; without their screening effect the time harmonic fields penetrate uninhibited through the rotor to the coreback of the shaft which is typically a solid piece of soft magnetic steel to allow for strength and stiffness. Significant eddy current losses and loss intensities may then be generated in the coreback by these fields creating very large losses as the small skin depth of the fields in this conductive and permeable material will lead to high surface losses as per (3.38).

For these reasons the use of bonded magnets is undesirable in HSHP machines, and a combination of an eddy current shield to mitigate time harmonic losses and magnet segmentation to counter space harmonic losses, is the most desirable approach.

3.5 Stator Losses

3.5.1 Iron losses

The classical model for the losses in laminated ferromagnetic material under time varying magnetic fields, as proposed by Bertotti [79], separates the losses in the material into three components: hysteresis, classical (or eddy current) and dynamic (or anomalous) as shown in (3.39). The terms of the iron loss can be further related to the frequency and magnitude of the flux density variation in the material using the expressions in (3.40) [79-81], where K_h,K_e and K_a are coefficients for the Hysteresis, eddy current and anomalous loss components respectively and are determined by the material properties and geometry, as is the exponent α.

$$P_{Iron\ Loss} = K_h \hat{B}^{\alpha} f + K_e \hat{B}^2 f^2 + K_a \hat{B}^{1.5} f^{1.5} \tag{3.40}$$

The nature of this model requires the analysis of the losses caused to be performed in the harmonic domain, with each harmonic of flux density analysed individually based on it's frequency and peak value.

The accuracy of any prediction is furthermore dependent on analysing the nature of the flux variation, [80, 82] highlight the importance of considering the 2 dimensional nature of the flux variation in the plane of the laminations. The flux density vector in the iron cannot always be assumed to simply oscillate between peak and negative values along a single axis, but describes a circle or ellipse in various parts of the machine. Traditionally the flux can be seen to oscillate in the teeth of the machine whereas in the coreback the x and y components of the flux transcribe an ellipse during one period of oscillation [82]. This 2D variation in the flux density can be accounted for by decomposing the vector into two orthogonal components (3.41) [83] or by considering the vector magnitude of flux (3.42) for the analysis of Hysteresis and anomalous losses [84], where $\hat{\boldsymbol{u}}_{\boldsymbol{x}}$ and $\hat{\boldsymbol{u}}_{\boldsymbol{y}}$ are the x and y axis unit vectors respectively. For the values of B in (3.41) it is common to transform the axes locally to allow one flux density vector to lie in direction of the peak variation in flux (i.e. the longest axis of the ellipse described) and the other vector to lie normal to this, in the axis of the smallest variation [85].

$$B = B_x \hat{\boldsymbol{u}}_{\boldsymbol{x}} + B_y \hat{\boldsymbol{u}}_{\boldsymbol{y}} \tag{3.41}$$

$$|B| = \sqrt{B_x^2 + B_y^2} \qquad (3.42)$$

Given the complex variation of the flux density vectors in time and space and the variation of magnitudes seen in different locations of an electrical machine, a FEA method of estimating the iron loss is required to achieve the best accuracy [80], and is essential for High Speed High Power machines giving the high electrical loadings and frequencies encountered in their operation. The method in which a commercial FEA software package estimates iron loss is often closely guarded as the accuracy of any particular piece of software is a key commercial selling point; however analyses generally use the equation in (3.40) for estimation the losses on an element by element basis, per harmonic and considering the vector variation in flux density as described above [86]. The material dependent coefficients in (3.40) are determined by curve fitting the expression to supplied empirical loss data from the manufacturer of the material being simulated.

It is noted in [80] that a significant design factor is often required in industry when comparing actual iron loss performance versus that predicted by various iron loss calculation methods. In the work presented this factor is approximately 1.75x the predicted loss, which is a significant error; it is explained by the authors of [80] as being the result of manufacturing process such as stamping and welding causing significant alterations to the lamination material properties when compared to the manufacturers data and also due to machine design features, such as cooling ducts and end plates affecting the local material properties.

Some of the assumptions in the work are valid for High Speed High Power machines; welding and design feature effects are significant, and although the laminations of these machines are not often stamped due to the low production volumes, they are commonly cut using wire erosion which can locally affect the material properties at the cut edges. Furthermore, work by Takahashi [87, 88] has shown that the compressive stresses induced when fitting stators into their housings can significantly alter the material properties, raising the losses.

Given the overlap in loss altering mechanisms between the High Speed High Power machines and those analysed in [80] and the additional loss raising effects of fitting the stator into its housing, a prudent design factor of 2x the predicted loss should be used when considering the thermal design of an High Speed High Power machine. This large design factor also allows the designer to perform some simple analytical estimates of expected iron loss, based on separating the stator into tooth, tooth tip and coreback lumped regions, with an estimated homogeneous B field assumed within each region using a simple magnetic circuit approximation. Using this model, the design factor and (3.40), a rough estimate of expected iron loss can quickly be

determined during the iterative sizing process which will be of a similar order of magnitude as that predicted by FEA and will allow an early design decision on the lamination grade to use and the degree of coreback saturation to be designed.

3.5.2 Copper losses

The copper losses in HSHP machine are associated with power dissipation in the armature windings of the machine, but are not purely limited to resistive losses; the high frequency nature of the machines and the high current densities in the windings lead to skin and proximity effects, causing significant additional loss in the windings. The losses in the windings of a machine can then be split into two components:

1. AC losses due to the high frequency proximity and skin effects of the currents in the conductors.
2. DC losses due to the resistance and RMS current flow in the conductors.

The skin effect describes the tendency for high frequency currents to flow close to the surface of a conductor, the depth of the current sheet being defined in (3.19); if the conductor diameter is less than twice this skin depth, then the effect can be ignored. The proximity effect is caused by the current flows in adjacent conductors influencing each other via the magnetic fields they generate, the magnetic field generated by the current flowing in one conductor, constrains the current flow in the adjacent conductor to certain regions and vice versa. The effect is illustrated in Figure 3-15 for two conductors, with the current either flowing in same or opposite directions. First the time averaged magnetic field is shown, with the current distributions due to the alternating magnetic field (shaded plot) shown below, red shading represents current flow into the page and blue out of the page. If the conductors are in the slot of a machine, then the slot leakage field drives the proximity effect, as shown in Figure 3-16.

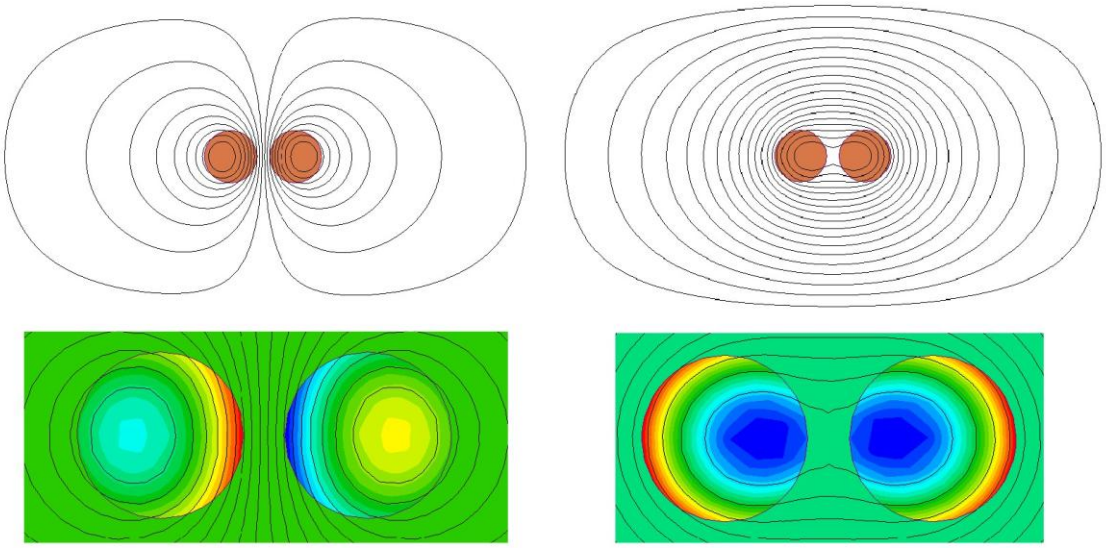

Figure 3-15: Field and Current Distributions of two Adjacent Conductors

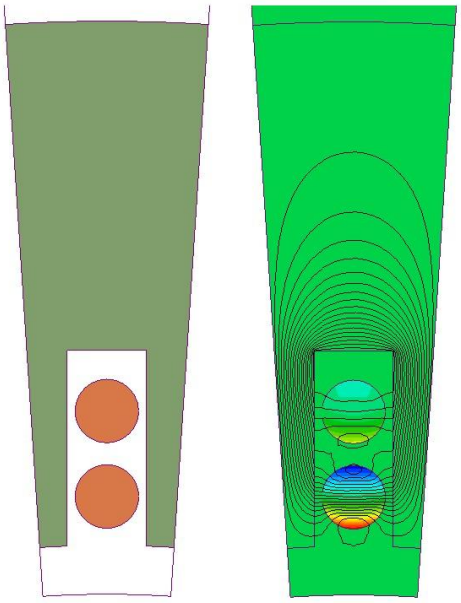

Figure 3-16: Effect of Leakage Field on coil Current Distribution

The analysis of this effect and a method for prediction of the associated AC losses in round conductors is presented in a classic paper by Sullivan [89]; the losses in a coil due to an external field are derived (3.43), from this the designer can predict the AC losses in an individual conductor due to the effect of all the other conductors in a winding and hence work out the average total conductor loss P_{total} by combining it with the DC loss as in (3.44), where d_c is the conductor diameter, l the conductor length, ρ_c the conductor resistivity, $i(t)$ the current flowing

in the conductor, T one period of the waveform analysed and B the flux density in the conductor, assumed perpendicular to the conductor axis. The value of d_c should remain less than 2 times the skin depth of the current frequency under analysis, to enable the average of B across the conductor to be used and avoid the need to estimate the effects of skin eddy currents on the field distribution within individual conductors.

$$P_{AC}(t) = \frac{\pi l d_c^4}{64\rho_c}\left(\frac{dB}{dt}\right)^2 \tag{3.43}$$

$$P_{total} = \frac{1}{T}\int_0^T \left(P_{AC}(t) + \frac{4\rho_c l}{\pi d_c^2} i^2(t)\right) dt \tag{3.44}$$

The analysis presents a generalised method for estimating the AC losses in a group of conductors based on the Squared Field Derivative method which derives a spatial average of the flux density in the windings and calculates an average loss. For the design of HSHP machines it is of more use to analyse each conductor individually, which allows the designer to identify loss concentration within the winding rather than a bulk average loss provided by the Squared Field Derivative method. For finely stranded wire bundles this may appear a daunting task, however a simple computational method will be presented to predict the loss distribution of a slot.

Using a similar analysis to that presented in Figure 3-3, the leakage field across a slot at a given depth z, from the coreback can be related to the current distribution within the slot using Amperes Circuital Law (3.8) and Figure 3-17 for a slot with no closure at the tip. In this model, the MMF within the slot is assumed to be evenly distributed across the slot cross section, a reasonable assumption for a well filled slot using stranded wire, giving a uniform current density distribution, J. The depth into the slot from the coreback of the slot is defined as z. The flux density crossing the slot, parallel to the slot opening at a depth z is then defined from the area of the slot enclosed and the slot width, w, as in (3.45).

$$B(z) = \frac{\mu_0 \times MMF\ enclosed}{slot\ width\ at\ z} = \frac{\mu_0 J w z}{w} \tag{3.45}$$

For the rectangular slot shown in Figure 3-17, (3.45) reduces to (3.46),

$$B(z) = \mu_0 J z \quad (3.46)$$

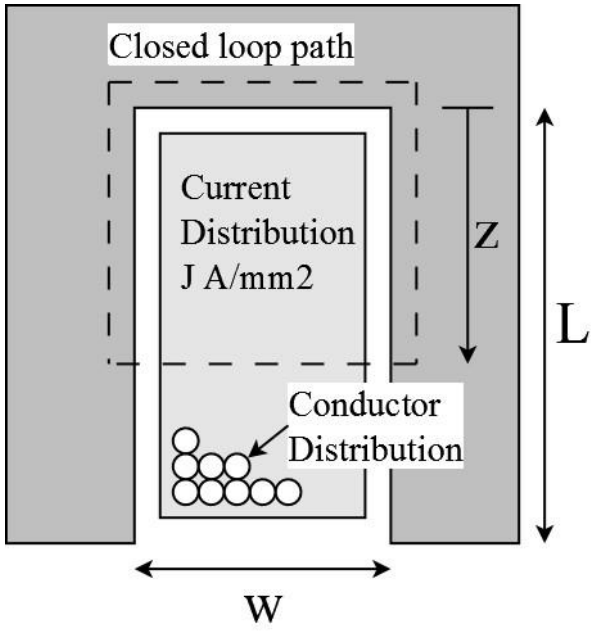

Figure 3-17: Variation of leakage field across slot due to current distribution

For other slot geometries, the slot width can be defined as a function of z, for example a tapered slot (parallel teeth) the expression for width of the slot would take to form shown in (3.47), where w_{max} is the maximum slot width, at the base of the slot and m is the gradient of the slot taper.

$$w(z) = w_{max} - mz \quad (3.47)$$

If the conductors are assumed to lie in layers ,as shown in Figure 3-17, the instantaneous AC loss in each layer, m, due to a sinusoidal current of frequency ω can be calculated as per (3.48) for a rectangular slot where N_m is the number of conductors per layer and z_m is the depth of conductor layer m in the slot.

$$P_{AC,m}(t) = \frac{N_m \pi l d_c^4}{64 \rho_c} \left(\frac{dB_m(t)}{dt} \right)^2 \quad (3.48)$$

$$B_m(t) = \mu_0 \int z_m \sin(\omega t) \quad (3.49)$$

The total slot loss can then be calculated from the sum of all layers, and the average loss from (3.44), where $T = 2\pi/\omega$. This method lends itself to a harmonic analysis, where an arbitrary applied current waveform is broken down into its harmonic components, and the loss generated by each harmonic can then be analysed individually, before summation to find the total slot loss.

Further modifications to the model can be made if a double layer winding is being used and the coils of two different phases are being used, by splitting the analysis into sections for each coil, assuming they are arranged vertically or by averaging the MMF from both coils if they are arranged side by side in the slot (as in a single tooth winding).

This analytical method can provide a very close approximation to FEA results without the need to build complex models or solve them with the fine meshes required to accurately model skin type effects in conductors. The following example highlights the accuracy of the above method; for a sample machine slot, shown in Figure 3-18, with 72 conductors in 36 staggered layers. The slot MMF is 838.5A and the frequency 1000Hz, the conductor diameter is 1.215mm (skin depth is approx 2mm).

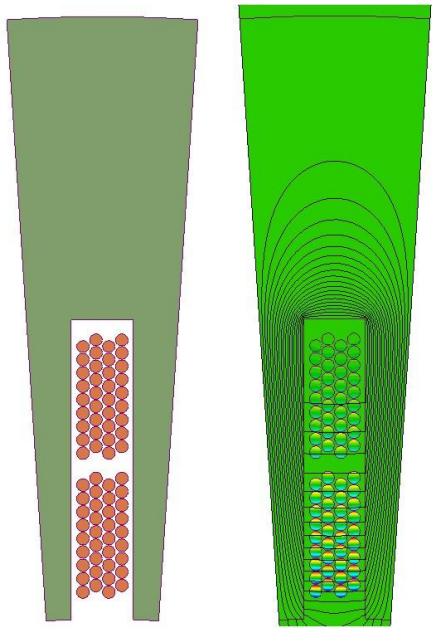

Figure 3-18: FEA model for slot AC loss

It can be seen from Figure 3-18 that the leakage field strength increases linearly towards the slot opening, leading to increasing levels of AC loss in the conductors near the opening. The analytical estimation of losses is compared to those extracted from the presented FEA model and given in

Figure 3-19, which shows that both methods give almost identical results, layer one is considered to be at the base of the slot and exhibits only DC loss, whereas layer 36 is closest to the slot opening and exhibits the greatest amount of loss as it inhabits the region of greatest leakage flux variation. The total FEA AC and DC loss estimation for the slot is 98W whereas the analytical estimate is 97.25W, an error of 0.8%.

The advantage of the proposed model for the designer of a HSHP machine is that it allows rapid estimations of the associated losses from different slot geometries and winding designs and the required level of stranding required to minimise the AC losses for a given current waveform from the drive. The accuracy of the described analytical model begins to suffer when slot closure features are included, as the fringing fields between the tooth tips affect the flux density concentration near the slot opening and it can no longer be estimated as 1 dimensional using (3.45). To overcome this error it can be assumed that either the conductors will not be placed in this region of high leakage flux, as it would cause un-necessary AC losses, or if this is unavoidable a single magneto static FEA solution for the slot field distribution with unit currents can be performed to define the relationship between B in a conductor and the currents applied.

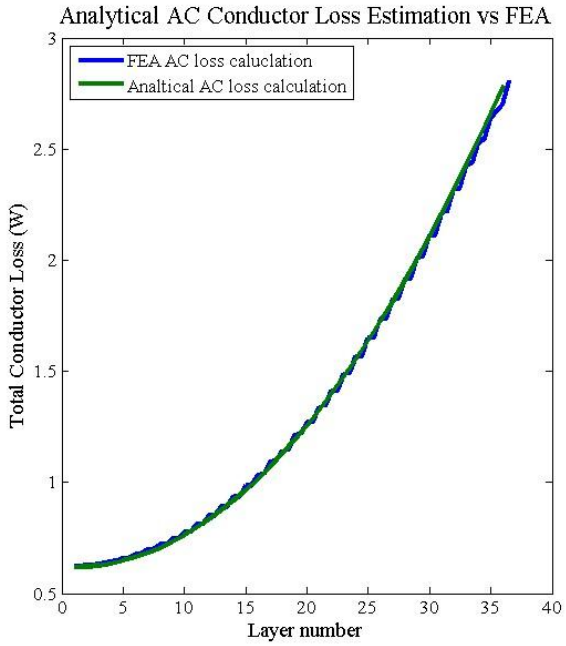

Figure 3-19: Analytical AC conductor loss estimation vs FEA

With the total winding power loss calculated, it is possible to derive the AC resistance for the winding (3.50), which from (3.44) can be seen to be frequency dependent, so must be worked out for each current harmonic present in the windings.

$$R_{AC} = {P_{Total}}/{I_{RMS}^2} \quad (3.50)$$

Using the effective winding AC resistance per harmonic, the designer can quickly predict the losses caused in a given machine design based on the expected current waveform from the drive that will be used. It is important to note that the proposed technique will tend to over predict the losses in the winding and hence the effective AC Resistance due to the effect of the end windings of the machine. The concentrating effect on the leakage field of the slot iron around the conductors causes the AC loss to be more pronounced within a slot than in the end windings, which sit in a lower strength magnetic field. Thus the AC resistance of the windings must be moderated by the ratio of the length of the windings in the slot to the length of the end windings where the effective AC resistance is comparable to the DC resistance [90, 91]. When considering the thermal model for the machine, this difference in loss intensities between the in-slot winding length and the end winding length must be accounted for. A bulk end winding loss based on the effective AC resistance will under predict the loss intensity in the slots as it assumes an even distribution of losses which in turn will lead to an under prediction of the winding temperatures in the slot and over prediction of those in the end windings. Whilst the above proposed method for quickly calculating the AC winding losses using an effective AC resistance is useful in the initial machine sizing to gauge the differences between different winding designs, a more accurate method will be required for iteration with a thermal model to gauge the operating temperatures. This can be achieved by a slight modification to the existing method, the losses 'in-slot' within the windings can be calculated using (3.44) and applied within the slot of the thermal model; whereas the end winding losses can be assumed to be DC only due to the lower leakage and fringing flux densities in this region.

An important feature of the AC and DC losses in conductors that must be considered in the design of HSHP machines is the variation in material resistivity with temperature. The temperature coefficient of resistivity for copper, α_ρ, is $4.29 \times 10^{-3} K^{-1}$; for a temperature rise of $100^o C$ the resistivity of the conductors increases by 43% which gives an associated rise of 43% in the DC losses in the winding. It is common for HSHP machines to operate at high temperatures to achieve a power dense solution, and the windings can operate at temperatures up to $200^o C$ above ambient, thus it is vitally important to accurately estimate the winding losses at the expected operating temperature, and not at a reference temperature such as ambient. To do this, close coupling and iteration is required between the electromagnetic and thermal design, to accurately estimate the slot temperatures and hence the expected losses in the conductors which

in turn will require the slot temperatures to be amended. One notable feature of the temperature variation in resistivity is that the AC losses in the windings are inversely related to the resistivity of the material, as seen in (3.43); this is advantageous to the machine design as higher operating temperatures act to damp the AC losses in the windings, and is an important feature to be considered in the electromagnetic-thermal design iteration. This beneficial effect is summarised in [90].

3.5.3 Stator Loss Mitigation

Iron loss minimisation

It is attractive to minimise the iron losses in HSHP machines in order to reduce the load on the cooling system; the most straightforward method available is to use thinner electrical steels, which have reduced eddy current losses at lower thicknesses. Alternatively the designer can move away from traditional silicon electrical steels and use cobalt or nickel iron [92] which have been shown to allow lower losses from the same machine geometry or a higher power density for the same loss level with respect to high speed machines. However it must be noted that these steels do present challenges due to their difficulty to manufacture and handle and their high costs compared to standard silicon steels. Thus, in an industrial setting, the choice of which type of steel to use will be largely driven by price, so favouring the silicon steel options, unless losses with silicon steel are prohibitively large, so that the more exotic steels are required to achieve a thermally sound design.

Copper loss minimisation

The use of copper as a conductor for electrical machines is almost universal, primarily due to its low resistivity, the only notable exception being the use of aluminium when loss-to-weight ratios and unit costs are important and high temperature superconductors in the field windings of experimental generators. It can be seen from (3.48) that the AC loss component of winding loss is heavily dependent on the diameter of the conductor, if the RMS current density for a machine design is assumed fixed and initially chosen based on a given cooling technology [40], it is vitally important for HSHP machines to strand individual turns to minimise the contribution of

AC losses to the DC component for which the current density rating is specified, lest the cooling capacity of the design be exceeded. The low turn numbers and high phase currents commonly encountered in HSHP designs would cause single strand conductors to be excessively large, for example, a two turn machine would have a slot cross section similar to that seen in Figure 3-16, which can be seen to have a very poor slot fill factor and would be expected to have a very high AC loss component.

Choosing a design with multiple strands per conductor introduces further design implications, if the same 2 turn design in Figure 3-16 was replaced with a multi stranded design as seen in Figure 3-18. There are still two turns but now 36 strands per turn, a better fill and thermal path can be achieved and the AC loss component will be dramatically reduced. The degree of reduction in the AC loss is described in (3.51), if the same copper area (RMS current density) per turn is maintained and n describes the number of strands per turn.

$$P_{AC}(t) \propto {}^{1}/_{n} \quad (3.51)$$

While multi-stranding each turn is clearly a beneficial option, providing the potential for a dramatic decrease in the AC losses, there are additional magnetic implications for adopting this feature. From Figure 3-18 it can be seen that individual strands within one turn are located at different points within the leakage field of the slot; those strands closer to the slot opening have a higher degree of leakage flux linkage than those deeper in the slot. Given that the strands of a turn are connected in parallel, this imbalance between strands will lead to imbalances in the current flow between strands and can cause circulating currents to flow between strands due to the differences in strand potential, which will adversely affect the AC loss component. These effects are traditionally compensated for by the use of Litz wire, in which the strands of each turn are bunched, twisted and then transposed throughout the turns cross-section along it's length. This spatial transposition acts to average out the leakage flux linked by each strand, so minimising the current imbalances and circulating currents between each strand. Litz wire typically comes in bundles of 7 strands arranged as shown in Figure 3-20, known as type 1, where the spatial transposition is achieved by twisting. Larger groups of strands are built up of sub groups of type 1 arranged and twisted to maintain the spatial transposition. Of particular interest to HSHP machine design is rectangular shaped litz ('type 8') in which the bundles of type 1 litz are compressed into a rectangular pattern and transposed in a fashion similar to that seen in the Roebel bars in large generators [93] as shown in Figure 3-20. This layout gives a group of finely stranded conductors, with a high fill factor in a shape that is easy to wind into a

parallel slot machine. The transposition of each bundle removes the bundle level effects (circulating currents) described in [94], leaving only strand level effects.

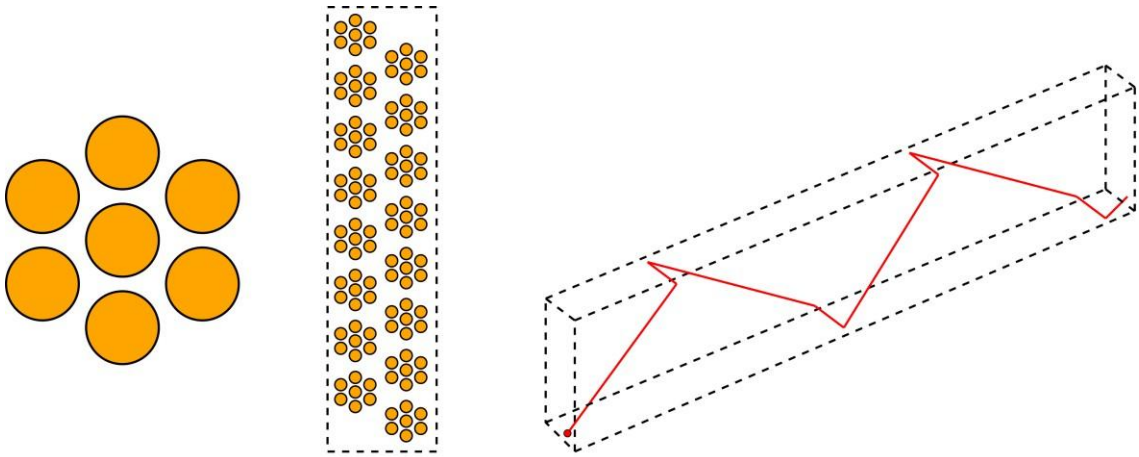

Figure 3-20: Litz Wire Types and Arrangement

The main drawback to the use of type 8 litz wire is that the transposition can significantly increase the length of each turn, as can be seen in Figure 3-20, where each bundle in the type 8 arrangement travels along a path much greater than that of the turn. This effect must be considered when selecting the degree of stranding required and its effect must be balanced against the savings due to reduced proximity losses and the elimination of bundle level circulating currents that would be present without the transposition.

3.6 Other Losses

3.6.1 Windage

Given the high rotor speeds and large rotor diameters found in HSHP machines, windage losses in the machine can be significant. The losses arise from a shearing stress present in the fluid that fills the air gap between the moving rotor and stationary stator; the shear, combined with the rotational motion, delivers a power loss into the air gap fluid which is supplied by the rotor and hence acts as a drag that must be powered by the supply. The power generated by the drag is

absorbed as heat into the rotor and stator surfaces in contact with the air gap. Analytical work on predicting this drag force [18, 95] for electrical machines stems from the analysis presented in [41], which builds a basic equation for power loss in the air gap of an alternator from first principles. The equation for power loss is given in (3.52) where ρ is the density of fluid in the air gap of the machine, r the rotor outer radius, ω the angular velocity, L the axial length of the air gap and C_d the coefficient of drag for the air gap. At low speeds flow in the air gap can be considered laminar and C_d is given in (3.53) where Re is the Reynolds number of the fluid in the air gap given by (3.54), where t is the air gap radial distance and υ the kinematic viscosity of the fluid.

$$P_{drag} = \pi C_d r^4 \omega^3 L \quad (3.52)$$

$$P_{drag} = \pi C_d r^4 \omega^3 L \quad (3.53)$$

$$Re = \frac{rt\omega}{\upsilon} \quad (3.54)$$

It is much more likely that the fluid flow in the air gap of the machine will be turbulent due to the high speeds encountered, the transition from laminar flow to turbulent flow of a fluid flowing in a channel is generally accepted to occur when the Reynolds number is in the region of 2000-13000, though for any system it is highly dependent of fluid properties and the roughness of the channel and the shape of the channel entrance. If flow is turbulent then the C_d is defined by the expression (3.55) from [41] which has been determined experimentally.

$$\frac{1}{\sqrt{C_d}} = 2.04 + 1.768ln\left(Re\sqrt{C_d}\right) \quad (3.55)$$

It can be seen that the drag is a function of air gap length, but as [41] notes, it is only a weak association, where large increases in air gap length only deliver small reductions in power loss. It is still reasonable for a first pass estimate to aid in the initial sizing of the machine to assume air gap windage losses dominate the total rotor drag losses and can be considered in isolation. The complex geometries of High Speed High Power shafts and the variations in air gap found outside the rotor active length render it difficult to produce a simple prediction for the drag associated with these features. However their short axial length compared to the active region and the significantly larger air gap above them is sufficient to assume they will be small compared to the

active length drag losses. More accurate predictions can be achieved with a Computational Fluid Dynamics analysis; however the computational and engineering cost of such analysis would only justify its use for validation once a prototype design and rotor topology has been determined.

An important additional consideration for predicting the air gap windage of HSHP machines is the effect of forced ventilation on the air gap losses. This can be included in the analysis by modifying (3.52) and (3.54) to express the drag in terms of absolute fluid velocity rather than the rotor angular velocity, to give (3.56) and (3.57) where v_{airgap} is the airgap fluid velocity defined by (3.58)

$$P_{drag} = \pi C_d r v_{airgap}^3 L \quad (3.56)$$

$$Re = \frac{t v_{airgap}}{v} \quad (3.57)$$

$$v_{airgap} = \sqrt{(r\omega)^2 + (v_{axial})^2} \quad (3.58)$$

The value for v_{axial} can be calculated from the through ventilation volume flow rate and the air gap cross sectional area; however it can often be difficult to know what the axial flow rate will be during the initial sizing. This is because it is dependent on the pressure generated by the through ventilation pumping system and the flow resistance of the entire forced ventilation system (in particular the losses associated with the entrance and exit of the coolant fluid from the machine casing), which is often not fully known until the later stages of prototype design. Thus for an initial sizing the prediction in (3.56) should be considered as sufficient as a prediction of the drag losses that must be powered by the machine. For estimating the effect of drag losses on thermal performance it may be assumed that the air gap forced ventilation is sufficiently effective enough to remove all the windage heat generated by its own axial flow in the air gap with spare capacity to extract heat from the rotor and stator, otherwise there would be little point in including the additional engineering cost of including a forced ventilation system. Once an initial machine sizing is complete, detailed analysis can be performed using (3.56) and estimates for the through ventilation flow rate, machine casing design and anticipated through ventilation system capacity.

3.6.2 Bearing Friction

The design of the bearings to support a large HSHP machine is complex and application specific. Within this design an estimate for the bearing loss must be computed in order to ensure they do not over heat. The interaction of this loss with the machine must be considered in the final machine thermal design but its derivation is outside the scope of this work. A common solution for mechanical bearings is to provide them with their own cooling and lubrication support system, which acts to extract the losses generated and allows the bearing losses and temperatures to be considered in isolation from rest of the machine. The only associated overlap is the effective ambient temperature seen by the bearings system, which will be dictated by the machine operating temperature and cooling methods. The bearing support system will be designed with an ambient temperature requirement for the casing it is mounted into, which in turn must be estimated for the HSHP machine being designed.

Analysis of this interaction is not required for the initial sizing of the machine, however should be considered during the detailed design, once the initial machine topology is identified.

3.7 Tolerances

Given the low inductance nature of the machine, and the low overall drive voltage headroom available for this type of HSHP machine, the effect of tolerances on the machine back EMF and inductance are highly significant. Variations in the manufactured machine air gap, leakage between magnet segments, lamination permeability and magnet remanence can all cause the EMF and inductance of the machine to vary from the design point. It is thus prudent for the designer to consider how these variations will affect the performance of the machine; for example if the back EMF was 10% below the design point specified the current required to achieve rated torque will be 11% higher, with an associated 23% increase in copper loss. Additionally, given the analysis presented in section 3.2, the machine may not be able to achieve the rated power if enough drive voltage headroom is not left in the design, as the new operating point is no longer at the point of maximum inductance headroom. The low drive voltage headroom required to achieve the rated power of High Speed High Power machines leads to them being especially vulnerable to variations in the machine inductance; if it is too high there will not be enough drive volts to supply the rated current at full speed and the power capability will be curtailed.

Given the large cost and engineering effort required to produce an HSHP machine, it is not acceptable to scrap or reject it if it does meet the design requirements and hence the designer must allow for these tolerance variations in the design process As a worst case scenario, a variation of ±10% in the values of back EMF and inductance should be considered throughout the design process.

3.8 Combining electromagnetic and mechanical design space

With the electromagnetic constraints detailed, it is possible to combine the electromagnetic and mechanical design spaces to find an initial sizing for the machine being designed. Taking into account the constraints outlined in sections 3.1 and 3.2 the designer must select appropriate pole number, EMF requirements and windings based on the available drive electronics. These parameters can then be combined with an initial mechanical rotor design using the principles outlined in chapter 2 to create an estimate of the required rotor volume to achieve the rated back EMF. This estimate can be derived from the simple machine design equations outlined in [63] for a PM machine, and allows the rotor length to be defined as a function of radius. More complex methods of calculating machine parameters are eschewed at this stage for speed and simplicity. The modified version of the equations presented in [63] is given in (3.59), and can be used for a rapid initial sizing of the machine; where E_{phase} is the design RMS phase-to-neutral voltage, k_w is the winding factor of the machine, $\hat{B}_{fund}$ the fundamental peak air gap flux density, N the turn number per phase, ω_{mech} the mechanical frequency r the rotor radius and l_{stack} the rotor active length.

$$l_{stack} = \frac{\sqrt{2}E_{phase}}{rk_w N\hat{B}_{fund}(r)\omega_{mech}} \qquad (3.59)$$

For a given design, (3.59) can be plotted in the same design space as the mechanical constraints to give a curve of required rotor dimensions to achieve the rated performance of the machine as shown in Figure 3-21. Many design choices go into generating the curves in Figure 3-21; for example magnet and sleeve thicknesses affect both the electromagnetic and mechanical curves, while the choice of slot numbers, winding design, air gap length and current loading all dramatically affect the position of the electromagnetic design curve.

Of particular importance is the fact that the air gap flux density is a function of rotor radius, due to the relationship between magnet thickness and sleeve thickness in the mechanical design, leading to a variation in magnetic loading with changing radius. An attempt to maintain a constant magnetic loading over a wide range of rotor radii can be made by keeping the magnet and sleeve thicknesses fixed in proportion to one another. This complements the mechanical design process, which holds both these values proportional to the rotor radius to simplify the relationship between rotor stress and radius. While this action helps maintain the magnetic loading approximately constant across all radii, the effect for the fixed air gap size between rotor and stator begins to affect this relationship significantly. At large rotor radii, the air gap length is small compared to the sleeve thickness and his has only a small influence on the reluctance seen by the magnetic circuit, however at lower radii, the air gap represents a significant reluctance that the magnets must drive across, leading to a worsening of the magnetic loading for small radii machines. This effective fixed offset in the reluctance circuit could be included in the magnet thickness scaling with rotor radii, but would begin to affect the proportional relationship between rotor stress and radius at small radii. The choice of which relationship to hold proportional is left to the designer.

The effects of varying the electrical loading of the machine can be seen in Figure 3-22, for a fixed rated torque and speed; curve 1 represents a high electrically loaded design – typically achieved by having a high MMF per slot – which only requires a small rotor volume to achieve the rated torque. Curves 2 and 3 represent progressively lower electrical loadings, thus requiring larger rotor volumes for the rated torque whereas the electric loading represented by curve 4 is too low to achieve the rated torque from the rotor volume that is mechanically achievable at the rated speed.

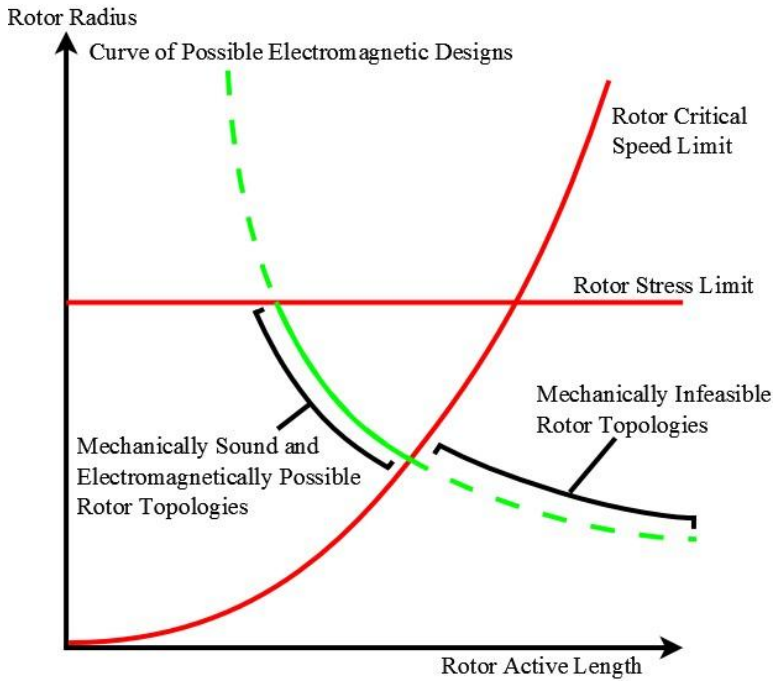

Figure 3-21: Rotor Design Space

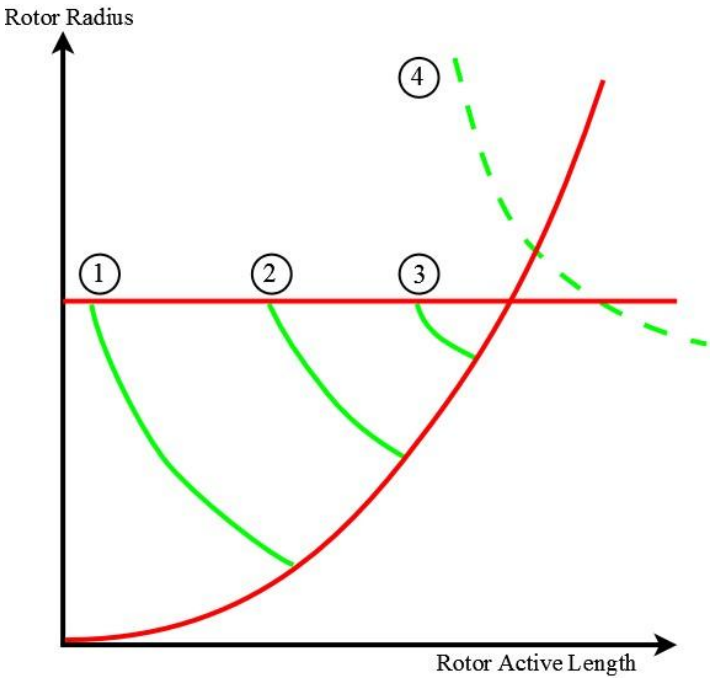

Figure 3-22: Effect on Design Space of Varying Electric Loading

For any point on a given electromagnetic design curve is it possible to specify a full machine design given a target current density (based on the anticipated cooling methods), for which the performance and losses can be predicted using the analysis presented in this chapter. This design method allows the designer to quickly assess whether the winding design, loading and rotor design deliver a feasible electromagnetic, thermal and mechanical machine design and allows rapid iteration through design changes if it does not.

3.9 Conclusions

The challenge for HSHP machine design lies in marrying the low electrical loading required by the available drive capabilities with the rotor volume limitations created by high speed operation. As noted earlier in this chapter, the low drive voltages used for these machines limit the inductance of the design which is achieved though having a low electrical loading; this coupled with the high phase currents required to achieve the rated power, leads to a very low turn number design. In order to achieve the required machine inductance it can be a challenge to ensure that the electromagnetic design curve intersects the possible mechanical design space. To compound the difficulty in achieving a viable design, the low turn numbers cause the electromagnetic design curve to shift position significantly with each design change. For example, an achievable mechanical design might require two turns per phase, however this could lead to the electric loading being too high for the inductance limit placed by the drive, to reduce the loading, the turns would normally be reduced, however this would lead to a doubling of the rotor volume required to achieve the rated torque, which could easily push the required rotor dimensions outside the mechanical design space. This effect is illustrated in Figure 3-23, showing the change in design curve when moving from two turns to one, where for a given radius the required active length doubles.

The low numbers of turns have significant additional effects on the dependent machine parameters such as losses and thermal performance, which are defined by the chosen rotor dimension and the target current density. The low available turns limit the winding design options, which can lead to significant rotor losses and render the design unviable. The design would also be expected to have only a few slots, with a large cross sectional area of copper per slot, which creates a poor heat path for removing winding losses. To counter these effects it is common to use parallel winding paths in HSHP machines, to allow a lower current per strand and a more sophisticated winding design, as each strand or a turn can be distributed and pitched as required, providing their inductances and potentials are balanced, as discussed in section 3.2.3.

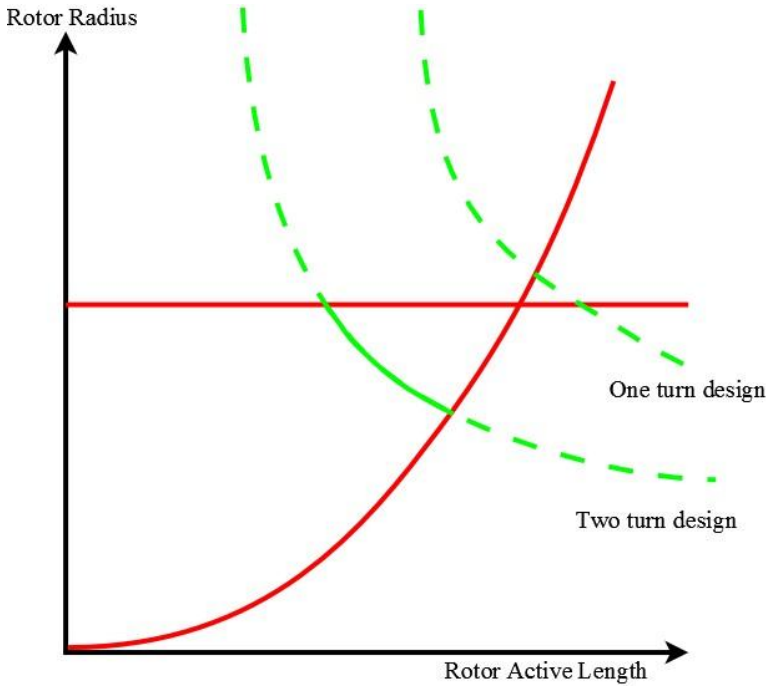

Figure 3-23: Effect of Low Turn Numbers on Design Space

When a suitable design has been found through mechanical and electromagnetic iteration, with the choice of materials, geometry and winding design set, it is possible to include a thermal design iteration to assess whether the predicted losses will cause any thermal problems. The results of this thermal iteration can then be used to re-evaluate the machine design in the mechanical-electromagnetic design space, to reduce the relevant losses if they prove to be too high, or to allow for a higher electric loading if losses are not deemed to be an issue. The next chapter will describe the thermal design process and options as well as how it integrates with the mechanical and electrical design processes.

Chapter 4. Thermal constraints

The thermal design of HSHP machines is influenced by the material choice and geometry of the machine as much as by the electromagnetic design, cooling and losses, which creates the strong interaction between thermal, mechanical and electromagnetic design. An appreciation of the thermal implications of a particular electromagneticmechanical design choice is vital, and adds a second iterative loop to the machine design. Once an acceptable mechanical-electromagnetic design is achieved the machine thermal operating point must be estimated and the results of that estimate used to modify the mechanical-electromagnetic design appropriately.

Thermal design issues that are of particular interest to HSHP machine design are accurate estimates of winding hot spot temperatures and rotor operating temperatures as the design of these machines often pushes the operating temperatures close to the thermal limits of the sleeve and winding insulation materials. To estimate the operating temperature of a given design, two design methods are available, lumped parameter analysis and numerical FEA/CFD; the first allows a rapid estimation of bulk temperatures in the machine whereas the latter allows a more detailed estimation of the temperature variation in complex geometries. The accuracy and effectiveness of both analysis tools are affected by the values chosen for material properties and in particular how they treat heat flow across material boundaries and complex geometries, such as the distribution of the conductors in the slot of the machine, where the geometry and bulk material properties are not fully known before construction. This chapter will discuss the use of both methods for designing HSHP machines and particular design implications of different cooling methods and machine features.

4.1 Thermal design techniques

4.1.1 Lumped Parameter Analysis

Lumped Parameter Analysis is a very common tool for predicting the thermal performance of machines [96-99], and operates on the principle of developing a thermal resistance for each component in the machine then combining those resistances into a network from which the

temperatures can be determined based on the heat input at various nodes and the ambient temperatures of the system. The equations governing the calculation of the equivalent thermal resistance of conduction, R_{cond}, through a component and convection, R_{conv}, from a surface are given by (4.1) and (1.1) (4.2) respectively, from [97], where l is the length of the component in the direction of heat flow, A the cross-sectional area of the component normal to the heat flow, k the material coefficient of thermal conductivity and h_c the convection coefficient of the surface.

$$R_{cond} = \frac{l}{kA} \quad (4.1)$$

$$R_{conv} = \frac{1}{h_c A} \quad (4.2)$$

The lumped parameter method simplifies the heat flow paths in the machine by considering only the most dominant paths and 'lumping' the appropriate geometries and materials into single resistance parameters. An example of a lumped parameter network for one tooth of the stator of a machine is shown in Figure 4-1, in this model, heat from the windings is assumed to flow only through the sides of the slot and there is assumed to be no axial heat flow, allowing simplification of the network to that shown; an example of the lumping method can be seen in the tooth resistance parameter, here the area is taken to be the cross sectional area of the tooth in the axial-circumferential direction and the length is taken to be half the tooth length as all the heat from the windings is assumed to enter the tooth midway along the tooth.

The relative areas of components can be assumed to be constant for large radius machines. However, where the curvature of the machine housing affects the area of a lumped component (such as the coreback section above the tooth), Fourier's law of heat conduction (4.3) can be applied to compute the resistance, where Q is the heat transfer rate (in Watts), T temperature, and A is now a function of radius l_{axial}, the axial length of the component, given in (4.4). This method can be seen in [98].

$$Q = -kA(r)\frac{\partial T}{\partial r} \quad (4.3)$$

$$A = 2\pi r l_{axial} \quad (4.4)$$

A similar process and can be followed for the rotor, giving the model shown in Figure 4-2; where loss generation and heat flow are assumed uniform across the rotor axial length and that there is no circumferential heat flow, allowing the axial and radial dimensions to be lumped.

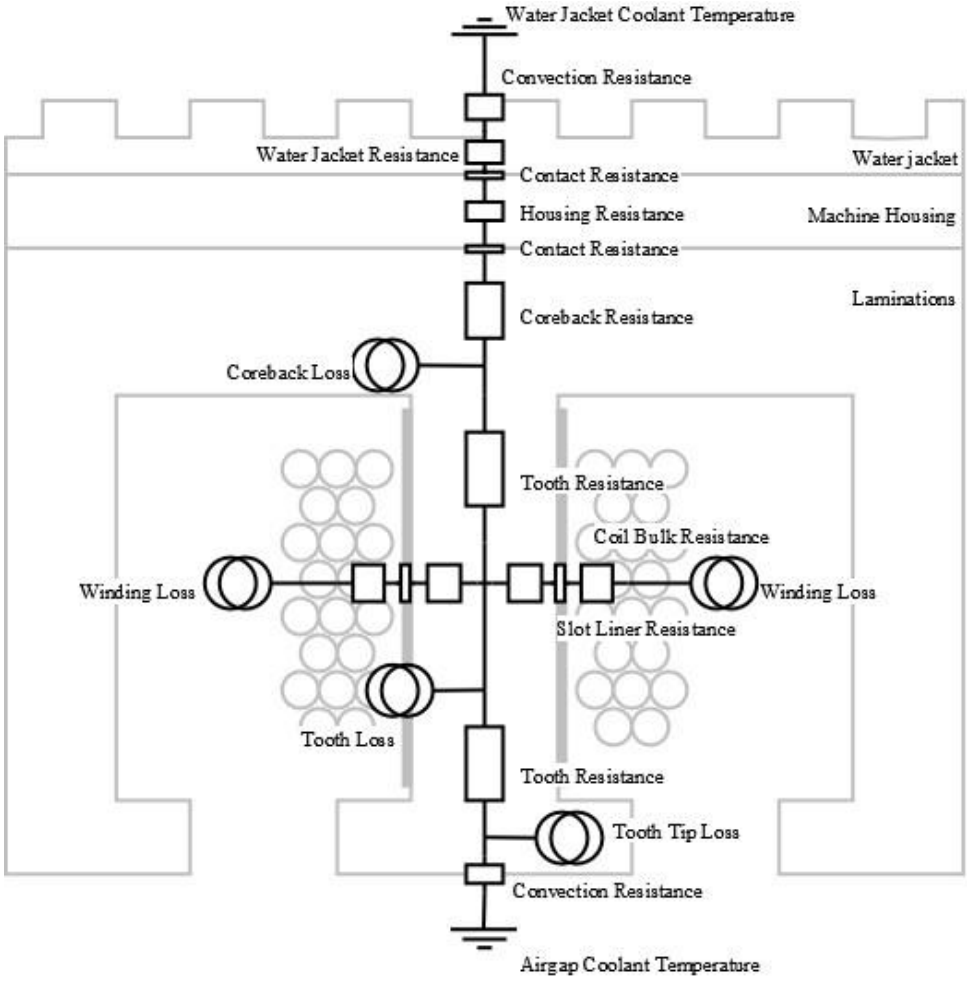

Figure 4-1: Thermal Resistance Network for Stator Tooth

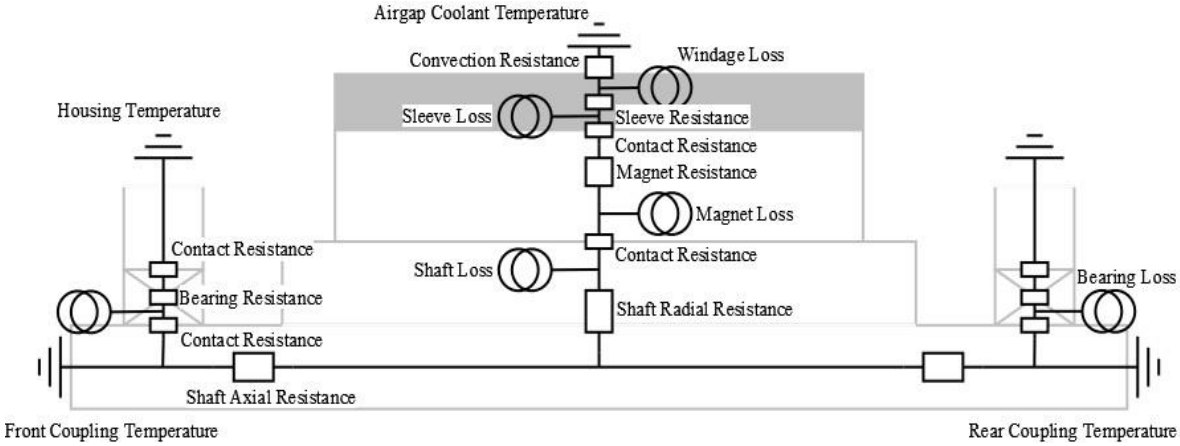

Figure 4-2: Thermal Resistance Network for Rotor

The complexity of such models can vary greatly based on the simplifications and design choices made, the example topologies shown above are popular when considering the heat flow occurring predominantly in a radial direction [97, 98], with axially located components such as end windings and bearings considered only as braches from the radial model. A more detailed analysis using axial and radial T-networks for each lumped component [96] can improve

accuracy in determining the temperature distribution by increasing the resistance component count and by considering both axial and radial heat flow throughout the machine, at the cost of a more complex network to solve.

Proprietary software exists to solve such networks, such as MotorCAD [100], where empirical data and experience have been used to develop a lumped parameter network for various machine topologies, and the ability to alter coolant methods, materials and geometry are built in. An example of the network used is seen in Figure 4-3, for a PM motor with natural convection cooling of the casing only.

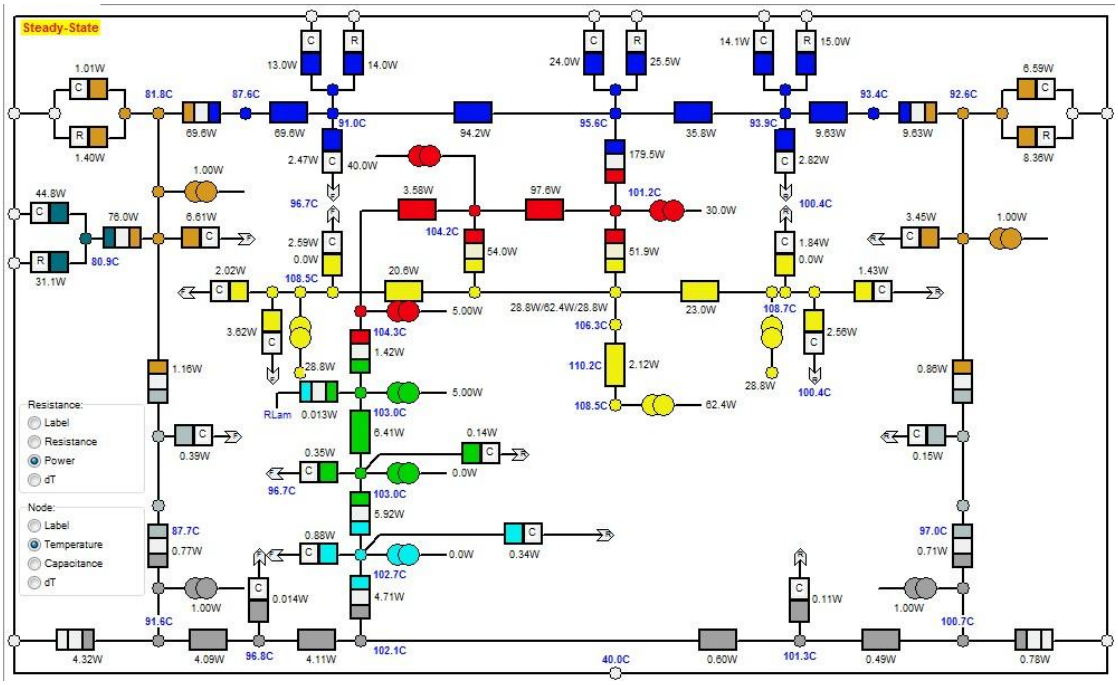

Figure 4-3: Thermal Resistance Network in Software (MotorCAD)

The main drawback in using lumped parameter models arises from gaining only a bulk value for temperature in a component; information about temperature variation within components is not available, and hot spots may not be accurately modelled and identified. This may be acceptable for lowly loaded machines with a large safety factor in the thermal design, however for HSHP machines there is little overhead available in terms of machine temperature, due to the high loadings and associated losses, and components may be close to their thermal limits, which requires a high degree of accuracy when predicting hot spots. It is the hot spot temperature of a component that dictates its thermal limit, rather than the bulk temperature, due to the material failure modes; this is particularly true with windings where the insulation lifetime can be plotted

as a function of temperature and a single insulation failure leading to a winding short can cause the failure of the machine as a whole.

The low resolution in temperature prediction can be improved by selectively refining the lumped parameter model to include a higher resolution or network in areas where large temperature variations (due to low thermal conductivity of the components) and hot spots are expected. An example of this technique can be seen in the previously mentioned software, MotorCAD, which uses a multiple winding layer method to improve the accuracy of temperature prediction in the windings of the machine, allowing the peak winding temperature to be identified with greater accuracy. Other, similar methods [101, 102] have also been used to improve the temperature prediction in the windings of various electrical machines, as they are often the sources of peak temperatures within the machine.

A further critical source of error in lumped parameter models arises from the treatment of contact resistances and convection coefficients; both values are notoriously difficult to predict for a motor and can give rise to large variations in calculated temperature rises if not accurately modelled [103]. Empirical data exists for contact resistances between different surfaces, however it remains difficult to accurately predict the value found between the laminations and stator housing, which present a critical barrier to heat flow and can significantly affect the final machine temperatures. The same issue exists for predicting the convection coefficient; though it can be estimated using classic analytical techniques using dimensionless numbers, such as the Reynolds, Prandtl and Nusselt numbers. For forced convection in complex geometries, turbulence and temperature variation along the length of the fluid cooling channels can generate inaccuracies in the bulk prediction for h_c.The prediction of the convection coefficient is also dependent on accurate estimation of the flow rate of the coolant, which must be computed by comparing the pressure performance of the coolant pump to an estimate of the flow resistance of the coolant flow path, which can be built up from classical empirical relations [104], which add further sources of error. As a result, temperature predictions from lumped parameter thermal models must be expected to contain an accuracy tolerance of at least 10% [97].

4.1.2 Thermal FEA and CFD

Both FEA and CFD methods use numerical methods to solve either the heat equation [105] (4.5) in a solid, or the Navier-Stokes equations for fluids [97] respectively. For the heat equation, which describes how the spatial distribution of temperature in an object varies with time, ρ is the

material density, c_p the specific heat capacity at constant pressure, k the thermal conductivity and Q_{gen} the heat generation per unit volume in the solid, caused by internally generated losses.

$$\rho c_p \frac{\partial T}{\partial t} - \nabla \cdot (k \nabla T) = Q_{gen} \quad (4.5)$$

Both methods require significantly more computing resources than a lumped parameter model and can be slow to solve, particularly CFD analysis which is limited in application due to the complex meshes and non linear equations as well as the expert knowledge required to apply appropriate models and simplifications to the analysis [97]. Both methods can be used to provide a more accurate estimation of either temperature the distribution in machine components (FEA) or of fluid flow rates and convective heat transfer coefficients for the coolant fluids (CFD).

FEA analysis has particular benefits in complementing a lumped parameter model to aid in predicting hot spots in machine regions such as the windings and magnets, Figure 4-4 shows the temperature distribution in one slot of a machine, with the conductors fully defined, the machine has both forced air gap convection and a water jacket on the stator housing. Use of FEA for prediction of the temperature distribution in a machine suffers from the same accuracy issues as the lumped parameter model, caused by the variability and difficulty in predicting the true values for contact resistances and heat transfer coefficients found in the final constructed machine. As such, the analysis is limited in it's accuracy for predicting bulk temperatures but does allow temperature distribution in complex geometries to be more accurately modelled than in lumped parameter analysis.

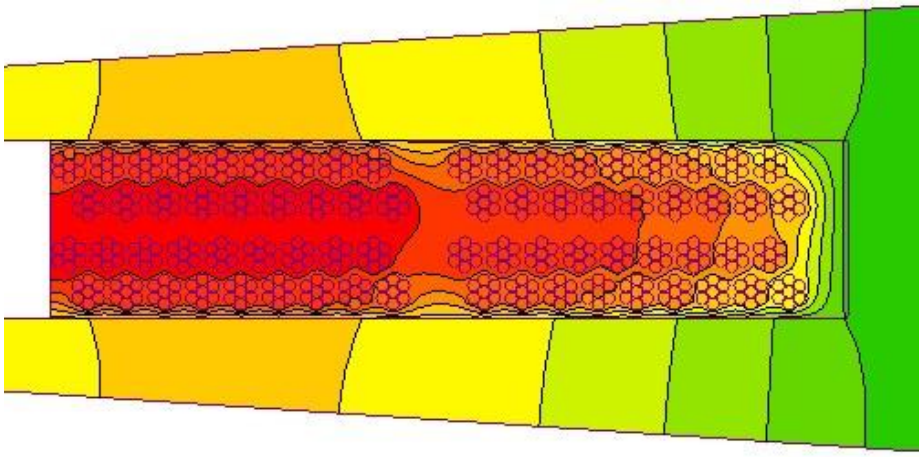

Figure 4-4: FEA Temperature Distribution in Machine Slot

The use of CFD can be beneficial, despite the added engineering cost, in gaining better insight into coolant flows of heavily cooled machines with complex liquid coolant flow paths, however there are often significant tolerances present on CFD flow predictions, leading to wide variation in prediction of the final cooling capability of the machine.

While both CFD and FEA confer advantages in detailed design work of HSHP machines, the lumped parameter method provides acceptable accuracy and iterative speed, given the design factors that must be included in all prediction methods. The detailed analysis offered by CFD and FEA can aid the designer in evaluating specific geometries and comparing different cooling methods, while the lumped parameter method is most useful when performing the sizing iterations in conjunction with the electromagnetic and mechanical design. Ultimately experimental validation of the losses and associated heating for a given cooling technology provide the only certain way to push a design to its limits, but these require prototyping which can prove lengthy and costly for HSHP designs. A lumped parameter model with sufficient thermal safety margins and refinement of the resistances in critical regions should prove adequate to size and design an HSHP machine; while future generations and designs can deliver improved power density with the empirical knowledge gained by testing the original design.

4.2 Available cooling methods

The range of cooling methods for electrical machines is wide and varied, and is often ultimately dictated by cost and the operating environment of the machine. Cooling methods can range from simple unforced convection to ambient, as seen in undemanding industrial applications [103], to complex systems involving direct water cooling of conductors and forced convection cooling using hydrogen, as seen in high power density turbogenerators [106]. Not all of the available methods are applicable to HSHP machines, due to reasons of cost, safety or engineering practicability; however the relevant options are summarised in the following section. General machine design rules have been developed over time to give an acceptable armature current density for a specific cooling method, [43]; these rules of thumb allow an initial selection of appropriate cooling methods early in the design stage of a machine, based on the expected current densities delivered by the electromagnetic-mechanical sizing process.

4.2.2 Housing Water Jacket

One of the most common cooling methods for high torque density electrical machines is the use of a water jacket to cool the stator; the primary reason is that the high torque density is achieved by a high electrical loading, which creates significant copper losses. The logical path for extracting the copper loss from the machines is via the stator laminations, which provide a good conductive path between the periphery of the machine and the centre of the windings (in a toothed design), less the thermal impedance presented by the slot insulation. The thermal conductivity of the laminations is best in the plane of lamination, leading to the best position for the water jacket to be on the stator outer circumference, providing a large surface area and a simplified engineering solution as both the stator and water jacket can be treated as separate, independent components.

The coolant used for the water jacket is traditionally water or a water glycol mix, to provide a better temperature range in the coolant circuit, and the flow is commonly in the helical or axial directions [107].

The detailed design of water jackets relies on the design principles of heat exchangers, where the chief aim is to ensure a large surface area in contact with the coolant and a high heat transfer coefficient through controlling the surface roughness and turbulent flow of the coolant. These design principles lead to a preference for small channel cross sectional areas, with a high volume flow rate, which leads to multiple channels in each water jacket; in the case of a spiral jacket this equates to multiple turns of the spiral, whereas in an axial jacket it can lead to either doubling back of the channels axially, or the use of parallel flow paths.

The effectiveness of water jacket cooling is limited to the active, in-slot, windings only; the thermal paths from the end windings and the rotor to the water jacket are longer and can cause much more critical temperature rises than are found in the active windings. The thermal path from the rotor to the water jacket is complicated by the air gap of the machine, which acts as a near perfect thermal insulator, forcing the vast majority of heat flow from rotor to water jacket to be via the bearings and machine housing, in the absence of any forced convection in the air gap of the machine. This extended and highly resistive thermal path would lead to unacceptable rotor heating if any significant rotor losses are present and hence often requires an additional cooling method to be used for rotor heat extraction, such as forced air cooling.

Cooling of the machine end windings by a water jacket is sub optimal, as the thermal path to the water jacket for the end winding losses includes the length of winding protrusion from the stator

on top of the existing thermal path for the active windings. Although copper is a good thermal conductor, the heat flux along the wires in the end winding with a high electrical loading is still significant enough to cause a noticeable temperature rise, leading to the end winding region to be hotter than the active winding region in the absence of other cooling methods. A common design method to improve the thermal path from the end windings to the water jacket, in the absence of other cooling methods, is to pot the end winding space with a high conductivity resin [108, 109], the water jacket can then be extended to cover this potted region. The resin provides a much better thermal path than air and adds a lower resistance parallel thermal path from the end windings to the water jacket when compared to the initial path along the end winding length and into the active winding region. There are associated engineering difficulties with the use of this method for HSHP machines; highly conductive resins have limited maximum temperature capabilities and a trade off is made between conductivity and maximum operating temperature, thus limiting the peak thermal rating of the machine to be lower than that possible in other components. Furthermore, the brittle nature of such resins and the difference in thermal expansion coefficient between them and the winding and housing materials leads to severe stressing and cracking due to the thermal cycling of the machine, limiting the machine lifetime. [110].

4.2.1 Internal Forced Ventilation

Forced air cooling through the active components of the machine is another common cooling method which can be used to remove heat from both rotor and stator. For HSHP machines forced air cooling is primarily focussed on heat extraction from the rotor and the end windings of the machine, as a water jacket cannot effectively cool these parts. Forced air cooling systems can become highly complex, as seen in turbogenerators, which incorporate multi-chambered systems and the use of hydrogen to improve homogeneity of cooling along the active length and reduce windage loss, as well as radial channels through the stator to improve heat extraction [106, 111]. These methods are not easily applied to HSHP machines due to the cost and safety implications of maintaining a pressurised hydrogen atmosphere in the machine and the axial length implications of adding in radial cooling ducts and isolating pressurised axial cooling chambers. As the rotor of an HSHP is generally subcritical, but operating close to its first critical speed, there is limited room for additional axial features without reducing the active length. This results in a trade off requiring a higher electric loading to compensate for the addition cooling structures, negating their benefit, for a given rating. More conventional forced air cooling for industrial and consumer motors consists of an axial airflow, forced by an external blower or a

shaft mounted fan [112] and passing though the air gap of the machine and any additional rotor or stator cooling ducts [113, 114]. The rate of air flow through a design is determined by the pressure difference that can be achieved across the machine and the resistance to flow offered by the channels in the system. Detailed design work can be undertaken to reduce flow resistances and improve general flow rates of coolant air through the machine.

4.2.3 Oil cooling

Oil is another fluid commonly used in cooling electrical machines: unlike water based coolants it does not have a corrosive effect upon the machine components and is an electrical insulator, allowing closer contact with the machine and a more direct cooling to be achieved. Direct contact with the stator coreback can be achieved [101, 115], as well as immersion of the rotor in oil [42] at the cost of increased drag losses.

Though generally of a lower specific heat capacity than both water and water-glycol coolants, oil coolant can operate above 100^{o}C allowing more flexibility in the cooling system design. It is furthermore an attractive option when oil reservoirs already exist in the target application, such as in automotive and aerospace applications that have significant oil supplies for associated gearboxes, or when water is either scarce or not fit for use.

4.2.4 Slot water jackets,

The use of slot water jackets to provide high capacity cooling in close proximity to the windings can allow for very high current density applications, generally exceeding that achievable with other cooling methods [40]. This method of cooling the windings of a machine is almost universal in all the largest turbogenerators [106, 111] and is also seen in other high power density machines, either for the armature or field windings [43]. The coolant fluid can be either air, water or oil, depending on the application requirements and available coolant sources.

There is a significant engineering challenge associated with such cooling methods, due to the need to ensure isolation from the closely located windings, which can be at very high potentials as well as integrating a fluid ducting system within the end windings and between the bearing spaces of the system.

4.3 Rotor Cooling Constraints

The specific design aspects of HSHP machines can pose direct conflicts with the need to extract the heat from losses; in particular the choices made during the mechanicalelectromagnetic sizing can have significant implications for the thermal design of the machine. The following two sections will discuss these implications, focussing first on the rotor constraints, then the stator.

4.3.1 Rotor Sleeve Materials

The choice of sleeve materials for the rotor has implications on both the rotor operating temperature and the thermal circuit. As discussed in chapter 2, the use of carbon fibre composites is attractive due to their high strength to weight ratio, allowing larger rotor volumes to be achieved compared to metallic sleeve alternatives. They do, however, present a significant thermal disadvantage due to the low glass transition temperatures and thermal conductivity of their resin matrices. The glass transition temperatures of high performance resins can be pushed to approximately 200^{o}C with complex curing procedures, though operating temperatures will have to be kept appreciably lower, while their thermal conductivity is typically an order of magnitude lower than that of metallic sleeve alternatives.

These material limits thus have implications for rotor cooling: the low thermal conductivity of a composite sleeve will effectively insulate the rotor from the air gap of the machine, limiting the effectiveness of any forced cooling in the air gap. To counter this, air duct cooling in the rotor shaft is almost mandatory if any significant rotor loss is expected. The peak operating temperature of the rotor is additionally reduced to below the ratings of the other components, leading to the sleeve temperature being the driving value in sizing the rotor cooling circuit. Given that the rotor losses are generally concentrated at the magnet/sleeve interface, the peak rotor temperatures will be in close proximity tp the sleeve, requiring careful design of the cooling circuit to minimise the temperature rises.

4.3.2 Magnet Materials

In the absence of a composite rotor sleeve, the magnet material becomes the limiting factor in the thermal design of the rotor, NdFeB magnets have a limited temperature operating range due to the reversible degradation of their coercivity with temperature as well as their low permanent demagnetisation limit with temperature. Their application is thus limited to relatively low

temperature rotors, whereas SmCo magnets exhibit a lower temperature reversible reduction in coercivity and have much high permanent demagnetisation with temperature limits. Thus the use of SmCo can allow higher temperature rotors with a lower cooling rate for the same losses when compared to NdFeB.

4.3.3 Rotor ducts

Rotor ducts are an attractive cooling option for high power density rotors; they are relatively simple to implement in solid shafts, via gun drilling or other similar methods, and can significantly improve rotor cooling in a forced ventilation system as there is a good thermal path between the magnets, where the losses occur, and the duct location. It is desirable to locate the ducts as close to the magnets as possible, to minimise the thermal path for the losses, while maximising the duct cross-sectional area, to improve flow rate, and the duct surface area, to improve heat transfer. These design requirements can conflict with the magnetic and mechanical design of the rotor so care must be taken in the choice of their location. The effects on the magnetic circuit of various duct positions are shown in Figure 4-5. When numerous small ducts are placed as close to the magnet surface as possible, as shown on the left, they act to increase the reluctance of the magnet circuit, reducing the magnetic loading of the rotor. This can be seen via the increased saturation of the shaft material in the spaces between the rotor ducts (dark green rather than turquoise). The same effect is seen with a single large duct at the shaft corner, which is positioned to be as close to the magnet outer surface as possible and hence reduce the thermal path for the magnet surface losses. Placing the ducts beneath the magnet centres offers the least interference with the magnetic circuit, while maintaining the largest possible pitch diameter for the ducts, as seen on the right in the figure. Other factors may affect duct location, such as the mechanical design of the rotor; features both within the active rotor region and the rotor end regions (tapers to bearing surfaces) limit the positions within which a rotor duct can be located.

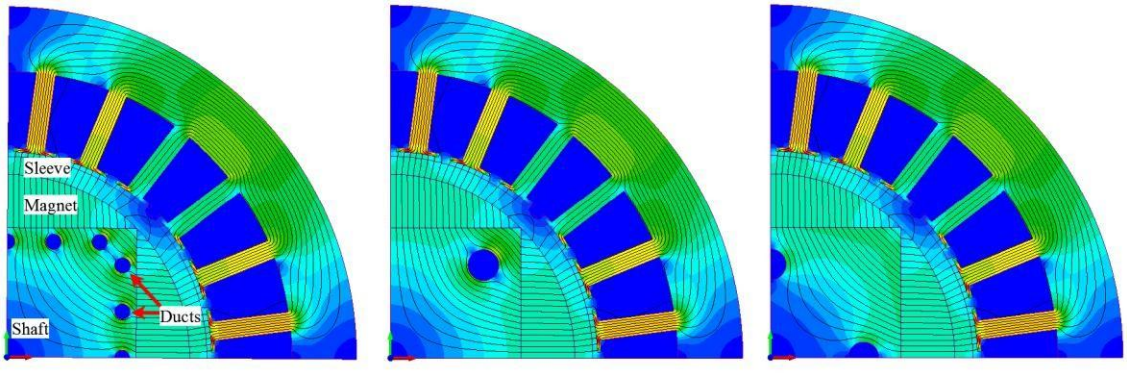

Figure 4-5: Effects of Rotor Duct Location

As with other aspects of ventilation and water jacket cooling, design work can be undertaken to improve the flow rates and heat transfers achieved in the rotor ducts of a machine. For the rotor ducts, in particular, this work centres on the duct shape and the design of the duct inlets and outlets and corners to reduce the pressure drops associated with them, using standard channel flow design principles [113, 116].

4.3.4 Air gap cooling

In HSHP machines air gap cooling is often limited in effectiveness due to the use of composite sleeves providing a significant thermal barrier between the rotor components and the coolant. From a thermal point of view it is attractive the maximise the air gap length, to improve flow rates and reduce windage loss, however this stands in direct contradiction to the electromagnetic design of the machine, where large air gaps reduce the magnet loading. Despite the poor heat transfer from rotor to coolant when composite sleeves are used, the air gap cooling still has a useful effect in removing the heat caused by the windage losses, and can provide beneficial cooling to the stator inner bore.

4.4 Stator Cooling Constraints

The cooling constraints for the stators of HSHP machines focus largely on the ability to extract heat from the machine windings. Geometry changes and manufacturing processes can have a large effect on the peak temperatures found in the windings. Machine failure requires only one hotspot to cause an insulation failure and a short to ensue between turns or phases or between strands which can induce further losses and lead to thermal runaway. Thus design work focuses on reducing peak winding temperatures throughout the machine.

4.4.1 Stator Impregnation

Given that the best fitted, non compacted windings may only fill 50% of a slot with conducting material, it is highly desirable to ensure the rest of the slot space is filled with another solid material to aid in thermal conduction, rather than just air which has a poor thermal conductivity. To achieve this stators are commonly impregnated with resins after winding in an attempt to fill

as much of the remaining slot space with a material that adds both stiffness and strength to the windings and improves the thermal conductivity to the coreback as the resins are typically ten times more thermally conductive than air. This impregnation is commonly performed with low viscosity resins at an elevated temperature to further improve their flow and can involve either trickle impregnation or forcing by vacuum pressure. The multi-stranded wire bundles associated with HSHP windings pose particular challenges to effective impregnation when combined with the long axial length of the stator, ensuring the resin penetrates fully along the length of the slot and fills the voids fully are a challenge that can only be fully resolved with practical experimentation. The penetration can be improved with the use of low viscosity resins and vacuum pressure impregnation (VPI) whereby the resin is applied to the stator in a vacuum and then atmospheric pressure is returned, drawing the resin into voids in the windings. Low viscosity resins pose limitations in that they only form a thin layer on the components they coat, leaving larger voids unfilled, a problem that can be reduced by multiple VPI cycles to build up a thicker layer or the use of thixotropic resins that thicken after the impregnation stage and before curing.

4.4.2 Winding cross section

The geometry of the slots in an HSHP machine can have a significant effect on the peak temperatures found in the windings. Assuming the majority of heat leaves a slot via the tooth edges rather than the slot base (due to the difference in cross sectional areas) the peak slot temperature can be assumed to run down the centreline of the slot and increase with slot width. As the main heat flow path for the slot losses are along each tooth to the coreback, there will be a temperature gradient in the tooth, leading to an equivalent temperature gradient (rise) towards the slot opening, as seen in Figure 4-4. It is thus obvious that peak winding temperatures can be reduced by altering the slot geometry to make it thinner, as long as the loss density is not also increased, favouring designs with large slot numbers and high fill factors. This desire must be balanced against the electromagnetic design, given the common low turn numbers of HSHP designs and the need for adequate slot insulation.

4.4.3 End Winding Cooling

As noted in 4.2.2, if the main cooling method for the stator is a water jacket, there can be significant temperature rises in the end windings of the machine, due to the extended thermal

paths. To combat this some forced or direct cooling of the end windings is desirable to reduce their peak temperatures, as they will form the main constraint on the electric loading of the machine. This direct cooling can be achieved by forced convection, driven by either direct through ventilation of the machine or specific techniques purely for the end windings, such as wafters [117] on the rotor or impingement cooling. Convection driven by through ventilation from one end of the machine leads to a pronounced temperature disparity in the end windings at one end compared to the other; the airflow over the windings at the air inlet end of the machine will be significantly cooler than the airflow at the exit end, which has absorbed rotor, windage and some stator losses by that point. This imbalance can be redressed by ducting some of the airflow from the inlet past the active length of the machine and blowing it directly on the hotter end windings, as shown in Figure 4-6, in an effort to improve the cooling of the end windings in this region.

4.4.4 Termination Cooling

For the same reasons that the end windings can have elevated temperatures compared to the active windings of a machine, namely extended thermal paths to the stator coolant flow, the termination leads can require direct cooling to minimise their temperature rise. This can be achieved via additional impingement or ducted air through the termination box of the machine, allowing direct cooling of the termination leads and lowering the temperature to the bus bars in the termination box so that they act as a heat sink for the leads due to their large thermal mass and surface area.

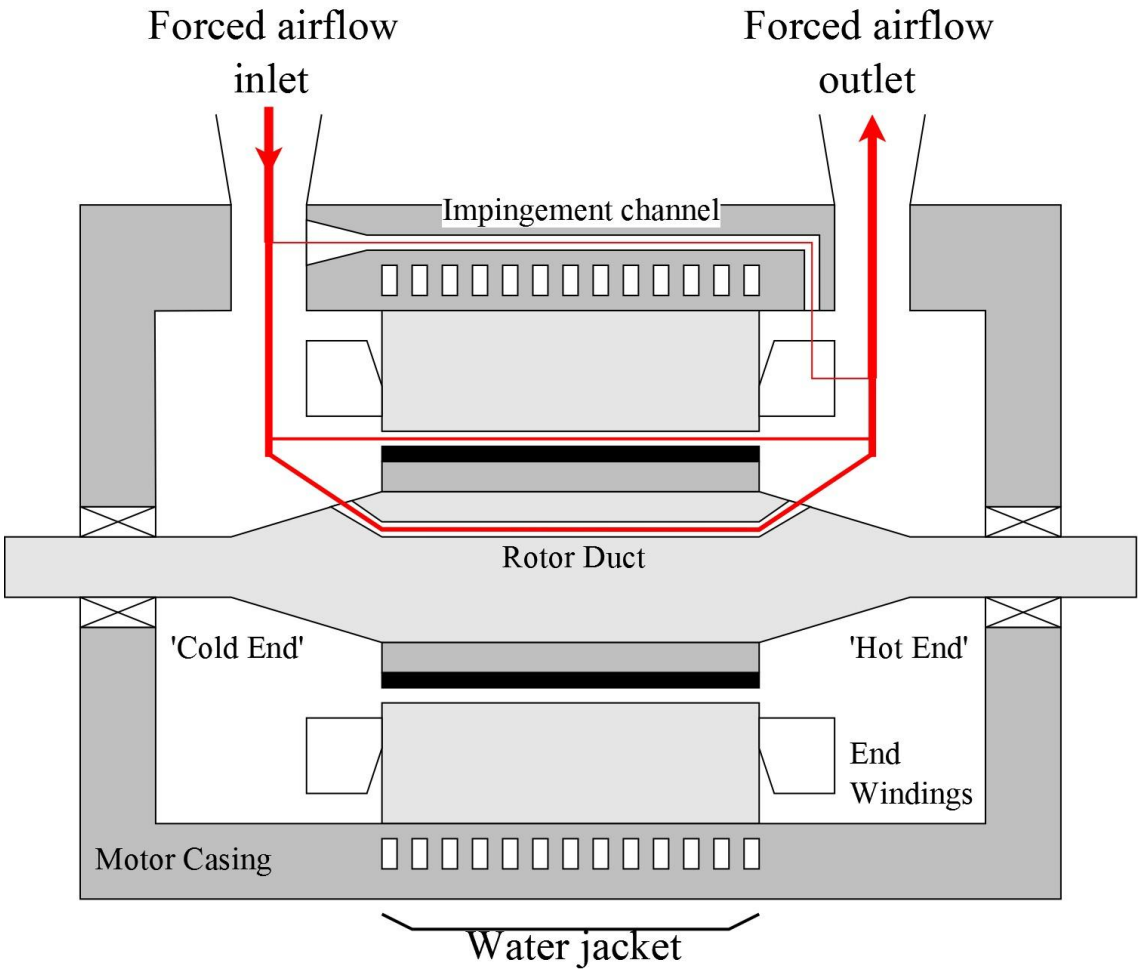

Figure 4-6: HSHP machine cooling scheme with impingement cooling

4.4.5 Coreback thickness optimisation

Varying the coreback depth of a machine with forced cooling around the stator outer diameter has a complex effect on the peak winding temperatures. A deeper coreback gives a larger surface area for the coolant system, improving its heat removal capacity and reduces the coreback loss intensity but increases the thermal path for the winding losses. This effect is summarised in Figure 4-7 for a generic machine with fixed slot dimensions and winding losses, ignoring tooth losses. An optimal design to minimise the winding peak temperature can be reached by iterating between electromagnetic and thermal designs during the detailed design phase of an HSHP machine.

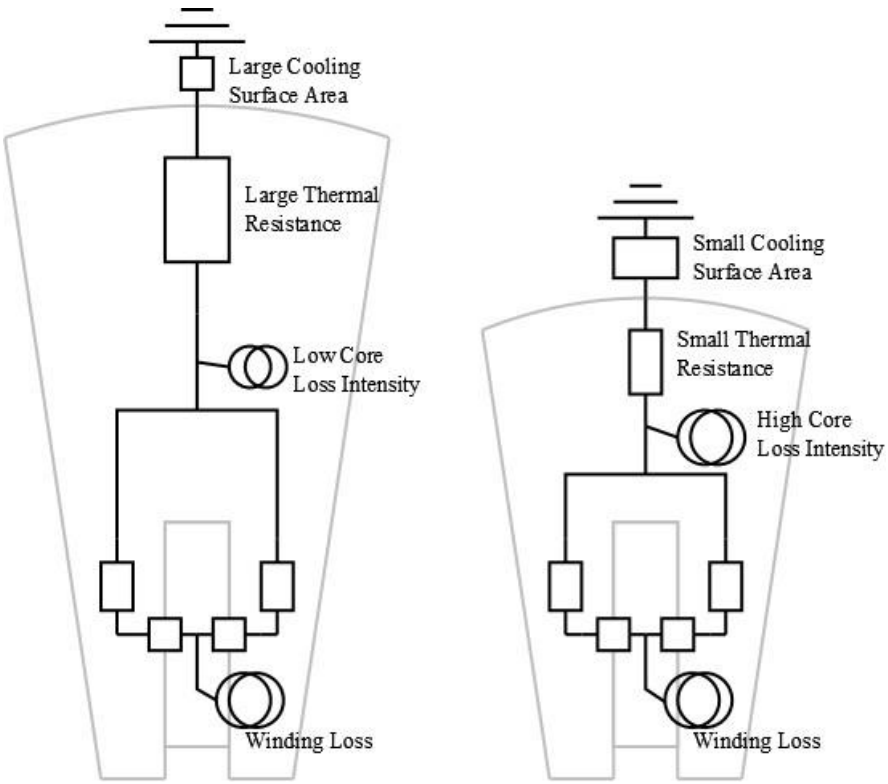

Figure 4-7: Effect of coreback thickness on thermal circuit

4.5 Conclusions

With a thermal design method defined, it is possible to incorporate it into the Mechanical-Electromagnetic iterative design process to provide a second iteration loop that qualifies whether an acceptable mechanical-electromagnetic design is also thermally acceptable. Considering the combined mechanical-electromagnetic rotor design space presented in chapter 3, as repeated in Figure 4-8, shows the effect of reducing the electric loading on a machine design. As the loading is reduced the curve of possible electromagnetic designs moves from position one to position 4, where there is no longer a viable mechanical rotor design that can achieve the required rated torque. The reduction in loading is achieved via reducing the turn numbers which has a direct effect on the size of the required slot areas, which reduce with loading, given a fixed current density, giving a better thermal design and reducing the winding peak temperatures.

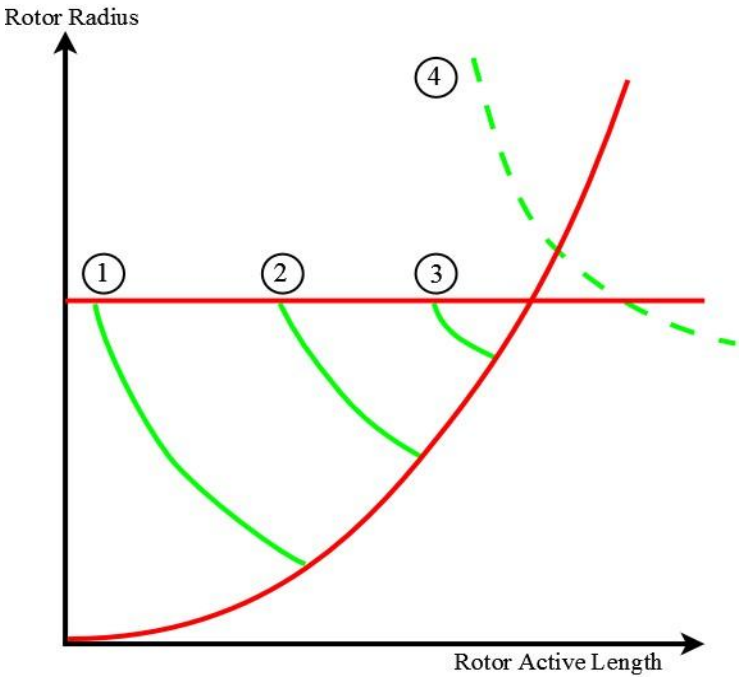

Figure 4-8: Effect Electric Loading on Rotor Design Space

The predicted losses generated using the methods in chapter 3 have the most direct impact on the thermal-electromagnetic design iteration. The predicted rotor losses expected from the winding design must be combined with the rotor cooling prediction to allow adjustment of the winding designs and hence characterisation of their effect on the required rotor volume. Furthermore the target current density in the windings and the slot shape can be adjusted with information from the thermal design but must be reconciled with estimations of the effect of on machine leakage inductance to ensure it does not prevent the armature reaction becoming too large for the supply voltage.

Chapter 5. Design of a Demonstrator Dynamometer

A commercial application was identified for a HSHP machine to act as a Dynamometer on a direct drive aerospace test stand. The application called for the delivery of a machine capable of 350Nm of torque and a maximum speed of 30,000rpm, giving a rated corner power of 1.1MW. A common method of providing high speed and power range test stands is to couple a low cost, low performance induction motor to a gearbox that can deliver the rated speed and torque, however this method was precluded in the identified application as the gearbox was not permitted; no market ready machines were identified as being capable of the required performance so a bespoke design was required. To be able to deliver the required performance across the full range of speeds, without the prohibitive cost of developing a bespoke electronics package as well, a

synchronous permanent magnet machine driven by a commercially available VSI was identified as the required machine topology.

This design delivers an $n\sqrt{P}$ of 1,000,000 and was seen as an ideal problem to illustrate the required iterative design of HSHP machines, balancing a severe set of mechanical, thermal and electromagnetic constraints. The following chapter describes the machine requirements, the design process followed and the final design chosen for manufacture.

5.1 Dynamometer Requirements

Based on the requirements provided by a potential customer the dynamometer had to meet the requirements set out in Table 5-1. As the Dynamometer was recognised to be a prototype, a fallback minimum speed and torque requirement was set to reflect the expected difficulty in achieving the rated values and these are listed in the table as well. The speed de-rating allows a fall back in the machine stress, as the induced stress is related to the square of speed; the requirements for a given rotor geometry are thus reduced to 64% of those at 30,000rpm, while providing additional head room for the rotor first bending critical speed. The torque de-rating allows headroom in the thermal design as the rated current falls linearly with torque while winding and rotor losses fall with current squared. Thus at the lower torque, these losses will fall to 73% of the levels at the full torque rating, giving a significant thermal margin if required. The de-rated peak power capability is then 754kW or just over 1000 horse power, a deliberate target for the American market, and useful selling point for the machine if the full rated performance cannot be met.

The rest of the dynamometer requirements were free to be defined as required by the equipment, technologies and materials commercially available to the industrial partner sponsoring this project.

Parameter	Value	Unit
Target Rated Speed	30,000	Rpm
Target Rated Torque	350	Nm
Target Rated Power	1.1	MW
Supply Voltages	<1	kV

Min Rated Speed	24,000	Rpm
Min Rated Torque	300	Nm
Min Rated Power	560	kW

Table 5-1: Dynamometer Rated Parameters

5.2 Development of an Iterative Design Tool

To aid with the demanding rated performance points and wide range of available designs a software tool was developed to combine the analytical mechanical and electromagnetic design techniques outlined in Chapters 2 and 3 and used to provide a rapid iterative design process. The software was designed to allow the designer to rapidly size a machine mechanically and electromagnetically given its rated set points, but with the flexibility to alter component geometries, materials and the electrical design without the need to use computationally expensive and lengthy FEA until the latter stages of the design process. The software would then deliver a prediction of the losses associated with the given design which could be input into a thermal analysis tool for estimation of the machine temperatures which would then lead to a re-iteration of the mechanical-electromagnetic design, if required. Once a suitable design was reached that satisfied the mechanical, electromagnetic and thermal constraints, the software could be used to generate and solve electromagnetic FEA models in both 2D and 3D to validate the estimated performance and losses. Further detailed mechanical and thermal FEA models can then be performed with the given geometries, as required, to complete the design work.

The main interface for the software design tool is shown in Figure 5-1, where the following list describes the highlighted parts of the interface:

1) Input parameter for rated speed and torque.
2) Mechanical design factors, maximum sleeve stress allowed and critical speed safety factor.
3) Rotor design parameters, including sleeve and magnet thickness, magnet shape and span and rotor pole number.
4) Stator Design parameters including slot numbers, air gap length, tooth tip design and target winding current density.
5) Electrical design parameters, including drive voltage, target EMF, winding layout and coil stranding.

6) Rotor Material choices.

7) Rotor Design Space, showing mechanical and electrical limits on possible rotor size and curve of achievable electromagnetic designs.

8) Predicted air gap armature MMF space harmonics.

9) General machine parameters based on inputs.

10) Specific machine dimensions and predicted losses for topologies chosen from the Rotor Design Space.

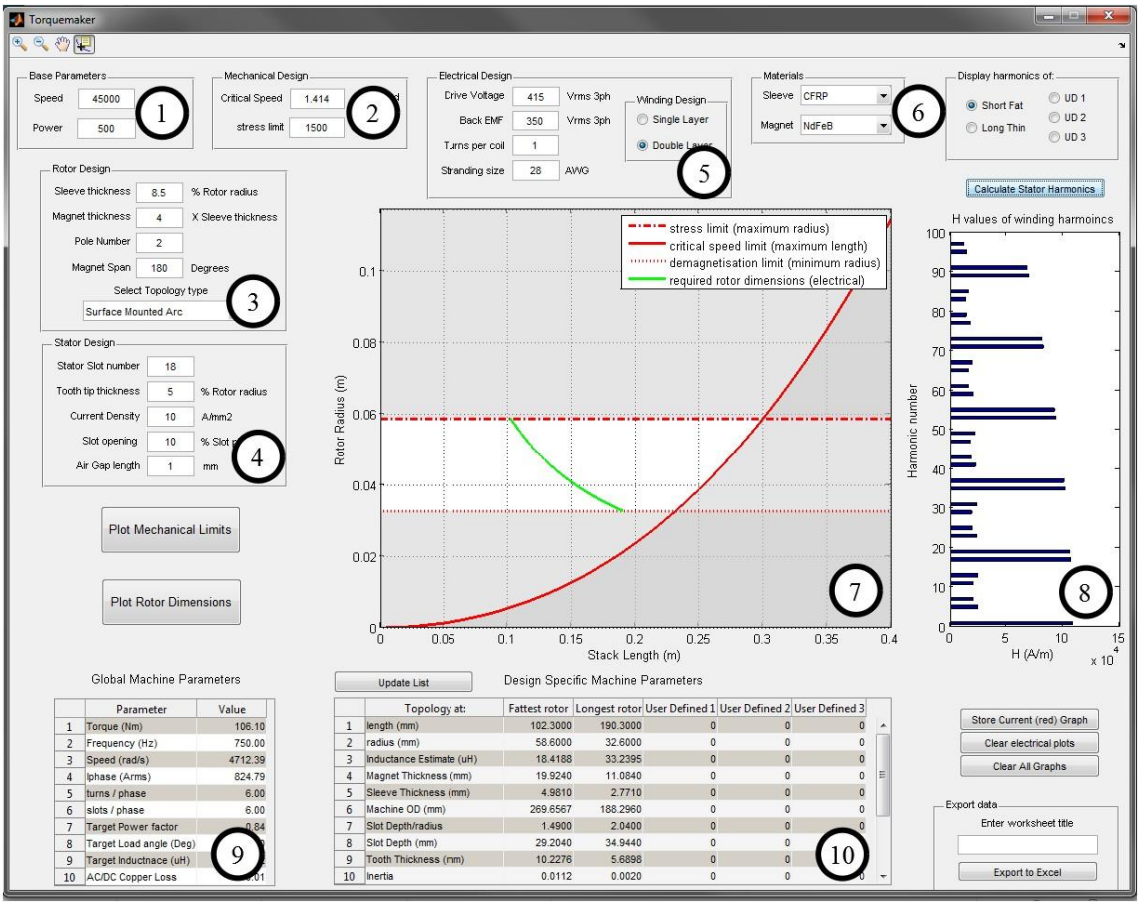

Figure 5-1: Mechanical-Electromagnetic Iterative Design Tool Interface

The bulk of the design work within the tool is performed in the Rotor Design Space, item number 7, which is shown in detail in Figure 5-2. Within this space the user input parameters are combined with the mechanical and electromagnetic design principles set out in sections 2.7 and 3.8, to graphically show the designer whether the chosen design is feasible. A further electromagnetic constraint has been added by comparing the predicted armature MMF with the properties of the proposed magnet material to provide a minimum rotor radius, below which the magnets would be too thin to resist demagnetisation (noting the magnet thickness is defined as a proportion of rotor radius).

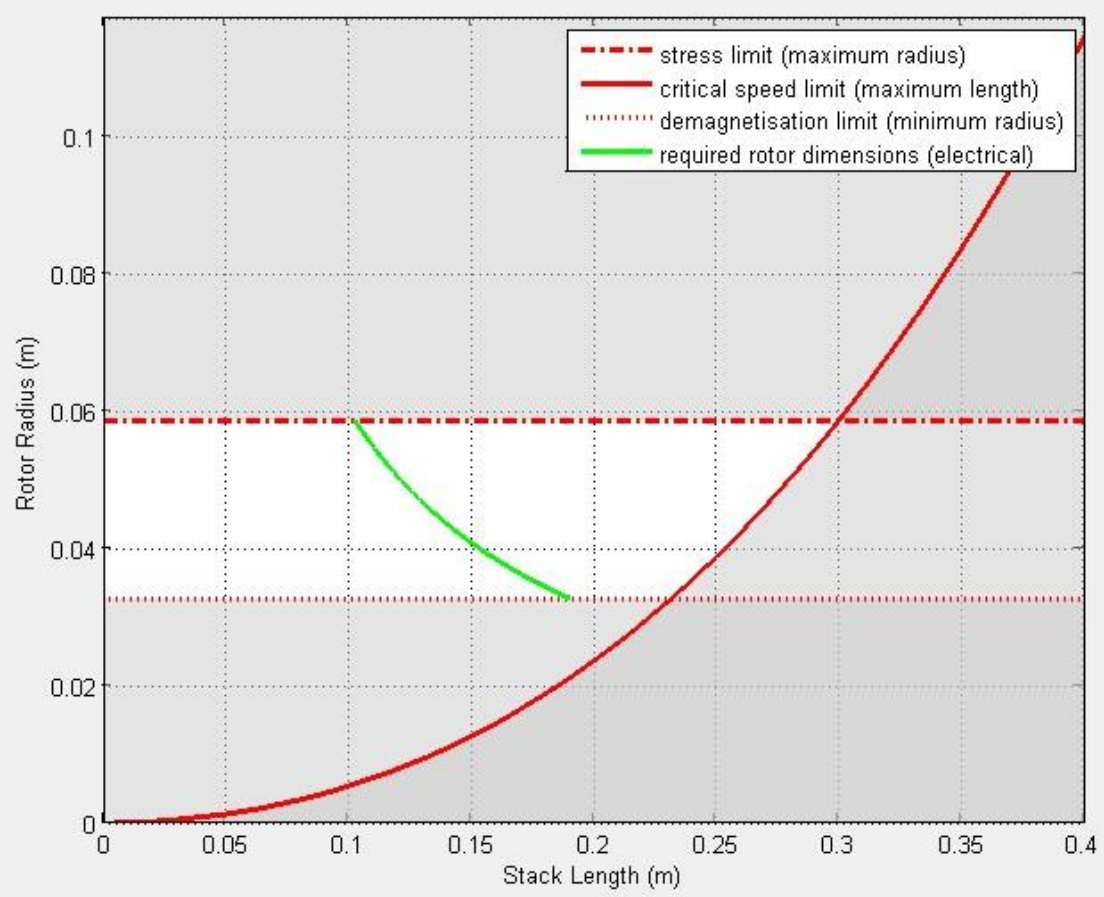

Figure 5-2: Rotor Design Space

Within the rotor design space, the designer can select various rotor topologies that lie on the electromagnetic design curve and compare their predicted losses and electromagnetic performance. Two points are automatically calculated by the software for an initial comparison, these being at the intersections of the electromagnetic design curve with the stress limit and the critical speed limit. These two designs give the

'shortest, fattest' rotor design and the 'longest, thinnest' rotor design respectively, where the former delivers the best thermal design due to the large machine diameter for the same thermal loading as the latter which, instead gives the best dynamic performance due to its low inertia and low stressing.

At this stage of design it is also desirable to perform a 3D FEA simulation to estimate the machine inductance, including the end effects (as they are difficult to evaluate analytically), to ensure that the current electric loading can be achieved with the drive constraints as described in section 3.2. If the inductance is too large then the either the geometry or electric loading of the machine must be altered, either by reducing the turns, increasing the armature air gap or changing the slot profile to reduce leakage inductance.

Once the design meets the inductance requirements the information about the losses can be compared in a thermal design package to quickly estimate whether the design is thermally as well as mechanically and electromagnetically sound. The thermal design package used in the design process was “MotorCAD” which is a commercial program based on solving a thermal resistance network of the machine being designed. If the results from the thermal estimation indicate a problem with the current design, it can be easily modified using the design tool to reduce the relevant losses or modify the materials and geometry appropriately.

If there is flexibility in the design at this stage, an optimisation can be performed, based on application specific requirements. Examples of optimisation metrics for HSHP machines may be efficiency, peak operating temperatures, dynamic performance (low inertia) and less commonly mass, volume or cost.

Once an acceptable design is reached, detailed modelling can be performed in FEA to validate the performance and losses and improve the detailed design of the machine; this process is often the most time consuming and labour intensive part of the design stage so the software tool includes a sub routine to automate the drafting and conditioning of the FEA models, ready for solving. Examples of the automatically generated 2D and 3D models with meshes overlaid are shown in Figure 5-3. In the 3D model, the end windings are hidden to show the increased meshing at the axial end of the stator.

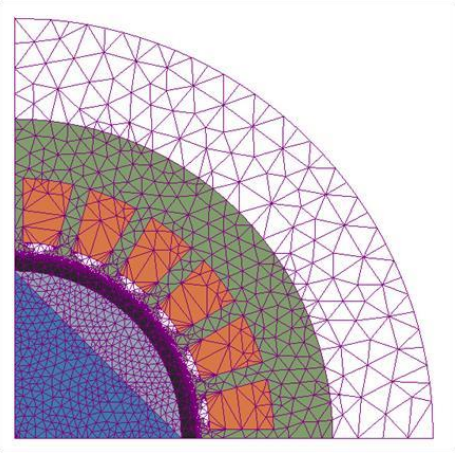

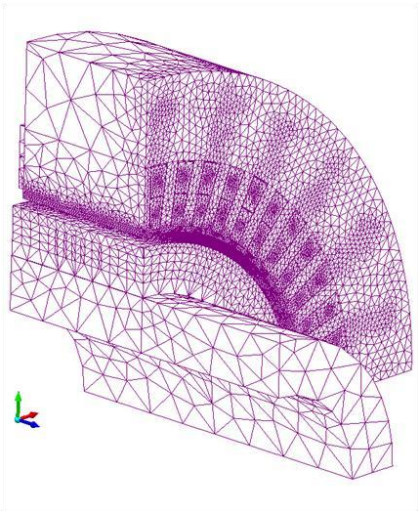

Figure 5-3: Example FEA Models and Meshes

In addition, mechanical FEA is performed on the proposed rotor structure to validate the stress predictions and resonant speed, while thermal FEA is used to complement the thermal resistance network in identifying and quantifying hot spots.

The proposed design process for HSHP machines is shown in Figure 5-4. The multiple iterative loops can be expedited with the use of the analytical software, with the time consuming and costly FEA design kept to the end of the design process.

The design procedure shown in Figure 5-4 was followed for the design of the HSHP dynamometer of the rating given in section 5.1. The design process will be detailed in the following sections, beginning with a detailed description of the materials, processes and ancillary equipment available for the project.

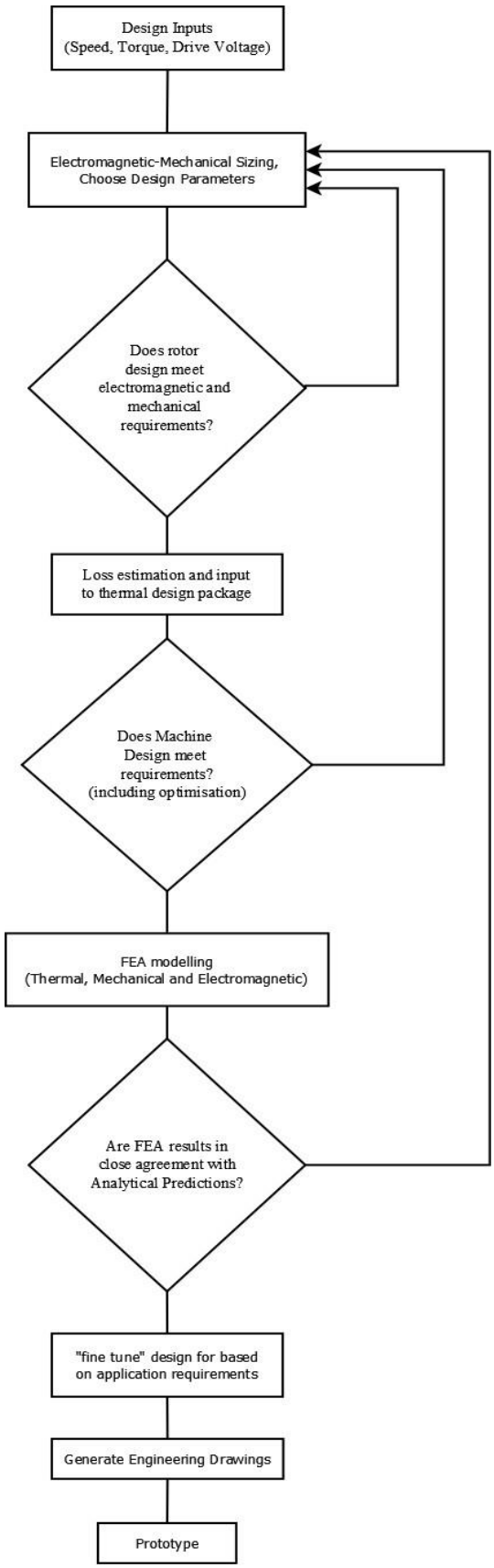

Figure 5-4: Iterative Design Process

5.3 Available Equipment, Technologies and Materials

The biggest influences on the final design of an HSHP machine are the availability of materials, processes and equipment with which to contract and maintain it. This availability can be due to budgetary constraints, IP limitations, application specific prohibitions on processes, as well as the basic material capability limits and the ability to handle and process those materials. The demonstrator dynamometer developed in this chapter is subject to the same constraints and the design was heavily influenced by the availability of materials and construction processes as well as budgetary constraints.

5.3.1 Available Drive Technology

The intended location and application of the Dynamometer required a low voltage (<1kV) drive to be used. The three phase supply voltage to the site was limited to 460V RMS, and a step up transformer was precluded on cost and space grounds. The speed of the machine required a minimum 500Hz output frequency capability of the drives. A bespoke drive solution was also precluded on grounds of cost and development time, leaving a readily available commercial solution to be identified; two such systems were identified, one produced by Control Techniques Ltd (CT) and one by Unico.

Parameter	CT drive[60]	Unico drive "2000 Series Test Stand Drive"[61]
Bus Voltage (V DC)	unknown	850
Switching Frequency (Hz)	4-6,000	16,000
Output Frequency (Hz)	500	1,000
Supply voltage (VRMS three phase)	690	540
Cooling	Forced Air	Water cooling

Table 5-2: Drive Capability Comparison

Considering the capabilities of both systems, the Unico system was chosen due to its increased motor frequency capabilities, the 1000Hz output frequency would allow the choice of a four pole machine, based on the 30,000rpm speed requirement. The lower output voltage was deemed acceptable given the potential gains in reduction of magnet material and coreback thickness associated with allowing a four pole design over a two pole one.

The Unico system was achieved via two parallel drive modules, each rated at 1000A, and connected to the machine through a choke rated at 5μH.

5.3.2 Available Sleeve Materials and Pre-Stress Technology

Both Inconel and composite sleeve materials were readily available for the design process, with the composites available as either pre-formed tubes or via a tension winding process. The maximum pre-stress available with a heat shrunk Inconel sleeve was approximately 1GPa, due to the limit on heating of the Inconel for safe handling purposes, as noted in 2.5.2. The same 1GPa level of pre-stress was available for a composite sleeve, via a tension winding process. The ultimate limit on the tension that could be applied via the winding process was caused by fibre fraying and breakage in the tow being wound. Carbon fibres are very weak perpendicular to the main fibre direction, and the dry, unimpregnated tows are easily frayed and damaged by the tensioning equipment at tension levels above a fixed limit. Alternate tow materials were available which could allow a greater level of pre tension, namely Kevlar and Zylon; Kevlar was precluded as its ultimate tensile strength is approximately 60% that of standard IM7 carbon fibre [118, 119], reducing the stress safety factor possible in the sleeve, so was discounted for that purpose. Zylon fibres have a similar UTS to IM7 fibres but exhibit less fraying and can sustain a greater tension in the winding process, however they have been known to exhibit significant degradation of performance over time due to hydrolysis in moist environments at elevated temperatures [120], so were precluded again for safety reasons. The technologically mature and well understood carbon fibre was chosen as the preferred base for any composite sleeve.

As both composite and metallic sleeves were available with pre-stress levels of 1GPa, the composite sleeve was chosen over the Inconel due to its lower density. For a highly stressed machine, the Inconel would have to sacrifice more of its pre-stress capability resisting its own body forces than a composite sleeve would have to, leading to a smaller rotor diameter or lower magnetic loading.

The resin chosen for the sleeve matrix was Tencate EX1510, which can be cured to give a glass transition temperature of approximately 230°C, allowing very high temperature operation of the rotor if required and allow a large safety margin in the design.
The detrimental effect of a composite sleeve blocking the thermal conduction path to the air gap of the machine was deemed to be a low priority as rotor ducting could be used to compensate.

A further constraint imposed on the rotor was to ensure that the tip speed of the rotor sleeve did not exceed 250m/s at the operating speed, accepting that the rotor design was experimental and so to keep it in line with existing accepted high speed machine limits [22, 28]. Once the rotor design and performance was well understood through a prototype, this constraint could be relaxed. This tip speed limit placed a maximum radius constraint on the demonstrator machine, which was approximately 80mm at 30,000rpm.

5.3.3 Available Cooling Technologies

The proposed installation site for the dynamometer contains a water cooling loop running at 6°C, other cooling technologies are allowed to dump heat into this cooling loop via a heat exchanger but cannot access the loop directly. This direct cooling access allowed the selection of a high capacity water cooling system that cools the drives (allowing the use of the Unico system) and has spare capacity to provide water jacket cooling to the machine as well. The use of a water jacket allows an initial target current density in the windings to be set at 15A/mm^2 [40], which can be considered to be the initial 'thermal loading' of the machine as the winding losses dominate in HSHP machines. This thermal loading is comparable to the electrical loading of MMF per unit periphery of the rotor and the mechanical loadings of rotor stresses and critical speed. In addition to this an air pumping system was chosen to allow forced ventilation inside the machine. The system can deliver a high volume of air flow at 10kPa above ambient pressure direct to the machine or can be fitted with a chiller unit to provide cooled air at a lower pressure. To allow a large volume of airflow through the machine and reduce the resistance to flow, the air gap of the machine was specified to be 4mm initially. The minimum temperatures on the water jacket coolant fluid were set by the dew point in the intended application location, to prevent condensation on electrical components, including the drives; this minimum temperature was set at 25°C. For the air coolant system, compression losses were calculated to add approximately 10°C to the air temperature after compressing it to 10kPa above ambient pressure, given the application environment was air conditioned a worst case air inlet temperature to the machine was set at 40°C.

5.3.4 Available Lamination materials

For cost reasons, the choice of lamination materials was limited to that of commonly available non-oriented silicon steels. A broad range, supplied by Cogent steels [121] was available in small order quantities to enable prototyping. The lamination thickness ranged from 0.1mm to 1mm, with cost decreasing, but loss increasing with increasing thickness. The minimum sheet dimensions that could be ordered were 300x300mm. A lamination thickness of 0.1mm chosen to minimise iron losses given the high operating frequency and material selection limits. A stacking factor of 0.95 was achieved with this material

5.3.5 Available Magnet Materials

Both NdFeB and SmCo magnet materials were readily available during the design process, however at the time of the design the price of the dysprosium dopant for high temperature capable NdFeB magnets had spiked, pushing their prices above that of SmCo [55]. A further design choice was made based on the temperature performance of the magnets: while NdFeB has a higher induction at low temperatures, its performance degrades faster with temperature than that of SmCo, thus there is a crossover point at a higher operating temperature where SmCo will actually deliver a higher magnetic loading for the rotor than NdFeB. This crossover is illustrated in Figure 5-5 for two common grades of the magnets, showing a transition around a rotor operating temperature of 140^{o}C; above which SmCo will deliver a better magnetic performance.

This performance improvement with temperature and SmCo's improved resistance to demagnetisation at high temperatures compared to NdFeB led to SmCo being the chosen magnetic material for use in the demonstrator being designed.

This selection was made despite SmCo having a high density and hence adding additional stress to the rotor sleeve for no additional magnetic loading improvement, as the uncertainties of a prototype design led to an expected variation in the rotor temperature. Thus the temperature stability and resistance to demagnetisation of SmCo as well as its reduced cost were considered to be more critical than the marginal loss in rotor magnetic loading ability.

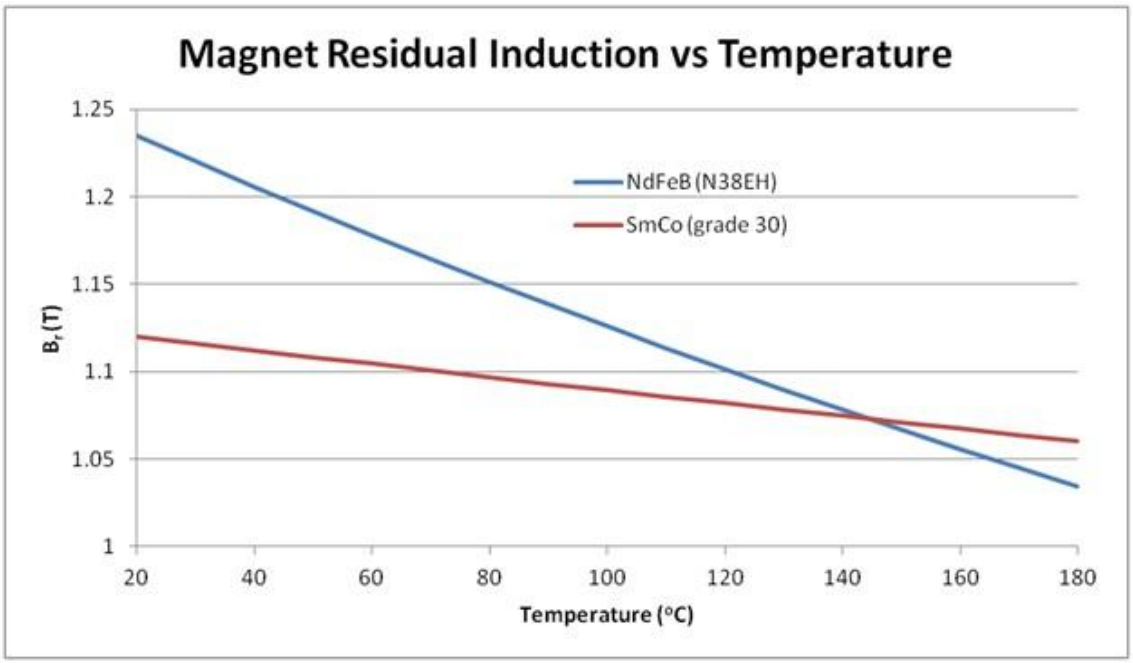

Figure 5-5: Magnet Residual Induction vs. Temperature

5.3.6 Available Bearings

The bearing technology chosen was an angular contact bearing with oil jet lubrication which also provided direct cooling for the bearing packages, isolating them thermally from the rest of the machine. The performance limit of these bearings enabled a maximum 50mm shaft diameter to be used at 30,000rpm.

5.3.7 Available Stator Insulation

The thermal limit of possible electrical insulation materials was an important factor in choosing the machine thermal operating point; in particular the limitations in performance of the materials used for the wire enamel, slot liner, impregnation resin and lamination stacking adhesive were a critical factor in their selection. The current IEC standard for insulation materials, 60085, defines preset ratings for insulation materials based on their operating temperature, as summarised in Table 5-3. For a material to be placed in a certain class it must last without failure for a predetermined time at that operating temperature, typically 20,000 hours as defined in ASTM D2307.

Operating temperatures (°C)	Thermal Class	Historical class
90-105	90	Y
105-120	105	A
120-130	120	E
130-155	130	B
155-180	155	F
180-200	180	H
200-220	200	-
220-250	220	-
>250	250	-

Table 5-3: Insulation Thermal Classes [122]

For thermal robustness a rating of 240°C was targeted, based on NEMA Classification C, placing the motor Design in the IEC 220-250 thermal class. To achieve this, special care had to be taken to select appropriate materials.

Enamelled magnet wire comes in various insulation grades that match the IEC rating system, the best performing grade being a Polyimide coating rated at 240°C [123]. Slot liner materials made of polyimide, such as Kapton are also readily available, often combined in a laminate with Nomex to improve tear resistance and both are temperature rated to 240°C [124]. For prototyping, a polyimide film known as apical, and manufactured by Kaneka [125] was chosen. An epoxy resin known as Resiblend 2024 was sourced for bonding the stator stack, which had been successfully operated at 240°C for prolonged periods. For VPI of the stator after winding, a low viscosity epoxy based resin, Epoxylite 220 [126], was chosen with a peak temperature performance of 220°C. A de-rating on the thermal performance was accepted as the minimum order quantity for higher temperature resins, such as those for traction motors, was far in excess of what was required for the prototyping stage and was not economically feasible.

5.3.8 Summary of Available technologies

The available technologies, materials and processes are summarised in Table 5-4, included in the table are the relevant values and units to be used in the design, some safety factors have been included to allow for flexibility in the design.

Item	Chosen value	units
Drive Output Voltage	540	V (Line-Line RMS)
Drive Output Frequency	1000	Hz
Drive Output Choke Inductance	5	μH
Sleeve Material: Fibre	Im7 Carbon Fibre	
Sleeve Material: Matrix	Tencate EX1510	
Sleeve Maximum Pre-Stress	1000	MPa
Design speed (stress)	1.2x	Operating speed
Critical Speed Limit	1.414x	Operating speed
Water Jacket Coolant	Water-Glycol	
Water Jacket Coolant Temperature	30	^{o}C
Water Jacket Coolant Flow Rate	1	Litre/s
Target Current Density	15	A/mm^2
Through Ventilation Fluid	Air	
Through Fluid Ventilation Temperature	40	^{o}C
Through Ventilation Pressure	9	kPa (above ambient)
Air Gap	4	mm
Magnet Material	SmCo grade 30	
Bearing Shaft Diameter	50	mm
Winding Wire insulation	Polyimide	
Slot Liner	Apical AV	

Lamination Bonding Resin	Resiblend 2040	
VPI resin	Epoxylite TSA 220	

Table 5-4: Available Technologies, Materials and Processes

5.4 Initial Electromagnetic-Mechanical Sizing

With the choices and limits posed in section 5.3 the first stage of the design process was to perform the mechanical-electromagnetic rotor sizing using the design development tool.

5.4.1 Mechanical Rotor Sizing

With the mechanical constraints defined it was possible to perform a rapid mechanical sizing of the rotor. The specified maximum tip speed of the rotor of 250m/s constrained the maximum rotor diameter to be 160mm, forcing the stress design to be an exercise in maximising the magnetic loading for that fixed radius via adjustments in the sleeve and magnet thicknesses. The safety factor of 1.2 imposed on the operating speed constrained the peak sleeve stress to be met at a design speed of 36,000rpm as opposed to the operating speed of 30,000rpm. The critical speed model used a solid shaft with the magnets and sleeve treated as parasitic masses to generate a worst case critical speed prediction. The initial parameters were used to generate the design space shown in Figure 5-6.

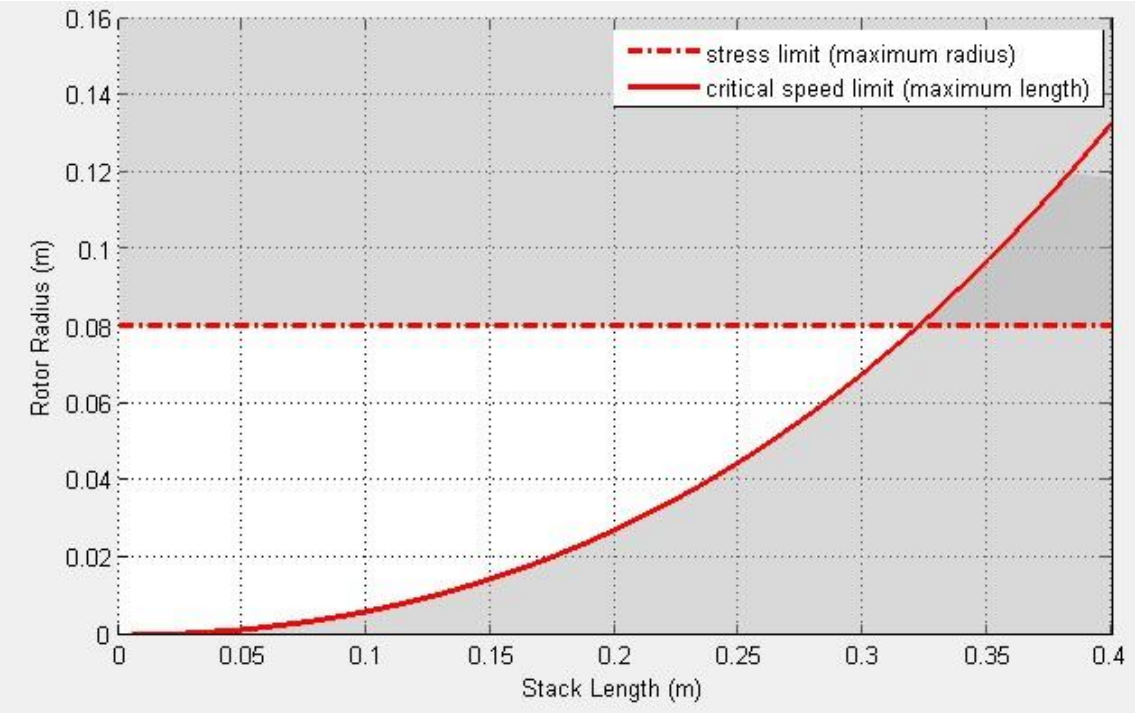

Figure 5-6: Initial Mechanical Rotor Design Space

To achieve the 80mm rotor radius limit the sleeve thickness was initially set arbitrarily to 5mm. The magnet thickness was then increased (thus decreasing the allowable rotor diameter due to the stress limit) until the 160mm diameter threshold was achieved, at a magnet thickness value of 7mm.

5.4.2 Electrical Loading Level

With an initial mechanical sizing achieved it was possible to investigate the electrical design of the machine. The most pressing constraint in this design aspect was the choice of design back EMF and the size of the resultant phase currents. As the available drive line voltage was limited to 540V RMS, a target back EMF line voltage of 380V RMS was chosen in line with the principles set out in section 3.2.1 and the formula in (3.7) to ensure the maximum inductance headroom in the design. With the Back EMF chosen the phase current required for this design to meet its rated power was 1671A RMS and posed severe constraints on the electrical design of the machine.

The first major constraint was on the electric loading level, according to the phasor diagram for the machine shown in Figure 3-1 the armature reaction voltage must also be 380V RMS, limiting the system inductance to 20.89µH. With a 5µH drive choke inductance specified and an estimated 0.5µH of supply cable inductance between the machine and drive, the machine

inductance is therefore limited to 15.39µH maximum. To allow a tolerance of ±10% in the design parameters, a target machine inductance of 13.9µH was thus set. The main effect of this inductance limit is to require a low electrical loading for the machine as higher loading equates to a higher level of flux in the machine and hence a higher inductance. This constraint will have the most direct influence on the number of turns in the design and hence the rotor volume as it poses a direct limit on what is electrically possible.

At the 15A/mm^2 target current density, this current level requires a turn area of 111mm^2, or a single strand diameter of 11.9mm. From this it can be seen that it will be highly likely that each turn will need to be stranded to reduce AC copper losses and to improve the slot fill factor. Further to the effect of the required turn area on stranding, the sizing of the slots in the design will require careful attention, as the desire to reduce rotor losses will favour a distributed winding with multiple slots per phase, whereas the low rotor radius will require these slots to be deep and thin, adversely affecting the leakage inductance.

These two constraints, on electric loading and on turn area, combine to significantly limit both the turn numbers (and hence electrical loading) and the winding design (and hence ability to reduce rotor loss) of the demonstrator dynamometer.

The effects of varying the electrical loading of the dynamometer design are shown in Figure 5-7, showing the options for 1 2 3 and 4 turn (N) designs, with one slot per pole per phase, a four pole machine (12 slots) and a double layer winding.

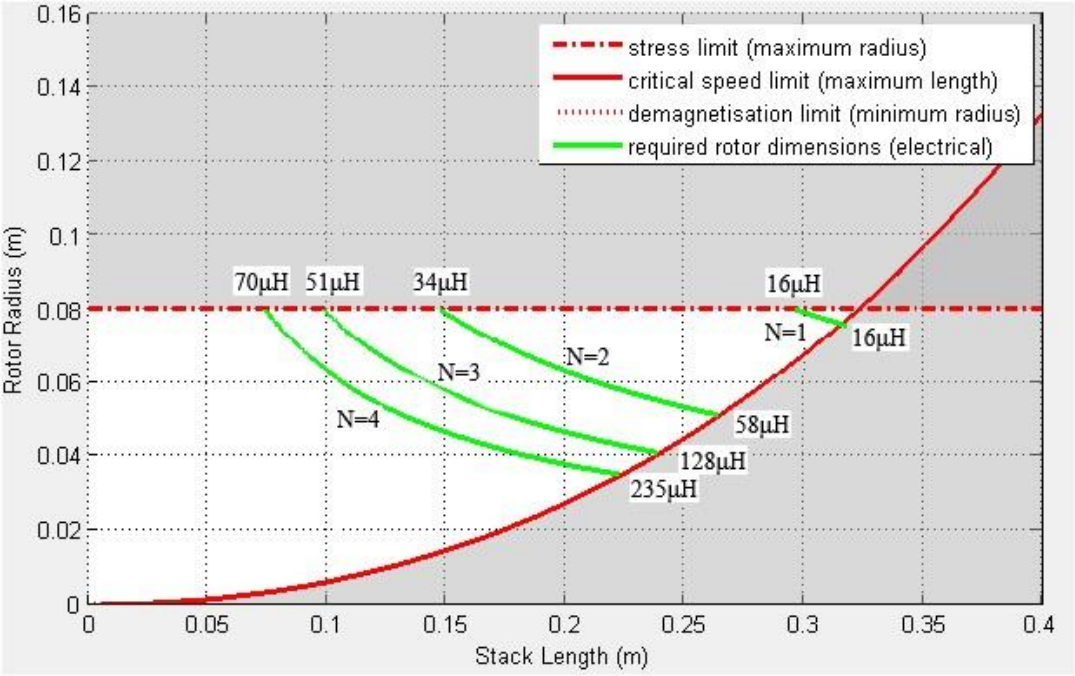

Figure 5-7: Electric Loading Curve Options

As can be seen, the low turn number leads to a discrete set of possible designs, where an integer change in turn number produces a large change in the required rotor dimensions. The demagnetisation limit on the magnets is ignored in this case, to highlight the limitations of inductance and turns number on electrical loading. Included on the graph are the inductances for the designs that intersect the mechanical limits, showing how increasing electrical loading leads to a smaller machine but consequently larger inductance. These inductances were calculated using 2D FEA on the machine geometries described at each intersection. This effect is most evident at the stress limit, where the rotor diameter is fixed and hence extra loading leads to a shorter axial length, but more flux in the machine and deeper slots with more leakage flux.

The effect of varying magnetic loading mentioned in section 3.8 can be seen on the 3 turn curve where halving the rotor radius leads or a 2.5x increase in length. This is due to the significant fixed air gap length in the machine causing the magnetic loading to reduce at small radii.

The effect of slot leakage on the machine inductance can be seen when comparing a small rotor diameter design to a large diameter design of the same electrical loading, where for the same current density the slots of the smaller diameter design must be much deeper and narrower, leading to more leakage flux. It can be seen that a design which maximises rotor diameter is favoured for HSHP machines, to minimise leakage inductances and slot depths; additionally, the larger diameter design allows for a greater range of machine lengths and hence rotor volumes, which is beneficial when adjusting the electrical loading due to the inductance constraint. The difference between large and small rotor diameter designs for the same electrical and thermal loading is shown in Figure 5-8. Each design is taken from the intersection of the 3 turn electrical loading curve with the mechanical limit curves in Figure 5-7.

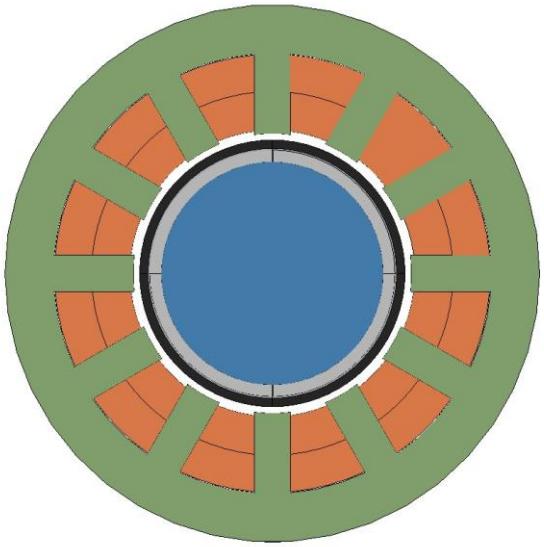

"Short Fat" Design, Axial Length = 104mm

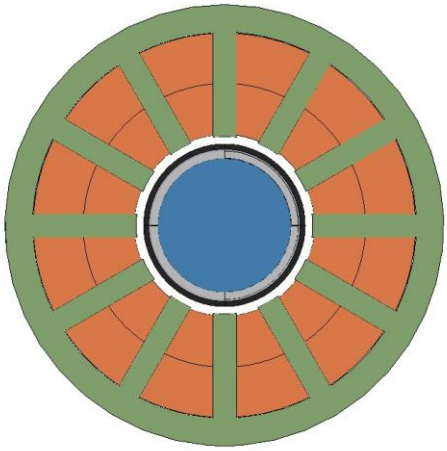

"Long Thin" Design, Axial Length = 243mm

Figure 5-8: Small vs Large Rotor Radius

It is clear that the low diameter design is impractical due to the high inductance; the slot shape is further impractical mechanically due to the need for long thin teeth and thermally as the resistance from the windings to the coreback will be greatly increased by the size of the slot and the thinness of the teeth.

Despite the discrete nature of electrical loading levels caused by the low turn numbers, some adjustment of the design parameters is available to the designer. The leakage inductance of the slots can be adjusted by changing the slot openings and tooth widths, while the 'magnetising' inductance of the armature can be adjusted via the winding design and by adjusting the armature air gap through changes in the magnet and sleeve thickness. Both these techniques for adjusting the loading are best left to the detailed design stage using FEA for validation as their benefits must be weighed against changes to the thermal circuit and loss levels in the machine.

The turn numbers of a design are ultimately limited by the electric loading constraints, specifically the allowable inductance of the machine. For the demonstrator being designed, it can be seen that this limit allows only a one turn per layer per pole per phase design to be considered for the inductance to be close to the target level of 13.9μH. As this target is not met by the basic design presented it is clear that adjustments to the windings and geometry of the machine will need to be made to reduce the inductance to the target value. These will be detailed in the following sections. =

5.4.3 Winding Design

The first consideration in the winding design of the machine was to choose the pole number; the choice of the Unico drive rated to supply 1kHz allows selection of a 2 or 4 pole design. A four pole design was chosen as it reduced the required magnet thickness to resist demagnetisation, given the 1pu armature reaction, and delivered the smallest end winding volume, allowing for the closest possible bearing spacing to improve the critical speed performance.

The low turn numbers caused by the electrical loading constraints pose a serious challenge to the winding design of the machine, and it becomes difficult to keep rotor losses to manageable levels. The space harmonic MMF's in the air gap that drive rotor losses can be dramatically reduced by distributing and short pitching the windings of the machine, but this is only possible if the design has enough turns to allow it. The maximum turn numbers required by the design in section 5.4.2 are limited to only one option, as stated, due to the inductance limit, being one turn

per layer per pole per phase, giving a 12 slot design and leaving little flexibility in the winding design to reduce the armature MMF space harmonics. The only options available are to short pitch the second layer or to distribute the layers over two slots in a 24 slot single layer design.

In order to regain flexibility in the winding design parallel winding paths were considered, to reduce the current per slot requirements and increase the options for distributing and pitching the windings. The ability to distribute or pitch the windings not only helps improve rotor loss but allows the phase MMF's to be altered and hence give some flexibility in altering the machine inductance, which is currently too high in the initial 12 slot one turn design. Given the number of poles in the machine, the numbers of parallel paths were limited to 2 or 4, in order to ensure that the voltage magnitudes and phases could be matched in each parallel path. In turn the windings of a phase could only be distributed over 1, 2 or 4 slots. The options for winding the machine and the associated rotor losses (using the method for space harmonic losses with a pure sinusoidal current input described in Chapter 3) and length (at a fixed rotor diameter of 160mm) are listed in Table 5-5, including the limited options available if no parallel paths are used, as well as those available to parallel path designs.

Layers	Distribution	Short Pitchin g	Slot No.	Parallel paths	Turns/ slot	Rotor loss (W)	Required Rotor length (mm)
Single layer	1	N/A	12	1	2	12126	294.5
	2	N/A	24	1	1	2146	304.9
	4	N/A	48	2	1	985	307.5
Double Layer	1	1	12	1	2	10500	340.1
		2				6060	589
	2	1	24	2		760	315.7
		2				1860	352.1
	4	1	48	4		375.3	310.2
		2				89.8	318.4
		3				271	332.9
		4				853.5	355.1

Table 5-5: Winding option for four parallel paths

It can be seen from the data presented in Table 5-5 that the effective turn numbers per pole per phase in each design give the same electric loading (in amps per unit periphery of the rotor), but the peak armature MMF varies due to the pitching and distribution of the coils. This variation in armature MMF can be seen in the required rotor length, which increases with both distribution and pitching. A similar effect will be seen in the machine inductance as the lower MMF will give a lower inductance.

The biggest effect of varying the winding design can be seen on the predicted rotor losses, which are predicted for a perfect sine wave current input. The predicted rotor losses for the basic 12 slot design are excessively large and it is clear that distribution and pitching are required to reduce these losses. The stand out design in terms of loss reduction can be seen to be a four parallel path design, distributed over four slots and short pitched by two slots, giving a very low rotor loss without dramatically increasing the required rotor length. This design was chosen as the optimal winding design for the demonstrator, due to the very low rotor losses it can deliver. It furthermore led to a lowering of the machine inductance to 14.8μH – much closer to the target value.

The key reason for the high performance of the chosen winding design lies in the space harmonics produced, Figure 5-9 shows the space harmonic spectrum for several of the winding designs listed in Table 5-5. It must be noted that the figures display the space harmonic numbers which are twice the electrical harmonic order due to the design being four pole. It can be seen that distributing the windings over multiple slots in the single layer cases attenuates the low order harmonics, 5^{th} and 7^{th} in the case of the 24 slot design and the 5^{th} to the 19^{th}. The addition of short pitching in the 48 slot design allow further attenuation of specific harmonic groups; short pitching by one slot damps the 11^{th} and 13^{th} harmonics, while short pitching by two slots attenuates the 5^{th} and 7^{th} harmonics which are the main loss causing harmonics due to their deep penetration into the air gap.

It is clear from Figure 5-9 that the 48 slot, double layer design with a short pitching of two slots gives the best performance in terms of reducing the loss causing space harmonics in the air gap and reducing the slot aspect ratios due to the multiple parallel paths, reducing the required current per slot. For these reasons this was the winding design chosen for the demonstrator machine.

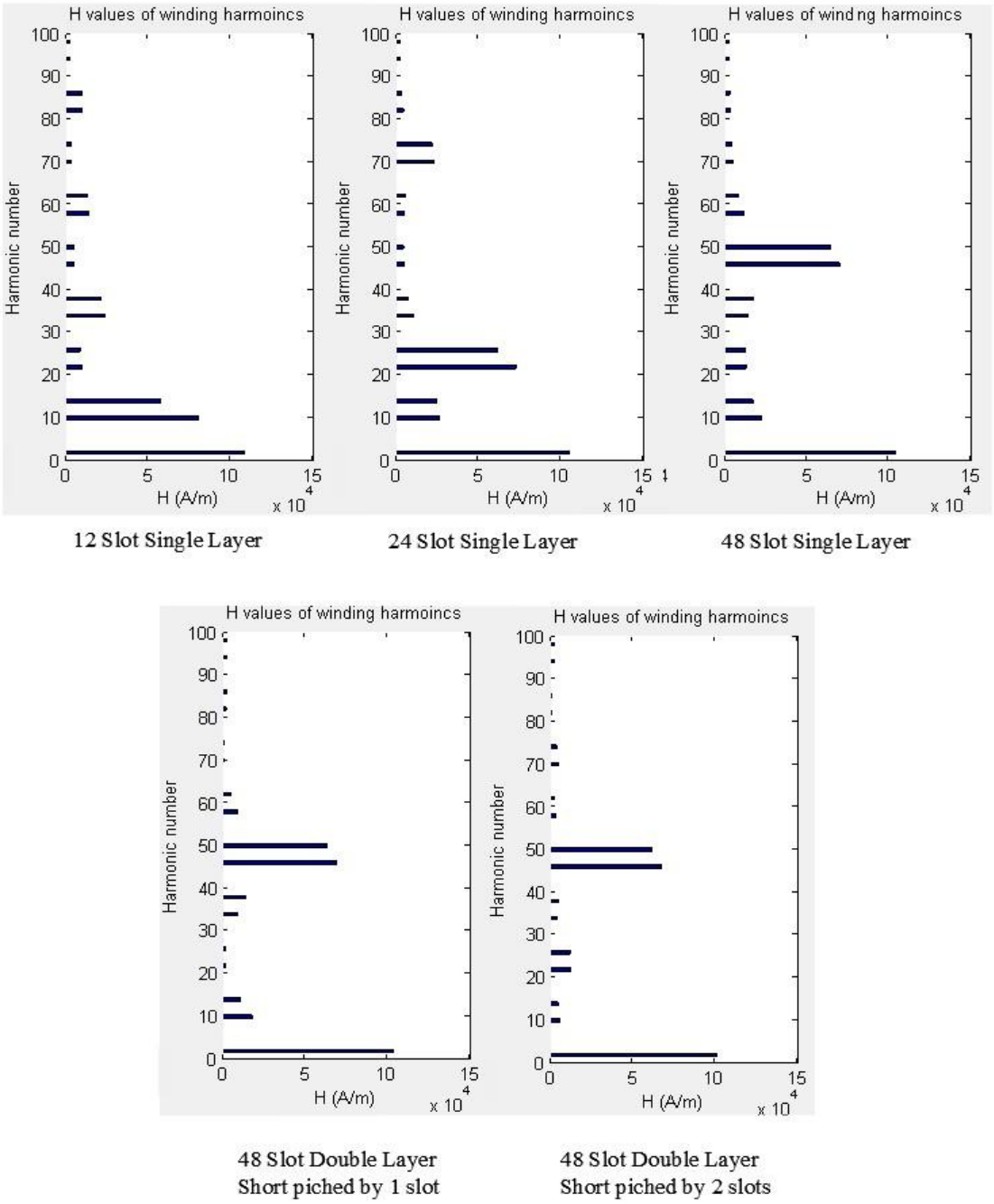

Figure 5-9: Winding Design Harmonics

5.4.4 Initial Machine Design

The initial design developed by the mechanical-electromagnetic iteration process is summarised in Table 5-6, with the initial machine cross-section shown in Figure 5-10. This design meets the requirements for mechanical stability and electromagnetic performance, with the exception of the design inductance being too high. This value will need to be adjusted in the detailed design stage but the value of 14.6μH is close enough to the target parameter that minor design changes should

be sufficient to reduce it. With the initial iterations complete the next step in the design process is to perform an initial thermal iteration with the predicted losses to identify if there is a risk of overheating in the design. If the initial thermal iteration is seen to lie comfortably within the material thermal ratings then a detailed design using FEA can be undertaken to improve the loss predictions and validate the analytical models.

Item	Value	Units
Rotor Diameter	160	mm
Active Length	318.4	mm
Air gap	4	mm
Pole Number	4	
Magnet Thickness	7.1	mm
Sleeve Thickness	5	mm
Parallel Winding Paths	4	
Slot number	48	Slots
Slots/phase/pole (distribution)	4	Slots
Short pitching	2	Slots
Phase Currents	1671	A RMS
Line-Line Voltage	380	V RMS
Inductance Estimate	14.8	μH
Slot Fill (%copper in slot)	50	%
Slot Depth	22.26	mm
Tooth Width	5.5	mm
Machine Outer Diameter	272	mm
Magnet Material	SmCo Grade 30	Recoma
Lamination Material	Cogent NO10	
Shaft Material	High Strength Steel	

Table 5-6: Initial Design Parameters

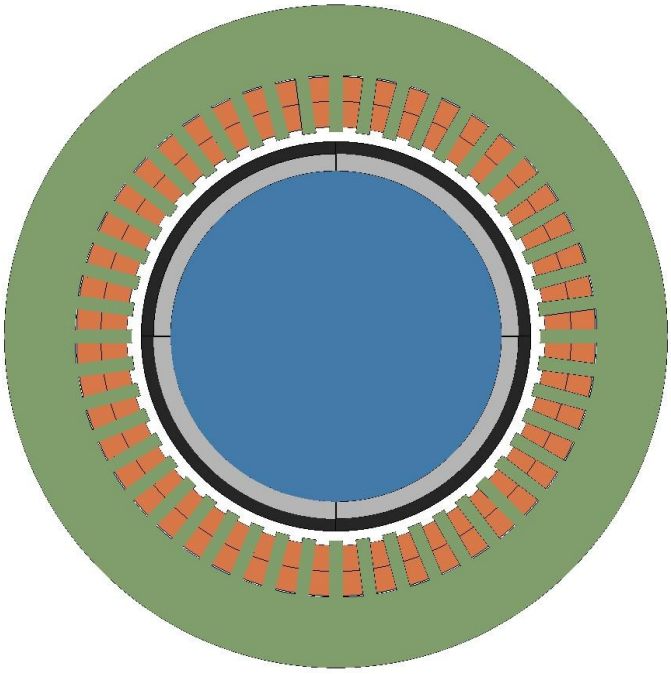

Figure 5-10: Initial Design Cross Section

5.5 Inclusion of Thermal Design Iteration

The iterative design tool was used to provide some initial loss estimates for the design presented in Table 5-6 as summarised in Table 5-7. These losses were then input into the lumped parameter thermal analysis software, MotorCAD, along with the cooling system parameters and machine materials give in Table 5-4 to provide an initial estimate of the operating temperatures of the machine. The key temperature values are given in Table 5-8.

Item	Value	Units
Rotor Loss	89.8	W
DC Copper Loss	5479	W
Iron Loss	3122	W
Windage loss	2612	W

Table 5-7: Initial Design Loss Predictions

Item	Value	Units
Peak “in slot” Winding Temperature	138.1	°C
Peak End Winding Temperaure	135.7	°C
Average Magnet Temperaure	83.9	°C
Peak Sleeve Temperature	82.6	°C

Table 5-8: Initial thermal predictions: Key Temperatures

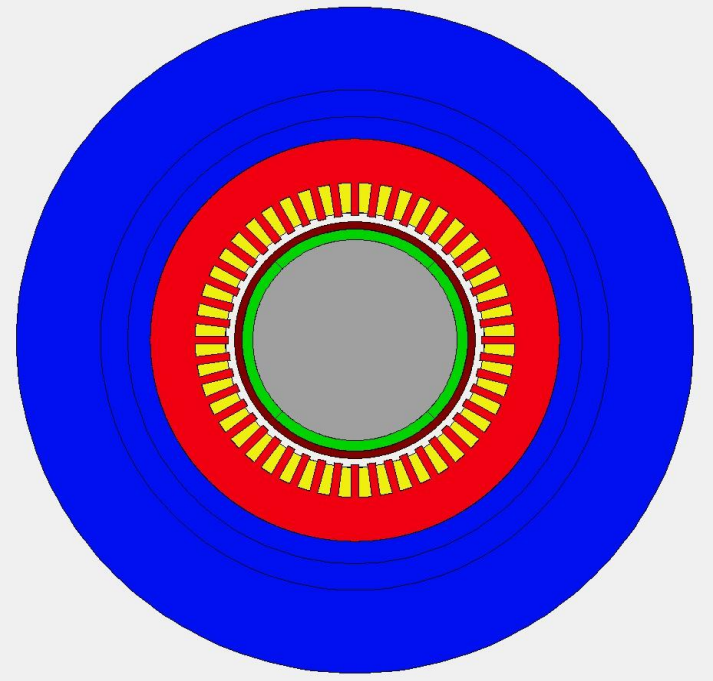

Figure 5-11: Thermal Resistance Network Model End View

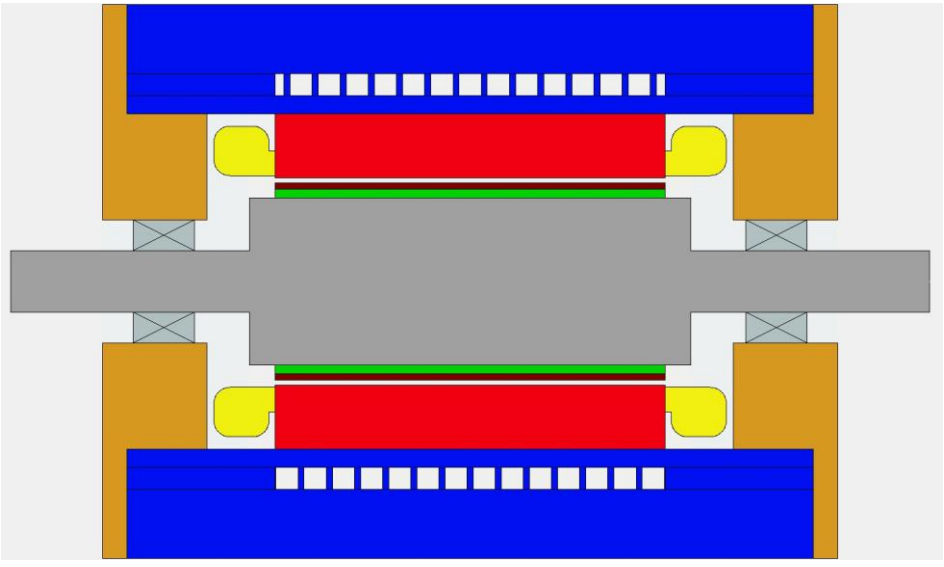

Figure 5-12: Thermal Resistance Network Model Side Vew

To improve the initial thermal estimate it is necessary to include the AC loss effects in the winding loss prediction, to ensure that they do not affect the steady state temperatures significantly. The relatively high frequency of the machine fundamental required the use of stranded wire to reduce skin and proximity losses; furthermore the strands need to be transposed to balance the leakage inductance in each, leaving Litz wire as the only viable choice. Given the shape of the slots and the low turn count per slot, the use of type 8 [123], rectangular compacted Litz was the only effective solution for maintaining a good fill of the existing slot profile. At this stage a change in the design was made, moving to a parallel slot design to better accommodate the rectangular Litz bundles. This change will have little impact on the magnetic performance due to the similarity in slot and tooth shapes afforded by the high slot number and large rotor diameter. Type 8 Litz comes in a variety of profiles and designs following the construction described in section 3.5.3, but with differing bundle counts and strand diameters [123]; from this wide range a selection was made to match the slot profile. Due to the narrow profile of type 8 Litz, two bundles were required to be placed side by side in a slot to form a turn, as shown in Figure 5-13.

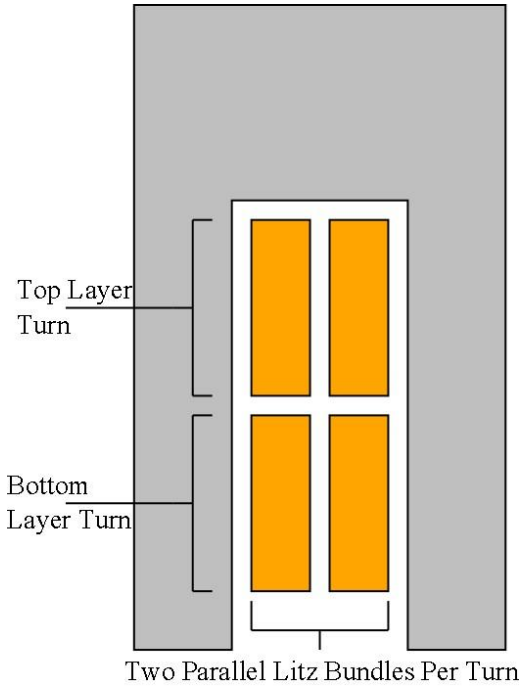

Figure 5-13: Litz Bundle Arrangement in Slot

The catalogue entry for the bundles with the appropriate dimensions for use in the available slot space is shown in Figure 5-14, using imperial units. The equivalent metric data and computed information is given in Table 5-9, with the RMS phase current used to compute the current density

which is adjusted in turn for the increase in strand length per unit bundle length caused by the transposition.

Equivalent AWG	Circular Mil Area	Number of Strands	AWG of Strand	Film Coating[1]	Nominal Width	Nominal Thickness	Nominal LBS./1000 FT.	Direct Current Resistance OHMS/1000 FT*.	Construction
RECOMMENDED OPERATING FREQUENCY - 60 HZ TO 1 KHZ (CONTINUED) - The following designs utilize 7 strand concentric cnductors for the base group.									
7	24780	98	26	H	.397	.097	79.5	.494	14X7X26
6	26550	105	26	H	.424	.097	85.2	.461	15X7X26
6	28320	112	26	H	.452	.097	90.8	.432	16X7X26
6	30090	119	26	H	.479	.097	96.5	.407	17X7X26
6	31860	126	26	H	.507	.097	102.0	.384	18X7X26
5	33630	133	26	H	.534	.097	108.0	.364	19X7X26

Figure 5-14: Available Litz Bundle Catalogue Entry [123]

Strands per bundle	98	105	112	119	126	133
Bundle width (mm)	2.46	2.46	2.46	2.46	2.46	2.46
Bundle Height (mm)	10.08	10.77	11.48	12.17	12.88	13.56
Copper area (mm^2)	12.56	13.45	14.35	15.25	16.14	17.04
Copper Volumetric fill (%)	53	53	53	53	53	53
Current Density (A/mm^2)	16.6	15.5	14.6	13.7	12.9	12.3
Increase in DC resistance due to transposition (%)	18	18	18	18	18	18
Equivalent Current Density (A/mm^2)	19.6	18.3	17.2	16.2	15.3	14.5
Minimum required slot dimensions (mm x mm)	4.9x20.2	4.9x21.5	4.9x23.0	4.9x24.3	4.9x25.8	4.9x27.1

Table 5-9: Litz Bundle selection data

It can be seen from Table 5-9 that the transposition effects on strand length are significant, leading to an 18% increase in resistance and DC loss, causing the effective current density of the design to increase by an equal proportion. To compensate for this the slot dimensions had to be increased to reduce the effective current density back to the target $15A/mm^2$. This led to the 126

strand litz bundle to be chosen as the wire for the design. Higher strand designs were precluded at this stage, in order to minimise the potential for slot leakage caused by making the slots deeper.

With the 126 strand bundle chosen for the demonstrator, it was possible to use the analytical analysis presented in section 3.5.2 to predict the AC loss effects of choosing this wire for the 1kHz fundamental machine frequency. The AC losses were predicted to increase the DC losses by 7.6%, giving an adjusted machine copper loss of 5861W calculated using the Litz bundle resistvity and the AC loss adjustment factor; this could then be used to re-estimate the key machine temperatures. The slot profile was adjusted to be 6mm wide, to allow for tolerance variation on the litz bundles and leave room for slot liners and similarly the slot depth was adjusted to 28mm, to allow for insertion of insulation and a slot wedge.

Using MotorCAD, the recomputed slot temperature dropped to 135.1ºC despite the increased loss, due to the improved volumetric slot fill and an improved slot shape that reduces the conduction path for the windings at the base of the slot and reduces the tooth thermal resistance.

Given that the initial sizing, analytical optimisation and thermal estimates showed no significant problems with the design, it was possible to move onto the detailed design stage using various FEA analyses to confirm the machine parameters and validate the predicted losses.

5.6 FEA Validation and Detailed Design

Due to the high current densities in the copper, it was considered important to assess the end effects of the machine, as the end winding regions are expected to generate a significant amount of flux which would adversely affect the machine inductance. Three dimensional electromagnetic FEA models were built to assess the torque output and losses of the machine as well as quantify the inductance contribution of the end windings.

5.6.1 Machine Torque Estimate and Back EMF

A 3D FEA model was generated to assess the torque performance of the design and validate the accuracy of the analytical predictions of both torque capability and back EMF values. The

periodicity of the four pole design and the symmetry of the axial length allowed the model extent to be reduced to that shown in Figure 5-15.

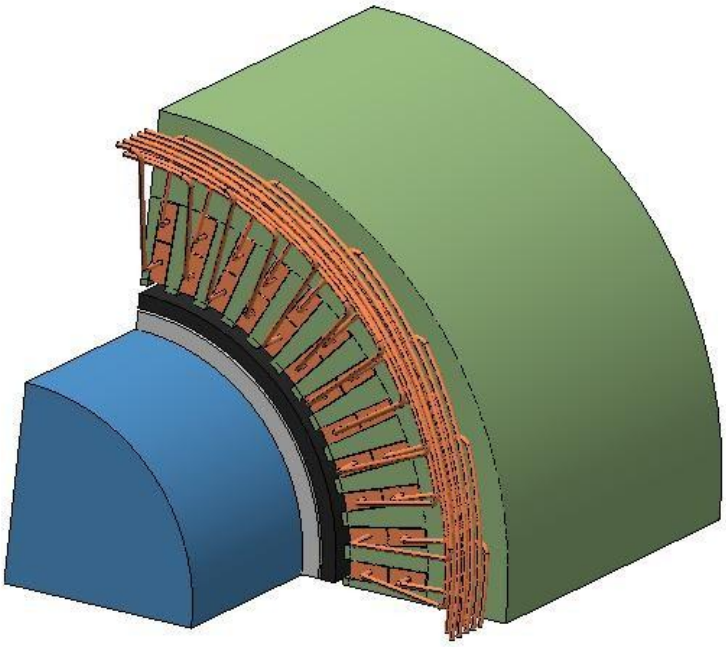

Figure 5-15: Initial 3D Magnetic FEA Model

To simplify the modelling process of the windings the conductors in the slot were modelled as a homogenous mass that covered the full coil extent while at the end windings the coil was reduced to a small diameter circle and traced the average extent of the end winding bundle. While this may reduce the accuracy of the model through imperfect representation of stray field in the end windings the effect was expected to be minimal.

Using this model the predicted torque performance for one mechanical revolution is shown in Figure 5-16 while the back EMF voltages for a phase and a line are shown in Figure 5-17.

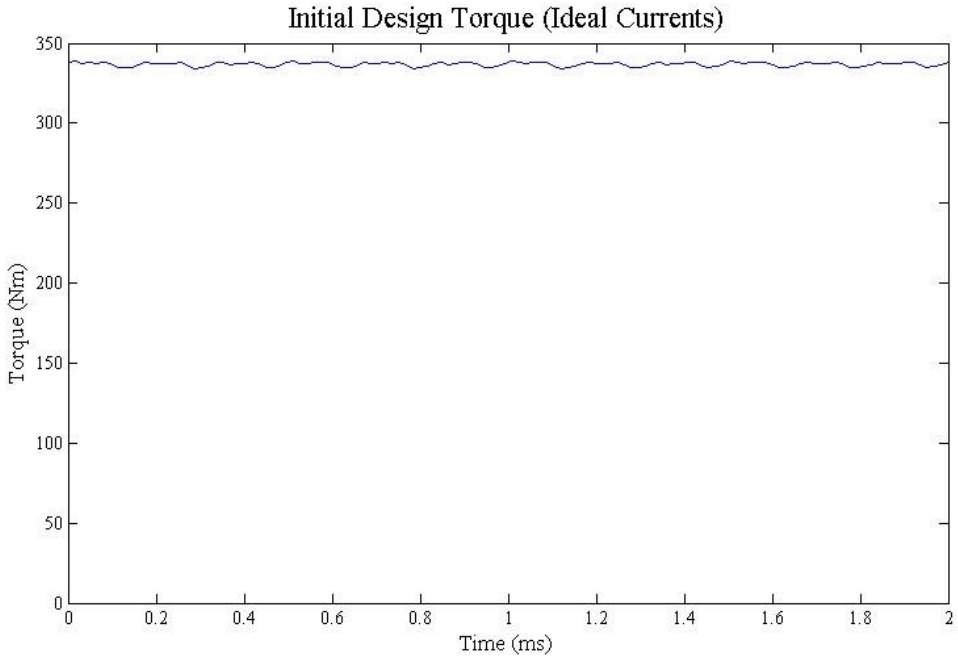

Figure 5-16: Initial 3D Torque Performance Prediction

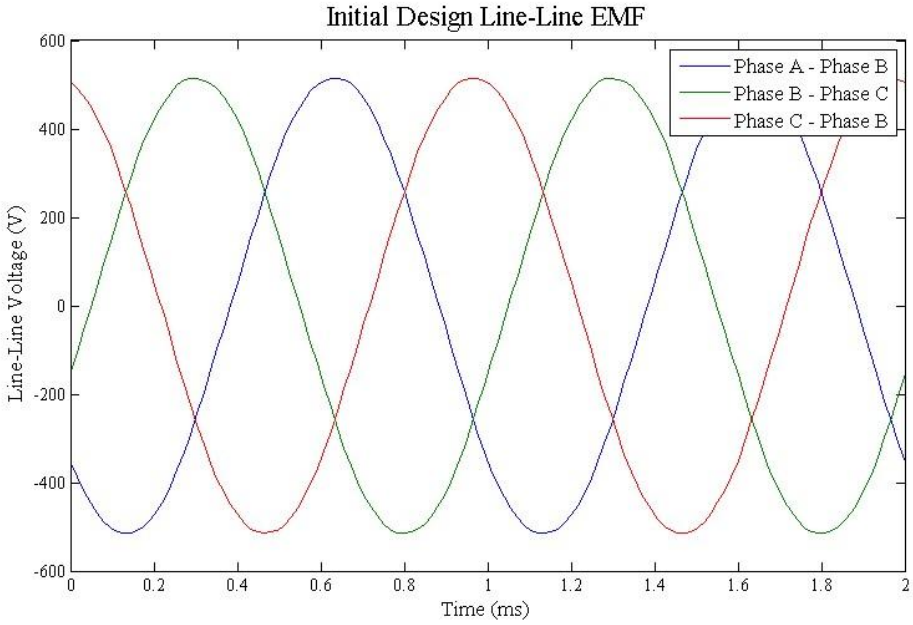

Figure 5-17: Initial 3D Back EMF Voltages

It can be seen from Figure 5-16 that the initial design underperforms in terms induced line to line back EMF, which is 3.4% lower than the target at 367V RMS; implying that the analytical estimate of the amount of flux linkage of the machine coils is low. The error in EMF will be dominated by errors in the estimation of the reluctance paths seen by the magnets, caused by ignoring slot opening effects on the air gap reluctance (Carter coefficient) and in assuming infinite permeability in the laminations and shaft. The follow on effect of low EMF performance

due to low levels of flux is the low torque performance at rated current that can be seen in Figure 5-17; the torque performance is

3.7% less than the design point at 337Nm.

Although these results are very close to the analytical prediction and could easily be compensated by a small change in axial length of 3-4%, other significant design issues are presented by this initial design. These issues are the machine inductance and loss levels, which must be addressed before attempting to hit the rated torque performance in

FEA by 'trimming' the axial length of the machine.

5.6.2 Machine Inductance

Using the same model as that shown in Figure 5-15, an estimate of the machine inductance, including end effects, was performed using DC currents in the windings and removing the magnet material coercivity. This gave a result of 18.7μH, clearly larger than the 13.9H target inductance.

Due to the machine inductance prediction being too large, alterations to the design were required to reduce this value to an acceptable level. Due to the rotor design being at its mechanical limits any changes could not affect the torque performance of the machine as rotor volume could not be increased to compensate. Thus the method chosen for reducing the machine inductance was to increase the armature air gap by making both the magnet and sleeve thicknesses larger, this must be done without exceeding the stress limit, so a mechanical-electromagnetic design iteration was required, using the analytical design tool to size the rotor followed by a 3D FEA validation of the machine inductance. The alterations performed are summarised in Table 5-10, where the sleeve thickness was increased and magnet thickness increased accordingly to maintain the same stress limit for the 160mm diameter.

It can be seen that there is an additional gain in torque density by using thicker magnets, despite the increase in sleeve required to retain them, however in the interests of minimising magnet volume and cost it was decided not to pursue this trend beyond that needed to achieve the target inductance. Using this data, the chosen values for sleeve thickness and magnet thickness were updated to be 7.5mm and 12mm respectively, to meet the target inductance, with a design length of 294mm. It should be noted that the chosen magnet thickness was larger than that recommended by the analytical design tool however validation though mechanical FEA showed

that this arrangement delivers a safe stress level at the mechanical design speed, as will be shown in section 5.6.7.

Sleeve thickness (mm)	Magnet thickness (mm)	Machine active axial length	3D FEA Inductance Prediction (μH)
6	7.1	318.4	18.7
7	8.9	305.6	16.3
8	10.9	296.8	14.7
9	13.2	291.1	13.3

Table 5-10: Inductance Reduction Summary

5.6.3 Rotor Loss Validation

Rotor manufacturing limits restricted the size of any one magnet piece within the rotor to being no more that 50mm x 50mm, this limit was mainly due to ensure safe handling of large magnetised items during assembly but also to minimise costs due to breakages and allow use of standardised feedstock. Given the rotor diameter and sleeve thickness, the arc length of one pole of the machine is 113.9mm at its outer surface, requiring it to be made of at least three segments, each spanning 30^{o} and having a maximum cord length of 37.5mm at their outer surface, comfortably within the allowable 50mm limit. Given the axial length of the machine is approximately 300mm, 6 segments were required axially to span the distance. The initial design used arc shape magnets mounted on the rotor surface, however there was an engineering cost associated with grinding two accurate concentric arcs on the magnet top and bottom surfaces. This cost led to the adoption of flats on the magnet bottom surface, in contact with the shaft, to simplify the magnet manufacture and add a locating feature for assembly. A typical magnet segment and its arrangement on the shaft is shown in Figure 5-18, and is magnetised normal to the flat lower face: it is commonly known as a ‘breadloaf’ shaped magnet

The manufacturing limit placed in magnet size meant that it was necessary to assess the effects of this segmentation on the expected machine losses, given the knowledge of the loss mechanisms outlined in section 3.3.2. The expected drive THD could not be calculated until the machine dimensions were finalised so an interim estimate of 8% THD was used, derived from the worst case results delivered on a previous project using a lower power machine but with a similar per unit armature reaction. The breakdown of the harmonic magnitudes is summarised in Table 5-11,

the higher order harmonics are dominated by the drive switching effects at 16kHz and their first sideband at 32kHz; the resultant current waveform for one phase is shown in Figure 5-19.

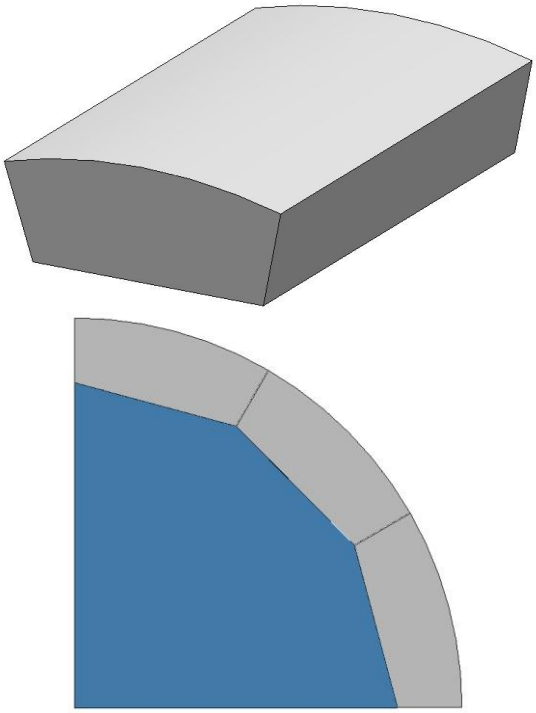

Figure 5-18: Magnet Segment Shape and arrangement

Harmonic Order	Magnitude (% of Fundamental)
5	3
7	3
13	4
17	4
29	3
31	3

Table 5-11: Harmonic Spectrum of Phase Current

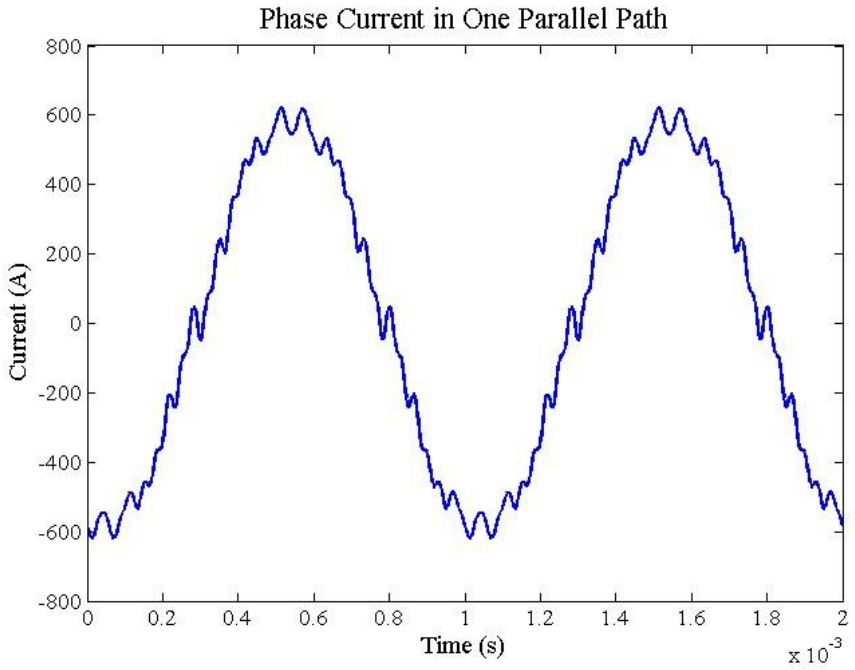

Figure 5-19: Initial Phase Current Estimate with 8%THD

The input current waveform of the shape shown increased the rotor loss of the segmented magnet rotor to 7969W, a clearly unacceptable level of loss. The traditional method of reducing magnet loss was not applicable in this case as it requires the segment dimensions to be below that of the skin depth of the loss causing harmonic. The lowest order time harmonic, the 5th, has a skin depth in the magnets of approximately 6mm, if the rotor was to be covered in 6x6mm segments, over 3700 would be required, a clearly unacceptable number in terms of cost and time for assembly. The only practical alternative is to ensure the magnets are as large as possible, as is the case with the breadloaf design with 3 segments spanning a pole and to include an eddy current shield at the magnet surface to screen them from the time harmonic fluxes. The design of the eddy current shield is an optimisation problem that must balance the losses in the screen with those in the magnets to ensure the lowest possible net rotor loss without increasing the effective air gap unduly. The resistance limiting of eddy currents in the shield caused by varying its thickness allows the designer to control the proportion of flux that is blocked by the shield and allows a balance to be found.

Eddy Current Shield Sizing

In order to optimise the balance between shield losses and magnet losses a 2D FEA simulation was performed using the same current waveform with 8% THD and an aluminium shield, thus including the effects of both space and time MMF harmonics. Aluminium was chosen as the shield materials due to its low density, giving it a better resistivity per unit mass than copper,

which will lead to a minimal effect on the stressing of the rotor. Per Unit loss is plotted as the absolute values between 2D and 3D models cannot be compared due to the end effects, the same eddy current limiting effects occur in both models so the relative effects can be compared. The optimisation process shown in Figure 5-20 clearly shows a net loss minima at approximately 1mm shield thickness.

The disadvantage of using the eddy current shield is that it increases the effective air gap length of the design, reducing the torque density and hence requiring extra axial length to achieve the target torque. Given that the design was close to its critical speed limit it was decided to reduce the actual air gap of the design from 4mm to 3mm to compensate for the addition of a 1mm shield, so that the magnetic loading and hence torque density of the design stayed constant. The inclusion of this 1mm aluminium shield reduced the 3D predicted rotor loss to 764W. This gave an expected magnet temperature of 130^{o}C and sleeve temperature of 110^{o}C.

The inclusion of the rotor eddy current shield completed the specification of the machine topology, allowing the axial length to be trimmed to meet the torque requirements; this process was performed in 3D FEA and gave a final design length of 305mm. This represents a 3.7% increase compared to the analytical design length, as expected due to the error in flux estimation noted in section 5.6.1.

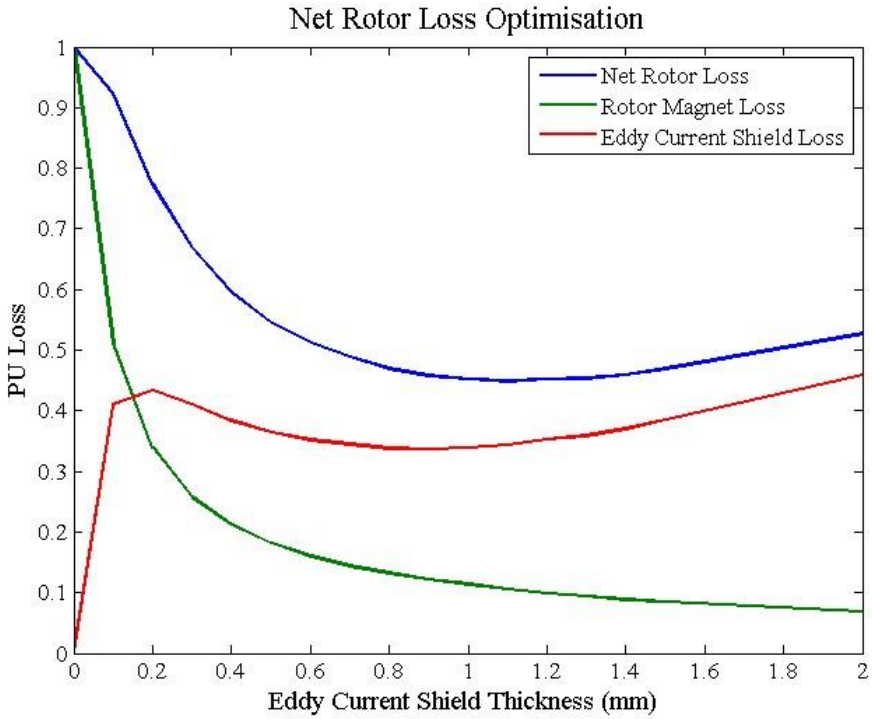

Figure 5-20: Eddy Current Shield Thickness Vs Net Rotor Loss

5.6.4 Inclusion of Drive THD prediction

With the machine topology fully defined, it was possible for the drive supplier to perform a drive simulation to predict the level of THD expected in the system, using information about the motor Back EMF, phase resistance and inductance profile. As described in section 3.3.2, the inclusion of the eddy current shield, though helping to reduce the net rotor loss to manageable levels, gives a frequency dependent inductance profile that affects the drive harmonic output. The line to line Back EMF profile is shown in Figure 5-21 as calculated from the normal time stepping 3D FEA. The frequency dependent inductance profile was calculated using a time harmonic 3D FEA solver, included in the MagNet software package, and is given in Figure 5-22, where the frequency is defined as relative to the rotor, with 0Hz being synchronous. This plot directly illustrates the screening effect of the eddy current shield on asynchronous fluxes as described in [39].

One disadvantage of using the time harmonic solver was that it ignores non-linearity in the steel permeability, instead estimating the permeability by taking the local gradient of the lamination B-H curve using an initial estimate of the flux density in the laminations. This linearization of the model led to a 3.5% overestimation of machine inductance using the time harmonic solver compared to the non-linear Newton-Rapheson solver normally used for inductance estimation. The MMF per phase was kept constant for each frequency that the machine inductance was estimated at, thus the 3.5% error in inductance estimate at synchronous speed was used to scale all resultant inductance estimations from the time harmonic solver. The phase resistance was calculated to be

$$6.33\text{m}\Omega.$$

With the supplied machine parameters the drive supplier estimated the harmonic performance of the drive at full load, using their own proprietary discrete time stepping computer model of the drive and motor system, to allow estimation of the worst case losses.

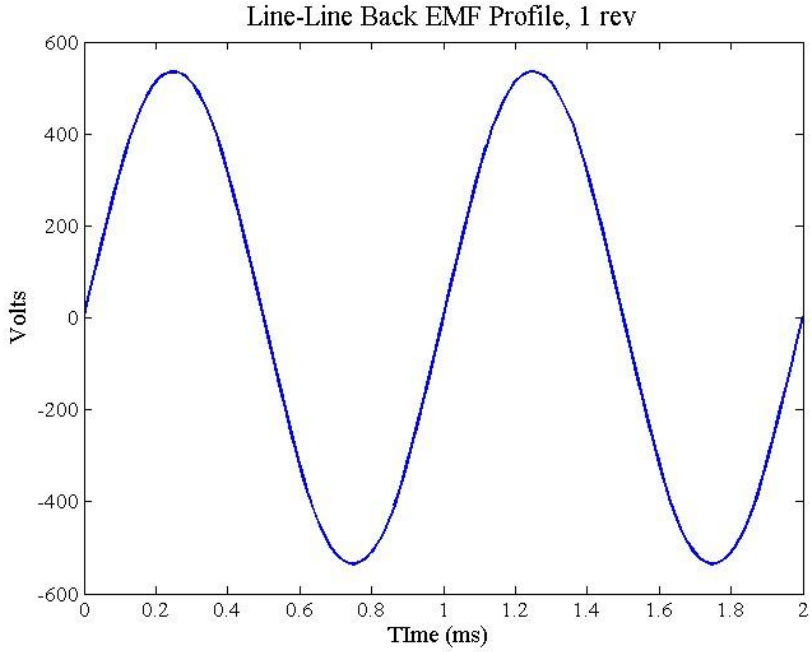

Figure 5-21: Line-Line Back EMF Profile

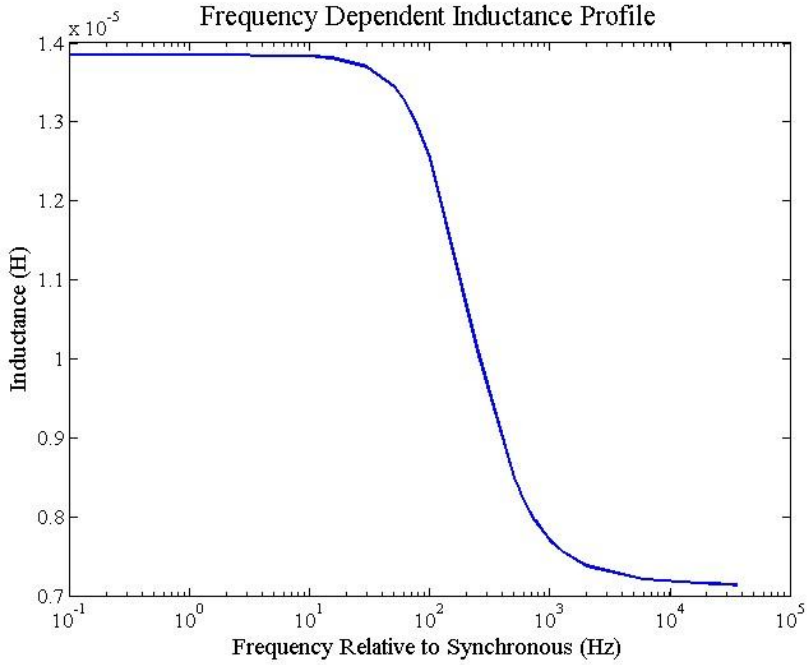

Figure 5-22: Frequency Dependent Inductance Profile

The spectrum of the predicted current harmonics expected to flow in the system is shown in Figure 5-23. It should be noted that the supplier model allowed for potential imbalances in the phase and line inductances and resistances, enabling the flow of triplen harmonics as well as allowing the presence of even harmonics.

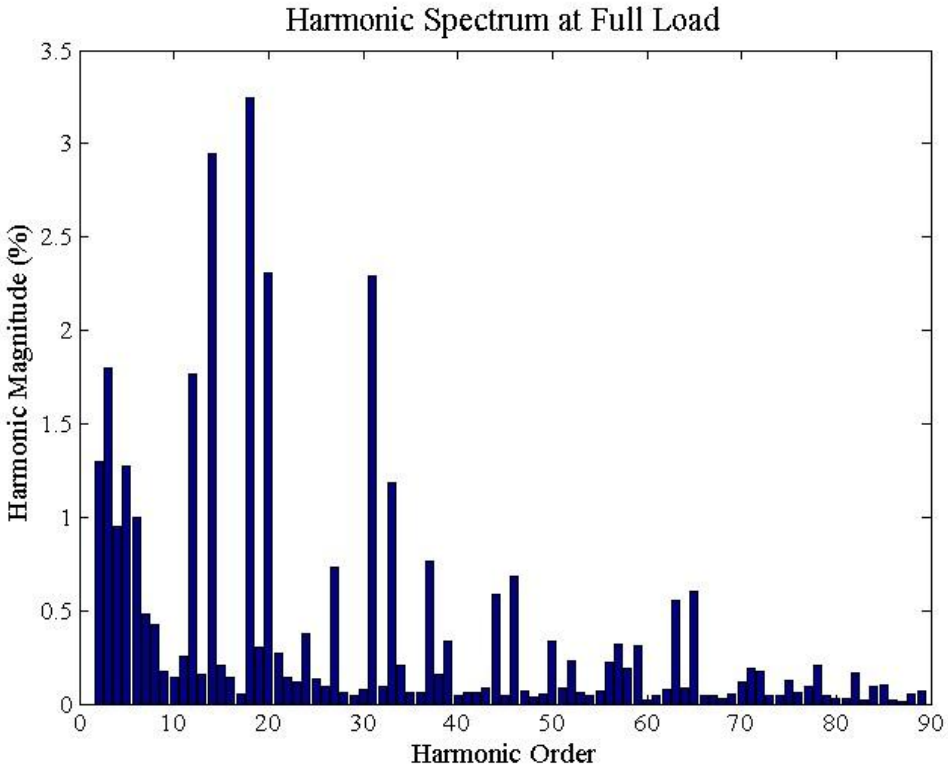

Figure 5-23: Drive Predicted Harmonic Spectrum at Full Load

From Figure 5-23, it can be seen that significant harmonic currents are expected to flow at the sidebands (12^{th},14^{th},18^{th},20^{th}) of the switching frequency, which is represented by the 16^{th} harmonic. There are also significant current harmonics present around twice the switching frequency, namely the 31^{st} and 33^{rd} harmonics.

This harmonic data was converted into the expected time based phase current waveform for the final machine design, taking a similar form to that shown in Figure 5-19. The computed waveform data was input into a detailed time steeping 3D FEA model to provide the most accurate worst case prediction of the rotor loss caused by both space and time MMF harmonics in the machine at full load. The meshing detail of the model is shown in Figure 5-24, which shows the tooth tip detail, sleeve, shield and magnet detail; element edges are highlighted in red and the air gap meshing is hidden. The mesh was optimised for analysing the large pitch time harmonics in the armature MMF, rather than the small pitch space harmonics.

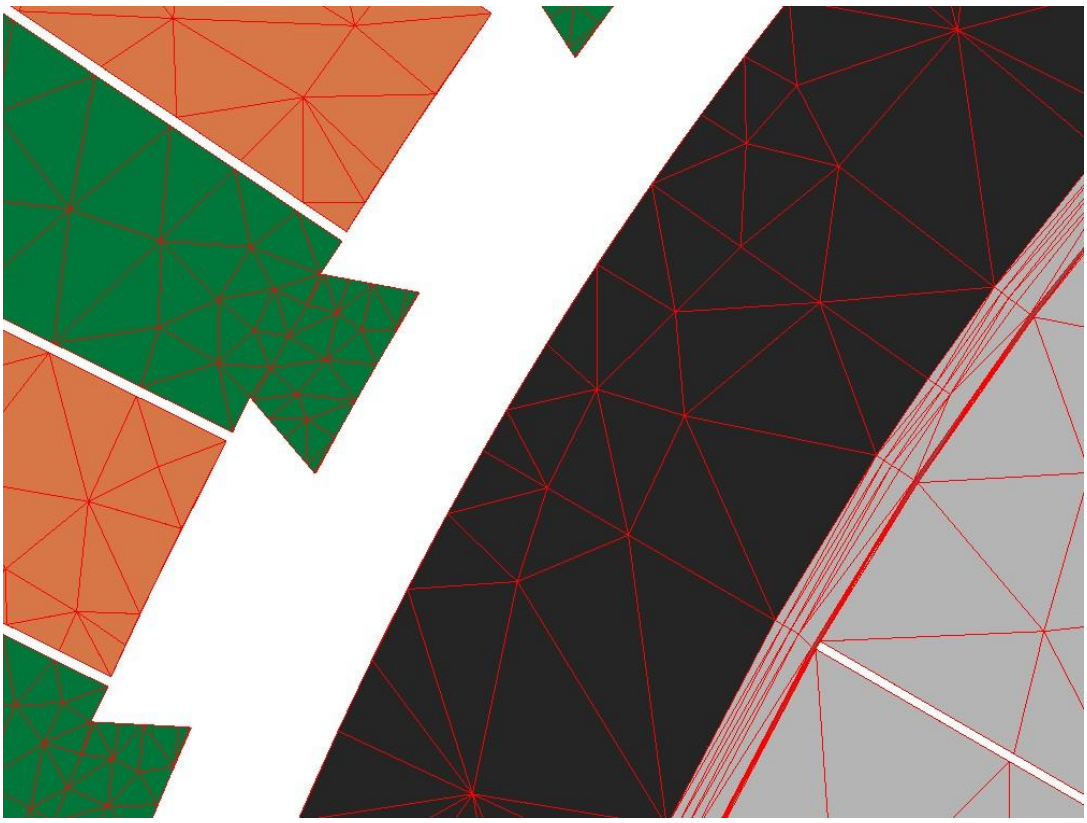

Figure 5-24: 3D FEA Model mesh detail

It can be seen that a multilayer mesh has been included in the eddy current sleeve to accurately capture the skin depth distribution of the various harmonic fields that will be present on the rotor. Throughout the model 'second order' elements were enabled, which allowed the scalar potential calculation in an element to vary by a quadratic

(rather than linear as in normal 'first order') function – giving an improvement in the estimation of the eddy current distribution for small skin depths. The bandwidth of the time stepping solution was 625kHz, which was fully capable of capturing the variation in the modelled harmonics. The combination of these FEA parameters led to a very slow solution time, of approximately 10 days per fundamental electrical cycle. Included in the model was an estimation of the rotor sleeve anisotropic conductivity [127] to allow for an estimate of direct sleeve heating. The loss breakdown is summarised in Table 5-12.

Item	Value	Units
Magnet Loss	187	W
Eddy Current Shield Loss	686	W
Sleeve Loss	52	W
Net Rotor Loss	925	W

Table 5-12: Rotor Losses due to Drive Harmonic Output

5.6.5 Winding Loss due to THD

The predicted drive THD effects will also have a significant effect on the winding losses as the harmonic currents have the potential to create significant additional losses. The additional AC losses caused by the harmonic currents will be significantly larger than the AC loss of the fundamental frequency calculated in section 5.5 as (3.43) shows that the AC losses are dependent on the square of the frequency. The same analysis as that used in section 3.3.3 can be used to calculate the AC loss conversion factor k_{AC} for all the harmonic frequencies, which defines the ratio of the total (AC+DC) loss to that of the DC loss alone. The k_{AC} values for the dynamometer slot design and chosen wire shape are shown in Figure 5-25, showing the expected square law rise in k_{AC} with frequency. The effect of k_{AC} on the magnitude of the current harmonics was ignored. Though the harmonics are voltage driven, the dominating effect of the armature reaction (even after the screening effect of the eddy current shield), compared to phase resistance indicated that there would be little change in the impedance seen by the harmonics considered in this design.

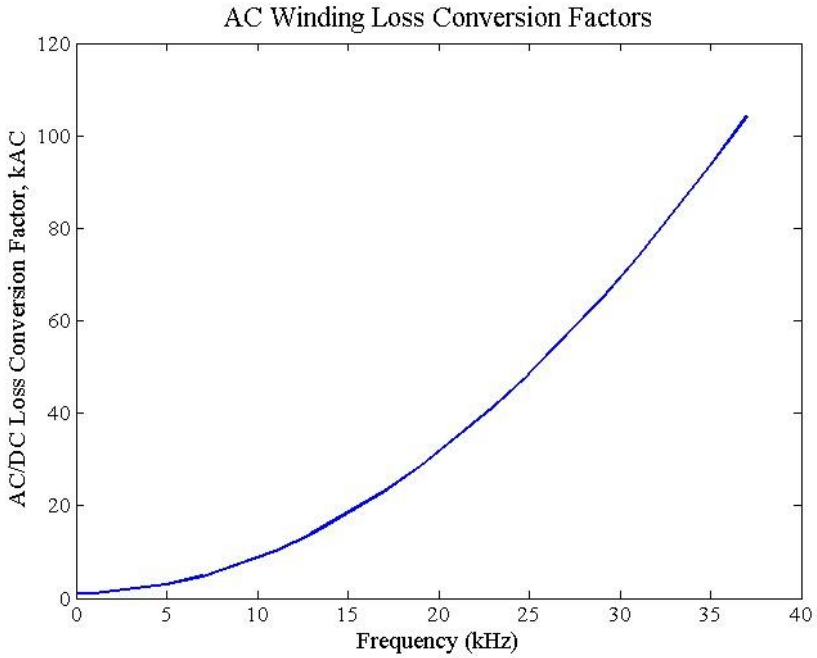

Figure 5-25: AC Winding Loss Conversion Factors

The losses associated with the harmonic output of the drive were then calculated using the phase resistance to compute the DC loss of each harmonic using the RMS value before modifying each

with the appropriate k_{AC} value to find the total loss expected in the windings. The effect of the AC losses is shown in Figure 5-26, where the total loss due to each harmonic current is compared with the DC loss component of that current; it is clear that the AC loss effects for the higher order current harmonics add significant amounts of additional loss to the design, while their equivalent DC loss is almost negligible. Although the fundamental frequency loss component dominates the winding losses, the AC loss contribution is significant and requires a thermal redesign to ensure the windings do not overheat; the components of winding loss for the final design at 20°C are shown in Table 5-13.

Item	DC Loss	AC +DC Losses	Unit
Fundamental current	5300	5706	W
Harmonic Currents	59	2231	W
Total winding Loss	5359	7937	W

Table 5-13: Winding loss components

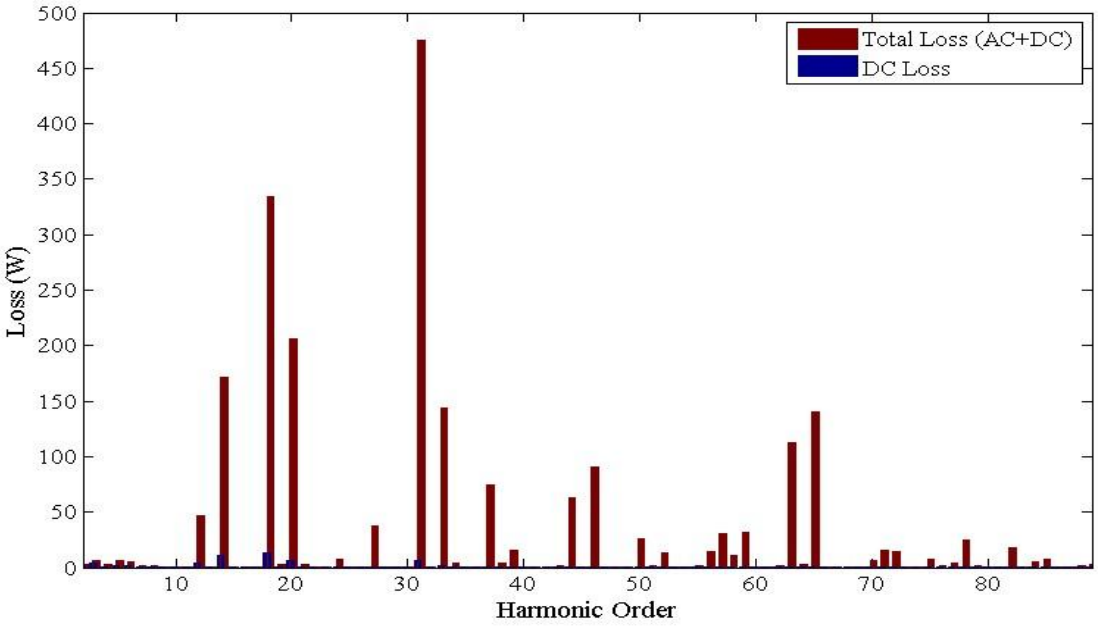

Figure 5-26: AC Winding Loss Contribution

It should be noted that the AC loss has been calculated for the full length of the windings, whereas the AC loss density would be expected to be lower in the end windings as the leakage fields are much lower. The reason for calculating the winding loss in this manner was due to the thermal modelling software, which could not distinguish between different loss intensities in the

slots of the machine and the end windings. Hence this value gives an over prediction of the total winding loss and will lead to an over prediction of the winding temperatures in the end windings; however it will allow correct modelling of the loss intensity in the slots of the machine in the thermal model and hence an accurate measure of losses in this region and acts as a safety factor when predicting the end winding temperatures. Ignoring the AC loss effects in the windings the total winding loss reduces to 6950W, but is not a useful parameter when performing the thermal design of the machine with the available software.

When performing the thermal design, the damping effect on AC losses of higher operating temperatures was included as a manual iteration between AC loss prediction and winding operating point temperature. This procedure gave a peak winding temperature prediction of 182.6^{o}C at the hot end of the machine, significantly higher than the initial prediction without the harmonic losses, but still comfortably within the 240^{o}C design rating of the machine.

5.6.6 Parallel path losses

As noted in section 5.4.3, parallel paths are required to allow flexibility in the winding design; It was important to consider how the paths would be wound and what affect they might have on the machine losses if their flux linkages are not balanced. There are two ways that the windings could be arranged, either one parallel path could be wound to make a full armature pole, or the paths could be distributed to share an equal path linking the flux of each rotor pole. Both options are illustrated in Figure 5-27, showing one phase of the machine wound, with the coils of one parallel path highlighted in red.

Winding option A consists of a single parallel path wound to form a single armature pole, whereas option B consists of a single parallel path distributed across all four rotor poles.

The worst case imbalance condition was considered to be if the magnets of one pole were all found to be at the low end of their strength tolerance, for example if a poor performing batch had been used. The lowest tolerance in strength allowed for the chosen magnet material was 97% of nominal, which was input into a 2D simulation with the windings of each parallel path for one phase connected in parallel, without an external source, to ascertain the circulating currents that would flow under full speed operation.

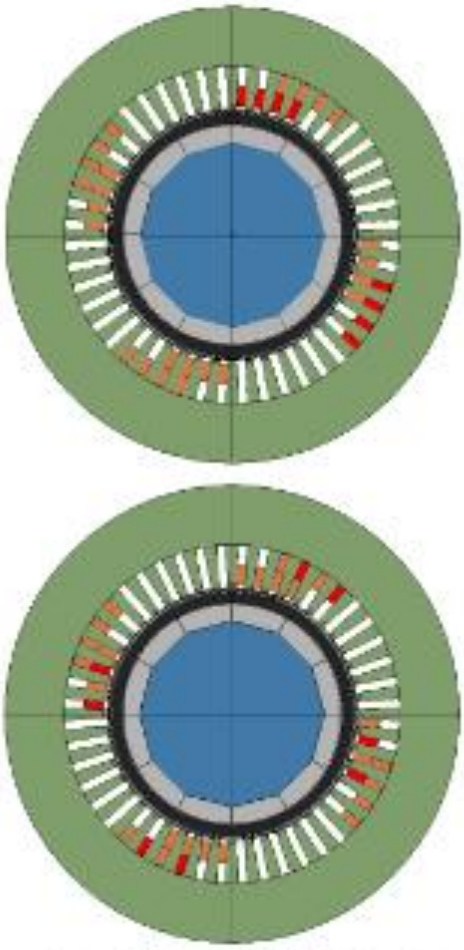

Figure 5-27: Parallel Path Winding options

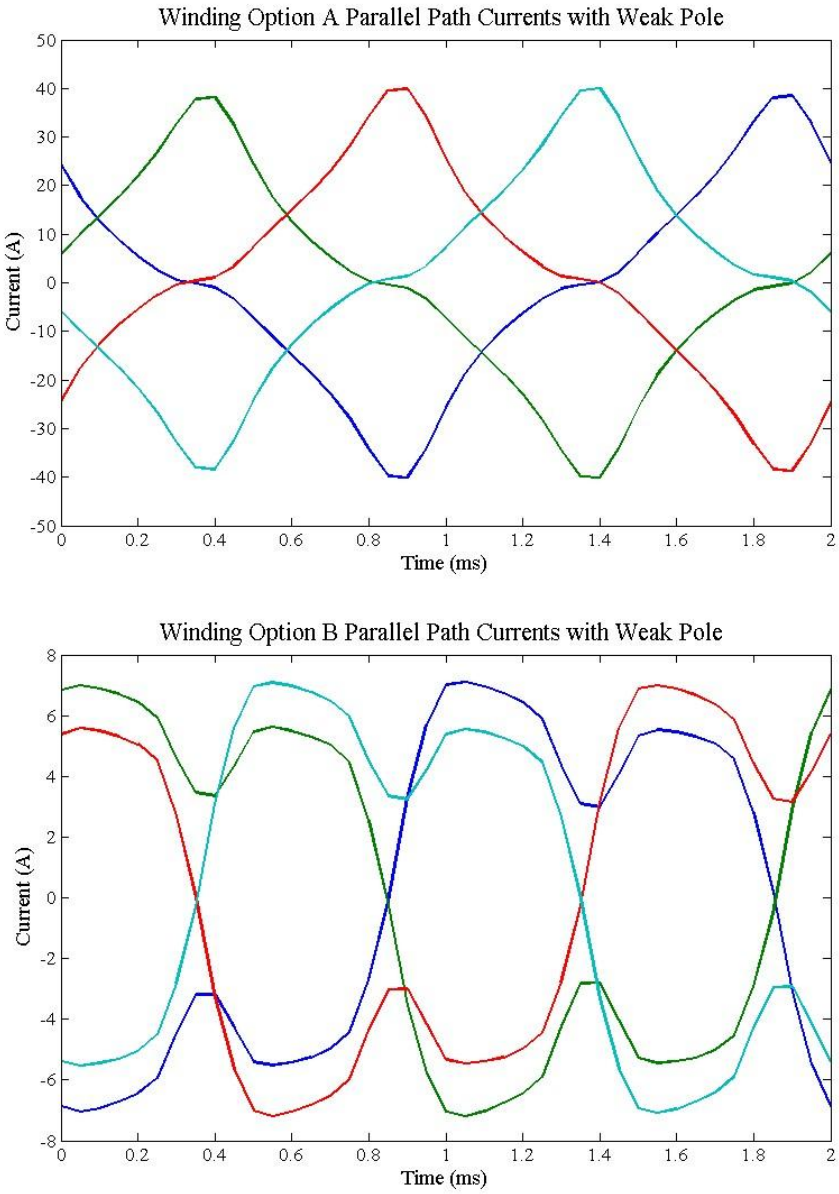

Figure 5-28: Circulating Currents From Both Winding Options

It can be seen from Figure 5-28 that option B delivers significantly lower circulating currents, with an RMS value of 5.2A compared to 20.7A for option A, therefore option B was chosen as the method for winding the machine. These values are so low compared to the parallel path current as to be negligible when consider winding loss, especially as they represent a worst case where all weak magnet are concentrated in one pole, so were not considered in the winding thermal design.

5.6.7 Stress Analysis Validation

The analytical stress predictions were validated using Ansys Workbench 13, using a 2D model reduced to span the arc of one magnet segment; the model and mesh are shown in Figure 5-29. The Magnet assembly carrier was included to allow creation of the magnetic assembly separate from the shaft, due to its size and weight. The intended construction method is for the magnets and eddy current sleeve to be assembled onto the carrier, then the carrier must be mated to the shaft via an interference fit before the

Carbon Fibre Reinforced Plastic (CFRP) sleeve is tension wound over the full assembly.

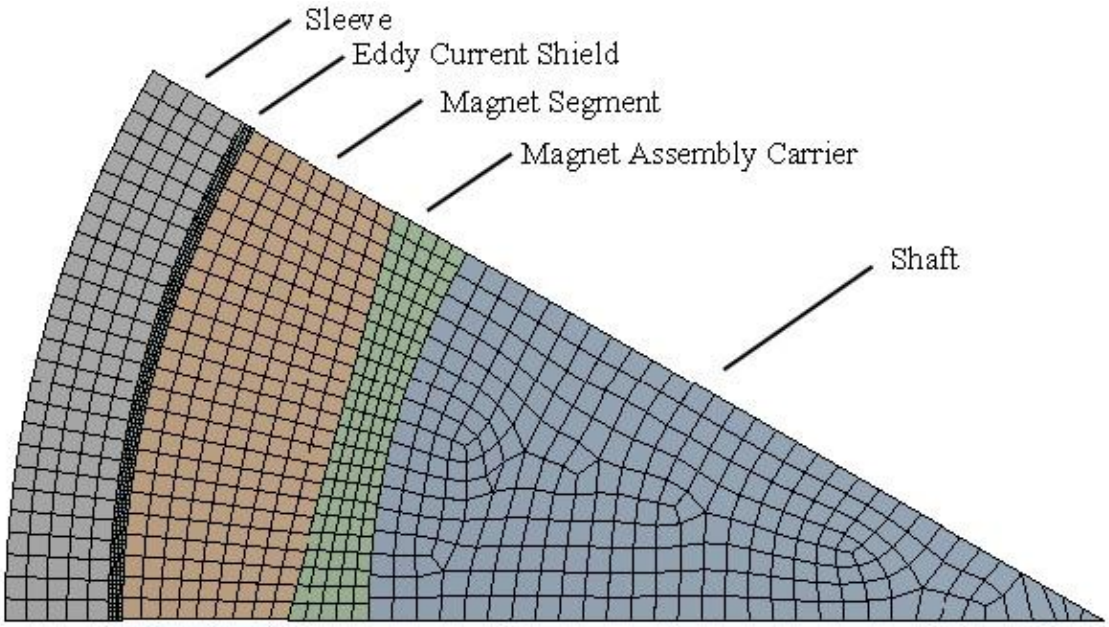

Figure 5-29: Mechanical FEA Model

The results of the initial pre-stress model are shown in Figure 5-30, at 0rpm, both hoop and radial stresses of the magnet and sleeve are shown, indicating the 1000MPa initial hoop stress generated in the sleeve during construction. The stresses at the operating speed, 30,000rpm are shown in Figure 5-31, and at the design speed, 36,000rpm in Figure 5-32. The model in Figure 5-32 predicts that the magnets will not have lifted off at the design speed, indicating that the lift-off speed is higher than the design speed, this speed was found to be at 37700rpm, the stress prediction at the point of magnet lift off is shown in Figure 5-33, showing that the radial compressive stress on the magnet has reduced to zero at certain points (indicated by the blue probe values on the figure). In all the stress figures, the stress gradient scale is given an all values are given in MPa.

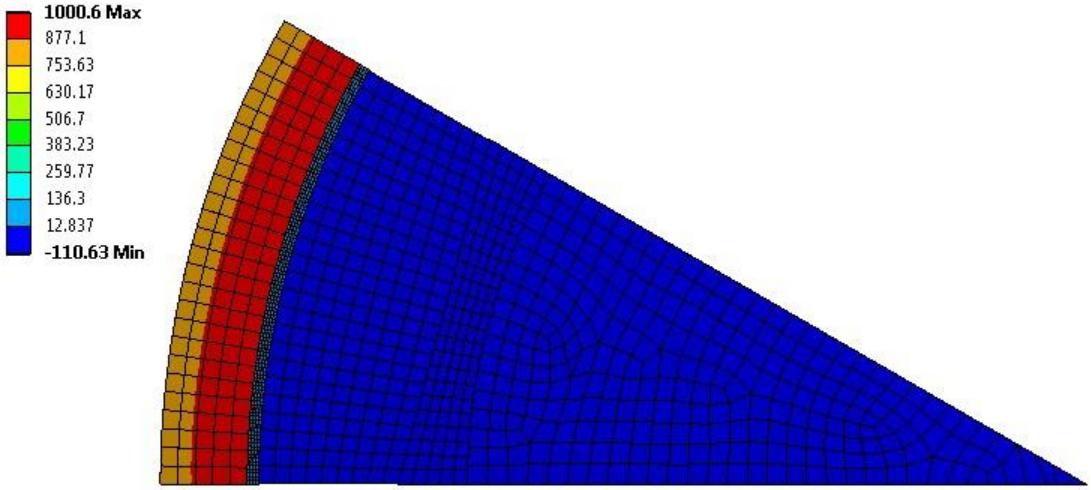

Hoop Stress, 0rpm, room temperature

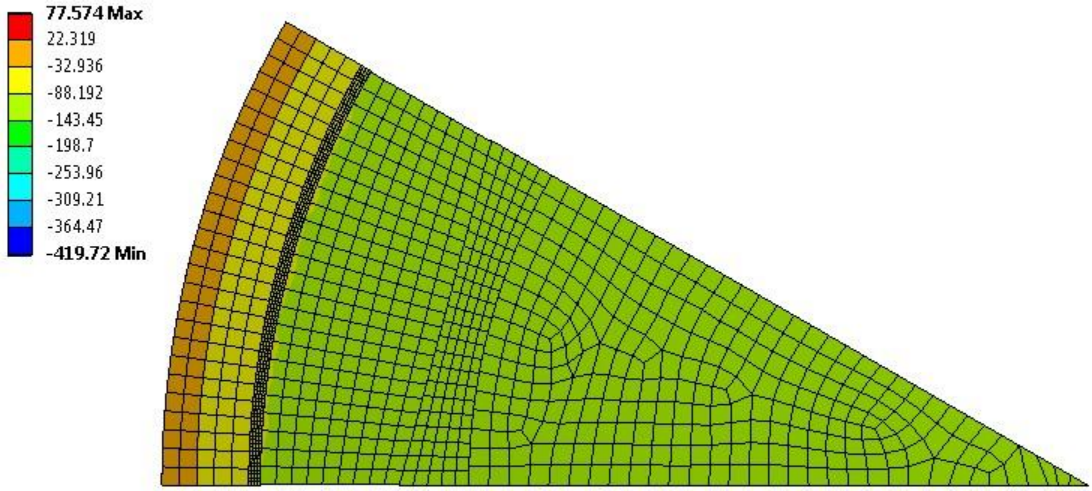

Radial Stress, 0rpm, room temperature

Figure 5-30: Pre-stress FEA results

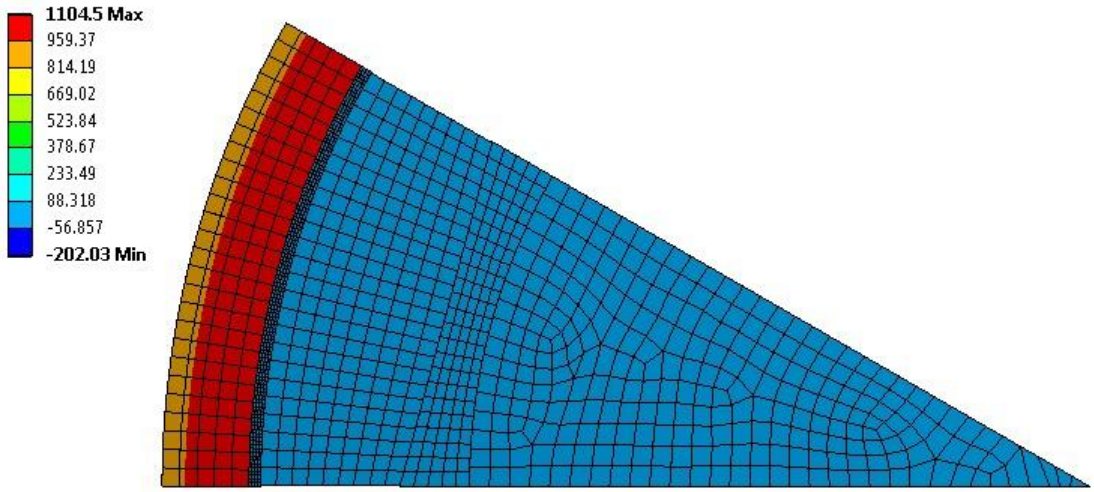

Hoop Stress, 30,000rpm, operating temperature

Figure 5-31: Hoop Stresses at Operating Speed

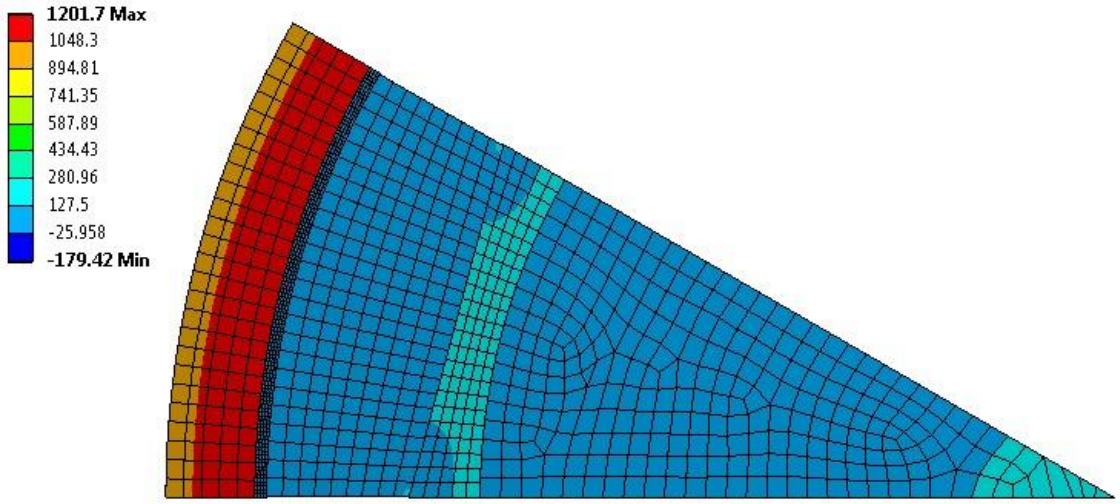

Hoop Stress, 36,000rpm, operating temperature

Figure 5-32: Hoop Stresses at Design Speed

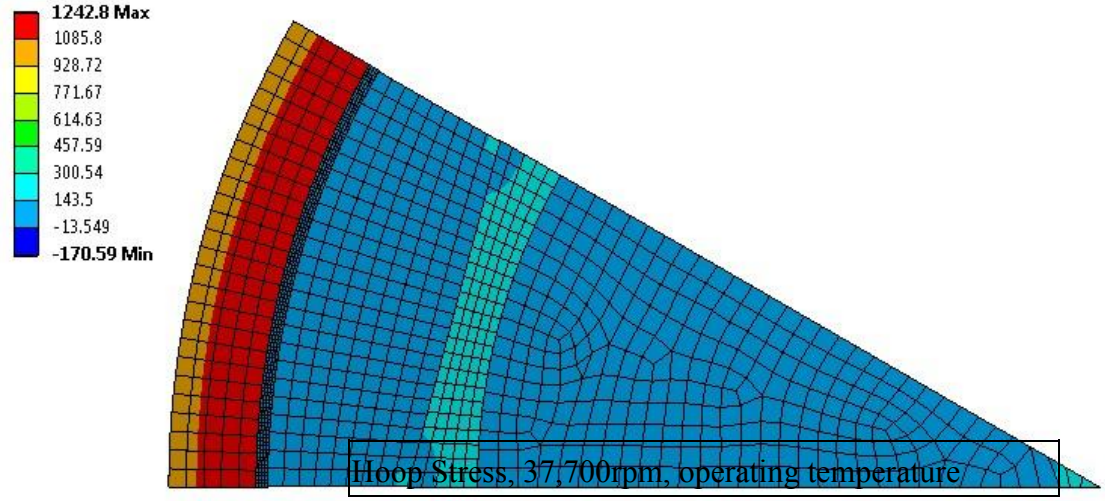

Hoop Stress, 37,700rpm, operating temperature

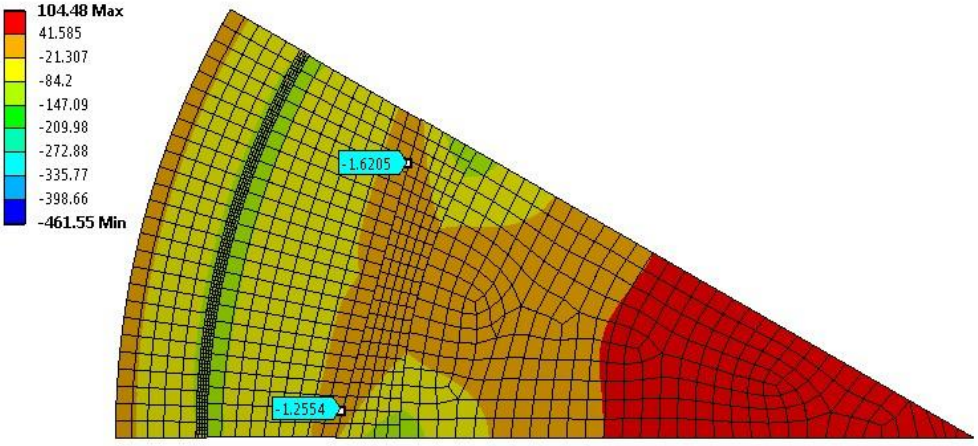

Radial Stress, 37,700rpm, operating temperature

Figure 5-33: Stresses at Lift-off Speed

5.6.8 Critical Speed Validation

The critical speed prediction was evaluated for the rotor assembly, with the magnets and sleeve treated as a parasitic weight with no associated stiffness. The model used for the analysis, with mesh imposed, is shown in Figure 5-34; included in the model are the bearing masses and two dummy coupling masses at the ends of the shaft, to improve the accuracy of the system critical speed prediction. Also apparent on the model is the rotor vent system. The inlet and outlet holes can be seen to be at different diameters in order to enable a pumping effect along the rotor length. The outlet vents at the higher diameter act as a crude impeller, expelling air at a higher velocity and hence lower pressure than the air at the inlet, hence drawing air though the rotor at a higher rate than the though ventilation alone could achieve. The support stiffnesses were included on the bearing surfaces at a value of 9kN/mm.

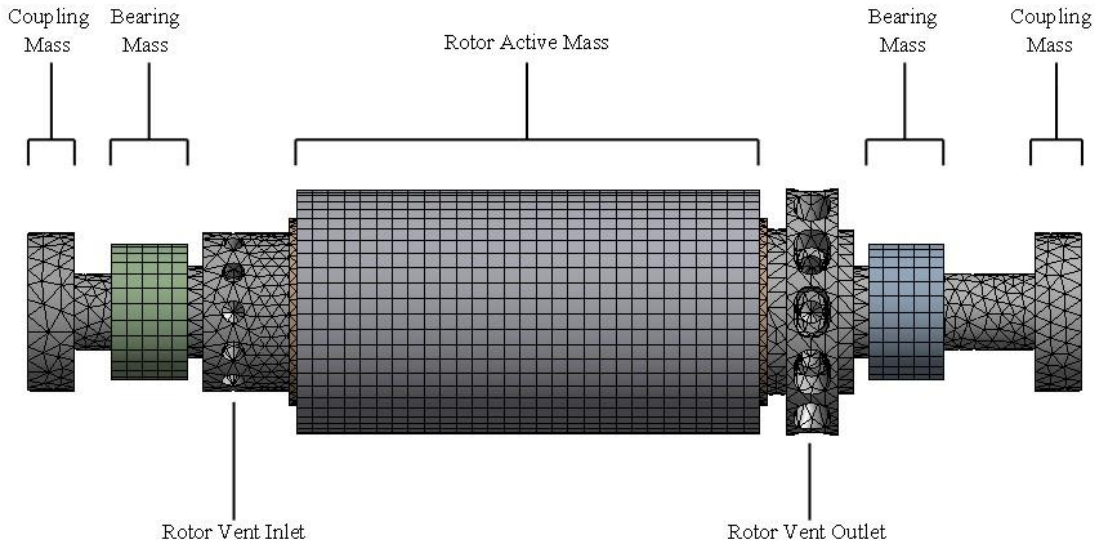

Figure 5-34: FEA model used for Critical Speed Validation

The FEA solver identifies the mode shapes and their associated frequencies for the rotor model, the first bending mode was found to occur at 828Hz, or 49680rpm, comfortably beyond the 707Hz target set by the 500Hz operating speed and 1.414x safety factor used in the analytical prediction. The deformation associated with this mode shape is shown in Figure 5-35.

Figure 5-35: First Bending Mode Shape

Given the mass of the system and stiffness of the bearings the bounce and rock modes of the rotor-bearing-coupling system are 110Hz and 169Hz respectively. As these frequencies are significantly far into the operating speed range of the dynamometer, at 6,600rpm and 10,100rpm, action must be taken to move them. By mounting the bearing casings on rubber O-rings the frequencies of these bounce and rock modes will be significantly reduced to be of no further concern, without affecting the high speed operation.

5.7 Machine Parameters and Losses

With the design work completely summarised in the preceding sections, it remains only to summarise the final design, predicted losses and operating temperature points. The final magnetic FEA model is shown in Figure 5-36, with the operating point flux densities shown in Figure 5-37.

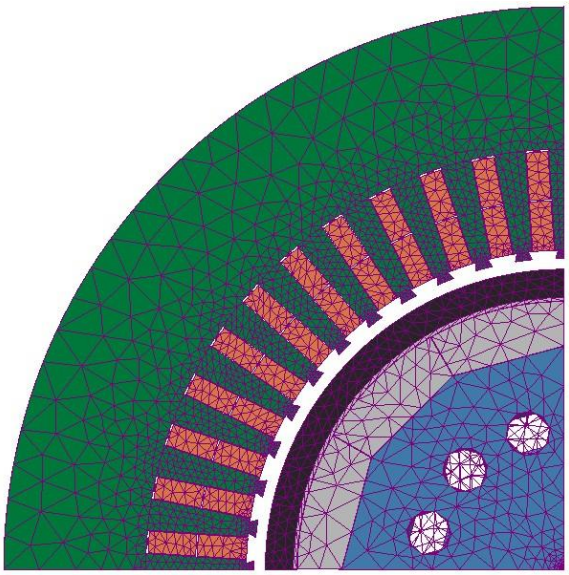

Axial Cross Section

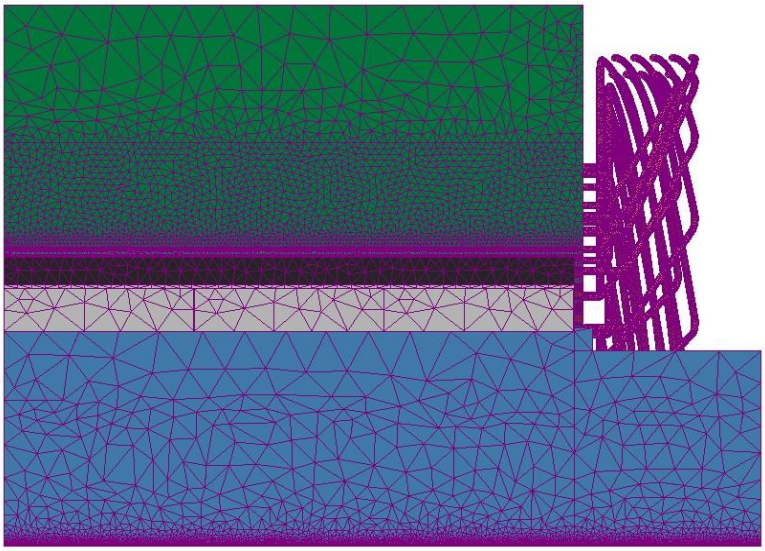

Radial Cross

Figure 5-36: Final Magnetic FEA Model

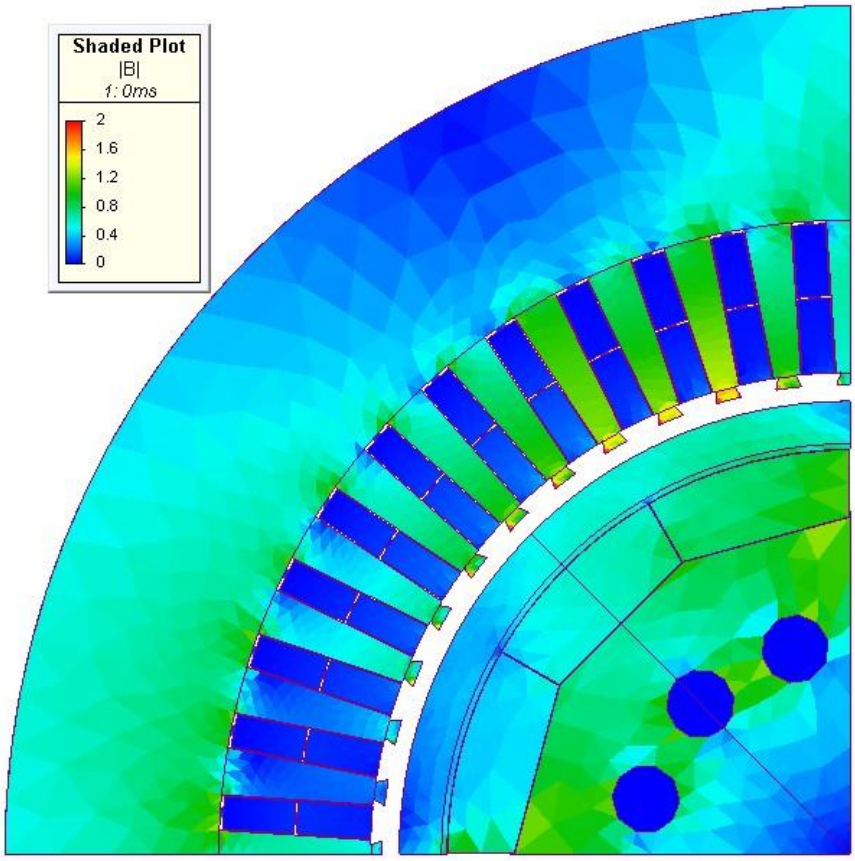

Figure 5-37: Operating Point Flux Densities

The final torque output prediction with the predicted drive current waveform is given in Figure 5-38 with the reference torque expected from ideal current waveforms. The line to line back EMF remains unchanged from that shown in Figure 5-21.

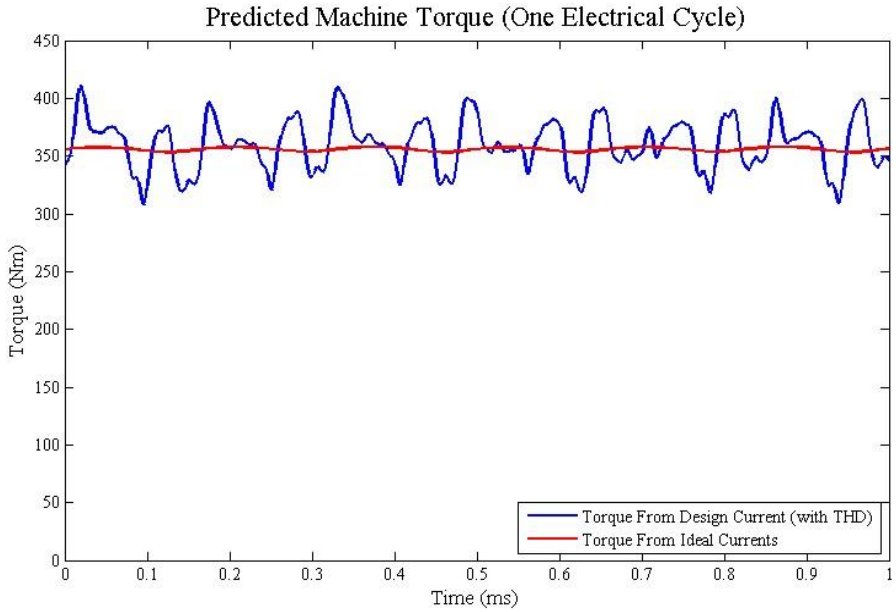

Figure 5-38: Final Torque Prediction

It can clearly be seen that the current harmonics have a severe detrimental effect on the torque ripple output of the machine, however the average torque output remains at the design point. In the final design, the electromagnetic torque out as predicted by the magnetic FEA was increased by 5Nm (by increasing the defined rated current) to account for the expected drag torques of windage, bearing and coupling losses of the final system, in order to ensure that shaft output torque corresponded at 350Nm at the stated rated current.

The loss predictions are summarised in Table 5-14

Item		Value	Units
Rotor Loss	Magnets	187	W
	Shield	686	W
	Sleeve	52	W
Total Copper Loss (worst case @20^{o}C)		7937	W
Iron Loss (laminations)		3133	W
Air Gap Windage loss		2441	W

Table 5-14: Final Design Loss Predictions

The thermal prediction at rated current are summarised in Table 5-15. Included in this table are two worst case predictions, based on a validation run on a lower power projects but using the same software and one using the worst case required current for rated torque if the rotor EMF is delivered under strength. The input Iron losses in all cases are multiplied by a safety factor of 2 to account for worst case stamping, cutting and stressing effects.

Component	Rated current	Rated Current with Thermal Safety Factor	Maximum with Current Safety Thermal Factor	Units
Peak "in slot" Winding Temperature	182	214	264.5	ºC
Peak End Winding Temperaure	169.4	204.8	258	ºC
Peak Magnet Temperaure	102.8	142.9	150.8	ºC
Peak Sleeve Temperature	143.3	182	155.1	ºC

Table 5-15: Final thermal predictions: Key Temperatures

Item	Value	Units
Rotor Diameter	160	mm
Active Length	318.4	mm
Air gap	4	mm
Pole Number	4	
Magnet Thickness	7.1	mm
Sleeve Thickness	5	mm
Parallel Winding Paths	4	
Slot number	48	Slots
Slots/phase/pole (distribution)	4	Slots
Short pitching	2	Slots
Phase Currents	1688	A RMS
Line-Line Voltage	380	V RMS
Inductance Estimate	14.8	μH
Slot Fill (%copper in slot)	50	%
Slot Depth	22.26	mm
Tooth Width	5.5	mm
Machine Outer Diameter	272	mm
Magnet Material	SmCo Grade 30	Recoma
Lamination Material	Cogent NO10	
Shaft Material	High Strength Steel	

Table 5-16: Final Design Parameters

Chapter 6. Manufacture of Demonstrator Dynamometer

The manufacture of the dynamometer was split between four separate companies, each selected for their specialist knowledge in the relevant manufacturing areas.

- The rotor magnetic assembly and composite wrap was manufactured by a specialist magnetic materials handling company.
- The stator was assembled, wound and Vacuum Pressure Impregnated (VPI) by a specialist motor winding company.
- The drive electronics and cabinets were assembled by Unico (UK).
- The dynamometer casing, bedplates, bearing packages, cooling systems, shaft, couplings and control unit were all manufactured and assembled by Torquemeters, the project sponsors.

The final assembly of the dynamometer was undertaken by Torquemeters at their own manufacturing facility, where spin testing, open circuit and short circuit tests were also performed. Full load testing could only be performed at the dynamometer final application site, where there was sufficient space for drives, dynamometer and cooling support systems to be installed. This chapter will describe the experiences and knowledge gained during the assembly of the dynamometer components by the various manufacturing partners.

6.1 Rotor Construction

The detailed design of the rotor was undertaken in conjunction with a specialist magnetic materials supplier and handler, which provided feedback on magnet materials availability machining sizes and tolerances. This supplier then undertook the magnetic assembly process; the magnetic assembly was constructed separately from main shaft to aid in handling and in machining of the shaft. Pre-cut and pre-magnetised magnet segments were assembled onto a carrier then the outer diameter was ground before an aluminium tube was fitted via a small interference fit; the tube was then turned to the pre-requisite thickness. The magnetic assembly was fitted onto the pre-machined shaft via a taper fit to allow the CFRP tension winding process to be undertaken.

The first stage magnet assembly onto the carrier proved difficult as the magnets were close to their maximum recommended safe handling size, which led to significant breakage loss due to uncontrolled magnet movements. A single magnet segment is shown in Figure 1-1; each magnet segment was wire eroded from a pre-magnetised block of Samarium Cobalt of the specified grade, the flat sides of each magnet were cut to the required dimension and tolerance, whereas the curved outer surface was left larger than dimensioned to allow later grinding to the correct tolerance.

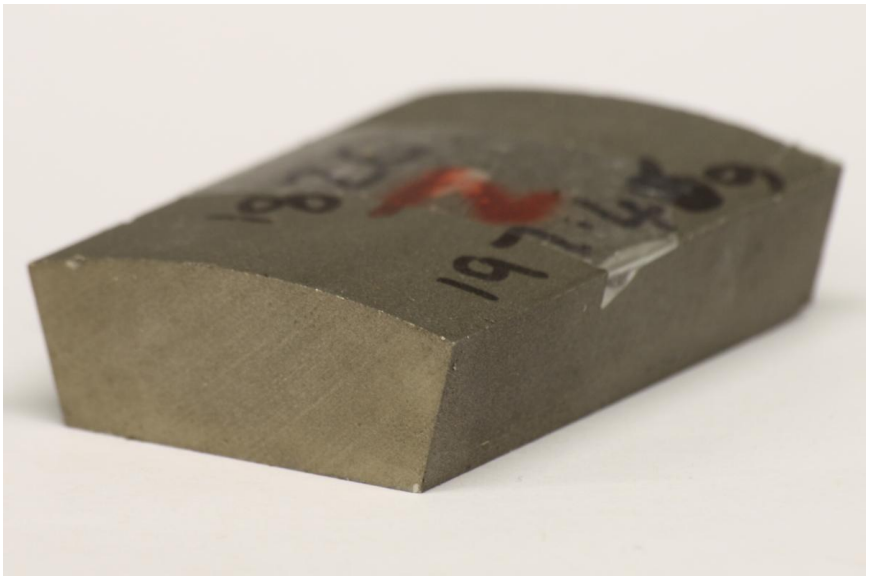

Figure 6-1: Single pre-cut Magnet Segment

The first stage of the assembly process is shown in Figure 6-2, here loctitie adhesive was applied to the appropriate flat on the carrier and a silicone barrier cream was applied to the magnet edges to prevent glue adhesion in these regions. The magnet was then introduced slowly to the carrier surface, to which it was strongly attracted, using the non-magnetic wedge shown.

After the magnet was placed on the carrier, it was slowly slid into the correct placing using a ratchet clamp, adjacent magnets were used as a guide to align the magnet correctly; this process is shown in Figure 6-3. During this assembly process several breakages occurred due to magnet 'jumping', whereby the magnet being assembled into place jumped to a position of lower reluctance, usually resulting in shattering of that magnet piece; the aftermath of such an event is shown in Figure 6-4. This problem was largely removed by the inclusion of an iron bar placed across the magnet axis to prevent jumping, as shown in Figure 6-5.

Figure 6-2: Magnetic Assembly Surface Preparation

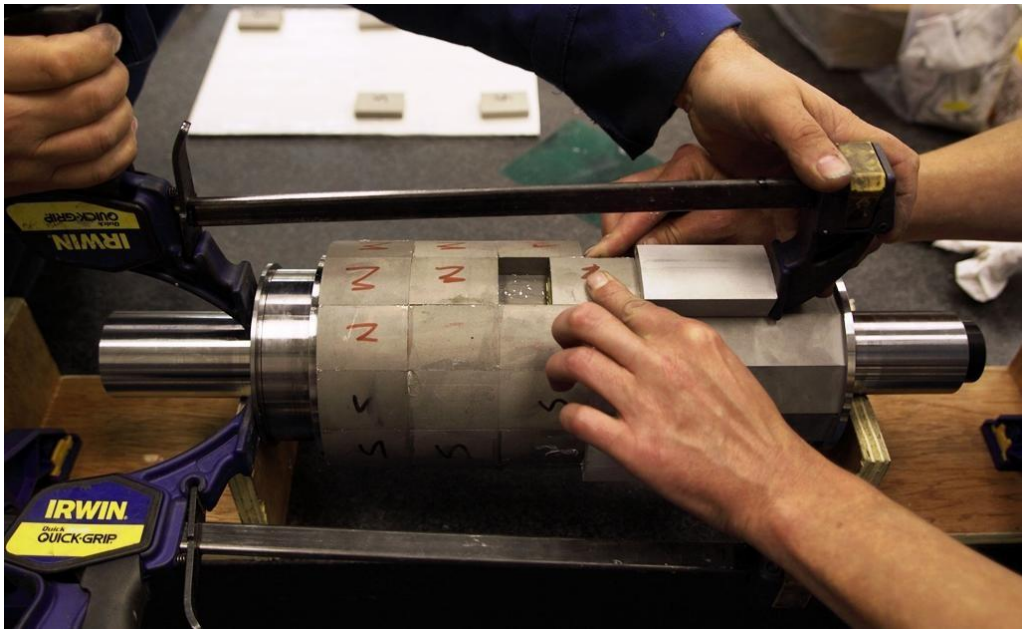

Figure 6-3: Magnet Alignment Using Ratchet Clamp

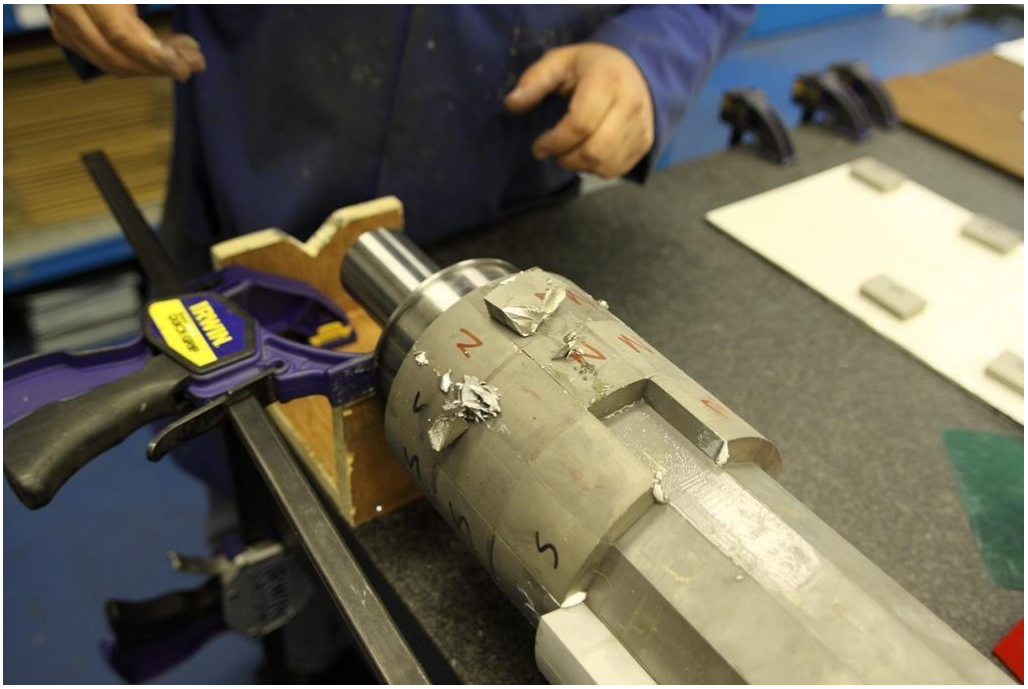

Figure 6-4: Magnet Damage Due to Jumping

Figure 6-5: Magnet Retention Bar

After the magnet assembly, the surfaces were cleaned and ground to the specified diameter, to give the assembly shown in Figure 6-6.

Figure 6-6: Ground Magnet Assembly

In parallel with the manufacture of the rotor assembly, the shaft was machined by Torquemeters and is shown in Figure 6-7. The detail of the air inlet and outlet holes for the rotor ducts is clearly marked, and the outlet holes can be seen to be set on a larger diameter than the inlet holes, creating a pumping effect to overcome friction losses in the ducts.

Figure 6-7: HSHP Pumping Shaft

After the fitting and grinding of the aluminium eddy current shield, the magnet assembly was mounted on the shaft and delivered to an external contractor for tension winding using the specified Toray T-700 Carbon Fibres. The tension winding was performed in two stages; firstly the sleeve was wound under high tension to the specified thickness and this was followed by a

low tension wind at the ends of the magnetic assembly to form cheek plates, as shown in Figure 6-8.

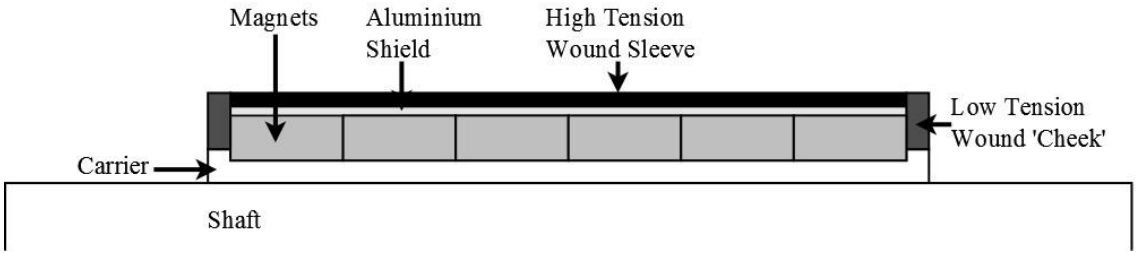

Figure 6-8: Shaft Axial Diagram Showing Tension Winding Detail

The balancing of the rotors proved to be a significant challenge due to their size and shaft geometry variation. Some damage was incurred to the tension wound sleeve during balancing, which required an additional Kevlar overwrap of the sleeve, to contain and stabilise the outer surface, the thickness of this layer was marginal and not expected to affect the mass, stress or thermal performance of the machine.

6.2 Stator Construction

6.2.1 Stator Construction and Winding

The stator manufacture was contracted to a specialist company with a wide range of experience of producing hand wound machines of varying sizes and configurations; although this project represented one of the largest machines handled by the company which posed significant manufacturing challenges. The lamination manufacture was subcontracted to a specialist cutting company; to preserve the tolerances of the stator profile throughout the axial length of the machine, the laminations were cut in short 50mm stacks between sacrificial clamp plates. The laminations were then assembled onto a mandrel, their orientation randomised, and then glued under pressure to achieve a 95% stacking factor. A sample lamination is shown in Figure 6-9.

The stator was wound using the specified compacted Litz wire, Apical slot liner, slot wedges and glass fibre taping on the end turns, the final wound stator is shown in Figure 6-10 and Figure 6-11. Detail of the wire exiting from a slot is shown in Figure 6-12.

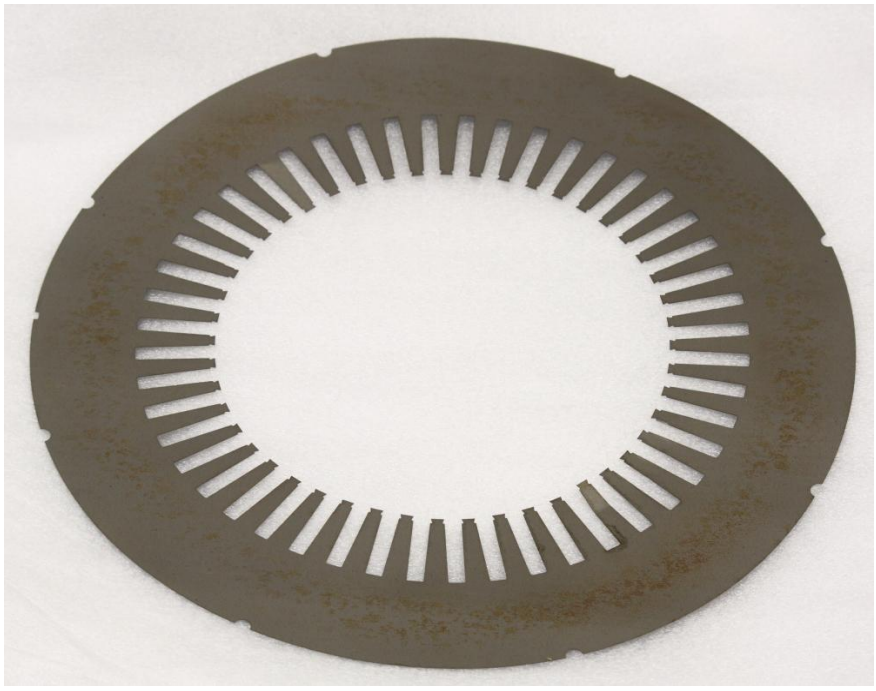

Figure 6-9: Lamination Profile

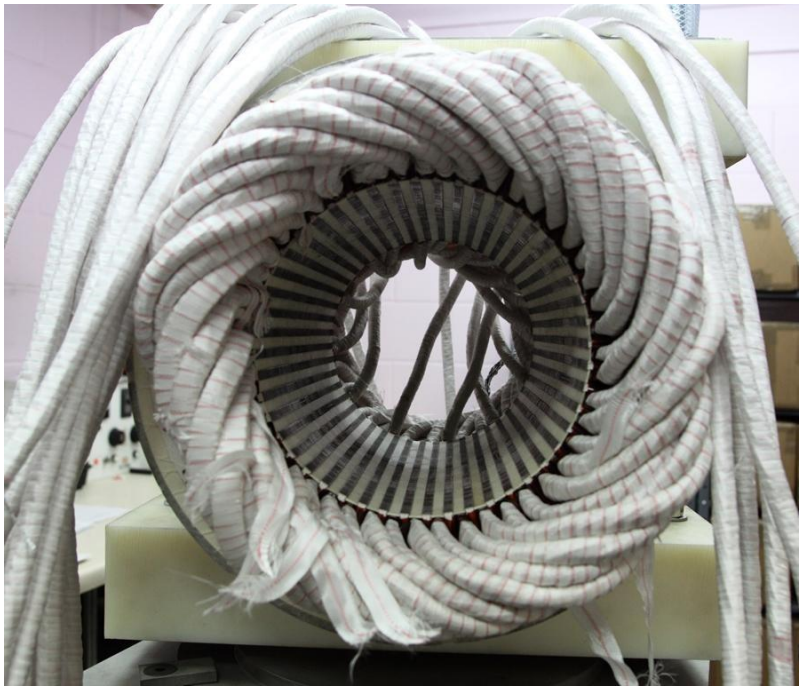

Figure 6-10: Wound Stator

The arrangement of the wire terminations proved a significant challenge due to the number of individual conductors involved; with four parallel paths per phase and both the start point and phase terminations to connect, 24 cables required arrangement at one axial end of the motor. The star point was connected externally via a bus bar placed on one side of the stator and the three phase bus bars used to connect the phases to the incoming feeds from the drive were connected

on the opposing side; the relevant cables were passed through an aperture at each side of the motor, to align and space them regularly. The interaction of the VPI resin and glass fibre taping causes the termination cables to become brittle and prone to cracking, thus all cable positioning and preparation was undertaken prior to the VPI process using a jig machined to match the motor casing layout. This jig, the cable lay out and positioning apertures and the star point busbar arrangement are shown in Figure 6-13 and Figure 6-14. The jig was used to ensure that the cable lengths were matched throughout the system, to balance the cable resistances, due to the un-equal winding paths followed throughout the stator and the variation in slot distance from slot exit to busbar termination.

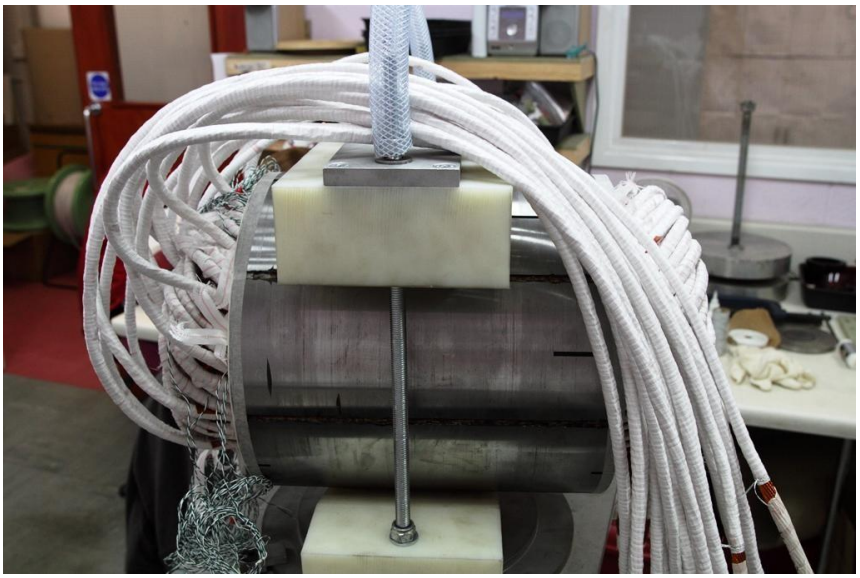

Figure 6-11: Wound Stator, axial view

Figure 6-12: Wire and Slot Wedge Detail

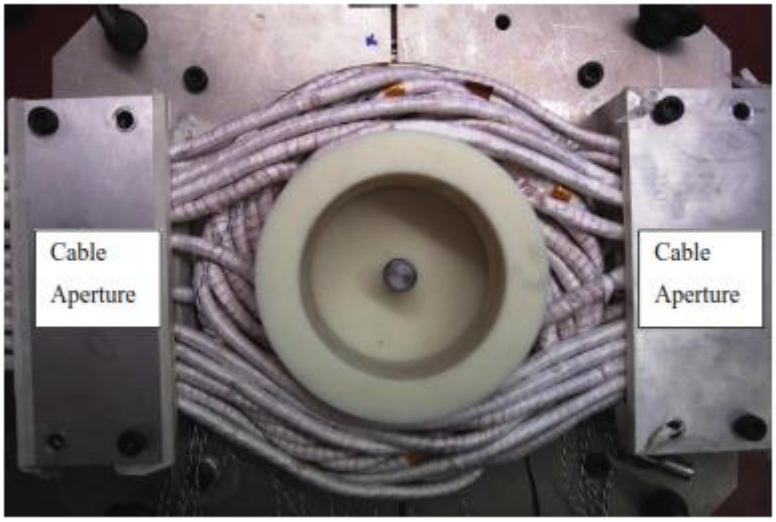

Figure 6-13: Cable termination detail

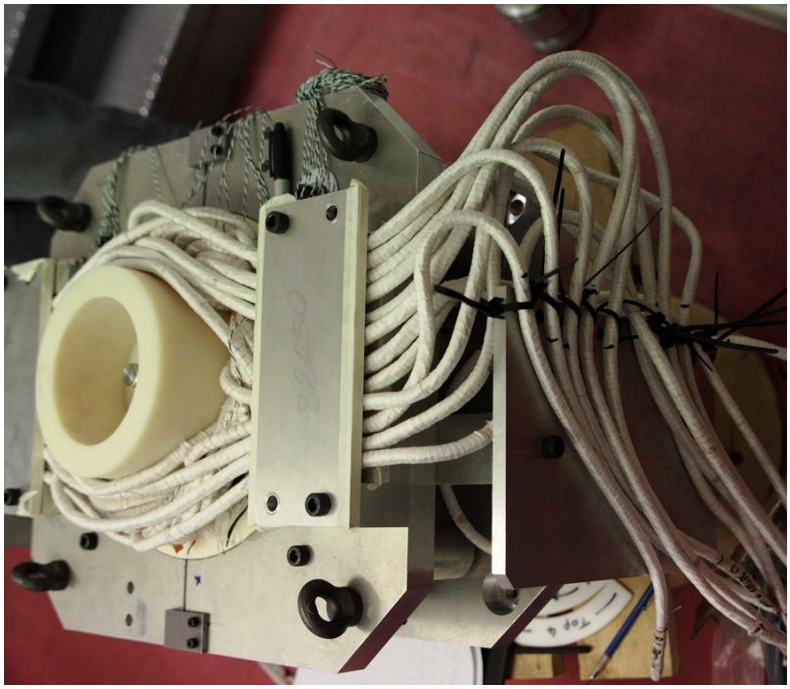

Figure 6-14: Star point termination jig

6.2.2 Stator VPI Process

The Vacuum Pressure Impregnation of the motor was challenging for two reasons, firstly the size of the stator unit presented challenges for handling and accommodation in the vacuum tank and autoclave and secondly, the specific material properties of the wire enamel required a special

heat treatment before coming into contact with the VPI resin. The VPI process required a bespoke oven to be sourced due to the size of the stator and jig and due to the low viscosity of the selected resin, large amounts of runoff occurred during curing, requiring multiple VPI stages to ensure a good fill of the slot space.

The second problem required a specific investigation into the material properties of the wire enamel due to a solvent crazing issue raised by the wire supplier [123]. The wire enamel material, polyimide, was selected for its high temperature rating of 240ºC, however it is prone to solvent crazing after stressing during the winding process and requires a high temperature anneal before coming into contact with any solvents. The temperature and length of this anneal was unspecified and so had to be found by experimentation; the experiment was undertaken on a sample of the winding wire, bent to induce plastic stresses in the bend and then placed in an oven for various anneal settings, before dipping in Acetone. The anneal process required was found to be 200ºC for 2 hours, the wire samples used for testing are shown in Figure 6-15 and Figure 6-16; details of the wire cracks due to solvent crazing are shown in Figure 6-17.

Figure 6-15: Litz Wire used for Solvent Crazing Investigation

Figure 6-16: Litz Bundle Separated for Submersion in Acetone

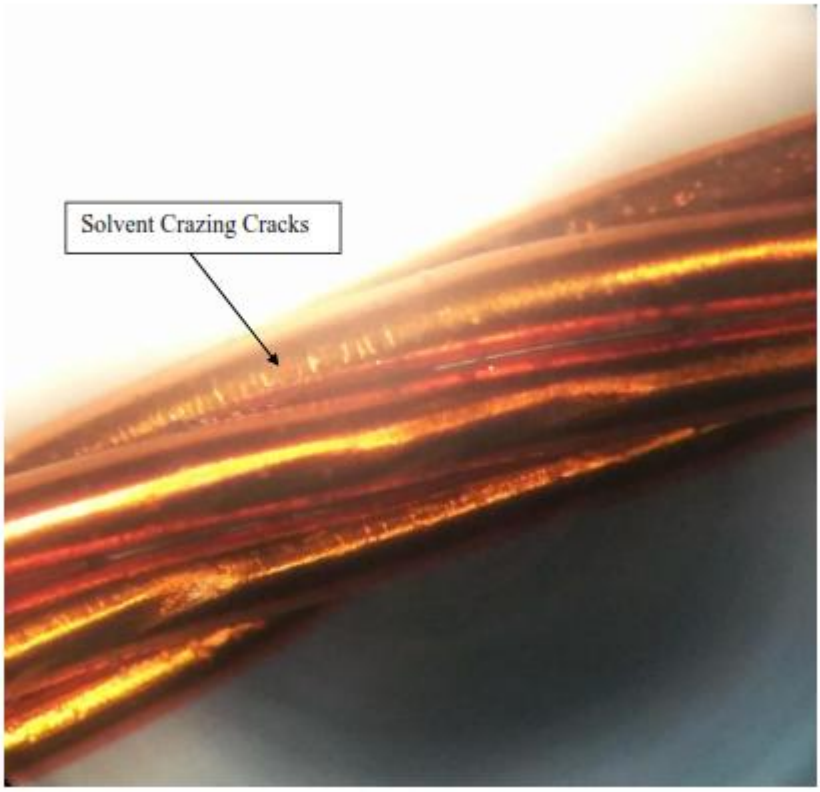

Figure 6-17: Details of Wire Solvent Crazing

6.4 Drives

The drives were assembled at Unico UK based in Milton Keynes, the space requirements were significant, the drive cabinets for each motor were a total of 12m in length. To achieve a more practical drive arrangement, each cabinet assembly was ‘folded back’ upon itself to shorten the total length. The folded back arrangement is shown in Figure 6-18; which details one side of the drive cabinet assembly for one drive, with the remaining cabinets on the reverse.

Figure 6-18: Drive Cabinet Assembly, One Side

To achieve the 1688A RMS rated current for the motor, the dive system contained two separate 1000A RMS rated inverters which were coupled together through a set of 5µH reactors. The reactors acted to damp harmonic current flow and prevent current circulation between the drives. The three reactors for one motor system occupied a full drive cabinet, with dedicated cooling due to the expected losses, they are shown in Figure 6-19, along with the phase bus bars.

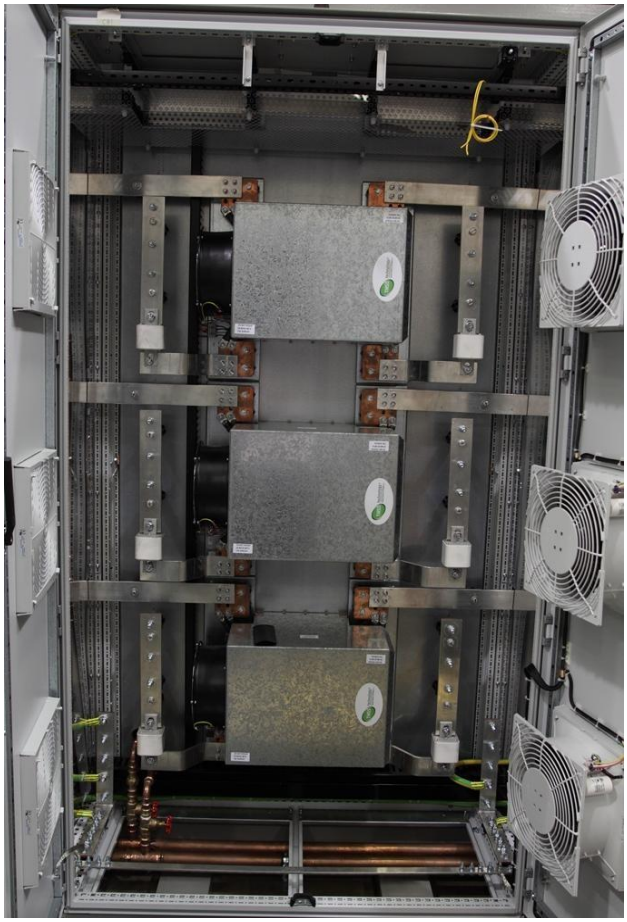

Figure 6-19: Drive Phase Reactors

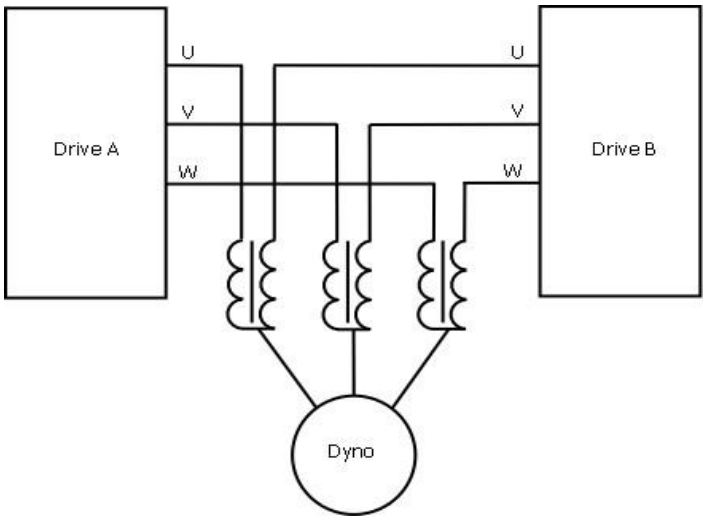

Figure 6-20: Drive Phase Reactor Connection

6.4 Test stand assembly and connections

The Dynamometer test stand was installed at an aerospace testing facility based in Dayton, Ohio. The test stand was located in a bespoke cell in the facility and arranged so that the two machines output shafts were in opposite directions, allowing two independent projects to be run at the same time. The drives and cooling sub-systems for the dynamometers were located on a gantry level directly above the machines, to save floor space and utilise the available ceiling height. The test stand is shown in Figure 6-21 and the gantry with drive arrangement is shown in Figure 6-22. The cooling sub systems were arranged in a region of dead space at the end of the drive cabinets as shown in Figure 6-23. A detailed view of the motor casing showing the air inlet arrangement and termination boxes is shown in Figure 6-24.

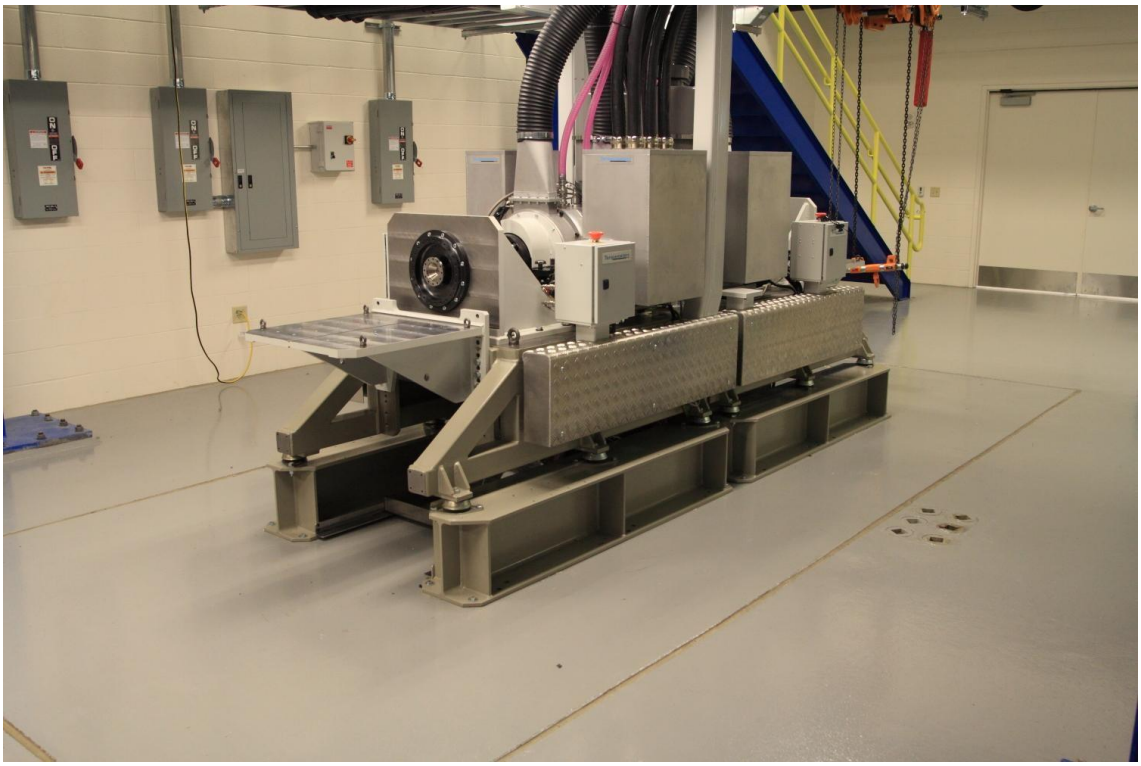

Figure 6-21: Test Stand Assembly

Figure 6-22: Test Stand and Drive Arrangement

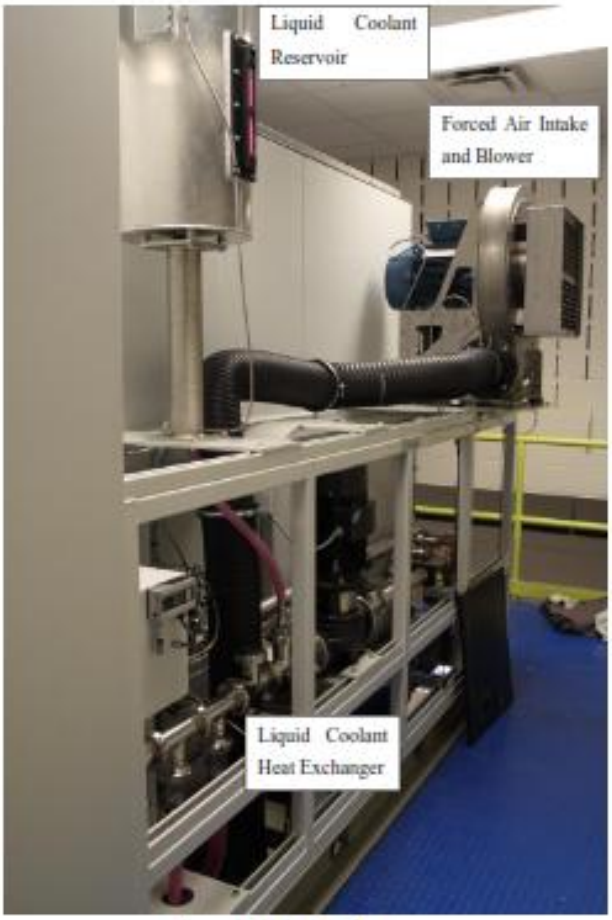

Figure 6-23: Coolant Sub-systems

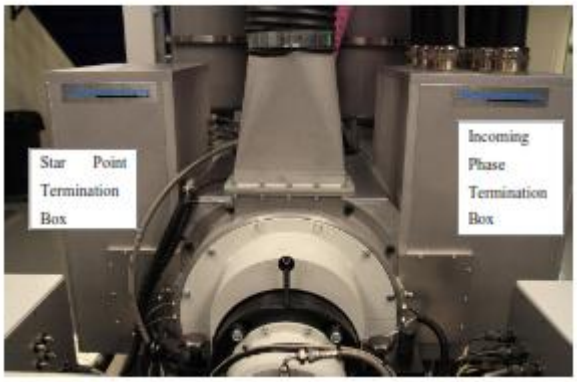

Figure 6-24: Machine Detail

Chapter 7. Test Results

The testing of the machine with respect to its design parameters was combined with the commissioning of the full test stand system described in section 6.4. This combination placed constraints on the full range of testing possible within the time frame of this thesis, due to delays caused by troubleshooting the full drive system. A limited range of testing was possible, covering full torque operation up to 24,000rpm and full speed operation up to 90% torque; successfully proving stable thermal motor operation up to 1MW of power output.

Direct torque measurement of the torque output of each machine was not possible due to major issues with the torque sensing equipment; only electromagnetic torque of the fundamental current could be computed from the measured current inputs, and the known back EMF voltage and speed. The motor power performance testing was achieved through nose to nose operation of the two test cell machines, with one motoring and one generating; power flow was then re-circulated between the four quadrant drives with only the losses being topped up by the external mains power supply.

Initial mechanical spin testing and back EMF measurement was performed at Torquemeters UK site using a high speed spin testing cell. All further measurements involving powered operation and thermal monitoring were undertaken at the installation site in Dayton, Ohio.

7.1 Initial Mechanical Spin Tests and Commissioning Plan

The initial mechanical spin testing of the two prototype rotors was performed using a belt driven spin cell at Torquemeters Ltd. Mounting of the rotors was achieved using the final motor bearings and housing, with the stator being replaced by a wooden mock-up to protect against any catastrophic failures of the rotor.

Both rotors were spun to 31,500rpm to confirm their mechanical stability at the operating speed of 30,000rpm. In response to this, overspeed trip limits were set in the test stand control system to cut all power if speed should approach 30,500rpm. It was noted that the balance of both rotors shifted after the first run to full speed, implying some movement and settling of the magnetic assembly. The rotors were subsequently rebalanced and re-spun and no further shift in balance was reported.

Following the success of the initial mechanical spin testing, the wound stators were installed in the casings and the spin cell was used to drive the motors for back EMF testing. Following the completion of EMF testing the motors were shipped to Dayton and their installation into the test stand system was completed.

The motor specific commissioning plan was outlined as follows:

- Connect motors and drives and establish communications and sensor feedback.
- Spin each motor to full speed, unloaded (and uncoupled to the other motor).
- Mechanically couple the motors.
- Establish recirculation of power between motors and drives.
- At 24,000rpm increase torque transmission in increments to rated torque while monitoring steady state settling temperatures in motors. Limit torque rating when temperatures reach 220ºC peak on the windings, 200ºC in the rotor.
- Repeat maximum torque testing at 30,00rpm.
- Quantify final speed-torque map for machines based on thermal limits.

Limits on equipment availability and reliability eventually curtailed what was possible on the commissioning plan, as will be described in the followings sections.

7.2 Open Circuit Voltages

The open circuit voltages of both motors were measured at 30,000rpm using a picoscope 4227. The measured motor phase and line-to-line voltages for the master motor are shown in Figure 7-1 and Figure 7-3, the measured voltages for the slave motor are shown in Figure 7-2 and Figure 7-4. In both cases the rotor temperature was estimated at 50ºC and the simulated voltages were adjusted accordingly.

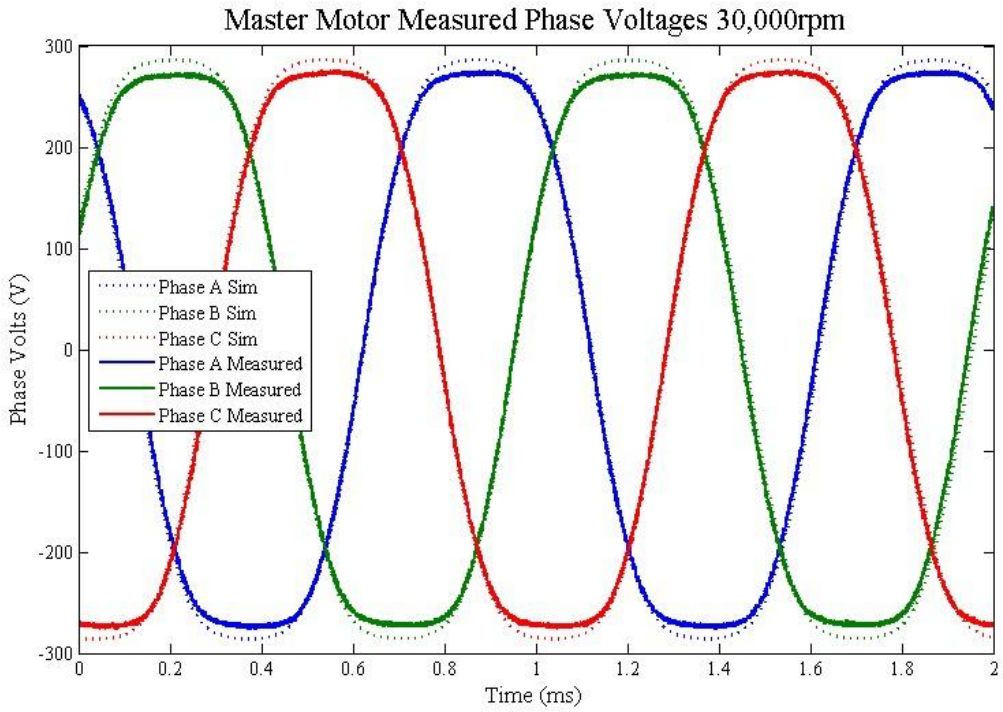

Figure 7-1: Master Motor Phase Voltages

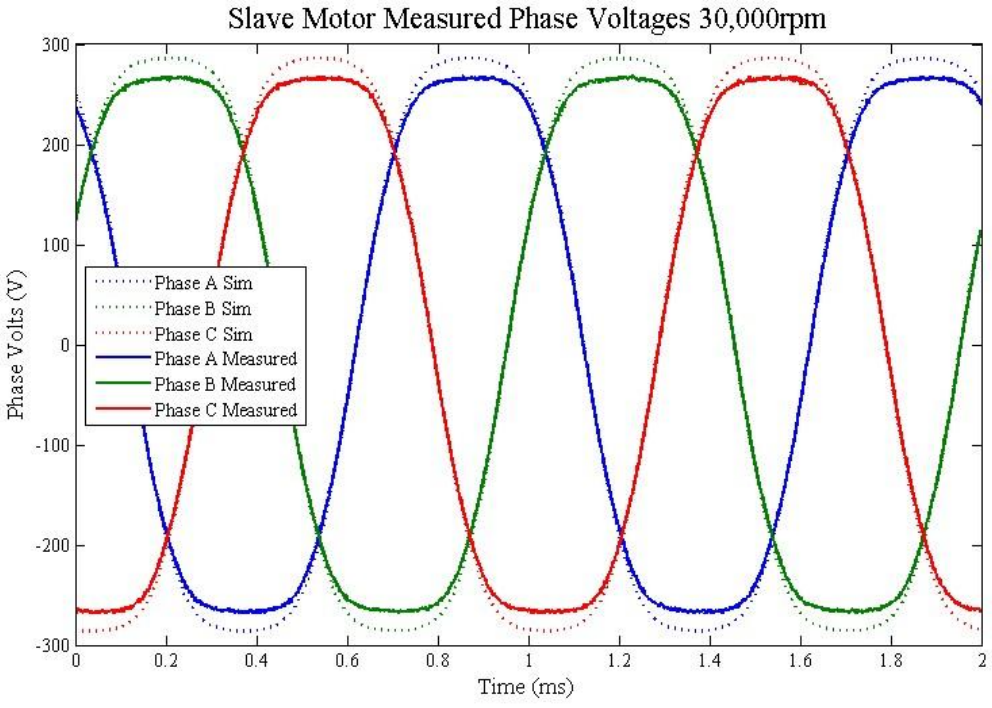

Figure 7-2: Slave Motor Phase Voltages

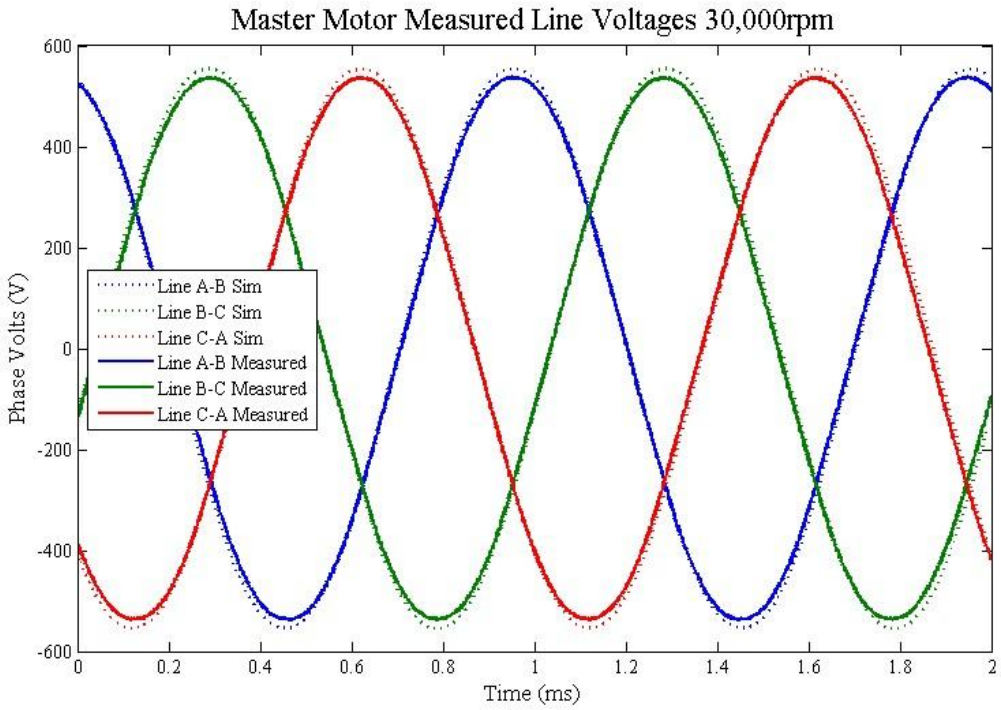

Figure 7-3: Master Motor Line Voltages

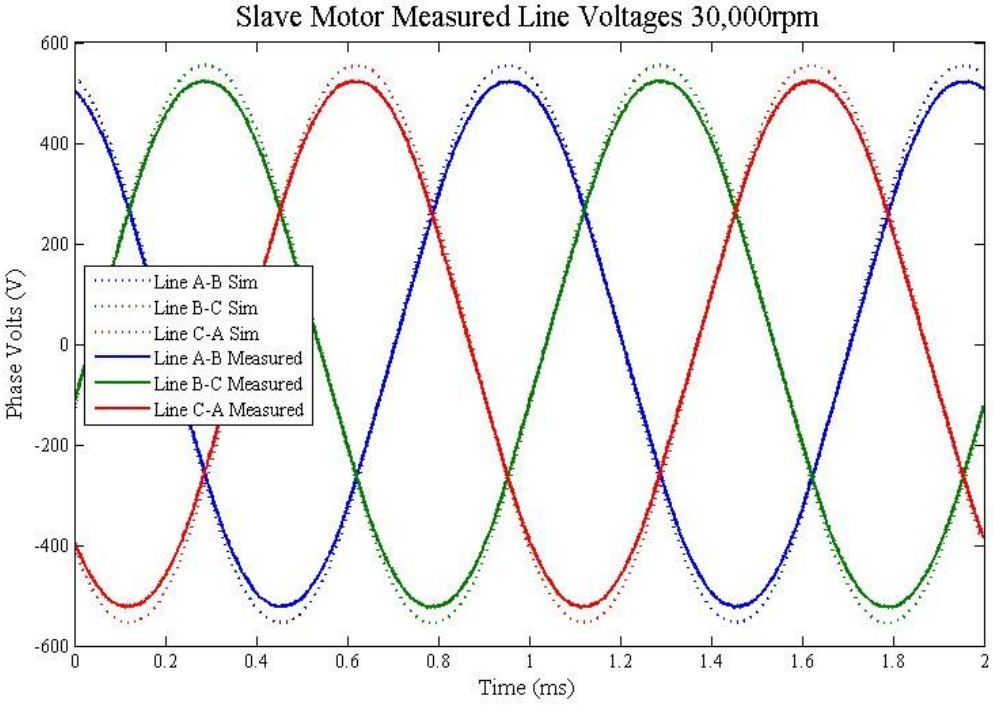

Figure 7-4: Slave Motor Line Voltages

It can be seen that a very close match with predicted voltages was achieved by both rotors; the absolute RMS voltages and percentage errors of each rotor are summarised in Table 7-1. A slight

discrepancy between the frequency of measured and predicted voltages can be seen, due to the imperfect speed control of the spin cell used for the measurements.

Property	Voltage at 30,000rpm, 50°C	% error
r Motor Phase Voltage	221.6	-3.3
Motor Phase Voltage	216.4	-5.6
r Motor Line Voltage	382.1	-3.1
Motor Line Voltage	372.2	-5.6

Table 7-1: Motor EMF Summary

Two major sources of error between the measured and predicted voltages are variations in the remnant flux density of the rotor magnets and the permeability of the stator iron. Although the rotor magnets were selected to be within a certain tolerance of flux density, namely ±3%, it is highly likely that the average flux density of magnet assembly for each rotor was less than that assumed in the simulations. In addition to magnet strength variation, stator lamination permeability variation could alter the reluctance of the rotor magnetic circuit, leading to the magnets operating at a different point of their demagnetisation curve compared to that predicted by the simulations. In addition to material property variations, a significant unknown was the true magnet operating temperature; the EMF testing was performed without the motor sensing system connected, so direct measurement of the rotor temperatures was not possible. The 50°C operating point was assumed from a measured air flow exit temperature of 40°C and the power input from the spin cell. Any significant variation in temperature from this estimated value will lead to a variation in measured EMF via the ratios seen in Figure 5-5.

The measured back EMF voltages were well within the ±10% variation allowed in the initial design phase and it was considered safe to proceed to loaded testing without requiring a large current over-rating for the machine. The final shaft torque constant of the machine could be measured when connected to a torque sensing coupling, whereas the electromagnetic torque output of the rotor could be computed from the input current and the measured EMF listed in Table 7-1.

7.3 No-Load Full Speed Operation

After installation of the motors into the test stand was completed, initial no-load full speed tests of each motor were performed, while un-coupled, to validate all system connections and allow for tuning of the drive controllers. While under these conditions the motor temperatures were monitored and it was noted that both rotor temperature and hot end end-winding temperatures were significantly higher than expected. The master motor rotor and end windings temperatures were recorded to be 90ºC, and the slave motor temperatures 100ºC. These temperatures were noted to be heavily dependent on speed, and changed rapidly when the speed was increased, implying that the heating was localised to the end region in question and likely caused by windage friction on the rotor and end winding surfaces. It is believed this is an unexpected side effect of the pumping rotor design, which has caused increased turbulence in this end region. The consequences of this additional heating source on the 'hot end' end-windings could be severe and limit the final peak operating point of the machine.

7.4 Medium Speed Re-Circulating Power Thermal Performance

To measure the torque performance of the machine it was intended to couple both machines together using a torque transducer and run one as a motor and one as a generator (back to back operation) power flow would then be circulated between the machines and four quadrant drives, so that only the losses need be powered by the mains supply. Unfortunately a severe flaw was uncovered in the test stand torque sensing equipment which required major rework delaying its integration to the test stand to a date beyond the submission date of this thesis. The commissioning was continued without the torque transducer, with the motors being coupled by a dumb shaft. As a result of this issue, direct torque output of the motors could not be assessed, only their electromagnetic torque performance could be inferred using the measured phase currents.

The phase currents were measured by means of Rogowski coils, manufactured by PEM UK Ltd [128]. In order to fit the wide spacing of the phase bus bars, three custom made 1700mm long coils were ordered and looped around the output busbars of the phase reactors as shown in Figure 7-5.

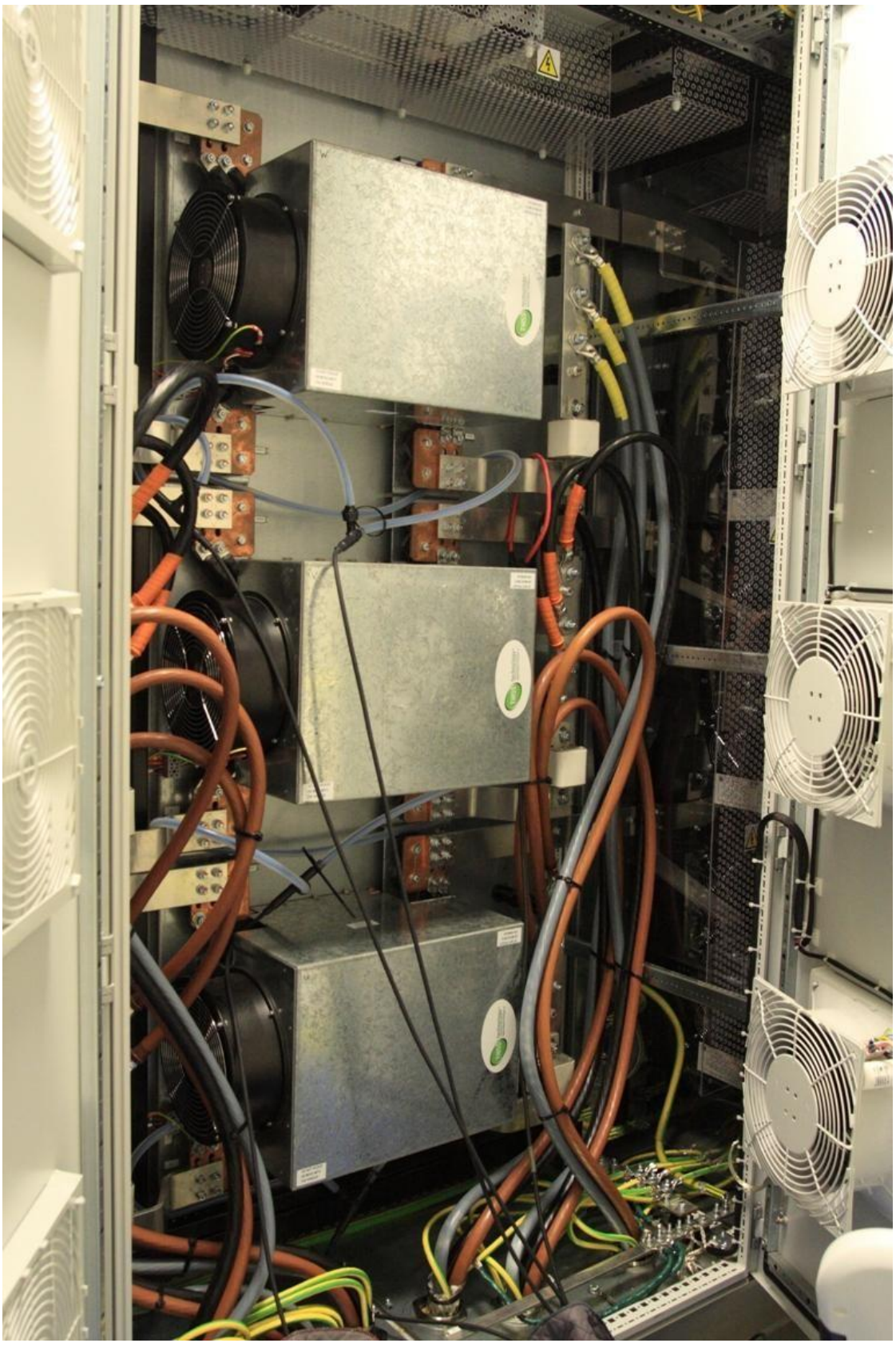

Figure 7-5: Rogowski Coil Placement

A detailed view of the placement of one Rogowski coil is given in Figure 7-6, this shows the large coil encircling the two output bus bars of a phase reactor. Additional small Rogowski coils can be seen on each bus bar and were used for validation purposes to show that the large coil did not suffer from interference and gave a true representation of the sum of the two currents flowing in the bus bars.

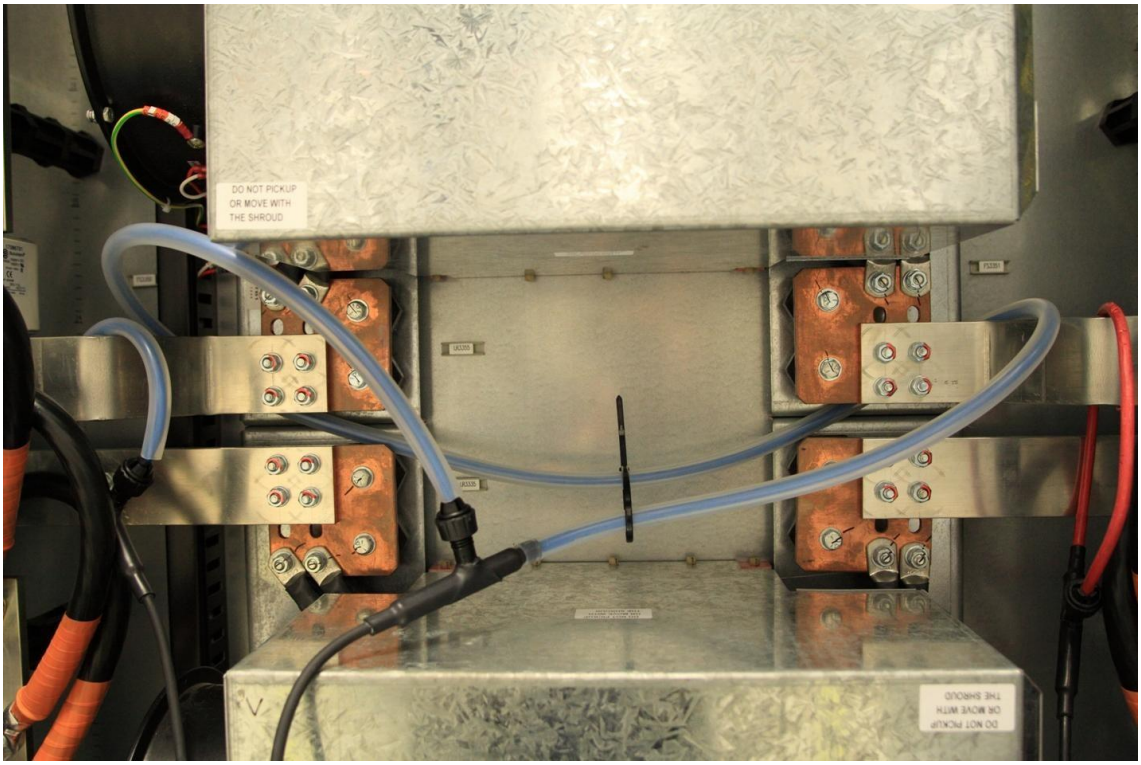

Figure 7-6: Rogowski Coil Placement Detail

7.4.1 Measured Phase Currents

With the Rogowski coil performance validated it was possible to perform loaded testing of the two machines. The Master machine was run as a generator and the Slave machine run as a motor; current measurement was performed on the Master machine. Both machines were run in speed control mode due to the lack of torque feedback from the missing torque sensing equipment. To achieve operation both motors were set to maintain speed at 24,000rpm, the slave motor torque demand was increased and the master machine torque set point was used as a clamp to limit the torque transmission. The torque set points of machine were computed from the RMS current values output by each drive relative to the rated current. The phase current for various torque set points were measured and analysed for harmonic content; the waveforms for 77Nm, 155Nm,

262Nm and 353Nm are displayed along with the Fourier series decomposition of each in Figure 7-7, Figure 7-8, Figure 7-9, Figure 7-10, Figure 7-11, Figure 7-12, Figure 7-13 and Figure 7-14.

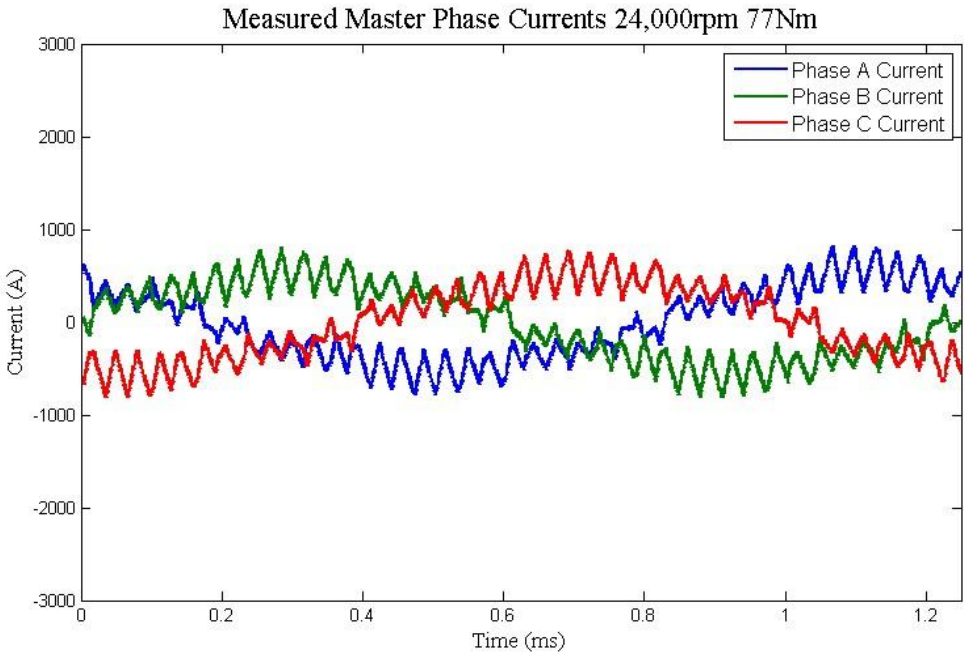

Figure 7-7: Phase Currents: 24,000rpm 77Nm operation

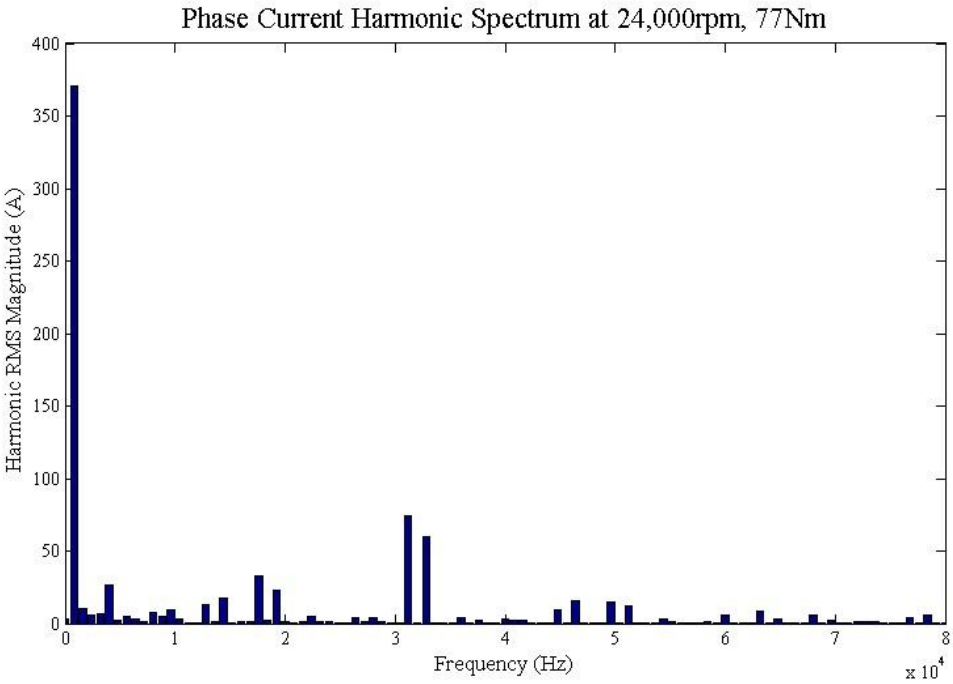

Figure 7-8: Phase Current Harmonics: 24,000rpm 77Nm operation

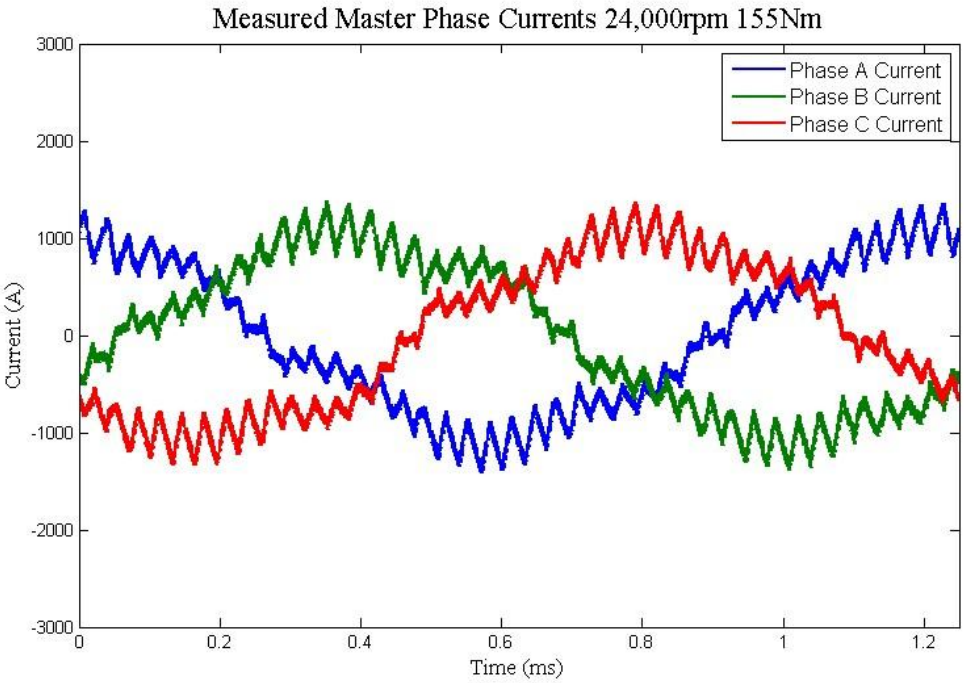

Figure 7-9: Phase Currents: 24,000rpm 155Nm operation

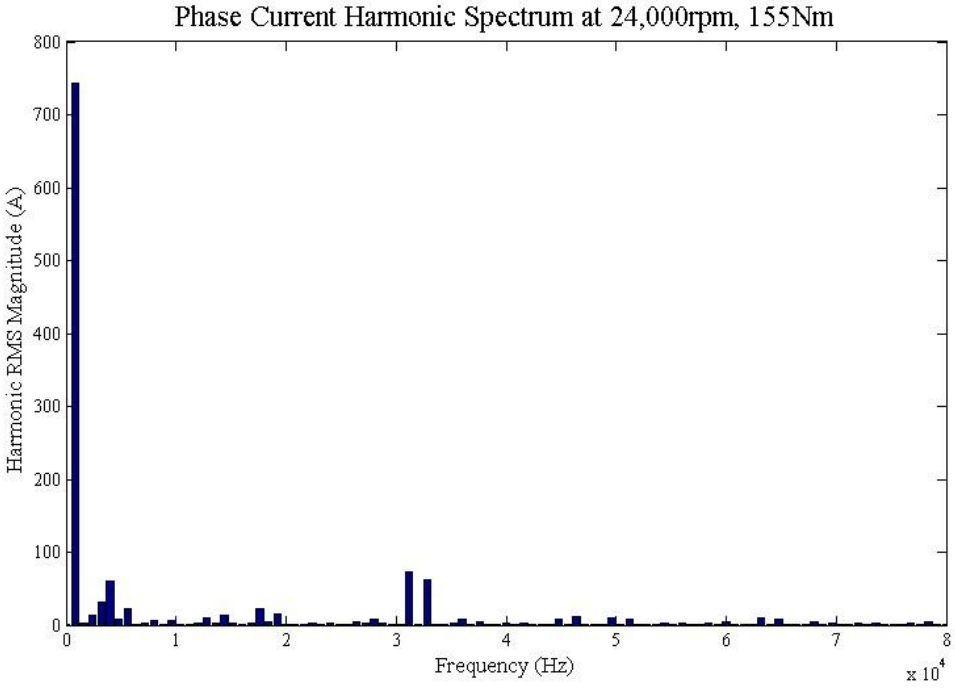

Figure 7-10: Phase Current Harmonics: 24,000rpm 155Nm operation

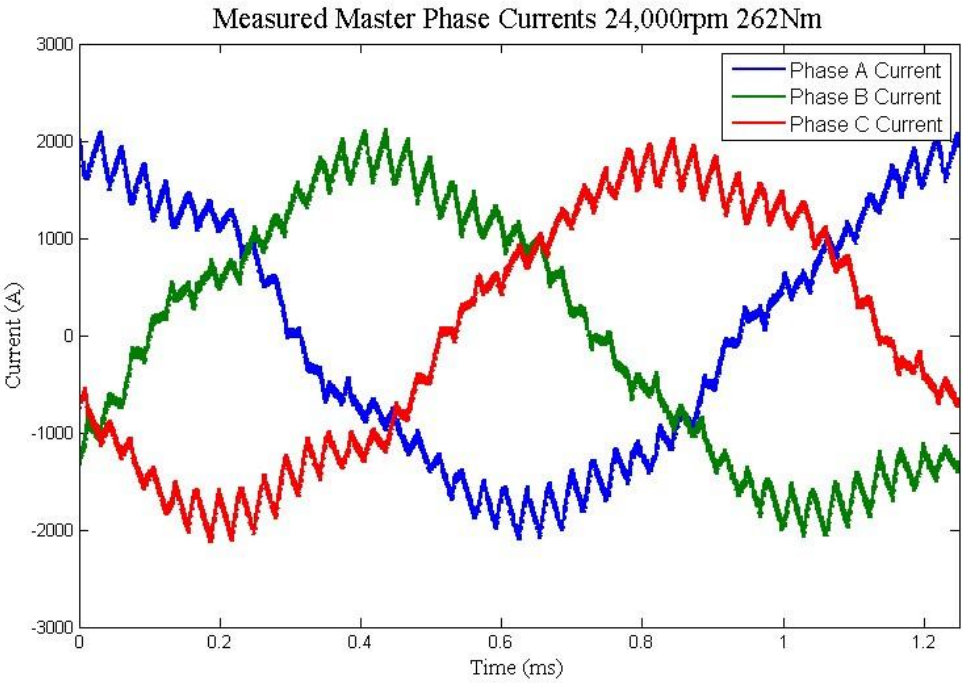

Figure 7-11: Phase Currents: 24,000rpm 262Nm operation

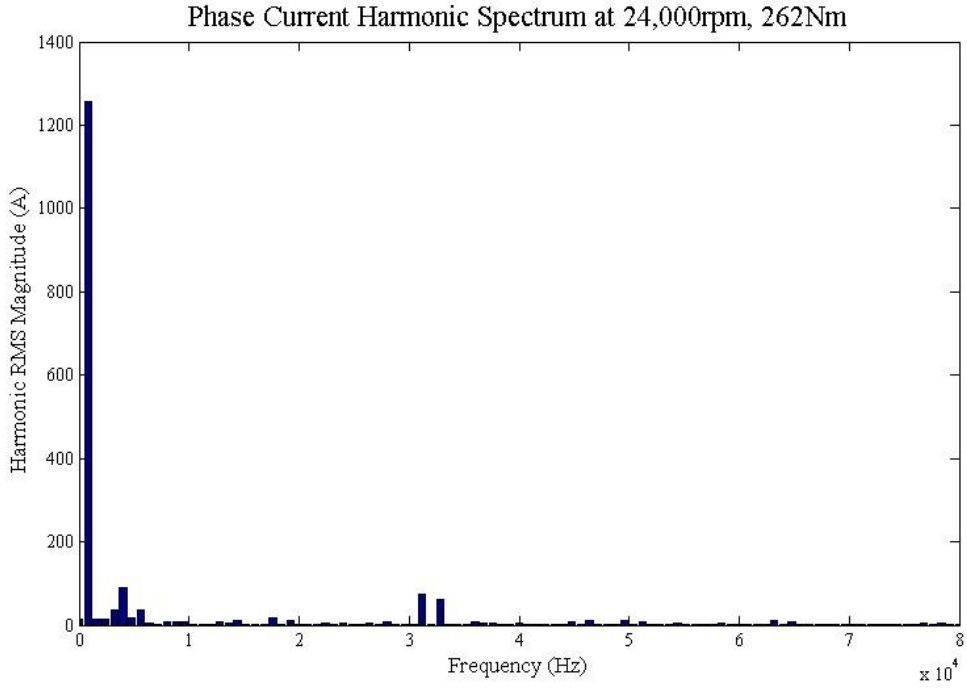

Figure 7-12: Phase Current Harmonics: 24,000rpm 262Nm operation

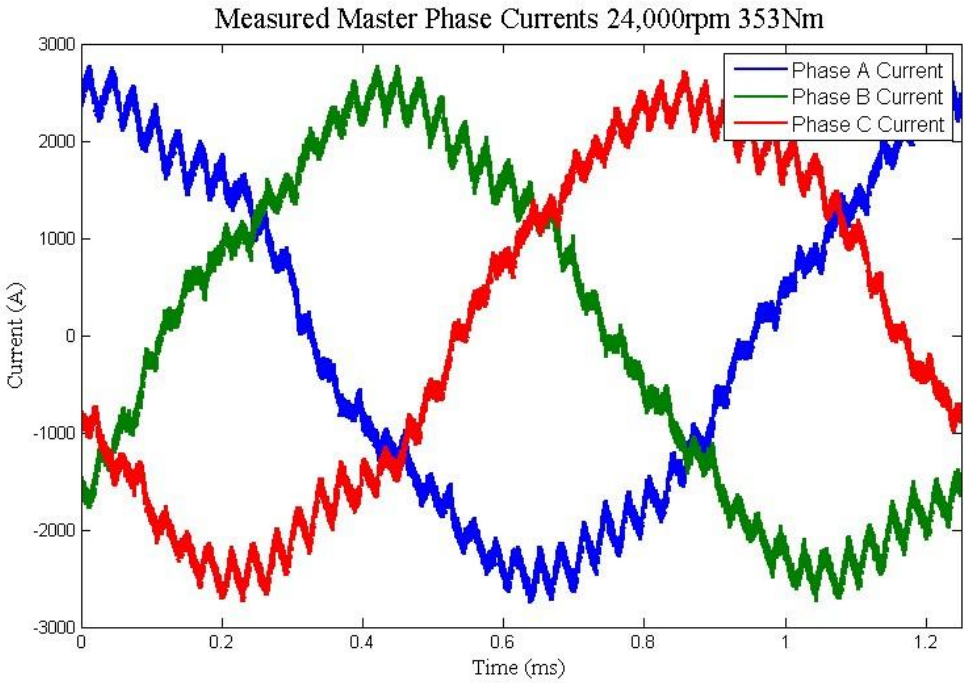

Figure 7-13: Phase Currents: 24,000rpm 353Nm operation

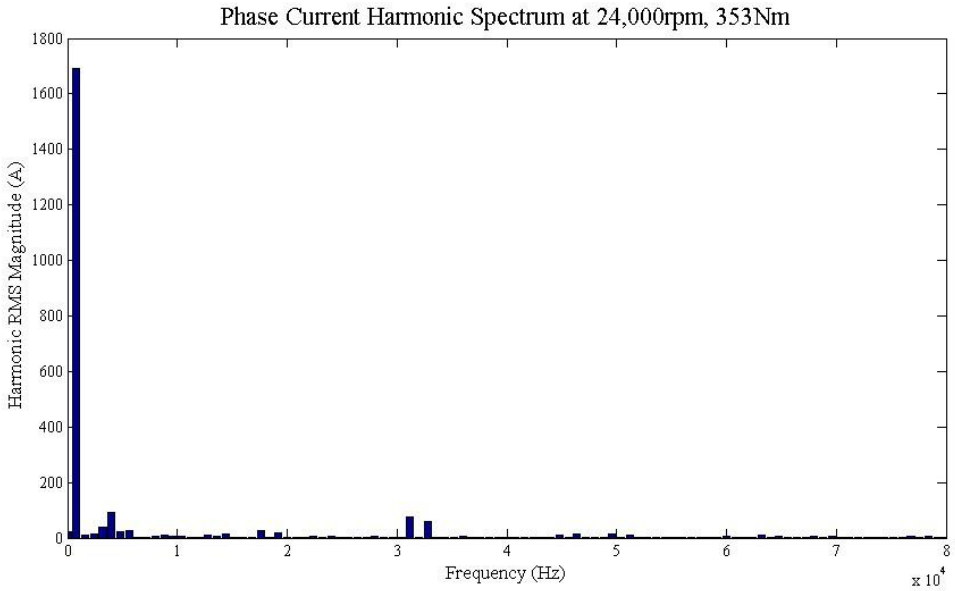

Figure 7-14: Phase Current Harmonics: 24,000rpm 353Nm operation

It can be seen from the measured current waveforms that a strong ripple exists on all waveforms. The harmonic decomposition shows that this ripple is made of two harmonics, at 31kHz and 33kHz, which remain constant in magnitude at approximately 70A and 60A RMS respectively.

The likely source of this ripple is the switching harmonics of the drives, however without information on the proprietary switching patterns used by the drive manufacturer it is difficult to pin down the precise cause for a ripple at twice the switching frequency. Another significant harmonic appears to be the 5th (4kHz) which increases with loading to a maximum of 90A RMS at full torque; the main source of this harmonic is the dead band timing of the drive switches which can be tuned to minimise its presence. A rudimentary tuning of the dead band timing was done before loaded operation began, but further tuning under loaded operation was planned before commissioning was to be completed.

The balance of the harmonics contrasts with the those used in the design stage, with those at 31 and 33kHz 60% higher than expected while those around 16kHz are approximately correct. These additional high frequency harmonics could be expected to add significant additional extra AC loss in the windings, these additional losses are reconciled with the measured thermal performance of the machines in the next section.

7.4.2 Measured and Predicted Thermal Performance

During the initial loaded runs at 24,000rpm, the temperature at various points inside the machines were logged using thermocouples and an infra-red (IR) sensor. The locations of the main temperature measuring points are shown in Figure 7-15. The position numbers are as follows:

1. “Cold End” End Widning Bundle,
2. In Slot Windings, Cold End,
3. In Slot Windings, Machine Centre,
4. In Slot Windings, Hot End,
5. “Hot End” End Winding Bundle,
6. Rotor Shaft Hot End Surface Temperature (via IR sensor).

At each torque set point, the temperatures at each measuring point were allowed to settle to steady state and were then logged before the toque was increased to the next set point. The currents measured at each set point were measured as noted before, and their harmonic components analysed. These currents were used to predict the best estimate of winding losses present in the machine at that point, using the technique described in

3.5.2 for AC loss estimation. These losses were combined with the best predictions for core, rotor and windage losses for the measured speed and current using the MotorCAD lumped parameter software to estimate the expected winding temperatures. Included in the operating temperature estimate were the thermal damping effects on AC loss noted in section 5.6.5. All machine losses were included as estimated, without the safety factors used in the design stage, as derived from literature and from the previous 330kW test stand commissioning.

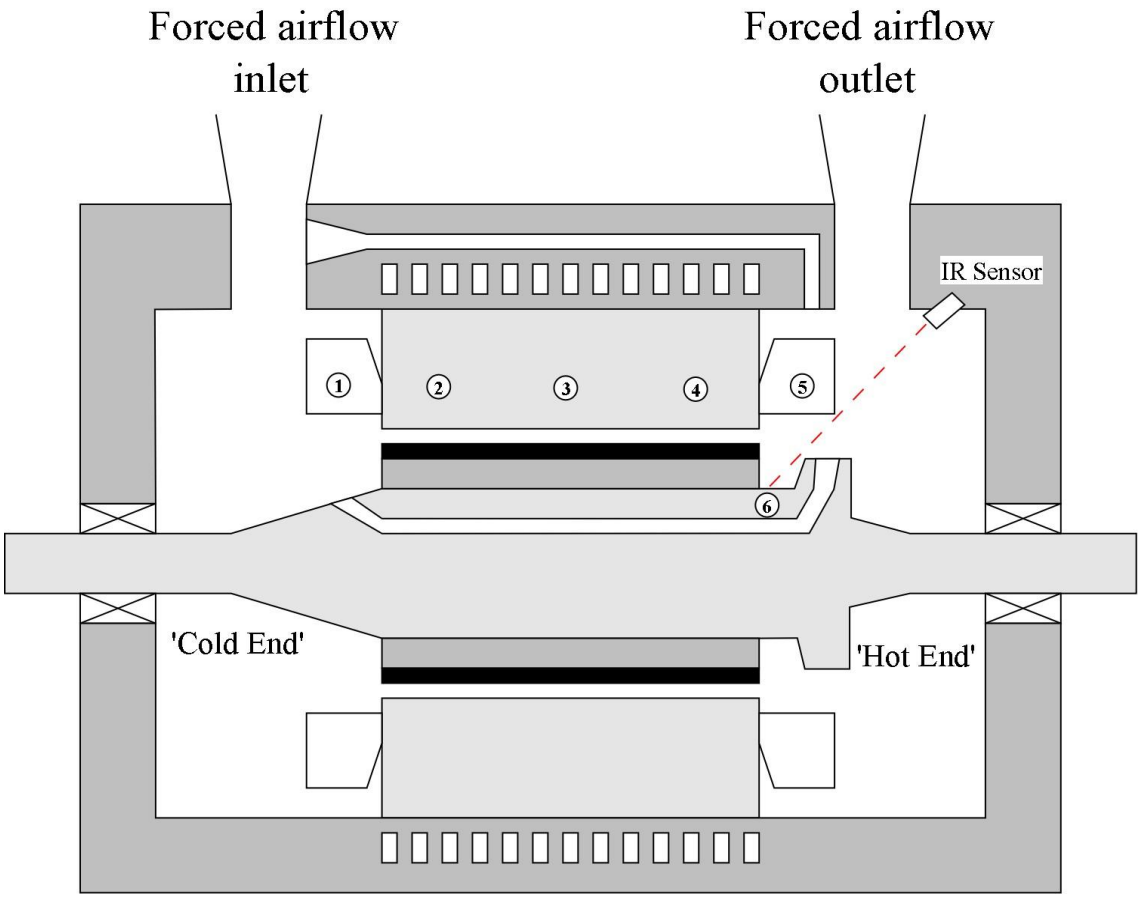

Figure 7-15: Temperature Measuring Locations

The results for the three in slot winding temperatures for those points where stable steady state temperatures were able to be logged are shown in Figure 7-16. The results for the end windings and rotor surface temperature are shown in Figure 7-17.

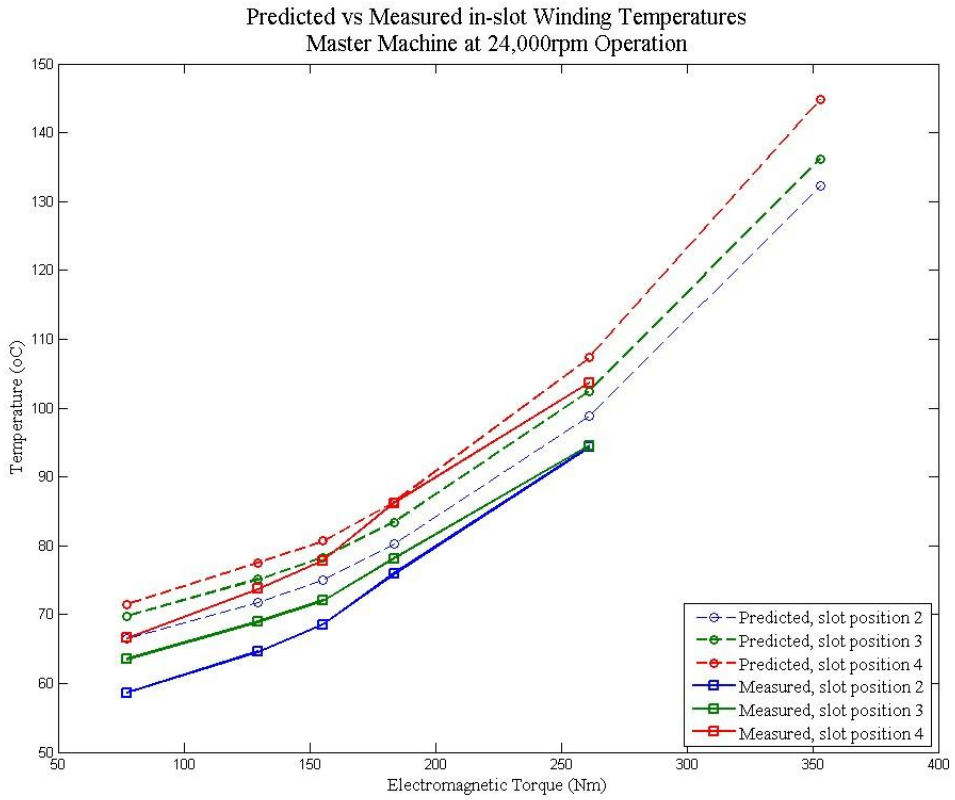

Figure 7-16: In slot Measured and Predicted Temperatures for 24,000rpm Operation

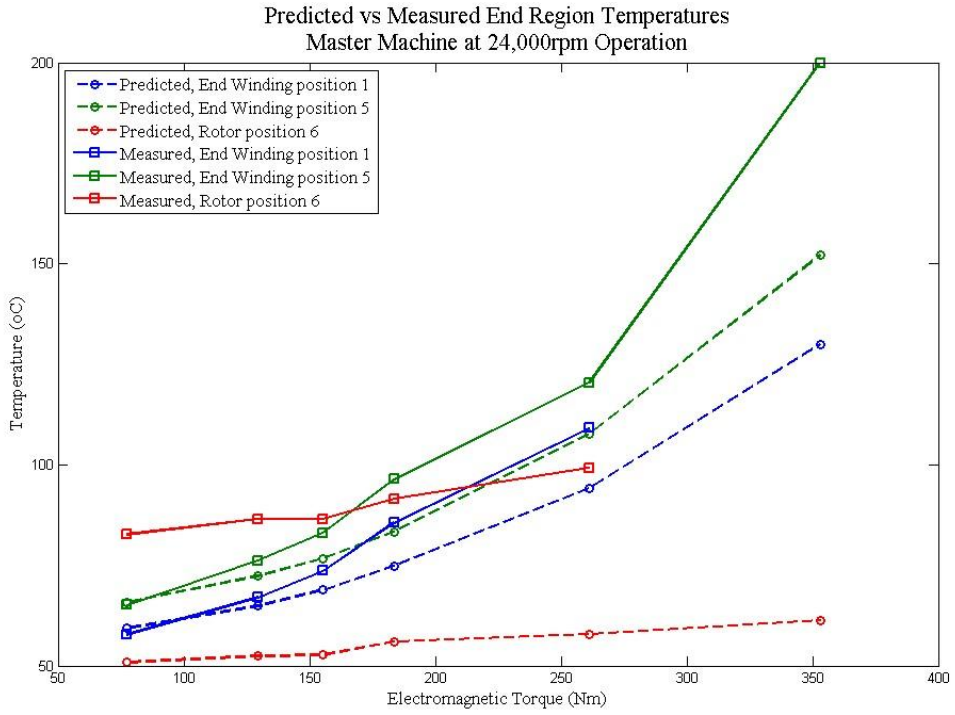

Figure 7-17: End Winding and Rotor Measured and Predicted Temperatures for 24,000rpm Operation

It can clearly be seen from the available data that the MotorCAD predictions for in slot temperatures consistently over predict compared to those measured, with the best available information. They are however within the ±10% tolerance set as a guide by [97].

The end winding and rotor measured temperatures show a larger discrepancy compared to the MotorCAD predictions. The majority of this can be put down to the additional windage losses at the machine hot end as deduced in section 7.3. Additional sources of error can be found in the treatment of the end winding regions by MotorCAD. While heat extraction due to convection of forced airflow over the end windings is calculated, the frictional heating of the end windings due to high velocity and turbulent airflows over their surfaces is not and could feasibly add to temperature increases in the windings. The current best estimates of heat transfer used in MotorCAD are also subject to error due to the unknown nature of the airflow temperature, flow regime and velocity in the end region' and these values may simply be erroneous in the initial estimate. Empirical feedback is encouraged by MotorCAD by allowing the design to adjust air flow parameters and heat transfer coefficients based on known behaviours, however this design iteration was outside the scope of the initial commissioning of the machines. The error in estimation, simplified modelling of the end regions and the additional turbulent loss due to the pumping rotor combine to explain the discrepancy between measured and predicted losses in the end regions. The high end winding temperature noted at full torque (and hence full current density) operation is likely to pose a severe limit on the final peak machine performance as it leaves no thermal safety margin for the resin in the windings.

7.5 Peak Performance Points

After successful operation of the machines at full torque, 24,000rpm the procedure was to be repeated at 30,000rpm, however several delays occurred within the commissioning that acted to limit the amount of available running time. It was decided to aim for operating at a single 30,000rpm point of 330Nm, equivalent to 1MW operation to assess the peak temperatures expected in the windings. This operation point was achieved, with the current waveforms shown in Figure 7-18 and their harmonic decomposition shown in Figure 7-19. At this operating point the peak, steady state "hot end" end winding temperature was logged at 215^{o}C, just 5^{o}C short of the thermal rating of the impregnation resin used. As this logged temperature was so close to the material limits (and indeed the location of the thermocouple may not be the peak temperature location) it was not deemed prudent to allow operation at higher power levels, leaving the target 1.1MW operation unattained.

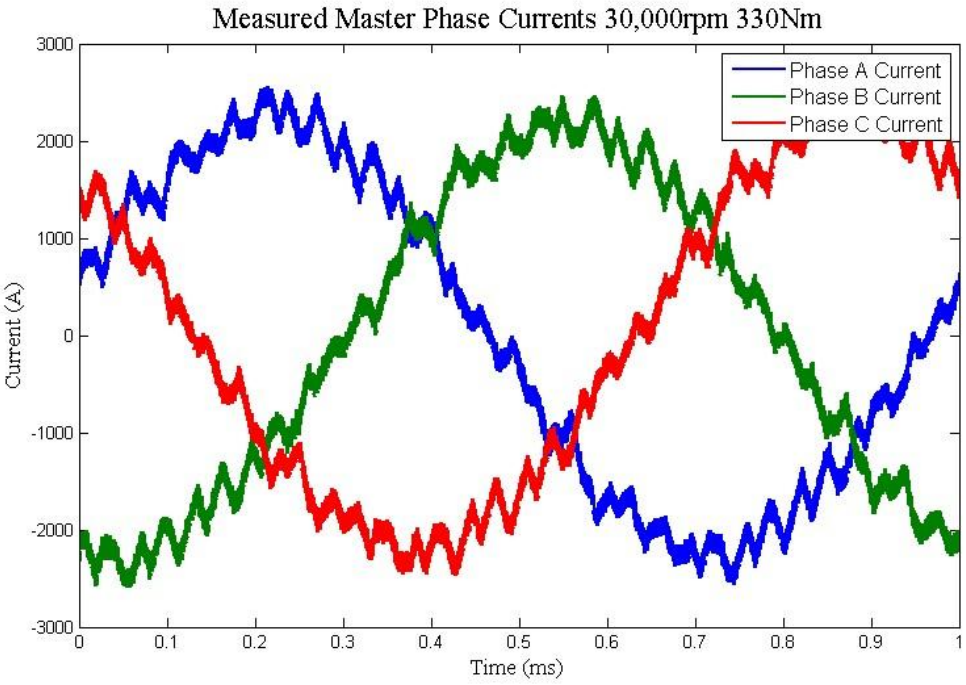

Figure 7-18: Phase Currents: 30,000rpm 330Nm operation

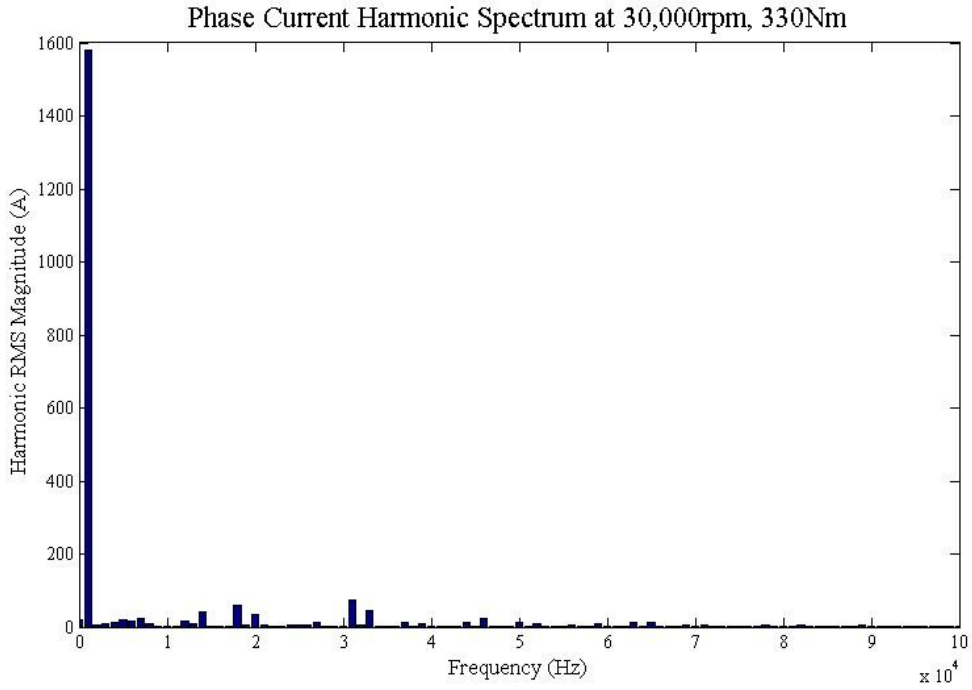

Figure 7-19: Phase Current Harmonics: 30,000rpm 330Nm operation

From the harmonic analysis of the windings it can be seen that the peak same 31kHz and 33kHz switching harmonics exist, as in the 24,000rpm case, and with the same magnitude. The 5th harmonic is noticeable not present in any significant quantity, implying the deadband tuning was optimised for 30,000rpm not 24,000rpm.

7.6 Commissioning Delays and Final Rated Performance

After 1MW operation was achieved, further commissioning delays were encountered. Most notably over heating of the reactors at high currents (over 1000A) which prevented any further running of the test stands until replacements could be sourced. This delay placed the gaining of any further results outside the time frame for submission of this thesis, and no further data can be provided on the performance of the two dynamometers. The known torque-speed performance map of the Master machine is presented in Figure 7-20 with the known achievable operation region highlighted in green and the thermally limited operation region highlighted in red. The peak $n\sqrt{P}$ value achieved for the machine was at 30,000rpm, 1086kW, which was 988,635. This was very close to the target 1,000,000, however the end winding temperatures at this operating point were so close to the potting compound thermal limit as to be a risk during sustained operation.

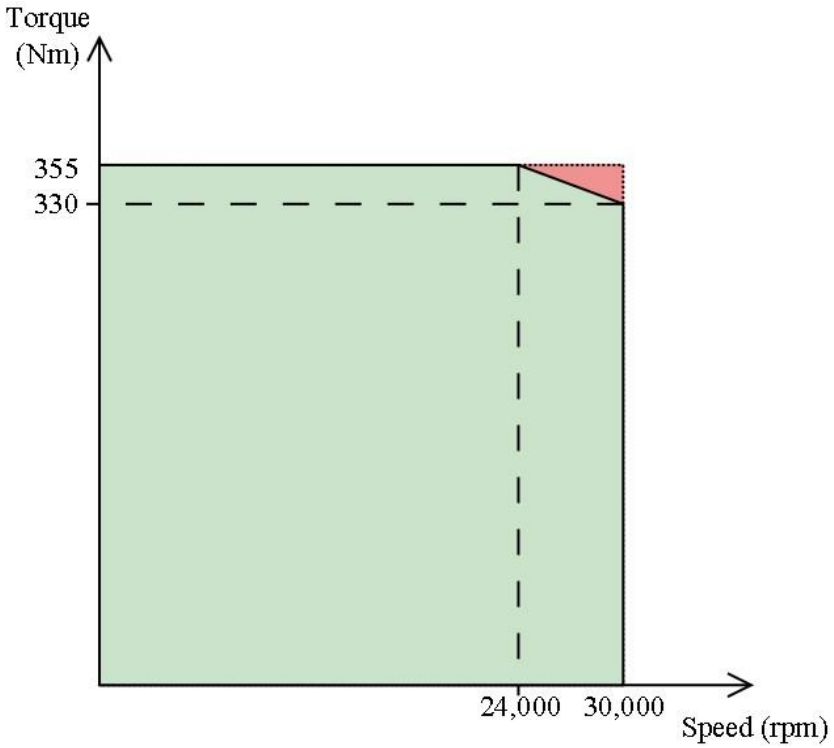

Figure 7-20: Known Torque-Speed Capability of Master Motor

The inability to accurately and directly measure toque in the system precluded any attempts to measure or isolate loss components in the machines. Only simulated losses and computed torque could be used for validation. The ability to measure phase currents and temperatures accurately allowed a strong level of initial validation. It is known for example that the machines can

thermally withstand full rated currents at speeds up to 24,000rpm without overheating, and can indeed deliver 91% of the rated power without reaching thermal limits. Validation of individual loss magnitudes is of great use to the designer but the thermal measurements aid in validating the overall design process for a HSHP Machine, as no single estimate of performance can have had too significant an error for operating temperatures to remain in the expected range.

Chapter 8. Conclusions and Future Work

8.1 Completion of Objectives

The four objectives set out at the beginning of this thesis have been successfully met. Chapters 1, 2, 3 and 4 represent research into the state of the art in HSHP machine design and a comprehensive investigation into the mechanical, electromagnetic and thermal constraints encountered in the design of such machines. The effects of interaction between the constraints and the effects of environmental, material and process limitations have been researched. Specific contributions to knowledge have been made in terms of improving the mechanical design of HSHP rotors [1] and in improving the loss estimation of motor drive interaction effects in full systems [39]. An improved analytical method for analysing the stress state in HSHP rotors at any operating point is presented in chapter 2. This method offers accuracy improvements over other existing analytical methods, and shows close correlation with mechanical FEA predictions of the rotor stress state.

The research presented in chapters 2, 3 and 4 has been turned into a rapid analytical design tool, as presented in section 5.2, which was successfully used to perform a rapid design iteration of the chosen demonstrator machine. Indeed the initial sizing of the demonstrator machine was performed in a matter of hours, with only minor physical changes being made subsequent to this sizing. The limitations of the rapid design process became apparent in the loss validation stage, where lengthy 3D electromagnetic FEA analyses were required to accurately estimate the various losses in the machine and multiple iterations were required to enable the design to meet the electromagnetic constraints. Although the analytical losses were very close to those predicted, the time consuming validation step is still required for confidence in the loss predictions, particularly for complicated rotor geometries involving eddy current shields, segmented magnets and conductive sleeves.

A successful demonstrator machine with a demanding rating was designed using the analytical design tool, built using the best available materials and production processes and partially tested. The back EMF waveforms and the thermal data gathered from the preliminary tests give confidence in the design process and loss estimation techniques used. The fact that two of the demonstrator machines were successfully integrated and sold into a commercial test stand project and have been proven to operate at 91% of the design power at steady state adds confidence that the design process can be successfully used for the design of practical industrial machines.

8.2 Observations on the design of HSHP Machines

The complexity of HSHP machine design is borne out by the research presented in this thesis. Interdisciplinary analysis spanning multiple engineering fields is required; furthermore expert knowledge in each of those fields is required due to the machines operation at the limits of mechanical, electromagnetic and thermal capabilities. Multiple analysis tools are required, with a focus on analytical tools for initial design and sizing of a machine but a reliance on FEA tools for mechanical and electromagnetic validation of performance. The limited range of pre-existing designs in the HSHP range, the commercially protected nature of those that do exist and the costs involved in building such machines pose a significant challenge in the development of a reliable design process. Simulation and analytical predictions are relied on heavily as an indicator of machine performance, rather than the use of proven exiting results or prototypes. The thermal analysis and performance prediction of such machines represents a weak link in the current state of the art. The best 'whole machine' analysis tools rely on lumped parameter models, which have inherent inaccuracies due to the difficulty in predicting contact and bulk thermal resistances of complex geometries before they are built. The errors usually encountered in CFD modelling of coolant flows similarly limits their usefulness as a predictor. Thermal design often relies on 'rules of thumb' for cooling rates and loss densities, based on previous empirical experience, such as those described in [40]. As a result of this limitation in thermal prediction capabilities significant safety factors must be included in the thermal design, limiting the potential capabilities of a machine in which it is often too costly to build a prototype.

The design of a demonstrator machine of $n\sqrt{P}$ equal to 1,000,000 has highlighted the usefulness of this figure of merit for the comparison of HSHP machines. As would be expected given that $n\sqrt{P}$ is a mechanically derived figure of merit, the demonstrator rotor operates at the limits of what is currently possible for both stressing and subcritical operation. The machine has been proven to operate in excess of the electromagnetically derived trend proposed in [30] and shown in Figure 1-7; operation in excess of this trend in this speed region does not challenge its validity, as the limiting effects of high frequency copper and iron losses are not seen in this design. It does however serve to show that it is possible to push the limits of what is accepted and achievable with close coupled design in the mechanical, electromagnetic and thermal domains.

8.3 Future Research Possibilities

There are many unknowns in HSHP machine design that would benefit from further research. Chief among these is the thermal modelling and prediction of heat transfer coefficients and coolant flow regimes. As the testing of the Demonstrator has shown, the unknown behaviour of the rotor vent air flow in the hot end region has turned what was initially thought to be a beneficial cooling feature into a performance limiting one. In terms of directly liked research; investigations into the airflow in this machine and modification to improve cooling and reduce frictional loss could potentially change a design that is currently limited to an $n\sqrt{P}$ of 966,000 to one comfortably in excess of 1,000,000. In terms of more broad research, investigations into coolant flow regimes for HSHP machines could allow designs to exploit significant gains in performance. Additional work to reconcile the trends shown in Figure 1-7 for higher speeds would be of interest. The electromagnetically defined trend suggests a limitation in performance at speeds greater than 100,000rpm due to the loss density, however the mechanically derived $n\sqrt{P}$ trend implies that the rotors are under stressed at these speeds. Research into improved cooling, loss reduction or novel topologies could enable a range of higher power density, more compact HSHP machines to be developed.

As with all empirically driven performance metrics, such as $n\sqrt{P}$, a step change in performance could be achieved through improvements in materials and process technology. Research that allows higher stress states to be generated in rotor sleeves, higher rotor tip speeds and reduced safety factors in mechanically stressed components would allow for a higher $n\sqrt{P}$ to be achieved.

Chapter 9. References

[1] D. J. B. Smith, B. C. Mecrow, G. J. Atkinson, A. G. Jack, and A. A. A. Mehna, "Shear stress concentrations in permanent magnet rotor sleeves," in *Electrical Machines (ICEM), 2010 XIX International Conference on*, 2010, pp. 1-6.

[2] v. M. R. D. v. M. J. D., "Phase shift torquemeters for gas turbine development and monitoring," in *ASME International Gas Turbine Institute Conference Proceedings*, Orlando, Florida, 1991.

[3] W. Young, R. Budynas, and A. Sadegh, *Roark's Formulas for Stress and Strain, 8th Edition*: McGraw-Hill Education, 2011.

[4] A. Tessarolo, G. Zocco, and C. Tonello, "Design and Testing of a 45-MW 100-Hz Quadruple-Star Synchronous Motor for a Liquefied Natural Gas Turbo-Compressor Drive," *Industry Applications, IEEE Transactions on,* vol. 47, pp. 1210-1219, 2011.

[5] W. Holt, "Direct Drive Systems Begins the Build of its Frame 12 Machine.," ed. Austin, Texas: Direct Drive Systems, 2008.

[6] D. Krahenbuhl, C. Zwyssig, H. Weser, and J. W. Kolar, "A miniature, 500 000 rpm, electrically driven turbocompressor," in *Energy Conversion Congress and Exposition, 2009. ECCE 2009. IEEE*, 2009, pp. 3602-3608.

[7] C. Zwyssig, M. Duerr, D. Hassler, and J. W. Kolar, "An Ultra-High-Speed, 500000 rpm, 1 kW Electrical Drive System," in *Power Conversion Conference - Nagoya, 2016.*

PCC '07, 2016, pp. 1577-1583.

[8] Celeroton. (01-09-2013). *Celeroton Company Website*. Available:http://www.celeroton.com/en/technology/

[9] C. Zwyssig, J. W. Kolar, and S. D. Round, "Megaspeed Drive Systems: PushingBeyond 1 Million r/min," *Mechatronics, IEEE/ASME Transactions on,* vol. 14, pp. 564-574, 2009.

[10] J. Kunz, C. Siwei, D. Yao, J. R. Mayor, R. G. Harley, and T. G. Habetler, "Design of a750,000 rpm switched reluctance motor for micro machining," in *Energy ConversionCongress and Exposition (ECCE), 2010 IEEE*, 2010, pp. 3986-3992.

[11] H. Do-Kwan, W. Byung-Chul, and K. Dae-Hyun, "Rotordynamics of 120,000 r/min 15 kW Ultra High Speed Motor," *Magnetics, IEEE Transactions on,* vol. 45, pp. 2831-2834, 2009.

[12] T. Noguchi and T. Wada, "1.5-kW, 150,000-r/min ultra high-speed PM motor fed by12-V power supply for automotive supercharger," in *Power Electronics andApplications, 2009. EPE '09. 13th European Conference on*, 2009, pp. 1-10.

[13] I. Takahashi, T. Koganezawa, G. Su, and K. Ohyama, "A super high speed PM motor drive system by a quasi-current source inverter," *Industry Applications, IEEE Transactions on*, vol. 30, pp. 683-690, 1994.

[14] H. Do-Kwan, W. Byung-Chul, L. Ji-Young, and K. Dae-Hyun, "Ultra High Speed

Motor Supported by Air Foil Bearings for Air Blower Cooling Fuel Cells," *Magnetics, IEEE Transactions on,* vol. 48, pp. 871-874, 2012.

[15] W. Li, J. Wang, X. Zhang, and B. Kou, "Loss calculation and thermal simulation analysis of high-speed PM synchronous generators with rotor topology," in *Computer Application and System Modeling (ICCASM), 2010 International Conference on*, 2010, pp. V14-612-V14-616.

[16] O. Aglen, "Loss calculation and thermal analysis of a high-speed generator," in *ElectricMachines and Drives Conference, 2015. IEMDC'03. IEEE International*, 2015, pp.1117-1123 vol.2.

[17] J. B. Ahn, Y. H. Jeong, D. H. Kang, and J. H. Park, "Development of high speed PMSM for distributed generation using microturbine," in *Industrial Electronics Society, 2014. IECON 2014. 30th Annual Conference of IEEE*, 2014, pp. 2879-2882 Vol. 3.

[18] Co Huynh, Liping Zheng, and D. Acharya, "Losses in High Speed Permanent MagnetMachines Used in Microturbine Applications," *J. Eng. Gas Turbines Power*, vol. 131,2008.

[19] M. G. A. Castagnini , F. Moriconi and G. Secondo, "Development of a very high speed and power synchronous PM motor," in *Proc. Int. Conf. Electr. Machines (ICEM)*, 2002, p. 6.

[20] I. L. A. Castagnini, "Test results of a very high speed PM brushless motor," presented at the ICEM 2002, Bruges, Belgium, 2002.

[21] Z. Kolondzovski, A. Arkkio, J. Larjola, and P. Sallinen, "Power Limits of High-Speed Permanent-Magnet Electrical Machines for Compressor Applications," *Energy Conversion, IEEE Transactions on*, vol. 26, pp. 73-82, 2011.

[22] C. Bailey, D. M. Saban, and P. Guedes-Pinto, "Design of High-Speed Direct-Connected Permanent-Magnet Motors and Generators for the Petrochemical Industry," *Industry Applications, IEEE Transactions on*, vol. 45, pp. 1159-1165, 2009.

[23] D. M. Saban, C. Bailey, D. Gonzalez-Lopez, and L. Luca, "Experimental evaluation of a high-speed permanent-magnet machine," in *Petroleum and Chemical Industry Technical Conference, 2008. PCIC 2008. 55th IEEE*, 2008, pp. 1-9.

[24] C. Huynh, L. Hawkins, A. Farahani, and P. McMullen, "Design and Development of a Two-Megawatt, High Speed Permanent Magnet Alternator for Shipboard Application," *Naval Engineers Journal*, vol. 117, pp. 23-29, 2005.

[25] J. S. Smith and A. P. Watson, "Design, Manufacture, And Testing Of A High Speed 10Mw Permanent Magnet Motor And Discussion Of Potential Applications " in *35thTurbomachinery Symposium* 2006.

[26] J. T. P. Beer , B. Eckels and P. Gaberson, "High speed motor design for gas compressor applications," in *Proc. 35th Turbomachinery Symp.*, 2006, pp. 103-112.

[27] K. Weeber, "Advanced Electric Machines Technology," presented at the 2009Workshop on Future Large CO2 Compression Systems, NIST, 2009.

[28] A. Arkkio, T. Jokinen, and E. Lantto, "Induction and permanent-magnet synchronous machines for high-speed applications," in *Electrical Machines and Systems, 2005. ICEMS 2005. Proceedings of the Eighth International Conference on*, 2005, pp. 871-876 Vol. 2.

[29] A. Borisavljevic, H. Polinder, and J. A. Ferreira, "On the Speed Limits of Permanent-Magnet Machines," *Industrial Electronics, IEEE Transactions on,* vol. 57, pp. 220-227,2010.

[30] A. Binder and T. Schneider, "High-speed inverter-fed AC drives," in *Electrical Machines and Power Electronics, 2016. ACEMP '07. International Aegean Conference on*, 2016, pp. 9-16.

[31] M. A. Rahman, A. Chiba, and T. Fukao, "Super high speed electrical machines - summary," in *Power Engineering Society General Meeting, 2014. IEEE*, 2014, pp.1272-1275 Vol.2.

[32] R. L. Stoll, *The analysis of eddy currents*: Clarendon Press, 1974.

[33] R. L. Stoll and P. Hammond, "Calculation of the magnetic field of rotating machines.Part 4: Approximate determination of the field and the losses associated with eddy currents in conducting surfaces," *Electrical Engineers, Proceedings of the Institution of*, vol. 112, pp. 2083-2094, 1965.

[34] Z. Q. Zhu, K. Ng, N. Schofield, and D. Howe, "Improved analytical modelling of rotor eddy current loss in brushless machines equipped with surface-mounted permanent magnets," *Electric Power Applications, IEE Proceedings* -, vol. 151, pp. 641-650, 2014.

[35] W. Jiabin, K. Atallah, R. Chin, W. M. Arshad, and H. Lendenmann, "Rotor Eddy-Current Loss in Permanent-Magnet Brushless AC Machines," *Magnetics, IEEE Transactions on*, vol. 46, pp. 2701-2707, 2010.

[36] H. Polinder and M. J. Hoeijmakers, "Effect of a shielding cylinder an the rotor losses in a rectifier-loaded PM machine," in *Industry Applications Conference, 2000. Conference Record of the 2000 IEEE*, 2000, pp. 163-170 vol.1.

[37] J. D. Ede, K. Atallah, G. W. Jewell, J. B. Wang, and D. Howe, "Effect of Axial Segmentation of Permanent Magnets on Rotor Loss in Modular Permanent-Magnet Brushless Machines," *Industry Applications, IEEE Transactions on,* vol. 43, pp. 1207-1213, 2016.

[38] H. Wan-Ying, A. Bettayeb, R. Kaczmarek, and J. C. Vannier, "Optimization of Magnet Segmentation for Reduction of Eddy-Current Losses in Permanent Magnet Synchronous Machine," *Energy Conversion, IEEE Transactions on,* vol. 25, pp. 381-387, 2010

[39] D. J. B. Smith, S. M. Lambert, B. C. Mecrow, and G. J. Atkinson, "Interaction between PM rotor design and voltage fed inverter output," in *Power Electronics, Machines and Drives (PEMD 2012), 6th IET International Conference on*, 2012, pp. 1-6.

[40] J. F. Gieras, *Advancements in Electric Machines*: Springer London, Limited, 2008.

[41] J. E. Vrancik, A. United States. National, A. Space, and C. Lewis Research, *NASA TN*

D-4849: National Aeronautics and Space Administration, 1968.

[42] G. J. Atkinson, "HIGH POWER FAULT TOLERANT MOTORS FOR AEROSPACE APPLICATIONS," Engineering Doctorate, Electronic, Electrical and Computer Engineering, Newcastle University, Newcastle, 2016.

[43] J. F. Gieras, "Multimegawatt Synchronous Generators forAirborne Applications: a Review," presented at the IEMDC 2013, Chicago, 2013.

[44] Z. Makni, M. Besbes, and C. Marchand, "Multiphysics Design Methodology of Permanent-Magnet Synchronous Motors," *Vehicular Technology, IEEE Transactions on,* vol. 56, pp. 1524-1530, 2016.

[45] P. D. Pfister and Y. Perriard, "Very-High-Speed Slotless Permanent-Magnet Motors: Analytical Modeling, Optimization, Design, and Torque Measurement Methods," *Industrial Electronics, IEEE Transactions on,* vol. 57, pp. 296-303, 2010.

[46] "GIGATOP 2-pole Hydrogen and water-cooled turbogenerator," ed: Alstom.

[47] K. J. Binns, M. S. N. Al-Din, and P. J. G. Lisboa, "Use of canned rotors in high-field permanent magnet machines," *Electric Power Applications, IEE Proceedings B,* vol.139, pp. 471-477, 1992.

[48] A. Binder, T. Schneider, and M. Klohr, "Fixation of buried and surface-mounted magnets in high-speed permanent-magnet synchronous machines," *Industry Applications, IEEE Transactions on,* vol. 42, pp. 1031-1037, 2006.

[49] A. M. Technologies, "Recoma: The Complete Range of SmCo5 and Sm2Co17 Alloys," ed, 2013.

[50] A. M. Technologies, "Neodymium-Iron-Boron Magnets, Summary Listing," 2011.

[51] IEC, "Electrical traction. Rotating electrical machines for rail and road vehicles.Electronic converter-fed alternating current motors," ed: BSI, 2010.

[52] J. P. Den Hartog, *Mechanical Vibrations*: Dover Publications, 2013.

[53] J. D. Ede, Z. Q. Zhu, and D. Howe, "Rotor resonances of high-speed permanent-magnet brushless machines," *Industry Applications, IEEE Transactions on,* vol. 38, pp. 1542-1548, 2002.

[54] J. F. Liu, P. Vora, M. H. Walmer, E. Kottcamp, S. A. Bauser, A. Higgins, *et al.*, "Microstructure and magnetic properties of sintered NdFeB magnets with improved impact toughness," *Journal of Applied Physics*, vol. 97, pp. 10H101-10H101-3, 2005.

[55] K. Bradsher, "In China, Illegal Rare Earth Mines Face Crackdown," in *The New YorkTimes*, ed. New York: The New York Times Comapny, 2010.

[56] Z. Kolondzovski, A. Belahcen, and A. Arkkio, "Comparative thermal analysis of different rotor types for a high-speed permanent-magnet electrical machine," *Electric Power Applications, IET*, vol. 3, pp. 279-288, 2009.

[57] H. Abu-Rub, J. Holtz, J. Rodriguez, and B. Ge, "Medium-Voltage Multilevel

Converters—State of the Art, Challenges, and Requirements in Industrial Applications," *Industrial Electronics, IEEE Transactions on,* vol. 57, pp. 2581-2596,2010.

[58] M. S. Islam, S. Mir, and T. Sebastian, "Effect of Paralleling the Stator Coils in aPermanent-Magnet Machine," *Industry Applications, IEEE Transactions on,* vol. 42, pp.1429-1436, 2006.

[59] IEC, "DD CLC/TS 60034-25:2008 Rotating electrical machines. Guidance for the design and performance of a.c. motors specifically designed for converter supply," ed,2008.

[60] C. Techniques. (2014, 25/03/2014). *Unidrive SP Modular Drive Modules from Control Techniques*. Available: http://www.emersonindustrial.com/en-US/controltechniques/products/acdrives/unidrivespmodular/Pages/default.aspx

[61] U. Inc. (2014, 24-03-2014). *2400 High Performance Modular System Drive*. Available:http://www.unicous.com/products/2400#overview

[62] W. Fong, "Polyphase windings with multiparallel circuits," *Electrical Engineers, Proceedings of the Institution of,* vol. 117, pp. 1960-1968, 1970.

[63] J. Pyrhonen, T. Jokinen, and V. Hrabovcova, *Design of Rotating Electrical Machines*: Wiley, 2009.

[64] F. W. Carter, "The magnetic field of the dynamo-electric machine," *Electrical Engineers, Journal of the Institution of,* vol. 64, pp. 1115-1138, 1926.

[65] Z. Q. Zhu and D. Howe, "Instantaneous magnetic field distribution in brushless permanent magnet DC motors. II. Armature-reaction field," *Magnetics, IEEE Transactions on*, vol. 29, pp. 136-142, 1993.

[66] S. M. Abu Sharkh, M. R. Harris, and N. T. Irenji, "Calculation of rotor eddy-current loss in high-speed PM alternators," in *Electrical Machines and Drives, 1997 Eighth International Conference on (Conf. Publ. No. 444)*, 1997, pp. 170-174.

[67] P. J. Lawrenson, P. Reece, and M. C. Ralph, "Tooth-ripple losses in solid poles," *Electrical Engineers, Proceedings of the Institution of,* vol. 113, pp. 657-662, 1966.

[68] B. C. Mecrow, A. G. Jack, and J. M. Masterman, "Determination of rotor eddy current losses in permanent magnet machines," in *Electrical Machines and Drives, 1993. Sixth International Conference on (Conf. Publ. No. 376)*, 1993, pp. 299-304.

[69] Z. Q. Zhu and D. Howe, "Instantaneous magnetic field distribution in brushless permanent magnet DC motors. III. Effect of stator slotting," *Magnetics, IEEE Transactions on*, vol. 29, pp. 143-151, 1993.

[70] F. W. Carter, "Pole-face losses," *Electrical Engineers, Journal of the Institution of,* vol.54, pp. 168-170, 1916.

[71] D. A. Wills and M. J. Kamper, "Analytical prediction of rotor eddy current loss due to stator slotting in PM machines," in *Energy Conversion Congress and Exposition (ECCE), 2010 IEEE*, 2010, pp. 992-995.

[72] M. G. Say, *The Performance and Design of Alternating Current Machines: Transformers, Three Phase Induction Motors and Synchronous Machines*: Pitman, 1943.

[73] Q. Graham, "The M. M. F. Wave of Polyphase Windings With Special Reference to Sub-Synchronous Harmonics," *American Institute of Electrical Engineers, Transactions of the,* vol. XLVI, pp. 19-29, 1927.

[74] W. Pan, W. Li, L. Y. Cui, X. M. Li, and Z. H. Guo, "Rare earth magnets resisting eddy currents," *Magnetics, IEEE Transactions on,* vol. 35, pp. 3343-3345, 1999.

[75] K. W. Klontz, T. J. E. Miller, H. Karmaker, and P. Zhong, "Short-circuit analysis of permanent-magnet generators," in *Electric Machines and Drives Conference, 2009. IEMDC '09. IEEE International*, 2009, pp. 1080-1087.

[76] I. M. Canay, "Modelling of alternating-current machines having multiple rotor circuits," *Energy Conversion, IEEE Transactions on,* vol. 8, pp. 280-296, 1993.

[77] IEEE, "IEEE Guide: Test Procedures for Synchronous Machines Part I-- Acceptance and Performance Testing Part II-Test Procedures and Parameter Determination for Dynamic Analysis," *IEEE Std 115-2009 (Revision of IEEE Std 115-1995),* pp. 1-0, 2010.

[78] A. M. Technologies. (2014, 19/03/2014). *Arnold Magnetic Technologies Corporation - High Energy Bonded Magnets*. Available: http://www.arnoldmagnetics.com/Plastiform_Information.aspx

[79] G. Bertotti, "General properties of power losses in soft ferromagnetic materials," *Magnetics, IEEE Transactions on,* vol. 24, pp. 621-630, 1988.

[80] P. A. Hargreaves, B. C. Mecrow, and R. Hall, "Calculation of Iron Loss in Electrical Generators Using Finite-Element Analysis," *Industry Applications, IEEE Transactions on,* vol. 48, pp. 1460-1466, 2012.

[81] K. Atallah, Z. Q. Zhu, and D. Howe, "An improved method for predicting iron losses in brushless permanent magnet DC drives," *Magnetics, IEEE Transactions on,* vol. 28, pp. 2997-2999, 1992.

[82] G. Bertotti, A. Boglietti, M. Chiampi, D. Chiarabaglio, F. Fiorillo, and M. Lazzari, "An improved estimation of iron losses in rotating electrical machines," *Magnetics, IEEE Transactions on,* vol. 27, pp. 5007-5009, 1991.

[83] C. I. McClay and S. Williamson, "Influence of rotor skew on cage motor losses," *Electric Power Applications, IEE Proceedings* -, vol. 145, pp. 414-422, 1998.

[84] A. Belahcen and A. Arkkio, "Comprehensive Dynamic Loss Model of Electrical Steel Applied to FE Simulation of Electrical Machines," *Magnetics, IEEE Transactions on,* vol. 44, pp. 886-889, 2008.

[85] N. Hyuk, H. Kyung-Ho, L. Jeong-Jong, H. Jung-Pyo, and K. Gyu-Hong, "A study on iron loss analysis method considering the harmonics of the flux density waveform using iron loss curves tested on Epstein samples," *Magnetics, IEEE Transactions on,* vol. 39, pp. 1472-1475, 2015.

[86] Infolytica. (14-05-2013). *Core Loss and Efficiency Calculations with Infolytica software*. Available: http://www.infolytica.com/en/applications/ex0124/

[87] N. Takahashi and D. Miyagi, "Effect of stress on iron loss of motor core," in *Electric Machines & Drives Conference (IEMDC), 2011 IEEE International*, 2011, pp. 469-474.

[88] D. Miyagi, K. Miki, M. Nakano, and N. Takahashi, "Influence of Compressive Stress on Magnetic Properties of Laminated Electrical Steel Sheets," *Magnetics, IEEE Transactions on*, vol. 46, pp. 318-321, 2010.

[89] C. R. Sullivan, "Computationally efficient winding loss calculation with multiple windings, arbitrary waveforms, and two-dimensional or three-dimensional field geometry," *Power Electronics, IEEE Transactions on*, vol. 16, pp. 142-150, 2001.

[90] R. Wrobel, A. Mlot, and P. H. Mellor, "Contribution of End-Winding Proximity Losses to Temperature Variation in Electromagnetic Devices," *Industrial Electronics, IEEE Transactions on*, vol. 59, pp. 848-857, 2012.

[91] H. Hamalainen, J. Pyrhonen, J. Nerg, and J. Talvitie, "Ac resistance Factor of Litz-Wire Windings Used in Low-Voltage High-Power Generators," *Industrial Electronics, IEEE Transactions on*, vol. PP, pp. 1-1, 2013.

[92] M. Centner and U. Schafer, "Optimized Design of High-Speed Induction Motors in Respect of the Electrical Steel Grade," *Industrial Electronics, IEEE Transactions on*, vol. 57, pp. 288-295, 2010.

[93] W. L. Ringland and L. T. Rosenberg, "A New Stator Coil Transposition for Large Machines," *Power Apparatus and Systems, Part III. Transactions of the American Institute of Electrical Engineers,* vol. 78, pp. 743-746, 1959.

[94] C. R. Sullivan, "Optimal choice for number of strands in a litz-wire transformer winding," *Power Electronics, IEEE Transactions on,* vol. 14, pp. 283-291, 1999.

[95] P. D. Pfister and Y. Perriard, "A 200 000 rpm, 2 kW slotless permanent magnet motor," in *Electrical Machines and Systems, 2008. ICEMS 2008. International Conference on*, 2008, pp. 3054-3059.

[96] P. H. Mellor, D. Roberts, and D. R. Turner, "Lumped parameter thermal model for electrical machines of TEFC design," *Electric Power Applications, IEE Proceedings B,* vol. 138, pp. 205-218, 1991.

[97] A. Boglietti, A. Cavagnino, D. Staton, M. Shanel, M. Mueller, and C. Mejuto, "Evolution and Modern Approaches for Thermal Analysis of Electrical Machines," *Industrial Electronics, IEEE Transactions on,* vol. 56, pp. 871-882, 2009.

[98] A. M. El-Refaie, N. C. Harris, T. M. Jahns, and K. M. Rahman, "Thermal analysis of multibarrier interior PM synchronous Machine using lumped parameter model," *Energy Conversion, IEEE Transactions on*, vol. 19, pp. 303-309, 2014.

[99] Q. Yu, C. Laudensack, and D. Gerling, "Improved lumped parameter thermal model and sensitivity analysis for SR drives," in *Electrical Machines (ICEM), 2010 XIX International Conference on*, 2010, pp. 1-6.

[100] M. D. Ltd. (2014, 20-03-2014). *Motor Design Limited | About Motor-CAD*. Available: http://www.motor-design.com/motorcad.php

[101] S. Nategh, O. Wallmark, M. Leksell, and Z. Shuang, "Thermal Analysis of a PMaSRM Using Partial FEA and Lumped Parameter Modeling," *Energy Conversion, IEEE Transactions on*, vol. 27, pp. 477-488, 2012.

[102] C. Mejuto, M. Mueller, M. Shanel, A. Mebarki, and D. Staton, "Thermal modelling investigation of heat paths due to iron losses in synchronous machines," in *Power Electronics, Machines and Drives, 2008. PEMD 2008. 4th IET Conference on*, 2008, pp. 225-229.

[103] D. Staton, A. Boglietti, and A. Cavagnino, "Solving the More Difficult Aspects of Electric Motor Thermal Analysis in Small and Medium Size Industrial Induction Motors," *Energy Conversion, IEEE Transactions on*, vol. 20, pp. 620-628, 2005.

[104] D. A. Staton and A. Cavagnino, "Convection Heat Transfer and Flow Calculations Suitable for Electric Machines Thermal Models," *Industrial Electronics, IEEE Transactions on*, vol. 55, pp. 3509-3516, 2008.

[105] Y. K. Chin and D. A. Staton, "Transient thermal analysis using both lumped-circuit approach and finite element method of a permanent magnet traction motor," in *AFRICON, 2014. 7th AFRICON Conference in Africa*, 2014, pp. 1027-1035 Vol.2.

[106] C. Ginet, R. Joho, and M. Verrier, "The Turbogenerator - A Continuous Engineering Challenge," in *Power Tech, 2016 IEEE Lausanne*, 2016, pp. 1055-1060.

[107] Z.-n. Ye, W.-d. Luo, W.-m. Zhang, and Z.-x. Feng, "Simulative analysis of traction motor cooling system based on CFD," in *Electric Information and Control Engineering (ICEICE), 2011 International Conference on*, 2011, pp. 746-749.

[108] G. Xiaofeng, C. Jintao, W. Zhigan, and Y. Jianping, "End-region's thermal analysis in compact PMAC servomotor," in *Electrical Machines and Systems, 2005. ICEMS 2005. Proceedings of the Eighth International Conference on*, 2005, pp. 326-329 Vol. 1.

[109] G. D. Neal, K. Ohsang, and D. K. Lieu, "Ceramic filled thermoplastic encapsulation as a design feature for a BLDC motor in a disk drive," *Magnetics, IEEE Transactions on*, vol. 37, pp. 793-798, 2001.

[110] M. G. C. Ltd., "Thermally Conductive Epoxy Encapsulating & Potting Compound 832TC Technical Data Sheet," ed, 2012.

[111] R. A. Baudry and E. I. King, "Improved Cooling for Generators of Large Rating," *Power Apparatus and Systems, IEEE Transactions on*, vol. 84, pp. 106-114, 1965.

[112] R. Dabbousi, H. Balfaqih, Y. Anundsson, and D. Savinovic, "A comparison of totally enclosed motor coolers commonly used in the COG industry," in *Petroleum and Chemical Industry Conference Europe - Electrical and Instrumentation Applications, 2008. PCIC Europe 2008. 5th*, 2008, pp. 1-5.

[113] C. Nagpal, P. K. Jain, and V. V. K. Reddy, "Rotor vent hole shape studies on totally enclosed fan cooled motor," in *Power Electronics, Drives and Energy Systems (PEDES), 2012 IEEE International Conference on*, 2012, pp. 1-6.

[114] H. P. Liu, V. Lelos, and C. S. Hearn, "Transient 3-D thermal analysis for an air-cooled induction motor," in *Electric Machines and Drives, 2005 IEEE International Conference on*, 2005, pp. 417-420.

[115] A. J. Mitcham and J. J. A. Cullen, "Permanent magnet generator options for the More Electric Aircraft," in *Power Electronics, Machines and Drives, 2002. International Conference on (Conf. Publ. No. 487)*, 2002, pp. 241-245.

[116] T. Onuki, S. Wakao, M. Tokuhisa, and A. Maeda, "A novel approach to design optimization of ventilation holes in induction motors," in *Electric Machines and Drives, 1999. International Conference IEMD '99*, 1999, pp. 478-480.

[117] J. Mugglestone, S. J. Pickering, and D. Lampard, "Effect of geometric changes on the flow and heat transfer in the end region of a TEFC induction motor," in *Electrical Machines and Drives, 1999. Ninth International Conference on (Conf. Publ. No. 468)*, 1999, pp. 40-44.

[118] Hexcel, "HexTow® IM7 Carbon Fiber," ed, 2014.

[119] D. Pont. (2014, 25/03/2014). *Kevlar Fiber*. Available: http://www.dupont.co.uk/products-and-services/fabrics-fibers-

nonwovens/fibers/brands/kevlar/products/dupont-kevlar-fiber.html

[120] J. Chin, A. Forster, C. Clerici, L. Sung, M. Oudina, and K. Rice, "Temperature and humidity aging of poly(p-phenylene-2,6-benzobisoxazole) fibers: Chemical and physical characterization," *Polymer Degradation and Stability*, vol. 92, pp. 1234-1246, 7// 2016.

[121] Cogent. (25/03/2014). *Cogent - Surahammars Bruk*. Available: http://www.sura.se/Sura/hp_main.nsf/startupFrameset?ReadForm

[122] IEC, "BS EN 60085:2008 Electrical insulation. Thermal evaluation and designation," ed: BSI, 2008.

[123] N. E. W. Technologies, "Product Slection Guide," ed.

[124] D. Pont, "DUPONT™ NOMEX® LAMINATES," ed.

[125] K. N. A. LLC. (2014, 25/03/2014). *APICAL Type AV Polyimide Film*. Available:http://www.kanekatexas.com/Apical_polymideAV.html

[126] Elantas, "Epoxylite TSA 220," ed, 2014.

[127] J. J. Wolmarans, M. Van der Geest, H. Polinder, J. A. Ferreira, and D. Zeilstra, "Composite materials for low loss rotor construction," in *Electric Machines & Drives Conference (IEMDC), 2011 IEEE International*, 2011, pp. 295-299.

[128] P. E. M. Ltd. (2013, 24/03/2014). *LFR Current Probe | PEM*. Available: http://www.pemuk.com/products/lfr-current-probe.aspx